DNA Origami-Templated Synthesis of Semiconducting Polythiophene Filaments

Dissertation

zur Erlangung des akademischen Grades
Doctorum rerum naturalium (Dr. rer. nat.)
von

M.Sc. Johanna Zessin
geboren am 26. April 1989 in Dresden

vorgelegt dem Bereich
Mathematik und Naturwissenschaften
an der Technischen Universität Dresden

Eingereicht am 04.03.2019

Gutachter
Prof. Dr. rer. nat. et Ing. habil. Michael Mertig
Prof. Dr. Brigitte Voit

Die Dissertation wurde in der Zeit von 06/2015 bis 03/2019 am Leibniz-Institut für Polymerforschung Dresden e.V. und der Technischen Universität Dresden, Physikalische Chemie für Mess- und Sensortechnik angefertigt.

*"Why do humans do science? Why do humans do art?
These things that are least important to our survival are the very things that make us human."*

Savas Dimopoulos, The Particle Fever.

Kurzfassung

Die Herstellung funktionaler und strukturell wohldefinierter Nanostrukturen ist eine Voraussetzung, um hochentwickelte *Device* im Bereich der Nanoelektronik oder Nanooptik zu entwickeln. *Bottom-Up*-Verfahren, welche auf biomolekularen Selbstassemblierungsprozessen basieren, haben sich hierfür, aufgrund ihrer hoch parallelen Synthese, als besonders effizient erwiesen. In dieser Arbeit wurde die DNA-Origami-Technik genutzt, um eine funktionale Nanostruktur für elektronische Schaltkreise oder optische Anwendungen zu assemblieren. Planare DNA-Origami-Strukturen können als molekulare Steckbretter dienen, um funktionale Objekte mit Nanometer-Präzision anzuordnen. Diese Arbeit verwendete als solch ein Objekt ein π-konjugiertes Polymer. Im Vergleich zu anorganischen Nanoobjekten, wie metallische Nanopartikel, zeichnen sich diese Polymere durch mechanische Flexibilität und ein leichtes Gewicht aus. Aufgrund ihres π-konjugierten Rückgrates sind diese Polymere optisch und elektronisch funktional. Diese Eigenschaften können über ihre molekulare Struktur eingestellt werden. Dotiert sind diese Polymere Halbleiter oder sogar Leiter. Ihre Funktionalität wurde in diversen optoelektronischen und elektronischen Bauteilen, wie z.B. organischen Feldeffekt-Transistoren, bewiesen. Für Anwendungen auf der Nanoskala sind die Polythiophenderivate des Typ P3RT besonders interessant. Deren Synthese, die Kumada Katalysatorenübertragungspolykondensation, folgt einem kontrollierten Kettenwachstumsmechanismus. Die Polymere zeichnen sich durch eine eng verteilte, einstellbare Molmasse und definierte Endgruppen aus.

Im ersten Teil dieser Arbeit wurde das Polythiophenderivat designt und synthetisiert. Eine Oligoethylenglykol-Seitenkette gewährleistet die Löslichkeit in Wasser und Kompatibilität zur DNA. Über einen *ex-situ* Initiator wurde eine funktionelle Endgruppe eingeführt, um das Polymer zugänglich zur DNA-Origami-Assemblierung zu machen. Mittels verschiedener Charakterisierungen wurden die definierte Struktur und gute Löslichkeit in Wasser demonstriert. Im zweiten Abschnitt dieser Arbeit wurde die elektronische Aktivierung dieses Polythiophens durch molekulares Dotieren auf der Mikroskala untersucht. Der Einfluss des Dotierungmittels 2,3,5,6-Tetrafluoro-7,7,8,8-tetracyanoquinodimethan auf die optischen, morphologischen und elektronischen Eigenschaften des Polymers als dünner Film wurde untersucht, um optimale Dotierungskonditionen zu etablieren. Die dotierten Polymerfilme zeigten eine deutlich verbesserte Leitfähigkeit im Vergleich zu unbehandelten Filmen. Im dritten Abschnitt dieser Arbeit wurde die DNA-Origami-gelenkte Anordnung des Polythiophens untersucht. Hierfür wurde das Polymer zunächst an ein modifiziertes, synthetisches Oligonukleotid

gebunden. Das resultierende Blockcopolymer wurde dann ortsspezifisch an DNA-Überhänge angebunden, welche sich eng aufgereiht auf einer planare DNA-Origami-DNA-Origami-Struktur befanden. Die Polymer-DNA-Hybridstrukturen wurden mittels hochauflösender Rasterkraftmikroskopie charakterisiert. Aufgrund von π-π Stapelwechselwirkungen der Polythiophenrückgrate kam es zur Ausbildung supramolekulare Polymerdrähte. Die Abmaße dieser Drähte wurde über der Anordnung der DNA-Überhänge gesteuert. Es wurde gezeigt, dass durch schrittweises Aufbrechen der π-π-Stapelwechselwirkung die Fluoreszenz dieser Polythiophendrähte verändert werden kann. Die Fähigkeit könnte nützlich sein, um die optischen Eigenschaften dieser Drähte für photonische Leitungen einfach auf Sender und/oder Empfänger abzustimmen. Des Weiteren sind diese Wechselwirkungen nötig, um Ladungsträger durch diese Drähte zu transportieren. Mittels Leitfähigkeitsrasterkraftmikroskopie wurden erste Untersuchungen getätigt um die Fähigkeit dieser Polythiophen-DNA-Hybridstrukturen als elektronischer Draht zu evaluieren. Im Rahmen dieser Arbeit konnte kein Ladungstransport festgestellt werden.

Zusammenfassend wurde eine neuartige, funktionale Polythiophen-basierende Nanostruktur mittels der DNA-Origami-Technik synthetisiert. Solche Polymer-DNA-Hybridstrukturen versprechen eine vielfältige Anwendbarkeit als optische oder elektronische Bauteile in Schaltkreisen.

Acknowledgements

I cordially thank my supervisor Prof. Michael Mertig for giving me the excellent opportunity to work on such an exciting and multifaceted topic. I enjoyed all the scientific and non-scientific discussions. I like to extend my sincerest thanks to Dr. Anton Kiriy and Prof. Brigitte Voit for welcoming me at the IPF, for co-supervising me and introducing me to the field of polymer chemistry. I highly appreciate their excellent support at all levels of my doctoral studies. I am very grateful to Prof. Danny Porath and his group for hosting me at the Hebrew University of Jerusalem, Israel and for the excellent collaboration beyond my research stay. Furthermore, I thank Danny for his encouragement concerning my future scientific career.

The "Center for Advancing Electronics Dresden" (cfaed) of the TU Dresden belongs my grateful thanks to funding not only my Ph.D. position but in addition to it, granting me the Inspire Grant, which allowed me to go to Jerusalem for this valuable research stay. Additionally, I acknowldege the Leibniz-Institut für Polymerforschung Dresden e.V. and the Graduate Academy of the TU Dresden for their financial support.

During my PhD time I further collaborated with a lot of excellent scientists from different disciplines, just to mention a few (random order): Dr. Sisi Jia (John Hopkins University, Baltimore), Avigail Stern (Hebrew University Jerusalem Israel), Nitzan Yanay (Hebrew University Jerusalem Israel), Toni Haugwitz (Technische Universität Dresden), Julia Hann (Technische Universität Chemnitz), Türkan Bayarak (Helmholtz Center Dresden Rossendorf), Jingjing Ye (Universität Leipzig), Anja Steiner (Leibniz Institut für Polymerforschung Dresden e.V.), Max Schnepf (Leibniz Institut für Polymerforschung Dresden e.V.), Jakob Zessin (Technische Universität Dresden), Dr. Alfred Kick (Kurt Schwabe Institut Meinsberg, e.V.) and Dr. Juliane Posseckardt (Kurt Schwabe Institut Meinsberg, e.V.).

Special thanks go to Dr. Franziska Fischer for introducing me to the exciting topic of the DNA origami technique, for spending long hours at the AFM to teach me high-resolution imaging, proof-reading of many abstracts, posters, etc. and for general support.

I am very grateful to all the people, who helped me during the writing and proof-reading process of this thesis, especially: Dr. Andreas Heerwig, Dr. Anton Kiriy, Prof. Michael Mertig, Dr. Franziska Fischer and Uriel Josef Santiesteban.

I would like to thank the people of administration from IPF and TU Dresden who patiently helped me with any kind of bureaucracy and my poorly written "Dienstreiseanträge," namely Carmen Krause, Mandy Faulhaber, and Ines Kube.

Furthermore, I thank all colleagues from the IPF, the TU Dresden and the KSI Meinsberg for any help with analytic measurements, instrumentations, and general support, particularly (mentioned in random order): Dr. Doris Pospiech, Dr. Petr Formanek, Dr. Susanne Boye, Dr. Eva Bittrich, Dr. Klaus-Jochen Eichhorn, Dr. Mikhail Malanin, Dr. Hartmut Komber, Dr. Dieter Jehnichen, Dr. Yevhen Karpov, Andreas Janke, Dr. Ulrich Oertel, Dr. Katrin Günther, Dr. Andreas Heerwig, Dr. Mathias Lakatos, Dr. Juliane Posseckardt and Dr. Alfred Kick. Special thanks go to the guys of the lab P2 for making long lab hours enjoyable: Christoph Horn, Fabian Borrmann, Christopher Schutzeichel, and Tim Erdmann.

Über diese Arbeit hinaus, danke ich meiner Familie und meinen Freunden, die Anwandlungen von Frustration stets abgewendet haben und es mir leicht gemacht haben, die Doktorarbeit ab und an zu vergessen, um das Leben zu genießen. Besonderer Dank gilt dabei meinen Geschwistern Jakob, Matthes und Elisabeth, meinen Großeltern, meinem Liebsten Marcus, und meinen wundertollen Freunden Jenne, Laura, Gregory, UJ und der ganzen Schmäh-Gang. Mein größter Dank geht jedoch an meine Eltern, für ihre bedingungslose Liebe und Unterstützung. Von ganzem Herzen, allerliebsten Dank Mama und Papa!

Contents

List of Figures

List of Tables

1 Introduction and Objectives

1.1 Introduction

With his talk - “There’s Plenty of Room at the Bottom: An Invitation to Enter a New Field of Physics” in 1959 Richard Feynman encouraged research to deal with "the problem of manipulating and controlling things at a small scale".[1] In this talk, Feynman anticipated devices, such as quantum computers, new imaging techniques, and molecular robots, which are nowadays experimentally implemented. Today, this research is pooled under the general term nanotechnology defined by “the understanding and control of matter at dimensions of roughly 1 to 100 nanometers.”[2]
One primary aspect of nanotechnology, the development of functional nanostructures, is still actively investigated by research and industry. The organization of atoms and molecules determines their properties and, thus, their functionality. Feynman proposed biology as a model system, where the production of new substances, storing of information or the operation of motors proceeds at the nanoscale. Biological systems construct functional nanostructures by bottom-up approaches assembling molecule per molecule into the desired structure relying on the ability of self-recognition. The driving forces behind these processes are weak, non-covalent intermolecular interactions, namely van der Waals interactions, hydrogen bonding, and hydrophobic interactions. Individually, these forces may be weak, but collectively they exhibit strength. In contrast to top-down approaches, error-correction is possible during loosely joined intermediate states, thereby facilitating the creation of complex structures with structural accuracy. Moreover, such self-assembly processes proceed in parallel granting a high output of structures within one batch.
Accordingly, utilizing biomolecules, including DNA,[3] proteins,[4] liposomes[5] or viruses,[6] as building blocks appears natural to develop functional nanostructures. Structural DNA-based nanotechnology is particularly interesting due to the programmable nature of the Watson-Crick base pairing and the nanometer-sized dimensions of the DNA molecule. Since Ned Seeman introduced DNA as a programmable construction material in 1982,[7] numerous forms, such as crystal lattices,[8] nanotubes,[9] polyhedra,[10] and arbitrary two dimensional (2D)[11] or three dimensional (3D)[12] structures, have been synthesized by different assembly techniques. The DNA origami technique is the most significant because of its simple but precise design rules, with which diverse shapes can be formed with a high yield.[11] A DNA origami nanostructure can act as a molecular breadboard organizing functional hetero-objects spatially well-controlled in a highly parallel manner. A DNA origami-based breadboard provides a site-specificity down to 2 nm[13] and, in theory, even below 1 nm. Basic devices with plasmonic,[14] catalytic,[15] sensing[16] and electronic[17] functionality have been fabricated.
So far, mostly metallic nanoparticles and metallized DNA templates supply the optical or electronic functionality. These stiff and rigid inorganic materials can deform the soft DNA leading to a spatially less defined structure. Therefore, it

can be advantageous to use a π-conjugated polymer (CP), which is structurally similar to DNA. Such polymers possess optical and electronic functional properties.[18–20] Their molecular nature enables modification of their features by their structure.[21] Furthermore, CPs are mechanically flexible, light-weight and can be straightforwardly processed into low-cost and large-scale integrated circuits on flexible substrates. The majority of research focuses on the application of CPs as (semi-)conducting 2D bulk material in various (opto-)electronic devices, such as organic field effect transistor (OFET),[22] organic light emitting diode (OLED),[20] organic solar cells[23] or sensors.[24] However, CPs are not restricted to 2D bulk devices but have been further studied as single molecular wires[25] and as supramolecular, one-dimensional fibers.[26,27]

One of the most promoinent class of CPs are polythiophenes and their derivatives, particularly the class of poly(3'-substituted thiophene) (P3RT). Polythiophenes are stable in their undoped and doped state, offer a wide spectrum of chemical modifications and provide good solution processability.[28] They are one of the standard polymers in organic electronic devices, either as semiconducting or conducting layer.[29,30] In addition to their electronic functionality, polythiophenes provide excellent optical properties, and have been used for sensing devices.[31,32] P3RTs can be polymerized by a chain-growth polycondensation leading to well-defined structural polymers.[33] Such polymers are particularly interesting for an application at the nanoscale.

The molecular nature of CPs, such as polythiophenes, is not solely advantageous. Their conducting mechanism is complex and determined by weak intermolecular interactions leading to a low mobility and concentration of the charge carriers.[34] Therefore, these polymers are not as straightforwardly utilized beyond research as could be expected. Nevertheless, CPs are a promising material to incorporate functionality into DNA nanostructures.

Despite the structural diversity of CPs, only few polymers have been used so far as functional objects in DNA origami-based nanostructures.[35–37] At the start of this thesis, only two reports have been documented,[35,36] and, even now, CP functionalized DNA origami structures remain scarce in literature.[37–39] In a first approach, Wang *et al.* synthesized polyaniline by enzyme-catalyzed oxidative polymerization directly on the DNA origami template.[36] This approach is limited to polymers accessible by oxidative polymerization, which are commonly simple polymer structures. Furthermore, only mild synthesis conditions are applicable due to the direct fabrication atop the DNA template. Knudsen *et al.* pursued an advanced approach. First, a bottle-brush type polymer was synthesized composed of a polyparaphenylenevinylene backbone and oligonucleotide side-chains, and, in a second step, deposited on the DNA origami template.[35] This type of CPs are mainly applied in optoelectronic devices, such as organic solar cells,[20] but are not suitable for electronic devices. Furthermore, the polymer was obtained by a step-growth polymerization and thus, characterized by a broad molecular weight distribution.

Recent approaches to template CPs by DNA origami, have solely concentrated on the optical functionality of the respective CP, most likely due to the complex conducting mechanism.[37–39] The construction of DNA origami-templated functional nanostructures using CPs with electronic functionality is still missing.

In contrast to metallic nanoparticles or metallization of DNA, there are, so far, no established protocols on how to organize these polymers by DNA-based nanostructures. CPs assembled on DNA origami structures remain still scarce in literature.[35–39] In contrast to previous reports, the CP used herein, was motivated as electronic and not optical functional material. Consequently, this thesis aimed to establish an approach to organize a functional polymer - a polythiophene derivative - by the DNA origami method into a confined, functional nanostructure. These DNA-immobilized polythiophenes have been motivated as building blocks for self-assembled circuits.

1.2 Objectives of the Doctoral Thesis

The overall aim of this thesis to synthesize in a self-assembly process an electronic functional and spatially confined nanostructure composed of a semiconducting polythiophene derivative and a planar DNA origami template was performed by three subordinate objectives:

1. The first objective of this project was the design, synthesis, and characterization of a polythiophene derivative which is suitable for nanoscaled devices, compatible to the biomolecule DNA and accessible to the DNA origami-templated assembly.

2. The second objective of this thesis targeted to integrally view the polythiophene's fundamental electronic functionality as 2D bulk material. It was further targeted to comprehend the effect on the polymer's optical, structural and electrical properties when treated with the molecular dopant 2,3,5,6-tetrafluoro-7,7,8,8-tetracyanoquinodimethane (F4TCNQ).

3. The third goal of this thesis was to site-specifically arrange the polythiophene derivative on a planar DNA origami structure into a spatially confined, functional nanostructure. It was aimed to deposit the polymer *via* a controlled one-to-one attachment, where a supramolecular polymer provides the functionality.

2 Background

2.1 π-Conjugated Polymers

For a long time, applying plastics as electronic conducting material would have been considered outrageous. Quite the contrary, polymers were and are still used as insulators to shield wires and electronic devices. In the last four decades, a new class of polymers has changed this view of perspective though - the class of CPs. Under certain conditions, these polymers can conduct current.[18,19,40] However, the conducting mechanism entirely differs from inorganic (semi-)conductors (Section 2.1.1).

An essential treatment to enhance the conducting performance of CPs is doping. This process describes the external incorporation of charge carriers into the polymer system. Doped polymer films were firstly produced in similar experiments by Alan J. Heeger, Alan MacDiarmid and Hideki Shirakawa in 1977.[18,19] They found that polyacetylene possesses conductivity in the range of metals when oxidized by halogen vapor. This discovery was considered a breakthrough moment for CP-research and was, therefore, regarded with the Nobel prize in chemistry in 2001. Nowadays, molecular doping, where small organic molecules serve as dopants, is the state-of-the-art treatment to obtain stably doped polymer films (Section 2.1.2).[41]

Doped polyacetylenes did reach metallic levels of conductivity, but they were unstable in the presence of oxygen under operating conditions. Since then, a vast effort was and is still put into the development of new polymer structures to obtain better and better polymers. One of the most prominent types of CPs are the polythiophene derivatives P3RT. Their side-chain can be used to customize the properties concerning the desired application. Different synthesis approaches were reported to obtain P3RTs.[42–45] However, these early state synthesis approaches could not provide full control over structural features of the polymers. The so-called *ex-situ*-initiated Kumada catalyst-transfer polycondensation obtained the highest control over the polymer structure due to its quasi-living nature.[33] The well-defined molecular structure and corresponding ability to assemble into defined structures turns them into advantageous components for nanoscaled devices (Section 2.1.3).

2.1.1 Fundamentals of Conjugated Polymers

In bulk materials, the atoms' discrete energy levels fan out to bands, namely the valence band and the conduction band. Whether a material is insulating, semiconducting, or conducting depends on the availability of electrons in the conduction band. In case of insulators and semiconductors, conduction and valence band are separated by an energy gap E_g of forbidden states. For semiconductors, E_g is small enough ($<4\,\mathrm{eV}$) to be surpassed by external excitation. For inorganic solids, the energy band theory is suitable to visualize whether a material is conducting, semiconducting or insulating. However, the band theory does not adequately explain why CPs are conducting under certain conditions.

Through the eyes of chemists, the electronic functionality of CPs originates from

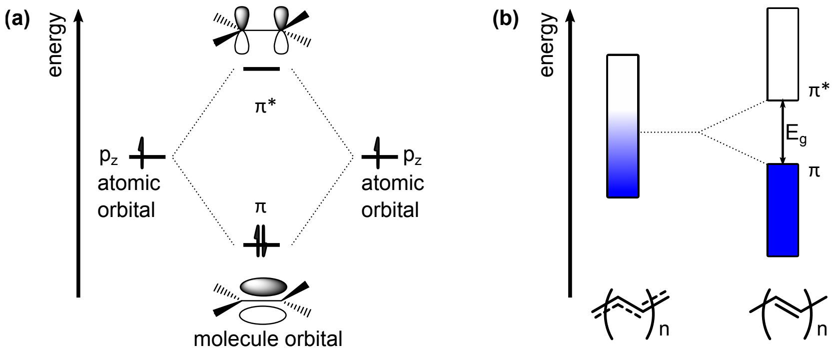

Figure 2.1: (a) Formation of a bonding π- and antibonding π*-bond through the electrons of two p_z orbitals. (b) Splitting of a theoretically expected half-filled band of fully conjugated polyacetlylene into two bands separated by an energy gap E_g due to the Peierls distortion.

their π-conjugated backbone. The simplest structure, the polyacetylene, is composed of sp^2-hybridized carbon atoms which are bound over alternating single and double bonds. Adjacent carbon atoms are connected by strong molecular σ-bonds which are split into a bonding and anti-bonding orbital. Due to the sp^2 hybridization of the carbon atoms, the free electrons of the p_z orbitals can form an additional bond, the weaker overlapping π-bonds. The corresponding bonding and anti-bonding π-orbitals are illustrated in Figure 2.1a. In the early state of CP-research, it was expected that these double and single bonds are delocalized, as depicted in Figure 2.1b on the left side. Correspondingly, the p_z orbitals would be continuously overlapping, and electrons would be able to move along the polymer backbone. However, since a CP molecule is a quasi-one-dimensional conductor, the so-called Peierls distortion[46] becomes effective, which describes the energetic instability of one dimensional (1D) conductors. Consequentially, the π-orbitals are not entirely overlapping but localized, as depicted in Figure 2.1b on the right side. Instead of a half-filled band, the bonding orbitals are filled with two electrons of antiparallel spin forming the valence band. The antibonding orbitals remain empty, forming the conduction band. Hence, a gap with the energy E_g develops. According to the molecular orbital theory, the bonding orbital π corresponds to the highest occupied molecular orbital (HOMO) and the antibonding orbital π* to the lowest unoccupied molecular orbital (LUMO) level.

Origin of Low Charge Carrier Concentration

The promotion of an electron from HOMO to LUMO through, e.g., the absorption of a photon, generates a neutral excited state (exciton) and is related to the $\pi \rightarrow \pi^*$ transition. The characteristic absorption wavelength to promote such a transition can range from the ultraviolet to the near infrared region but is typically around 400 to 500 nm. Accordingly, the E_g of these polymers range between 1.5 to 3 eV.[47] Such a bandgap energy would correspond to semiconductors. However, CPs are not conducting when excited by light and instead show insulating properties at room temperature.

The solid state of CPs, on the contrary to conventional semiconductors, is defined by weak intermolecular interactions, namely hydrogen bondings and van der Waals' interactions (including Keesom forces between permanent dipoles; London dispersion forces between instantaneously induced dipoles and Debye forces between a permanent dipole and a corresponding induced dipole). Due to this weak intermolecular interactions, the expansion of the electronic wave function is limited in the polymeric system which is expressed in low dielectric constants ε of around 2 to 4.[34] As a result, the excited states are localized at the molecule unit with a diffusion length of around 1 nm. The binding energy of so-called Frenkel excitons can be estimated from the Coulomb attraction and is 0.5 to 1 eV. This binding energy is larger than the available thermal energy at room temperature (0.025 eV). In comparison, for inorganic semiconductors with high dielectric constants ($\varepsilon > 11$), Coulomb attraction forces between hole and electron are negligible. The generated excitons, so-called Wannier-Mott excitons, are delocalized (diffusion length > 10 nm) in the inorganic crystal and correspondingly available for charge transport. The strongly linked excitons determine the electronic functionality of CPs.

Turning CPs (semi-)conducting and useful for devices requires the introduction of charge carriers and the increase of the charge carrier concentration to a reasonable level. Despite separating the neutral electron-hole pair, charged species can be introduced into the CP matrix externally. This process, where an electron is (electro-)chemically either removed from the valence band (p-type) or added to the conducting band (n-type), is called doping - analogous to inorganic semiconductors - and is further examined in Section 2.1.2.

Origin of Low Charge Carrier Mobility

In addition to the low charge carrier concentration being challenging in CPs, the low charge transport mobility presents challenges as well. In inorganic semiconductors, the charge carriers are mobile due to the strong covalent bonds resulting in a charge carrier mobility of around $1000\,\mathrm{cm^2\,V^{-1}\,s^{-1}}$ (crystalline silicon). The mobility in CPs is distinctly lower with only $10^{-5}\,\mathrm{cm^2\,V^{-1}\,s^{-1}}$. This issue is also a consequence of the weak intermolecular interactions acting in organic solids and the localized electronic wave function. Therefore, the charge transport properties are strongly influenced by disorder, caused by defects, chain ends, chain entanglement, voids or impurities. A further reduction of mobility is caused by additional trapping states and scattering centers due to the polarization of the environment and soft phonons.[47]

In general, charge carriers can move *via* two ways through immobilized CPs, as displayed in Figure 2.2a for a 2D bulk material. The first option is to move coherently along the polymer chain (intrachain transport), which is possible as long as the π-orbitals are in-plane (pathway 1 in Figure 2.2a). The length that the repeat units are in-plane is referred to as conjugation length. Due to conformational

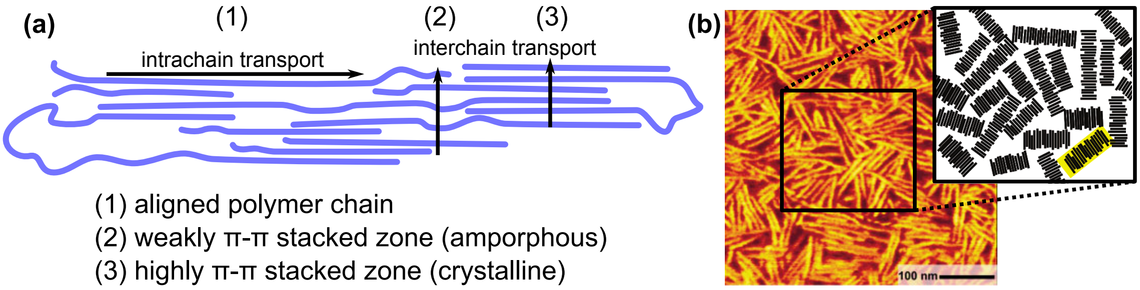

Figure 2.2: (a) Possible charge transport in conjugated polymers *via* intrachain (1) or interchain transport (2 and 3). (b) AFM image and scheme of a P3HT (MW<$4000\,\mathrm{g\,mol^{-1}}$) morphology with a highly ordered packing structure, reproduced from (*48*).

disorder, such as torsional twisting or defects, the effective conjugation length is commonly shorter than the polymer backbone's length. Prins *et al.* demonstrated by a pulse-radiolysis time-resolved microwave conductivity measurements on single polyfluorene molecules that the charge transport mobility strongly depends on the degree of coiling and the conjugation length.[25] While coiled polymers showed a mobility of around $1\,\mathrm{cm^2\,V^{-1}\,s^{-1}}$, the mobility of fully stretched polymers was almost 50 times higher ($45\,\mathrm{cm^2\,V^{-1}\,s^{-1}}$). The conjugated length determines the optoelectronic properties of the polymer, particularly the position of the HOMO and LUMO level. In CPs the standard deviation of the energy levels are in the range of 50 to 100 meV[49,50] and follow commonly a Gaussian distribution. One conjugation segment is considered as one independent chromophore unit.[51] Disorder, which results from the variation of energy levels between different conjugation segments, is referred to diagonal disorder.[52]

Second, the charge carriers can move beyond chain ends or the conjugation length through jumping to adjacent chains, which is referred to as interchain transport (pathway 2 and 3 in Figure 2.2). The mobility of this interchain hopping transport is distinctly lower than the intrachain transport[53,54] and depends on the packing order of the polymer chains. The polymer chains of CPs can self-organize due to π-π-interactions between the conjugated backbones. Especially in thin films, the polymer chains self-organize themselves into micro-crystalline regions with strong π-π-stacking interactions. However, these highly π-π-stacked zones are embedded in amorphous regions with low packing order and less intermolecular π-π-overlap between adjacent chains.[55] The number of crystalline regions depends on the polymer structure and processing conditions. The atomic force microscopy (AFM) image in Figure 2.2b illustrates exemplary a polymer film with high degree of crystallinity. Within zones of highly ordered polymer chains the π-π-stacking interactions provide high overlapping of the π-orbital leading. In such zones interchain transport can take place with reasonable mobility adopting a hopping mechanism (pathway 2 in Figure 2.2a). At grain boundaries between crystalline and amorphous regions, many trap states and scattering centers hinder the charge carrier transport. Impurities (e.g., dopant molecules, particle of dirt) in the polymer matrix also introduce further grain boundaries, which act as trap states. Within amorphous zones (pathway 3 in Figure 2.2a), only low overlap of the π-orbitals is warranted leading to distinctly lower mobility values.[56] The oscillation of the intermolecular interactions' strength between the chain segments results in a dispersed electronic coupling within the material and is termed off-diagonal disorder.[52]

Deductively, the charge carrier transport of CPs can be improved by either increasing the conjugation length of the polymer or by strengthening the intermolecular interactions, mainly the π-π-interactions. These issues were addressed by two approaches: either by synthesizing sophisticated polymer structures or by tuning the deposition process of the polymers. In doing so, mobility values for state-of-the-art polymer-based devices up to $10\,\mathrm{cm^2\,V^{-1}\,s^{-1}}$ were achieved.

2.1.2 Polarons and Molecular p-Doping of Polythiophenes

As mentioned in Section 2.1.1, pristine CPs are insulators due to their low charge carrier concentration. The charge carrier concentration can be enhanced by the introduction of external charges. Because polythiophene derivatives are electron donating units (p-type conductors), p-type doping is examined in the following. Even though the term doping is adapted from inorganic semiconductors, the mechanism is entirely different for CPs. Generally, the dopant and the polymer undergo a charge transfer (CT) reaction *via* redox processes, as displayed in Figure 2.3. An electron from the polymer's HOMO level is transferred to the dopant. The removal of one π-electron from the polymer backbone causes the deformation of the benzenoid (Figure 2.3a) towards a quinoid structure (Figure 2.3b).[57,58] The resulting radical cation is termed as a polaron.

The ionization of the polymer chain changes the electron distribution. As a result, the bond length readjusts and two new sub-bandgap states emerge which are referred to as P and P*. The unpaired electron stays in the bonding orbital P, as displayed in

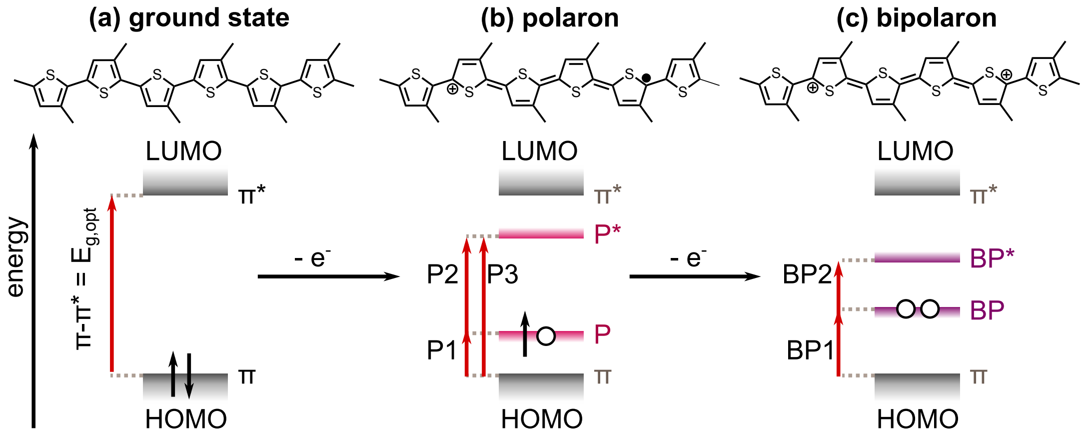

Figure 2.3: Chemical and bandstructure of a P3RT single chain in its (a) ground, (b) polaron and (c) bipolaron state. For the polaron and bipolaron state, new sub-bandgap states emerge. The optical transitions for each doped species are marked with red arrows.

Figure 2.3b. Upon further oxidation, a dication is formed, referred to as a bipolaron (Figure 2.3c). There, a stronger benzenoid-to-quinoid-deformation occurs. New sub-bandgap states BP and BP* are formed resulting in a further decrease of the bandgap. Calculations based on density functional theory (DFT) simulations and lithium-doping experiments proved that for polythiophenes the polaron state is energetically favored over the bipolaron state.[59,60] Each of these polymer states is characterized by defined optical transitions (red arrows in Figure 2.3) which appear at lower energies than the neutral compounds.[57] In amorphous zones with low intermolecular interactions, the polaron wave is localized on the conjugated segment of the polymer chain. In crystalline regions of the polymer matrix, the π-electron density is high due to short interchain distances. Consequently, the polaron wave function is delocalized over several chain segments, which promotes conductivity in the range of metals.[61]

At the beginning of CP-research, small inorganic compounds were applied to dope CPs. This class of dopants oxidized CPs efficiently and provided metallic levels of conductivity.[19] In contrast to inorganic semiconductors, these small ions are not covalently joined to the polymer matrix and therefore, tend to leak. Consequentially, the doped CPs were not stable under operating conditions.[62]

By applying organic molecules as dopants, the stability could be distinctly improved due to the formation of relatively stable charge-transfer complexes. Nowadays, this so-called molecular doping is the standard technique to dope organic semiconductors chemically. Molecular p-type dopants are strong electron acceptors which can stabilize negative charges. The electron affinity (EA) of these dopants should be in the range of the organic semiconductor's ionization energy (IE). In other words, the dopant's LUMO should be energetically on the same or lower level as the polymer's

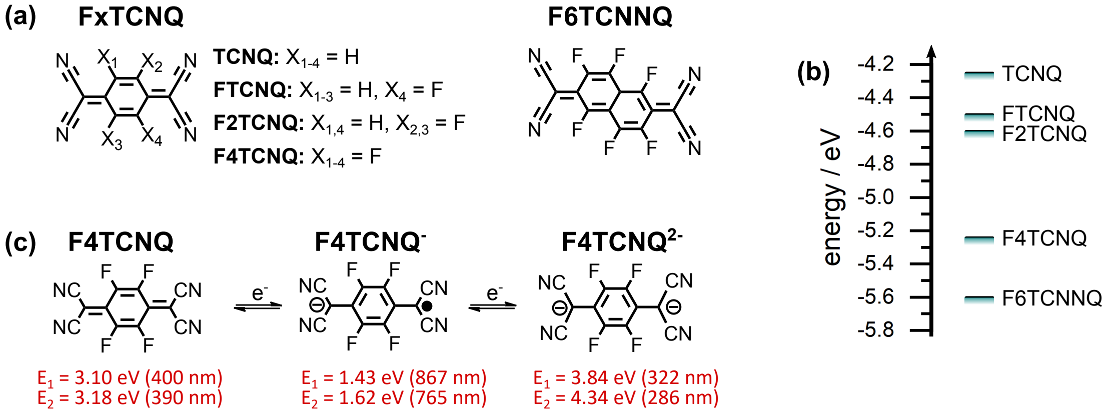

Figure 2.4: (a) Molecular structures of the tetracyanoquinodimethane (TCNQ)-based p-type dopants TCNQ, FTCNQ, F2TCNQ, F4TCNQ and the derivative 2,2'-(perfluoronaphthalene-2,6-diylidene)dimalononitril (F6TCNNQ). (b) LUMO energies of the TCNQ analogues.[63–65]. (c) Chemical Structure of F4TCNQ, F4TCNQ$^-$ and F4TCNQ^{2-} and their specific absorption peaks.[66]

HOMO. Strong electron withdrawing groups, e.g., nitrile-groups and fluorine-atoms, are conjugated to these molecules to increase the EA (or lower the LUMO level). Altogether with aromatic basic units, these groups provide stabilizing effects for radical anionic charges on the dopant molecules.
The standard p-type dopant for P3RT-type polythiophene derivatives is F4TCNQ (Figure 2.4a). F4TCNQ-doped polythiophenes showed conductivity enhancements of up to five orders of magnitude with values in the range of 0.1 to $10\,\mathrm{S\,cm^{-1}}$.[67–72] Its strong electron accepting properties originates from the very low LUMO of -5.24 eV. The HOMO level is at -8.3 eV.[63] Motivated to fine-tune the energy of the LUMO level further, F4TCNQ-analogues have been deployed based on the basic unit TCNQ. A selection and their respective LUMO levels are illustrated in Figure 2.4a,b. An additional advantage of TCNQ-based molecules is their planar structure[68,73] which enables easy incorporation into various host systems. The low evaporation temperature and the reasonable solubility in organic solvents provides processability. TCNQ-based show great solubility in polar solvents, such as acetonitrile or dimethyl sulfoxide (DMSO). Recently, even water-soluble dopants were reported by Karpov *et al.*.[74] Accordingly, these dopants are expected to be compatible for DNA-based devices.
Two stable anionic species of F4TCNQ are known, the radical anion F4TCNQ^{-} and the dianion F4TCNQ^{2-}, which are depicted in Figure 2.4b. The three species of F4TCNQ are characterized by distinct optical absorptions.[66,75] The neutral form has two weak peaks around 3.15 eV. F4TCNQ^{-} possesses two peaks at 1.43 and 1.62 eV. F4TCNQ^{2-} has two peaks at 3.84 and 4.34 eV.

So far, two fundamental dopant-polymer interaction mechanisms have been described, the ion pair (IPA) and the ground-state charge transfer (CTX) formation,[41] as displayed in Figure 2.5. The CT reaction is promoted by the general need to minimize the energy of both compounds. How the CT reaction occurs depends on the relative position of the dopant's LUMO to the polymer's HOMO.
The IPA mechanism applies when the EA of the dopant is larger or at least equal compared to the IE of the polymer. In that case, the energy difference between the energy levels promotes the transfer of one electron from the polymer's HOMO to the dopant's LUMO, as depicted in Figure 2.5a. In the oxidized polymer (polaron) remains a hole and the dopant carries an additional electron. Accordingly, an integer charge (= one electron) was transferred, which corresponds to an degree of CT δ of 1. As mentioned above, both the cationic (polarons and bipolarons) and anionic species (F4TCNQ^{-}, F4TCNQ^{2-}) are characterized by distinct absorption peaks (Figure 2.3b,c and 2.4b). By identifying these ionic species in several polythiophene-F4TCNQ-systems, the IPA mechanism was evidenced.[69,72,76,77] The low dielectric constants of CPs and corresponding Coulomb interactions can result in immobilized ions. According to Pingel *et al.*, most of the polymer-hole/dopant-electrons stay Coulombically joined and cannot contribute to charge carrier transport.[76] No interactions between adjacent doped chain segments were found, which emphasizes

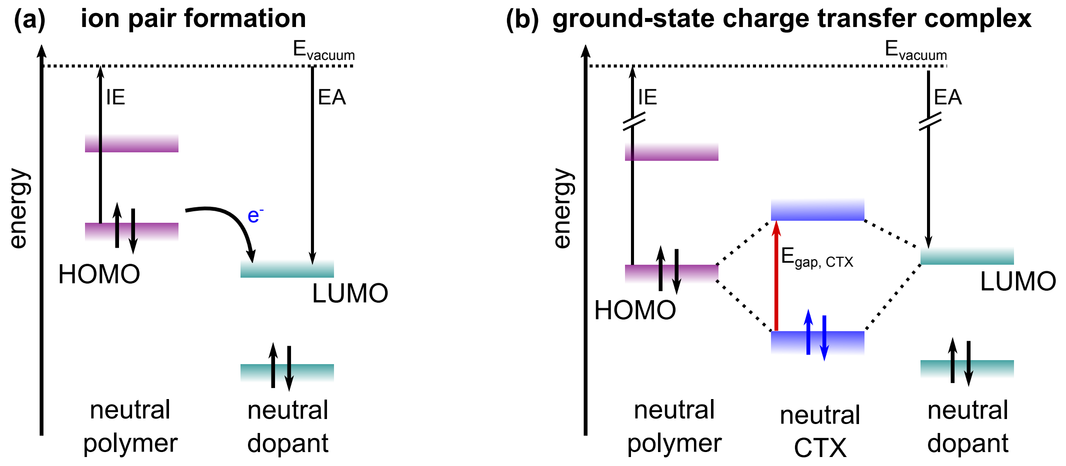

Figure 2.5: Energy level alignment of the polymer and the dopant for (a) the ion pair formation and (b) ground-state charge transfer complex. In case of the IPA formation, the EA of the dopant is higher than the IE of the polymer. In case of the CTX, the EA of the dopant is either the same or even smaller than the IE of the polymer.

the molecular nature of doped CPs.[71,76] Moreover, it was stated that one F4TCNQ^{-} anion is localized on a unit of four thiophenes in the polymer chain for poly(3-hexylthiophene) (P3HT).[76]

The CT reaction follows the CTX mechanism when the EA of the dopant is smaller than the IE of the polymer. In this case, new orbitals are formed through hybridization between the electron donor's (polymer) HOMO and the LUMO of the electron acceptor (dopant). This new supramolecular orbital is split into a binding and an antibinding orbital where the electron pair stays in the binding one.[41] Such orbital hybridization depends on the spatial overlap of the participating frontier orbitals. The resulting CTX complex is neutrally charged. In contrast to the IPA mechanism, an electron is not transferred but is instead split between polymer and dopant. As a result, a δ below one is obtained. How the transferred charge is distributed between polymer and dopant depends on the energy of the polymer's HOMO, the dopant's LUMO and how they overlap. By studying the relative position of the nitrile stretching mode of F4TCNQ in comparison to neutral F4TCNQ, Mendez *et al.* have analyzed whether an integer or partial charge tranfer occured.[69] Thereby, they found that F4TCNQ-doped quarterthiophenes are doped *via* the CTX mechanism (δ=0.21). In combination with the characteristic absorption features of the supramolecular hybrid energy levels, the CTX can be identified by spectroscopic methods. CTX was reported mainly for molecular organic semiconductors[69,78] but also for CPs.[77]

2.1.3 Synthesis of Polythiophene Derivatives

General Considerations

In 1980, the synthesis of unsubstituted polythiophene was independently reported for the first time by two groups.[42,79] Both followed a similar metal-catalyzed polycondensation approach. The monomer 2,5-dibromothiophene was converted into its mono-Grignard compound through the treatment with magnesium, and 2,5-coupled polythiophene was obtained as the main product. The polymers were stable and reasonable conducting in their doped state ($3.4 \cdot 10^{-4}$ to $10^{-1}\,\mathrm{S\,cm^{-1}}$).[42,80,81] Eventually, their insolubility in any solvent, even at low molecular weight (MW), hindered a further application of these polymers. An established concept to improve the solubility of macromolecules is the introduction of flexible side-chains.[82] Consequentially, the need for soluble polythiophenes was fulfilled by the attachment of long alkyl side-chains at the 3' carbon of the thiophene unit.[83,84] In the following, various side-chains were introduced to custom-tailor the solubility of these polythiophenes.[85–87] The side-chains were used beyond their solubilizing properties to tune the electron density of the aromatic systems in the thiophene backbone. Through intramolecular forces by either electron-donating or -withdrawing groups, the optical bandgap and location of the HOMO and LUMO level were modified.[88–90]

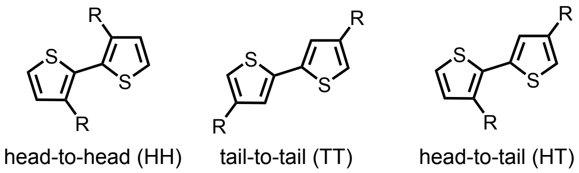

Figure 2.6: Possible thiophene-thiophene orientation in P3RT-type polythiophenes.

However, the integration of the side-chain at the 3' position of the thiophene unit introduced a further symmetry element, and thus, a new problem emerged. As depicted in Figure 2.6, with respect to the side-chain, three possible thiophene-thiophene orientations are possible: head-to-head (HH), tail-to-tail (TT) and head-to-tail (HT).

When all thiophene units in one polythiophene molecule are HT-coupled, all side-chains face the same direction (Figure 2.7a), which enables the ability to self-assemble into planar structures (Figure 2.7b).[91,92] Such a polymer is termed fully regioregular. When the thiophene units are additionally HH and TT coupled, as illustrated in Figure 2.7c, the polymer is termed regioirregular. The degree of regioregularity (= amount of HT-coupled thiophenes) is commonly given in percent, where 100% refers to a fully regioregular structure. In regioirregular P3RTs, sterical effects of the side-chains cause twisting of the polymer backbone (Figure 2.7d). This results in not only a decrease in the conjugation length, but also in the ability to assemble into planar, ordered structures, as illustrated in Figure 2.7d. Consequentially, regioregular P3RTs are superior to regioirregular P3RTs concerning

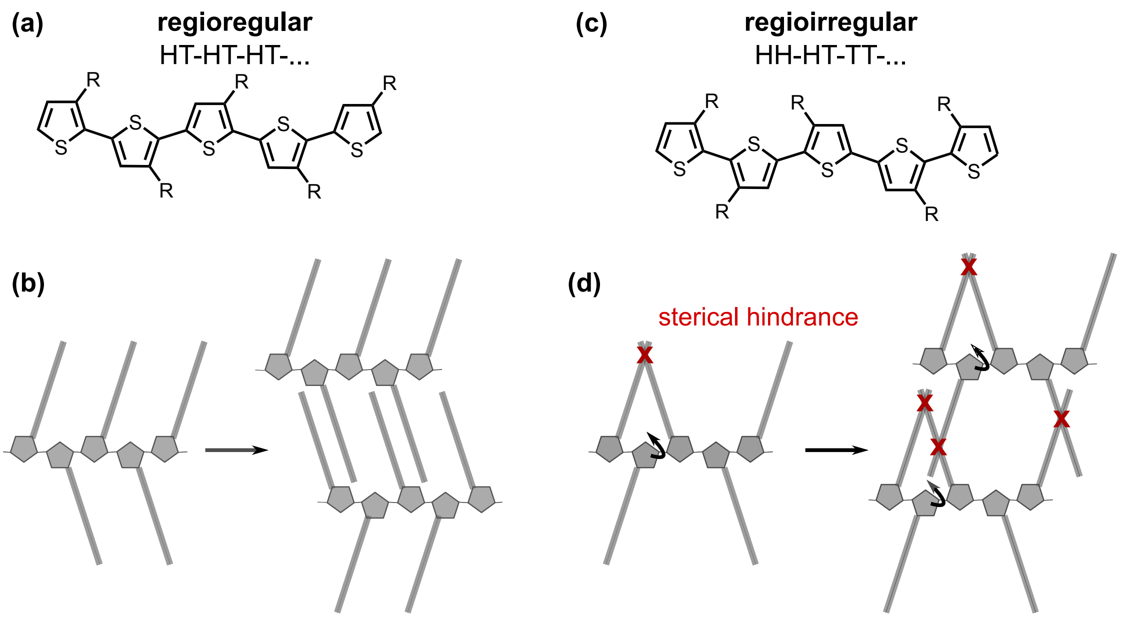

Figure 2.7: (a) Chemical structure of a regioregular P3RT and (b) scheme of its ability to self-assemble into ordered structures. (c) Chemical structure of a regioirregular P3RT and (d) scheme how sterically induced twisting prevents self-assembly into planar structures.

their electronic functionality.[93] Therefore, one major objective for P3RT synthesis is to obtain the highest possible degree of regioregularity.
Nowadays, these P3RT-type polythiophenes are one of the standard CPs in research due to their diversity, stability and functionality. Their optoelectronic properties and their performance in devices is determined by their molecular structure. However, their properties are not only defined by the chemical structure, but they are also defined by a complex synergy of intra- and intermolecular forces derived from their molecular structure, conformation and packing structure. Further parameters are the MW,[94] dispersity,[95] solution concentration,[96] and deposition method.[97,98]

Oxidative Polymerization

At the beginning of polythiophene research, the best-conducting polymer films were obtained by oxidative electropolymerization.[99] The polymers were grown on an electrode surface with an applied anodic potential E_{pa}. The general mechanism of the oxidative polymerization is displayed in Figure 2.8. First, a cationic radical forms by oxidation through the oxidizing agent or E_{pa}. The radical cation is stable due to resonance structures. The highest electron density is found at the α-position of the thiophene (blue structure in Figure 2.8). Second, a C-C-bond is formed by two radical monomers giving the dimer-cation. In the third step, the dimer cation stabilizes itself through the release of two protons. The polymer is obtained by a repeated sequence of these three steps. As shown in Figure 2.8, the C-C- bond is not

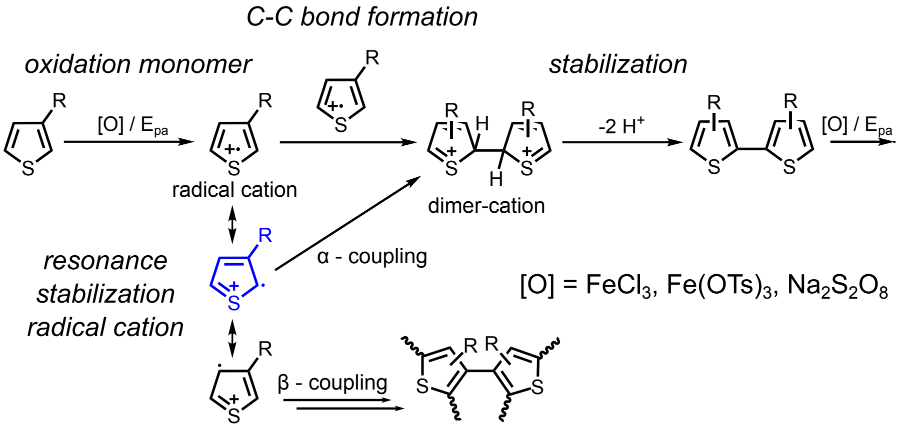

Figure 2.8: Mechanism of the oxidative polymerization of polythiophene derivatives and common oxidizers.

solely formed *via* α-coupling due to the radical mechanism. Moreover, β-coupling can also occur, which introduces dendritic defects.

The introduction of solubilizing side-chains enabled the chemical oxidative polymerization. The chemical approach offers a better control and requires less tedious adjustments of the synthesis conditions. Instead of E_{pa}, mild oxidizing agents with Lewis acid character[100] are used to form the radical cation. The most common are iron(III)-salts, such as $FeCl_3$, and sodium peroxidisulfate $Na_2S_2O_8$. The excess of the oxidizing agent leads to fully oxidized, doped polymers. With the introduction of side-chains at the thiophene monomer, another drawback of the oxidative polymerization and its radical mechanism came into view. It was not possible to control the monomer coupling. The resulting P3RTs were regioirregular and characterized by a broad MW distribution. By optimizing the synthesis conditions, a maximum degree of regioregularity of 88% was obtained.[43]

The issue of regioirregular coupled monomer units was avoided by applying symmetric structures, as in the case of poly(3,4-ethylenedioxythiophene) (PEDOT) where the monomer 3,4-ethylenedioxythiophene is symmetric.[101,102] For such polymers, the oxidative polymerization is still essential for the large-scale synthesis of conducting polymers due to the reasonable price of the reagents and its scalability.

Transition Metal-Catalyzed Polycondensation

The catalyzed reaction between organometallic compounds and Aryl (Ar)-halides, and the resulting formation of new Ar-Ar-bonds was a huge step forward for synthetic chemistry to approach new organic compounds. These early studies on such Pd-catalyzed cross-coupling reactions of Negishi, Heck, and Suzuki were therefore, awarded with the Nobel Prize in Chemistry 2010. Based on these cross-coupling reactions, the polycondensation of CPs with a well-defined, complex molecular structure catalyzed by transition metals was enabled.

The general mechanism of the transition metal-catalyzed polycondensation is

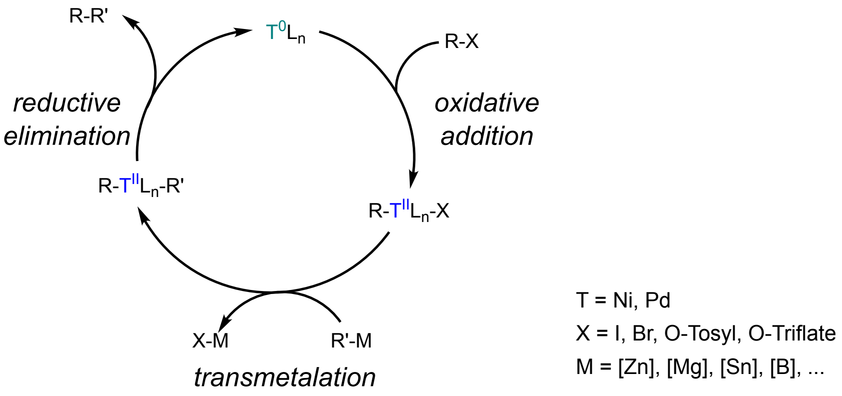

Figure 2.9: Mechanism of the transition metal-catalyzed cross coupling reaction.

conducted *via* three steps, which are displayed in Figure 2.9. *Via* an oxidative addition, the transition metal species T^0L_n, with L_n assigning the ligands, bonds into the electrophilic Ar-halogen R-X, followed by transmetalation with a nucleophilic, organometallic reagent R'-M. Eventually, by a reductive elimination step the desired product R-R' is obtained through the formation of a new C-C-bond while the catalyst T^0L_n is regenerated concurrently. Predominantly, complexes of the transition metals Ni and Pd are used as catalysts for such polycondensations.[103] A variety of organometallic compounds were investigated, namely zinc (Negishi), Grignard reagents (Kumada, Tamao), stannane (Stille, Migato, Kosugi), boron (Suzuki, Miyauri), copper reagents, silane, lithium and mercury. By combining the different reaction partners the most versatile CP structures were synthesized.

Yamamoto *et al.* were the first to report the synthesis of a polythiophene and a P3RT-type polythiophene by a nickel-catalyzed polycondensation (Figure 2.10a).[104] The group started from the monomer precursor di-brominated thiophene, which was converted by magnesium into the respective Grignard-compound. Due to the intrinsic asymmetry of such 3'-substituted thiophenes combined with an AA-monomer structure (di-brominated), it was not possible to obtain regioregular coupled P3RTs.

McCullough and Loewe improved the regioregularity of P3RT-type polythiophenes up to 91% by using Ni-catalysts and changing the AA into an AB-type monomer, with A being more reactive than B.[85] Even better results were obtained by activating the monomer 2-bromo-5-iodo-3-alkylthiophene by highly reactive Rieke zinc followed by a Ni-catalyzed Negishi-coupling.[107,108] Their optimized synthesis conditions resulted in polymers with a regioregularity of 98%. Similar high degrees of regioregularity were achieved for AB-type monomers by the Grignard metathesis, the Kumada coupling and the Pd-catalyzed polycondensation, as illustrated in Figure 2.10b for the Suzuki-Miyaura polycondensation.[45,105,109]

Another approach towards regioregular coupled asymmetric monomer units is to use two monomers - AA and BB - yielding an alternating AB-copolymer. Such polymers were realized by using dihalide and distannyl monomers which were coupled by Stille

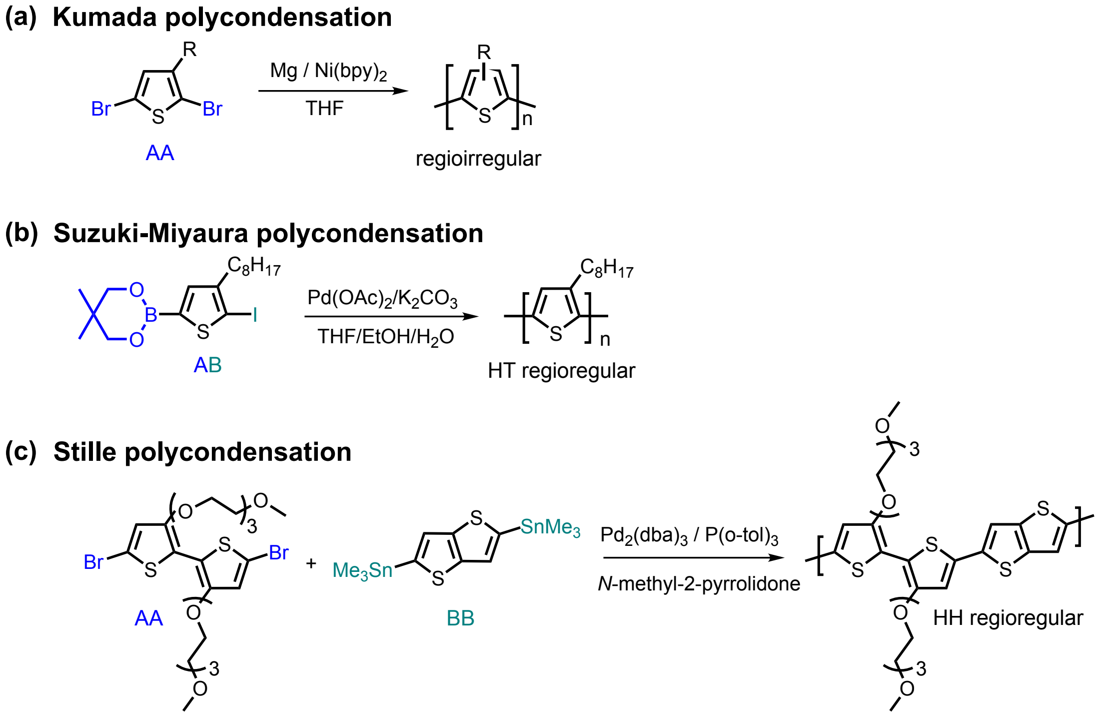

Figure 2.10: (a) Reaction scheme of the Kumada polycondensation towards regioirregular polythiophenes; reported by Yamamoto *et al.*[104] (b) Reaction scheme of the Suzuki-Miyaura polycondensation towards HT-regioregular polythiophenes; reported by Guillerez *et al.*[105] (c) Stille polycondensation towards regioregular HH-coupled polythiophenes; reported by Giovannitti *et al.*[106]

polycondensation (Figure 2.10c). Typical monomers are stannylated thiophenes or thieno(3,2-*b*)thiophenes and head-to-head coupled 3'-substituted dibrominated bithiophenes.[72] The resulting polymers are then not fully head-to-tail but head-to-head coupled. Such a HH-coupling leads to higher planarity of the polymers due to intramolecular sulfur-oxygen interactions.[110] The alternating, unsubstituted thiophenes (or thieno(3,2-*b*)thiophenes) prevent the backbone twisting through sterical hindrance.

Most of these coupling reactions, such as Suzuki or Stille, follow a step-growth mechanism. The resulting polymers are hardly controllable with regard to their MW and characterized by a broad MW distribution (dispersity > 2). The low control over the reaction further hinders the *in situ* introduction of functional end-groups into the polymer. In the case of 3'-substituted thiophene monomers, the degree of regioregularity was improved up to $> 98\%$. However, it was not possible to obtain fully regioregular P3RT-polymers. Deploying CPs in nanoscaled DNA-based devices demands polymers with well-defined properties, controllable size, and functional endgroups to provide accessibility for bioconjugation. These needs were fulfilled with the development of the *ex-situ* initiated Kumada catalyst-transfer polycondensation (KCTP), which was found to be quasi-living, chain-growth mechanism.

Ex-Situ Initiated Kumada Catalyst-Transfer Polycondensation

For a long time, a condensation-based polymerization with a "living" character was considered an oxymoron. For conventional polycondensations, oligomers and polymers are nearly as reactive as the monomers.[111,112] Therefore, the polymer-growth follows a step-growth mechanism. A living polycondensation, on the contrary, would follow a chain-growth mechanism. However, in biology many polymers, such as DNA,[113] are synthesized *via* a chain-growth polycondensation giving a perfectly monodisperse polymer (dispersity = 1). The approach of nature is to use first, an asymmetric monomer (5'-nucleotide-3') and second, superstructures or enzymes, such as the DNA polymerase which stays coordinated to the growing polymer chain and moves along it.

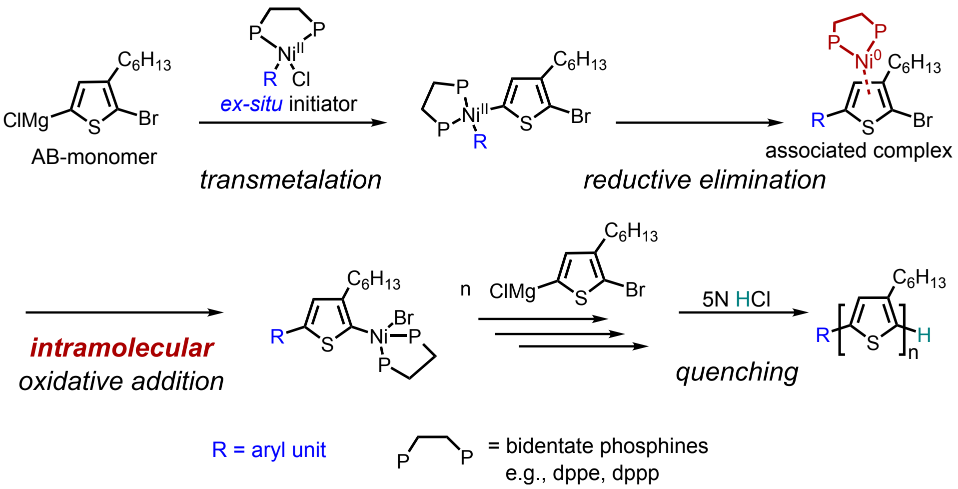

Figure 2.11: Mechanism of the *ex-situ* initiated Kumada catalyst-transfer polycondensation yielding fully (100%) regioregular P3RTs.

In 2004/2005, the groups of Ian McCullough[114,115] and Tsutomo Yokozawa[44,116] independently discovered that the nickel catalyzed Kumada polycondensation not only leads to regioregular P3RTs but follows a quasi-living chain-growth mechanism. The MW was directly dependent on the feed ratio of monomer to the catalyst and increased proportionally with the monomer consumption.[44] Both factors are attributes of chain-growth polymerizations. Furthermore, the resulting polymers were characterized by a narrow dispersity (<1.1), defined end-groups and adjustable MWs. Such a chain-growth mechanism was also found for the akin Grignard metathesis. Below, only the Kumada polycondensation is examined. The quasi-living character originates from an intramolecular catalyst-transfer, which is the reason for the term Kumada catalyst-transfer polycondensation.

In contrast to the Yamamoto-approach,[104] an asymmetric AB-monomer was used with a bromo- and Grignard as active groups. The same steps are executed as in the case of the transition metal-catalyzed step-growth polymerization (Figure 2.9). However, the Ni-center and the formed compound are not separated after one catalytic circle. Like an enzyme, which stays bound to the synthesized DNA strand, the Ni-center stays coordinately bound at the polymer's π-system (Figure 2.11). The one-by-one addition of the monomer is then achieved by a selective ring-walking procedure of the Ni-center along the conjugated system.[117–119] It should be noted that the KCTP does not entirely follow a chain-growth mechanism. It was evidenced by NMR-spectroscopic investigations that several side reactions occur, such as: chain initiation from both polymer sites, chain-termination, random catalyst ring-walking and reinsertion of the catalyst.[120,121]

When Ni^{II} complexes with bidentate ligands ($Ni(dppp)Cl_2$/$Ni(dppe)Cl_2$) initiate the KCTP, the polymer's starting group is derived from the first associated complex (*in-situ* initiation). As a result of the initial bithiophene-Ni-complex, such synthesized P3RTs always have a TT-defect at the chain end (Figure 2.12a). Senkovskyy *et al.* firstly demonstrated the use of external Ar initiators (*ex-situ* initiation) for P3HT, which eliminated the TT-defect and yielded fully regioregular polymers.[122] They conducted this polymerization in solution and on solid supports.[117,122,123] The initiator was obtained by oxidative addition of $Ni(PPh_3)_4$ to an Ar-halide (e.g., bromo-benzene) yielding the compound Ar-$Ni(PPh_3)_2$-Br. Then Ar-$Ni(PPh_3)_2$-Br started the polymerization as an *ex-situ* initiator (Figure 2.12b). Endgroup-analyses showed that over 98% of the polymer chains were equipped with an Ar-unit at one chain end. The ratio of polymer molecules equipped with the initiator to the molecuels without the initiator is termed as degree of functionalization (DF). However, the resulting polymers were characterized by a broad dispersity (>1.6). At a higher degree of polymerization (DP), reinitiation of the catalyst occurred. Therefore, the number of polymer chains without an Ar-unit increased distinctly.

The relatively lower structural quality of these polymers was assigned to disproportionation followed by homo-coupling reactions of the Ar-$Ni(PPh_3)_2$-Br initiator (yielding Ar-Ar).[125–127] The group of Christine Luscombe improved the quality of these *ex-situ* initiators by introducing a methyl group at the Ar-unit in *ortho*-position to the Ni center.[128,129] The methyl group in *ortho*-position stabilizes the Ni complex in a combination of steric and electronic effects and is essential to obtain quantitative initiation.[129,130] Thereby, homo-coupling reactions of the initiator were prevented. The performance of the *ex-situ* initiated KCTP was further improved by exchanging the non-stable, monodentate and toxic ligand PPh_3 with bidendate ligands, such as 1,3-bis(diphenylphosphino)propane (dppp), 1,2-bis(diphenylphosphino)ethane (dppe) or 2,2'-bipyridine (bpy).[124,127,128] An increase of the DF from 65 to 95% was obtained through the further reduction of side reactions (chain termination or reinitiation of the catalyst).[124]

The group of Anton Kiriy followed a similar approach by using bpy as a ligand (Figure 2.12c). This method turned out to be the most versatile because a greater amount of functional groups are tolerated without the need of the stabilizing methyl group.[33] Sophisticated CP structures, such as spherical brushes,[125] star polymers[126] and rod-coil block copolymers,[131] were successfully synthesized by this method.

To start from commercially available compounds and to aviod the non-stable

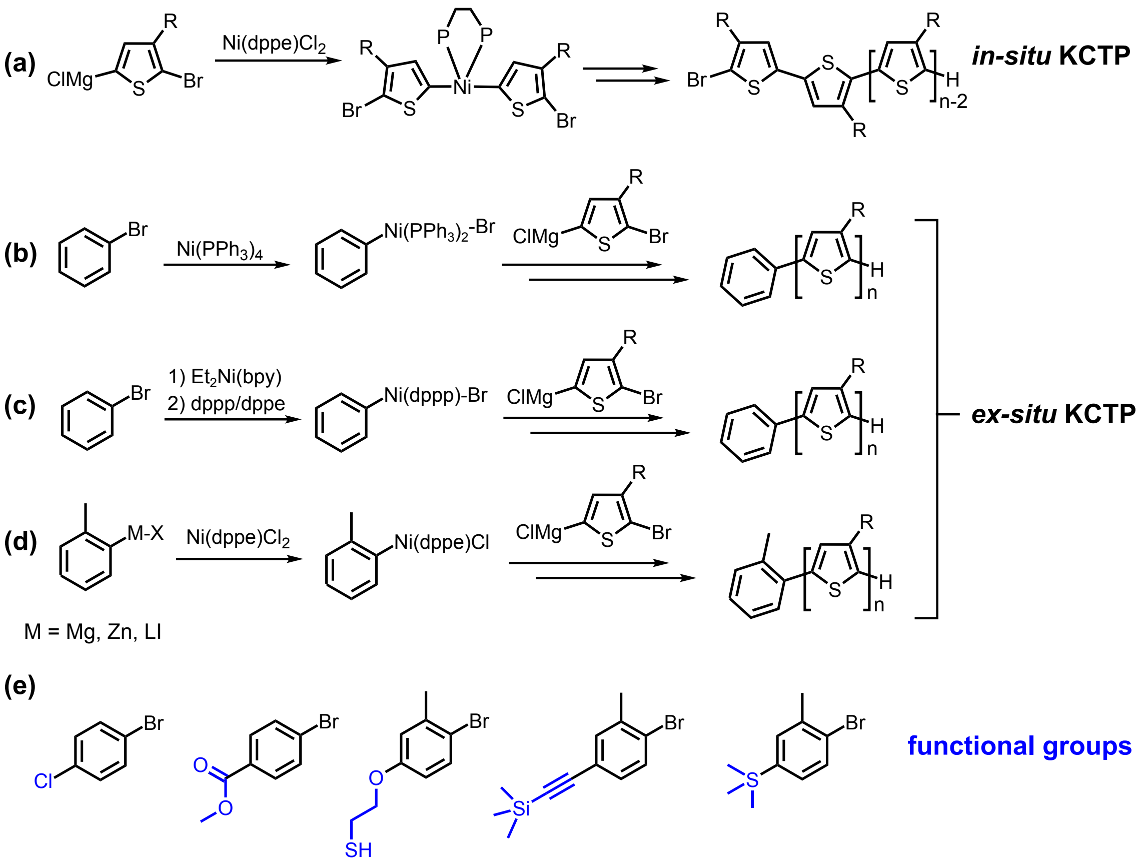

Figure 2.12: (a) *In-situ* initiated KCTP yielding P3RTs with a TT defect at the chain start. (b-e) *Ex-situ* initiated KCTP *via* various Ni-initiators reported by the group of Anton Kiriy. (f) Selection of functional Ar compounds introduced by the *ex-situ* initiated KCTP.[88,124]

intermediates $Et_2Ni(bpy)$ or Ar-$(PPh_3)_2$-Br, Senkovskyy *et al.* developed a novel approach towards Ar-Ni(dppp)Cl starting from Ni(dppp)Cl_2.[132] Sterically hindered Grignard reagents (*ortho*-substituted Ar) were used to avoind any further transmetalation reactions. With this method, they suppressed the occurrence of homo-coupling reactions (Figure 2.12d). The resulting polymer was structurally well-defined and characterized by a high DF.

The *ex-situ* initiator is not only useful to avoid the TT defect in the P3RT chain but enables the *in-situ* introduction of functional end-groups. A selection of functional groups incorporated *via ex-situ* initiators is displayed in Figure 2.12d. Due to the quasi-living character of the KCTP, functional end-groups can also be introduced *via* functional quenchers, as was demonstrated by different groups.[88,133] However, this method is more error-prone. Such prepared polymers generally have lower DFs or bis-functionalized chain ends due to side reactions, e.g., chain termination and reinitiation.

)

2.2 DNA-Based Templates for Confined, Functional Nanostructures

Since the 1980s, DNA has been used as a tool to precisely control and position materials. DNA is one of the best-understood biomolecules with structural dimensions in the nanometer range. The structural, chemical and mechanical properties of DNA are well-known (Section 2.2.1) so that generally-agreed construction rules could be established. Additionally, there are numerous standard protocols to synthesize, chemically modify and replicate DNA. Thus, DNA was deployed in research as a template to deposit numerous hetero-objects (Section 2.2.2).

For a long time, DNA-templated nanostructures were limited to one-dimensional structures. The ability of the DNA double helix to self-recognize and self-assemble is not only the fundamental principle of the genetic code but also for the structural DNA nanotechnology. DNA nanostructures can be reliably designed due to the predictability of the Watson-Crick base-pairing and almost endless sequence combinations. In the early 1980s, the unique properties of DNA motivated the crystallograph Ned Seeman to use DNA as construction material to build up programmable, well-defined structures on the nano- and microscale for the targeted arrangement of functional objects.[7] Inspired by the natural occurring Holliday junctions, Seeman introduced synthetic cross-overs with minimal intra-strand symmetry as a primary unit. As displayed in Figure 2.13a, single-stranded overhangs at the end of these cross-overs, so-called sticky ends, act as a linker to connect other cross-over unit leading to supramolecular frameworks. Eventually, the general linearity of the DNA double helical system was hurdled, and the foundation for the DNA nanotechnology was laid.

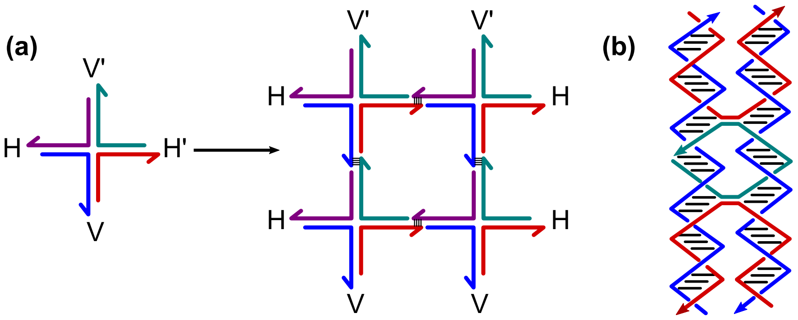

Figure 2.13: (a) Branched DNA molecule, inspired by the Holliday junction, formed by four single DNA strands with four sticky end overhangs, where red is complementary to purple and blue to green. Through hybridization of the complementary ends, a 2D crystal is created. (b) The double cross-over (DX) tile composed of four juxtaposed fourway junctions forming two double helices.

Based on the Holliday junction, further motifs were developed which enabled the construction of more complex DNA nanostructures. Nowadays, one of the most fundamental motifs, especially for planar DNA structures, is the double crossover (DX) tile. As illustrated in Figure 2.13b, the DX tile is composed of two double helices which are formed by four juxtaposed fourway junctions. The DNA nanotechnology took a huge step forward with the introduction of the DNA origami technique in 2006.[11] It was possible to create versatile 2D or 3D nanostructures in a highly parallel manner. Planar DNA origami structures are discussed as molecular breadboards to arrange hetero-objects with nanometer precision to build up functional nanostructures (Section 2.2.3). Fundamental applicability of such functionalized DNA-based nanostructures was demonstrated in the scope of photonics[134,135] and electronics (Section 2.2.4).[17,136]

2.2.1 Structure and Properties of Deoxyribonucleic Acid

The biopolymer DNA stores the genetic code that provides the instructions for growth, developing, functioning and reproduction for all living organisms and most viruses. Furthermore, DNA is one of the longest molecules in nature. It is highly charged and, particularly in the double stranded form, rather stiff. In a human cell around two meters of DNA are stored in few micron-sized nuclei. Hence, the DNA molecules must be able to cope with high mechanical stress due to tension and torsion. To fulfill all these tasks, nature has evolved a polymer with elaborate and, at the same time simple structural and mechanical features.

Structure of DNA

The chemical structure of DNA is displayed in Figure 2.14a. A nucleotide, which is the monomer unit of the DNA, is composed of three building blocks; a phosphate-group, a pentose sugar, and a nucleobase. The phosphate and the sugar deoxyribose form alternatingly the DNA backbone joined by phosphodiesters bonds. These bonds are positioned at the 3'- and 5'-carbons of the sugar; the respective ends of one DNA strand are asymmetric and called 3'- (hydroxy-group) and 5'-end (phosphate-group). The nucleobase is bound at the 1'-carbon of the sugar. There are four nucleobases in DNA. These aromatic, heterocyclic bases are adenine (A), guanine (G), cytosine (C) and thymine (T) with A and G being the five-ring purine and C and T the six-ring pyrimidine bases.

Three conformations of the DNA double helix structure have been described: the two right-handed A- and B-DNA and the left-handed Z-DNA. Figure 2.14b illustrates the B-form of the DNA. This is the conformation of DNA naturally-occurring in living cells under physiological conditions, and is the only form considered in the following. The structure of the B-DNA double helix was discovered by James Watson and Francis Crick in 1953.[137,138] Their model was based on the X-ray diffraction image acquired by Rosalind Franklin. The DNA double helix, as shown in Figure 2.14b, is comprised of two single DNA strands that are antiparallel aligned to each other. Bases from opposite strands form a base pair (bp). With few exceptions,

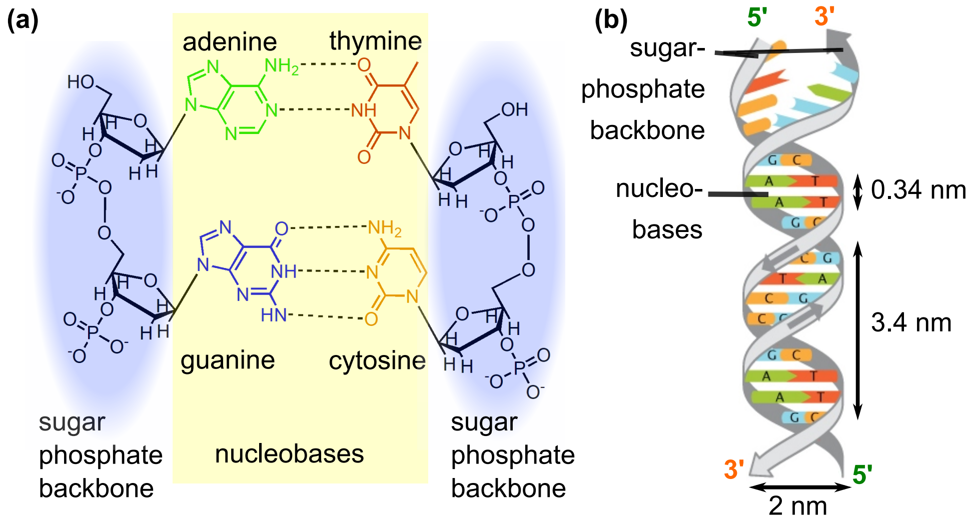

Figure 2.14: (a) The four DNA bases in the Watson-Crick base-pairing state adenine - thymine, guanine - cytosine. (b) 3D model of the B-form of DNA by Watson and Crick, reproduced from (*142*).

the base A can only bond to T and base G to C, which is called the Watson-Crick basepairing (Figure 2.14a). Accordingly, the position of the base in one strand determines the position of the base in the second strand, i.e., the strands must be complementary to each other. The paired bases orient themselves in the middle of the double helix shielded by the negatively charged phosphate-sugar backbone. The distance between the plane of two neighboring bp is 0.34 nm. There are two grooves in the helix: the minor one has a width of 1.2 nm and the major groove a width of 2.2 nm.[139] One complete helical turn is obtained after 10.5 bp.[140] The diameter of the double helix is 2 nm.[141]

Properties of DNA

The formation of the DNA double helix, so-called hybridization, is driven by the noncovalent π-π-stacking interactions and hydrogen bonding. As a cooperative effect of these two interactions, a binding energy of roughly k_BT per bp is generated, where k_B is the Boltzmann constant and T the temperature. The denaturation of the DNA double helix into two single strands is termed melting. Melting of DNA is typically achieved by an increased temperature but can be also induced by chaotropic agents, applied forces (stretching) or extreme pH values. The melting temperature T_m, which is the temperature where 50% of the double strand is separated into two single strands, is used as an indicator of the stability of a double stranded DNA molecule. Since A and T pair only over two hydrogen bonds and G and C over three, T_m decreases with higher A-T content.[143] Besides the sequence, the ion concentration influences T_m.[144] Ions in solution destabilize hyrdogen bondings and lower T_m. On the contrary, for denser packed DNA strands, as in artifical DNA nanostructures, cations are required to shield the negative phosphate backbone and to stabilize the structures.

On a small length scale DNA, is extremely rigid due to the charged backbone, the hydrogen bonding forces and the base-pair stacking ($k_B T$/bp). The Young's Modulus of DNA is estimated around 300 MPa, which is in the range of hard plastic.[145] However, on the longer length scale, the DNA double helix is highly flexible. Single stranded DNA is flexible with a persistence length of 1 nm, the persistence length of double stranded DNA is relatively high with a value of around 50 nm (ca. 150 bp) depending on the G-C content and the cation concentration.[146–148] As a result, DNA molecules with a length distinctly higher than the persistence length form random coils in solution, while short DNA molecules can be considered rod-like.

2.2.2 Linear, DNA-Templated Confined Nanostructures

DNA has been used as a platform for the synthesis of different nanomaterials since the late 1980s. In the first place, linear DNA molecules, such as λ-DNA or synthetic oligonucleotides, were used to fabricate confined functional nanostructures. Compared to their bulk counterparts these one-dimensional nanostructures possess unique optical and electronic properties. The fabrication of such nanowires was particularly motivated as novel building blocks for nanoelectronic devices.

The DNA molecule is an ideal template for such nanowires due to its small width of only 2 nm combined with a length up to micrometers. Furthermore, DNA provides different chemical functionalities enabling molecular recognition (Section 2.2.1). Crystallization seeds, in the form of metal ions, metal complexes or as metallic nanoparticles can be either coordinately bound to different DNA functionalities or

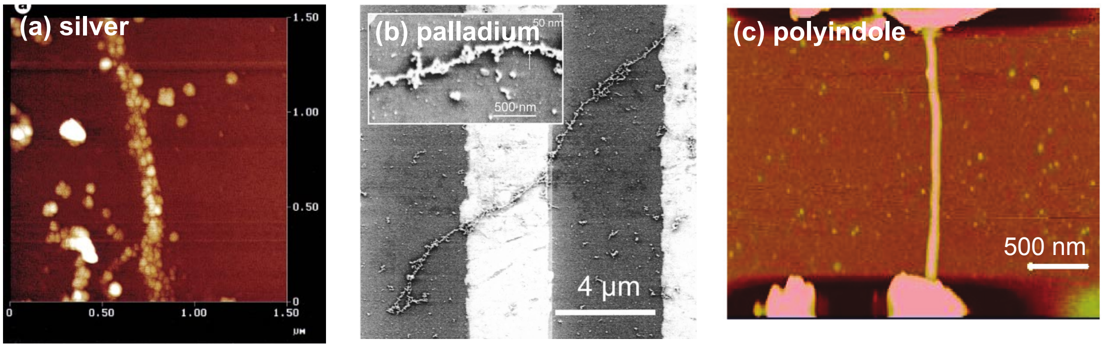

width 100 nm
length 12 μm
resistance 7 MΩ

width 60 nm
length 16 μm
resistance 0.0343 MΩ

width 5 to 30 nm
length 10 μm
60 to 100 MΩ

Figure 2.15: (a) First reported DNA-templated silver nanowire grown on a λ-DNA template, reproduced from (*149*). (b) Exemplary shown palladium nanowire grown on a λ-DNA with the typical dendritic, irregular metal structure, reproduced from (*150*). (c) Polyindol nanowire grown on a λ-DNA template between two gold electrodes with a very smooth, regular shape, reproduced from (*151*).

directly attached to the DNA strand.[149,152–155] These seeds are used to grow wires by further metalization processes. The first DNA-templated nanowire was reported by Braun *et al.* in 1998 (Figure 2.15a).[149] The silver wire deposited on a λ-DNA strand showed ohmic behavior with a relatively high resistance of 12 MΩ. In the following, further DNA templates, mainly λ-DNA or single-stranded oligodeoxynucleotide (ON)s, were used as templates and selectively metalized with various materials, such as silver,[149,156] gold,[152] palladium,[150] and platinum.[157] Linear current-voltage ($I-V$)-characteristics were obtained over micrometer length scales with resistance values in the kΩ region.[149,150,158] However, most of these metal-based nanowires were characterized by a rough and irregular structure. The growth of metals depends on the crystal faces and leads commonly to dendritic structures, as has been shown for palladium nanowires synthesized by Richter *et al.* (Figure 2.15b).[159] Furthermore, conducting nanowires with diameters below 10 nm remained scarce.[160–162]
The structural flaws of these nanowires were improved by the application of CPs as electronic functional material. The advantage of CPs is that their growth is not determined by crystal faces. Instead of overgrowing the DNA template, as in case of DNA-metalization, supramolecular polymers were obtained composed of the conducting polymer and the DNA template.[163] These polymer nanowires were in the presence of the DNA template synthesized by oxidative polymerization (Section 2.1.3). The intermediate - the cation-dimer (Figure 2.8) is electrostatically attracted to the negatively charged phosphodiester backbone of the DNA.[164] Figure 2.15c shows a polymer nanowire with a length scale (10 µm), which is in the range of metalic nanowires. The difference in their appearance is obvious. The polymer wire is smooth, regular and distinctly thinner (5 to 40 nm) than its metallic counterpart.[151,158,165] However, for thin polymer wires the resistance increased.[165] Different CPs, such as polyaniline,[166] polypyrrol,[167] polydithienylpyrrole,[165] polyindol[151], were deposited on DNA templates. Due to their molecular nature conducting polymers provide access to various chemical modifications to either tune their (opto-)electronic properties or to introduce chemical functional groups for further adjustments.[168]

Drawback of CP-based nanowires are the higher resistances compared to their metal counterparts and to CP-bulk material. Typical resistances in the MΩ-region were achieved. Furthermore, the synthesis approach is limited to polymers which are accessible to oxidative polymerization to provide the selectivity during the deposition step. Sophisticated polymers with a well-defined, complex molecular structure are not accessible. The sensitivity of the DNA template to pH, organic solvents and strongly oxidative reagents limits the applicable synthesis conditions further and thus, the choice of polymers. With respect to the deployed DNA templates, their linear nature limited the fabrication of more complex structures with controllable dimensions in all directions and the introduction of further features such as branches. A breakthrough was therefore, the development of structural DNA nanotechnology, particularly the DNA origami technique.

2.2.3 DNA Origami as Molecular Breadboard

The development of the scaffold-based DNA origami technique by Paul Rothemund in 2006[11] was a huge step forward for the structural DNA nanotechnology. A long single-stranded DNA strand, which is mostly viral DNA, e.g., M13mp18, serves as scaffold for the DNA structure. This scaffold strand is held and folded into a predesigned shape by about 200 short, synthetic ONs, so-called staple strands (Figure 2.16a). Therefore, Rothemund named the technique DNA origami. Adjacent double helices are connected by interhelical cross-overs, where both scaffold and staple strand can contribute. The advantages of this approach are its high versatility, less influence of impurities since the staple strands are added in excess and the accessibility to bigger objects (100x100 nm, limited by the length of the scaffold strand). Recent progress in the development of new computer-aided design principles enabled the formation of complex 1D, 2D, and 3D structures.[11,12,169] Even structures with dynamic elements, such as a box with controllable lid, were successfully synthesized by the DNA origami technique.[170] The Figures 2.16b-e illustrate an exemplary selection of different DNA origami structures.

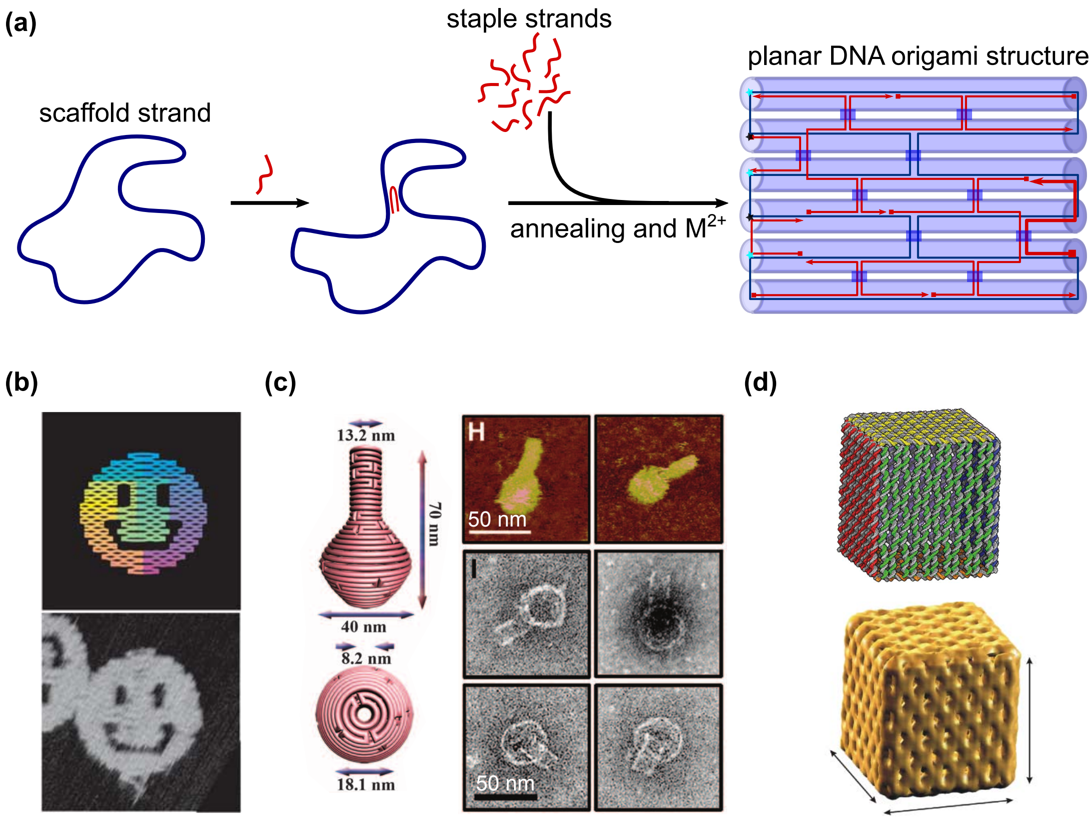

Figure 2.16: (a) DNA origami synthesis and folding scheme towards a planar single-layer DNA origami structure composed of a scaffold strand (blue) and the staple strands (red). (b) A planar origami structure ("Rothemund smiley"), reproduced from (*11*). (c) A 3D origami structure (vase), reproduced from (*169*). (d) A dynamic DNA origami structure (cube with controllable lid), reproduced from (*171*).

The application of DNA origami structures can be ranged in three categories. The first one uses DNA origami as building blocks to construct sophisticated structures with precisely controllable dimensions in two or three directions.[169,172] The second category applies DNA origami structures as mechanical devices with controllable moving parts.[173,174] The third application is to use the DNA origami as a molecular breadboard to organize and arrange hetero-objects.[175,176] The latter is addressed in the following section.

Each staple strand, which holds the scaffold strand together, is unique by its sequence and has a precise position in the final structure. Accordingly, these staple strands can be used as attachment sites to position hetero-objects site-specifically. Site-specificity up to three dimensions can be provided depending on the dimensionality of the DNA origami structure. However, when hetero-objects are arranged by DNA origami templates, the helicity of the DNA double helix must be considered. Therefore, the basic design rules are described firstly, followed by the positioning of hetero-objects onto DNA origami structures.

The packing order of the DNA double helices in a DNA origami structure is either in a square or honey-comb lattice. Planar DNA origami structures are based on the square lattice, which is, therefore, presupposed for the following design rules. As displayed in Figure 2.17a, the cross-overs are positioned with a offset looking. The distance between neighboring cross-overs along one DNA double helix is commonly 3 helical turns (32 bp), and 1.5 helical turns (16 bp) considering three double helices. To obtain an integer number, the DNA origami software calculates with 16 bases per 1.5 helical turns.[11,177] Correspondingly, one helical turn is executed after 10.67 bp and not 10.5 bp, as in natural B-DNA (Figure 2.17b). An established design approach is to locate one staple strand at three different positions at the scaffold strand (Figure 2.17c) with around eight, then 16 and again eight nucleotides.[11] The entire staple strand is then 32 nucleotides in length and three helical turns long. ONs are more reliably chemically modified at their chain ends. Hence, the ends of the staple strands are mostly used as attachment sites for hetero-objects. Due to the helicity of the DNA, the orientation of the staple strand must be considered to provide its accessibility. Depending on the position and helical turn direction of the scaffold strand the end of the staple strand either protrudes from the DNA origami surface (“face down” or “face up”) or is hidden in the DNA surface (Figure 2.17c). For staple strand being 32 nucleotides long, both ends protrude from one origami site. To get access to the other DNA origami face, staple strands can be separated or slightly shifted.

The attachment of hetero-objects is pursued by two approaches. A staple strands can be either chemically modified or extended. In the first approach, the functionalized staple strand is added to the usual folding process. This approach is straightforward, very robust, and gives high yields. However, there are limitations concerning its applicability. The chemical modification (functional group, fluorophore, ...) must be stable at least to the annealing temperature which is typically above 80 °C.

It is also limited to objects distinctly smaller than the DNA origami structure otherwise the folding process would be disturbed. Furthermore, it is not modular since each staple strand is unique what makes it costly.[178] The second approach uses staple strands, which are extended by 8 to 20 nucleotides. The hetero-object is functionalized with ONs bearing the complementary sequence to these extensions. The attachment proceeds by hybridization of this ONs to their complementary extensions of the staple strands. The required hybridization temperatures are distinctly lower (<40 °C), which increases its applicability.[179]

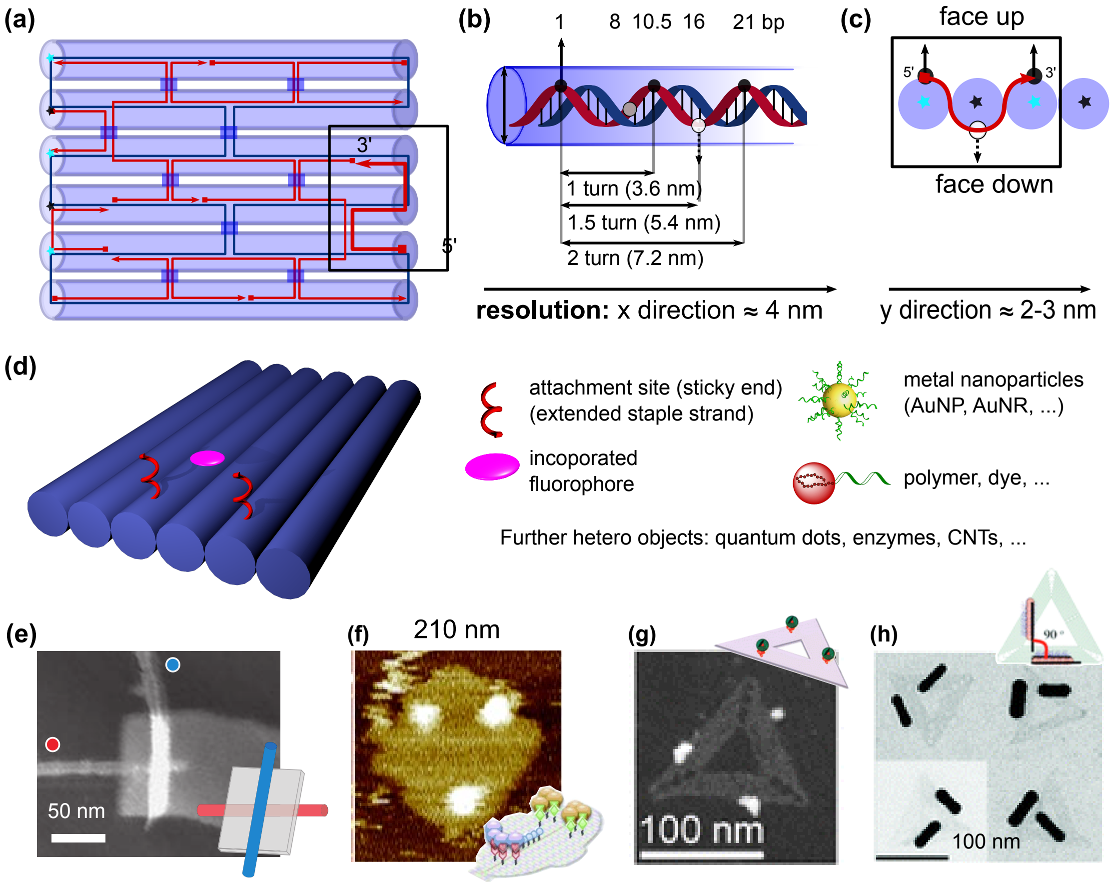

Figure 2.17: (a) Folding scheme of a 2D DNA origami structure. For simplification the DNA double helices are displayed as cylindrical-shaped tubes and the cross-over positions as blue squares. (b) Schematic view on the DNA double helix in a DNA origami structure (x direction). (c) Packing order of DNA double helices in y direction and orientation of one staple strand. (d) Scheme of 2D DNA origami with extended staple strands as attachment sites for different hetero-objects, including fluorophore (here directly bound to a staple strand), metal nanoparticles, quantum dots, enzymes, polymers, and more. (e-h) Different functional hetero-objects, namely (e) carbon nanotubes; (f) proteins; (g) quantum dots; (h) gold nanorods, arranged on 2D DNA orgiami structures, reproduced from (*180–183*).

Structure and packing order of the DNA double helices determine the resolution of the DNA origami breadboard. In the direction along one DNA double helix (x-direction), in theory, a resolution of below 1 nm could be obtained since each nucleotide of the DNA strand could be addressed. However, such resolutions have not been reported until now. On the supposition that the end positions of the staple strands are addressed and hetero-objects should protrude from one face, a resolution of 3-4 nm (one helical turn) can be achieved. The resolution in y-direction is determined by the interhelical gap, which is defined by the spacing of the cross-overs. A resolution of 2 to 3 nm can be obtained.

DNA origami structures have been deployed as molecular breadboards for various hetero-objects (Figure 2.17d), such as metallic nanoparticles,[176] quantum dots,[184] carbon nanotubes,[180] proteins,[181] fluorophores,[185] and synthetic polymers.[186] A selection is illustrated in Figure 2.17e-h. Since each staple strand is unique, different hetero-objects can be attached in parallel on one DNA origami template. Key accomplishments realized by the DNA origami technique were primary devices providing functionality as wave-guiding,[187] optical antennas,[188] reaction cascades,[189] light harvesting,[190] or as nanoscopic rulers.[185] To depict all of these DNA-templated nanostructures would go beyond this thesis. Below, the formation of confined and functional nanostructures is further examined with focus on potential applicability for nanoelectronics.

2.2.4 DNA Origami-Templated, Confined Nanostructures

With the development of the structural DNA nanotechnology and particularly the DNA origami technique, it was possible to fabricate confined functional nanostructures with arbitrary shapes. Furthermore, the higher rigidity of these DNA nanostructures compared to single DNA molecules further improved the quality of the obtained nanostructures.[191] For this purpose, the metal seeds, mostly metallic nanoparticles or nanoclusters, are site-specifically attached to the DNA origami template and then grown into continuous structures by metalization processes (electroless deposition). With this method it was possible to obtain complex structures, such as branched nanowires,[136] wires with a defined length,[17,192] metal rings,[17] and spheres.[193] A selection of different arbitrary shapes is illustrated in Figure 2.18a-c.

From the shown examples, it is evident that these metallic-based nanostructures face the same challenges as in the case of the linear DNA templates. The growing process of these materials is determined by their crystal faces. The obtained structures are irregular, low-defined and have visible grains. The dimensions of these structures are more extensive than the deployed DNA templates due to the low control over the metal deposition. At about the same time, the groups of Ralf Seidel and Peng Yin proposed a new technique on how to increase the structural quality of such confined nanostructures.[191,195,196] Instead of 2D DNA templates, they applied pseudo-3D DNA origami structures, so-called molds (Figure 2.18d,e). Gold-nanoparticles were planted into these molds as seeds. By electroless deposition, these gold-nanoparticles were grown into continuous and homogeneous nanowires with a width of around

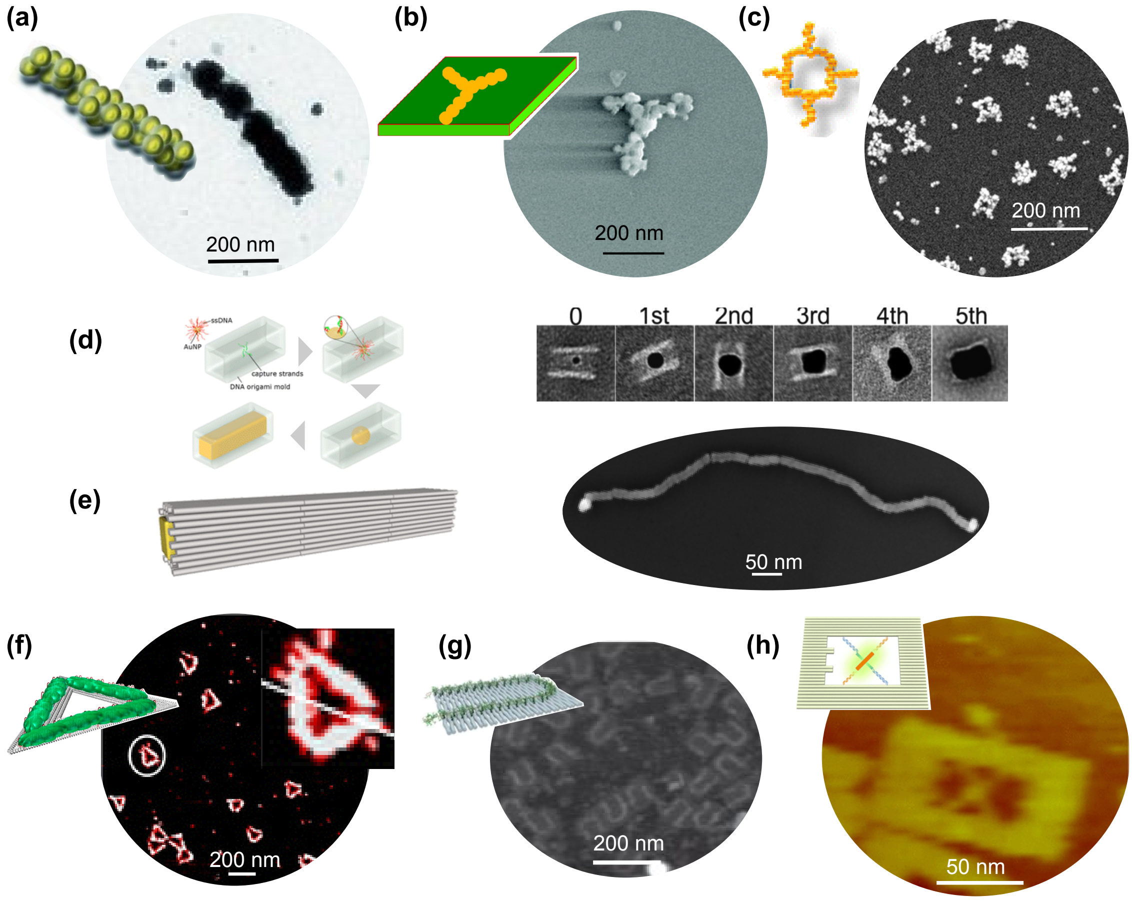

Figure 2.18: (a-c) DNA origami-templated confined metal nanostructures with different arbitrary shapes obtained by site-specific attachment of seeding centers (metallic nanocluster) followed by electroless metal deposition; (a) linear gold nanostructure, reproduced from (*17*) (b) branched gold nanostructure, reproduced from (*136*) (c) gold circular nanostructure, reproduced from (*194*). (d-e) Confined linear gold nanostructures which were grown in DNA origami-based molds. Reproduced from (*191*, *195*). (f) Polyaniline fabricated on a planar DNA origami triangle, reproduced from (*186*). (g) Poly(*p*-phenylene-vinylene) routed on planar DNA origami rectangular, reproduced from (*35*). (h) Oligoaniline and oligo(*p*-phenylene-vinylene) clamped in 2D DNA origami frame, reproduced from (*37*).

30 nm (Figure 2.18e). The molds confined the gold growth and correspondingly the dimensions of the nanowires. Some structures showed a reasonable resistance of 90 Ω. However, some wires were insulating with a resistance of 30 GΩ.[195] Even though these mold-based metal structures are a distinct improvement compared to previous works, the obtained widths of 30 nm are still rather large compared to the possible dimensions of DNA origami structures. Secondly, grain boundaries remained still an issue, which might explain the unsteady conductivity of the wires.

Wang *et al.* fabricated a confined, functional nanostructure by replacing the metals with a CP - a polyaniline.[186] DNAzymes were incorporated on a planar DNA origami triangle acting as catalytic centers (Figure 2.18f). The polyaniline was then site-specifically fabricated around these catalytic centers by oxidative polymerization. The obtained polymer-DNA hybrid structures were well-defined. The related UV/VIS spectra verified an optical response towards doping and de-doping of the polyaniline. As already mentioned in Section 4.3.6, such synthesized polymer-DNA-nanostructures are limited to polymers accessible by oxidative polymerization carrier out under mild conditions. As a consequence, CPs with sophisticated molecular structure are not accessible.

Therefore, it might be advantageous to synthesize the functional material not in the presence of the DNA origami template but beforehand. For metallic nanostructures, nanorods might be a potential alternative. For CPs this approach might be even more straightforward since their charge transport does not only occur intramolecularly but also intermolecularly. Furthermore, harsher conditions, as is customary for sophisticated organic synthesis, is possible. Correspondingly, the whole spectrum of organic chemistry can be applied to obtain a custom-tailored polymer.

The group of Kurt Gothelf firstly reported such an approach towards a functional polymer-DNA hybrid structure.[35] A bottle-brush-type poly(*p*phenylene-vinylene) with oligonucleotide brushes at the phenylene units was used. The obtained polymers were rather large (50 to 2900 $\mathrm{kg\,mol^{-1}}$) and characterized by a broad MW distribution. The oligonucleotide extensions at the polymer backbone were used to site-specifically rout the polymer on a planar origami template (Figure 2.18g). Poly(*p*apenylene-vinylene) derivatives are well-known as benchmark material for polymer-based photovoltaics[20] but are not relevant for electronic devices such as transistors. Additionally, the conductivity along one polymer chain requires a planar backbone (Section 2.1.1) and was so far only demonstrated for short oligo(*p*phenylene-vinylenes.[197] For these reasons, the group of Kurt Gothelf demonstrated so far only the optical functionality of the polymer,[38,39] even though the work was motivated as conducting molecular wire.[198]

Recent work of Wang *et al.* pursued a similar approach.[37] Two different conjugated oligomers, based on aniline and *p*-phenylene-vinylene, were then clamped like an X into a DNA origami frame (Figure 2.18h). By oxidation and re-oxidation of the oligoaniline derivative, it was possible to tune the optical output of the system. This system might be interesting for molecular electronics due to the possible alignment of the conjugated oligomer by the DNA frame. The applicability for longer polymer-based nanowires is unlikely due to similar reasons, as mentioned for the Gothelf-approach.

In general, CPs can be a valuable functional material for DNA-templated devices due to their structural kinship to DNA, their defined structural features and tunable optoelectronic properties. As has been shown in Section 2.2.2 polymer-based confined nanostructures are superior to their metallic counterparts concerning regularity, smoothness, and spatial resolution. However, the electronic functionality remains a challenge and reported conductivity values are distinctly lower than for metal nanowires. For DNA origami-templated CPs, it was not possible, so far, to demonstrate any electronic functionality. Several groups were able to indicate the applicability of these polymeric nanostructures as optical building blocks. However, taking into account the enormous spectrum of available conjugated polymers the number of reports is virtually zero.

2.3 Characterization Techniques for Conjugated Polymers and Functional Nanostructures

2.3.1 Structural Characterization

The chemical structure of a polymer is mostly elucidated by nuclear magnetic resonant spectroscopy (NMR). For polymers, various information can be derived, such as monomer-coupling (e.g. degree of regioregularity), repeat units, end-group composition (e.g. DF), tacticity, sequence analysis of copolymers and impurities can be obtained. Isotopes with a useful spins are ^{1}H, ^{13}C, ^{15}N, ^{17}O, ^{19}F and ^{31}P with ^{1}H-NMR spectroscopy being the most common one.

For linear polymers the DP, which is the number of monomer unit (MU) per chain, and therewith its size, can be computed from the MW. Synthetic polymers are normally not monodisperse, but their MW is distributed around an average value. Common average values are the number average M_n and the weight average M_w. The quotient of M_w and M_n is used as a measure for the distribution and is referred to dispersity. A dispersity of 1 corresponds to a monodisperse polymer. The MW and the dispersity are mostly analyzed by gel permeation chromatography (GPC). The dissolved polymer is pumped through a stationary, highly porous phase, the so-called column. Smaller polymers can diffuse in more pores and stay, therefore, longer on the column than larger polymers (elution: big > small). As a result, the polymers are physically separated by size or more specifically, by diffusion volume. When the separated polymer molecules leave the column, they are detected by concentration-dependent detectors, such as UV/VIS and refractive index (RI) detectors. The elution behavior is plotted as a chromatogram with the elution time correlating to the MW. The elution time can be compared to a calibration which is based on a polymer sample with known MWs. As a result, the MW of each polymer fraction can be computed relatively. Since the separation is purely physically, no information about chemical composure is obtained. The calculated MWs are only relative values but are important for the comparison of different polymer batches in a series.

Another method to separate polymers by size is the asymmetric flow field-flow fractionation (AF4). In contrast to GPC, no stationary phase is used to obtain separation but the mobile phase carrying the sample flows through a channel with a semipermeable membrane at the channel bottom. Thus, additionally to the laminar flow through the channel a flow perpendicular to the channel (crossflow) is induced because the solution permanently flows through the membrane. The particels are pushed by the crossflow to channel bottom but cannot pass the membrane. Through Brownian motion the particles diffuse then again into the middle of the channel. The Brownian motion for smaller particles is higher, which is why they elute faster from the channel. The separation is inverse to GPC (elution: small > big). The eluted solution is commonly detected by a combination of UV/VIS and light scattering detectors, enabling the calculation of absolute MW values. The advantage of the AF4 is that no stationary phase is needed. Thus, sample breakthrough or sample adsorption cannot occur.[199] Furthermore, the upper MW limit is $10^9\,\mathrm{g\,mol^{-1}}$ and hence, distinctly higher than for GPC.[200] Within one measurement a sample with a broad size range from 1 nm to 100 µm can be separated with a high resolution.[201]

2.3.2 Spectroscopic Characterization

CPs possess strong absorption and emission features in the visible range. Due to the strong dependency on weak intermolecular interactions, their position and shape is not only determined by their chemical structure but by conformation, disorder and packing structure (in solid state). Hence, CPs strongly respond to changes of the environment. That is why they are also discussed as chromophores in sensors.[24,28] The characteristic absorption bands of electronic transitions, such as $\pi \rightarrow \pi^*$, emerge in the visible range. Consequently, the optical bandgap is derived from the UV/VIS absorption spectrum. As illustrated in Figure 2.19, λ_{onset} of the absorption edge (to higher wavelengths, or lower energies, respectively) of the absorption band of the $\pi \rightarrow \pi^*$ transition is used to calculate the energy $E_{g,opt}$ of the optical bandgap. Equation 2.1 displays the relation between the energy E and the wavelength λ, where h is the Planck constant and c the velocity of light. $E_{g,opt}$ can be then calculated from λ_{onset}.

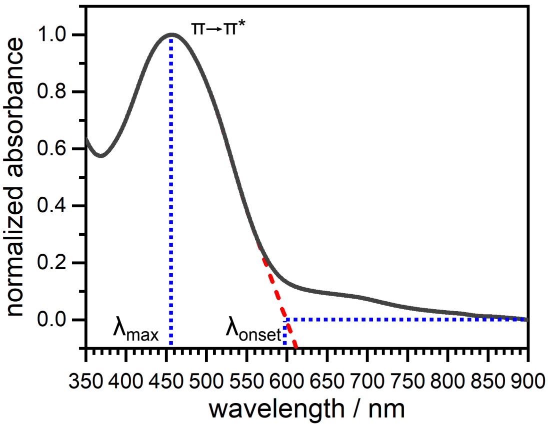

Figure 2.19: Determination of optical bandgap by the onset method, exemplary shown on the UV/VIS-spectrum of P3(EO)3T as thin film.

$$E = \frac{h \cdot c}{\lambda} \rightarrow E_{g,opt} = \frac{1240\, nm \cdot eV}{\lambda_{onset}} \tag{2.1}$$

Solidified in thin films, CPs do not possess a homogeneous microstructure but co-existing amorphous and crystalline regions. The interpretation of optical spectra are delicate but hold many information, such as conformational order and intermolecular interactions of the polymer chains. Spectroscopic studies beyond the optical range are essential for doped CPs. Diagnostic vibronic transitions were found in the near-infrared to infrared range. Furthermore, it was found that for p-dopants, containing cyano-groups, the amount of charge transferred can be estimated by comparing the position of the nitrile stretching band in the neutral and charged dopant.[69] Therefore, attenuated total reflection Fourier-transform infrared spectroscopy (ATR-FTIR) is commonly applied to study the CT mechanism upon p-type doping.

2.3.3 Imaging of Nanostructures

There are two techniques to image DNA-based structures with nanometer-sized features, which are AFM and electron microscopy, mainly transmission electron microscopy (TEM).

TEM is a microscope technique where the image is obtained from an electron beam which is transmitting a specimen. The change of the electrons' direction and energy due to absorption and scattering by the specimen is converted into the image. State-of-the-art microscopes provide a resolution below 1 nm.[202] TEM imaging is suitable for samples containing heavy elements, such as metallic nanoparticles,[183,193] or for 3D multi-layered samples, such as 3D origami DNA nanostructures.[169,171] However, flat biological or polymer samples are weak scattering centers for the electrons. The structures have a low contrast, as exemplarily shown in Figure 2.20a for a planar 2D DNA origami structure.

Planar biological nanostructures are commonly imaged by AFM.[11,35,181] In contrast to other methods, no electrons or photons are used but a sharp tip connected to a cantilever (the probe) scanning scanning the surface of the sample. The deflection of this tip is converted into a topographical image. The resolution of AFM imaging goes down to the subnanometer range, and depends mainly on the sharpness of the tip. Different operation modes are established how the tip scans over the sample, namely *contact mode*, *tapping mode* and *non-contact mode*. Tapping mode is nowadays the most prevalent mode for mechanically soft samples, such as polymers, DNA or proteins.[203] In this mode, the tip oscillates closely at its resonance frequency over the sample surface. The tip is shortly in contact with the surface and moves permanently between the attractive and repulsive force regime (concerning the sample surface). Only weak lateral forces are exerted by the tip to the sample surface.

AFM measurements can be conducted in ultra-high vacuum, air or in solution.[203]

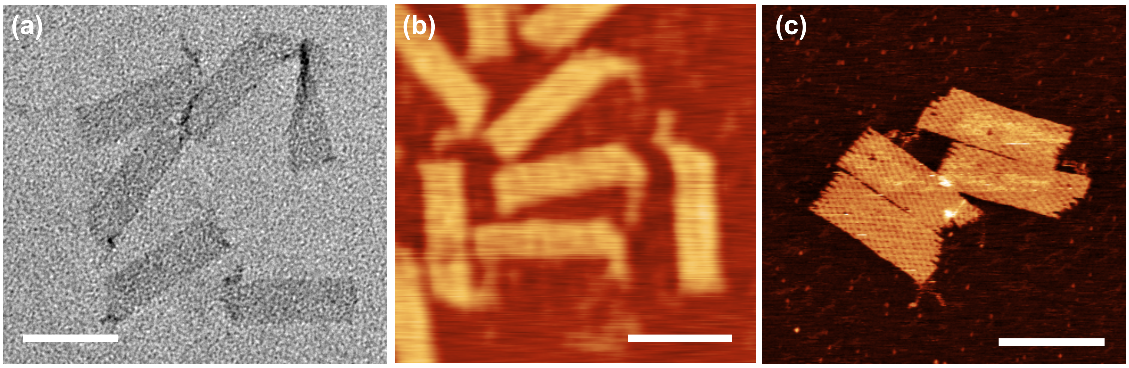

Figure 2.20: Images of a planar rectancgular DNA origami structure measured by (a) TEM, (b) AFM at air and (c) AFM in solution. Scale bars: 100 nm.

The latter is particularly advantageous for biological, soft samples because it enables to image them in their natural environment. Drying-effects, such as shrinking or even structure collapse, can be circumvented. Furthermore, the influence of ionic strength, pH or other parameters on the structural features can be studied. Figure 2.20b shows the planar DNA origami structure imaged by AFM in air. In comparison to the TEM image, the structure appears with a high contrast. However, despite its shape no further information are obtained from this image. The same structure was measured by AFM in a buffered solution containing Mg^{2+} ions (Figure 2.20c). The resolution of the structures is significantly enhanced. Features, such as the pattern of the DNA double helices, single strands protruding from the structure or missing staple strands are visualized. Consequentially, AFM imaging in solution is a highly suitable technique for flat, soft, nanoscaled specimen.

Despite topographical information, further material's properties can be extracted from the probe's motion during AFM measurements, such as magnetic, electrostatic or mechanic properties. Additional set-ups combined with modified tips, e.g., chemically functionalized or metalized, can be used to acquire further properties, such as binding forces between biomolecules or local $I - V$ characteristics. The latter is termed conductive atomic force microscopy (cAFM). In contrast to macroscopic measurements, the properties are locally probed at the nanoscale and not as bulk enabling the characterization of nanoscaled structures.

2.3.4 Electrical Characterization at the Nanoscale

A material is electrically characterized by $I - V$ measurements where the current I flowing through the device is plotted dependent on the applied voltage V. Position and shape of the obtained $I - V$ curve give valuable information over the material's electronic properties. For micro-circuits, various set-ups are established to measure the electrical properties of a material. The most straightforward set-up is to measure the current I flowing between two electrodes with a specific gap in dependency on the applied voltage U - the two-probe set-up.[204] The sample provides the conducting channel in the gap. In an idealized case of uniform current flow in a defined channel with a known cross-section area A and length L, the material's volume resistivity and the conductivity σ, as its reciprocal, can be calculated from the measured resistance R by Equation 2.2.

$$\rho = R \cdot \frac{A}{L} \tag{2.2}$$

While DNA-templated nanowires provide a length scale over micrometers,[149,150] DNA origami-templated nanowires are, so far, limited to the nanometer length scale.[192,195,205] The challenge is to contact a structure with nanometer features by macroscopic electrodes.

At the early state, electrodes with a nanometer-sized gap were produced by e.g., electron-beam lithography,[207] break junctions,[208] or shadow masks.[209] The concentrated sample was then distributed on these electrodes with the result that few structures were randomly positioned in this gap.[205] As apparent in Figure 2.21a), the probability is very low. This uncontrollable contacting is particularly disadvantageous when the quality of the structures is rather low.

The group of Arthur Erbe reported an improved method, where DNA origami-based metallic nanowires were selectively contacted by electron beam lithography (Figure 2.21b).[192,195] Thus, it was possible to pointedly measure an intact structure. First, the sample was immobilized on the substrate, and then the electrodes were fabricated on top of the sample. This approach is straightforward for metallic samples but adverse for biological or polymeric materials.[206] The sample could change or dissolve during the electron beam lithography procedure due to the exposure to organic solvents and the resist.

Another approach to specifically contact individual structures is the application

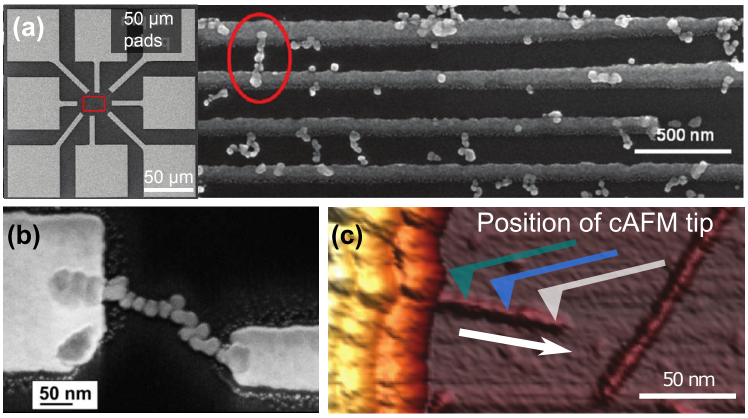

Figure 2.21: (a) Metalized DNA origami structure randomly deposited upon interdigitated electrodes with nanometer-sized gaps, reproduced from (*205*). (b) Metalized DNA origami structure specifically contacted by nanogap electrodes fabriacted by electron beam lithography, reproduced from (*192*). (c) G-quadruplex DNA protruding from a stationary gold electrode site-specifically contacted by a cAFM tip, reproduced from (*206*).

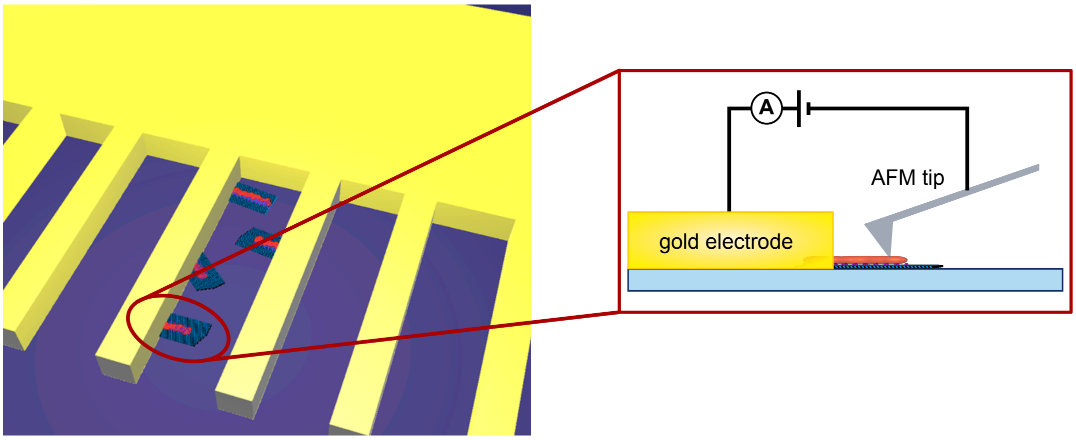

Figure 2.22: Set-up to electrically characterize a DNA origami-template polymer path by cAFM where one contact is given by the sharp-edged gold electrode and one by the AFM tip.

of top-contact junctions, such as scanning tunnel microscopy or cAFM.[210,211] Only one contact is provided by a deposited electrode, the second contact is provided by the probe, e.g., the cAFM tip. The challenging technical fabrication of nanogap electrodes would be obsolete. Furthermore, the resistance at different positions within one structure can be measured, a so-termed transmission line measurement. Thus, the contact resistant between structure and electrode is additionally measurable.[163] Based on cAFM a particularly, sophisticated approach to measure soft and sensitive structures was developed by the group of Danny Porath (Figure 2.21c).[206] A gold electrode was deposited on top of a randomly distributed sample by shadow mask lithography, which avoids the deployment of any chemicals. The gold film was only 20 nm thin and possessed a defined sharp edge. Porath's group demonstrated the applicability of this method for short and sensitive samples by measurements on G-quadruplex DNA molecules and thin metalized DNA strands.[206,212] As displayed in Figure 2.22, this method could be applied to DNA origami-templated polymer paths. The combination of imaging and measuring is further advantageous in the case of samples with a low overall yield. It should be noted, that this set-up is limited to fundamental investigations and is not usable in practical devices.

3 Experimental Section

3.1 Materials

All chemical reagents were purchased from abcr Chemicals, Sigma Aldrich Merck or Fisher. All chemicals and solvents were used without any further purification. Exceptions are mentioned in the text. The crosslinker azido acetate NHS ester was purchased from JenaBioscience. The scaffold strand M13mp18 was purchased from Tebu Biologies. Non-functionalized oligonucleotides were purchased from Eurofins Genomics GmbH. End-functionalized oligonucleotides (dibenzoyloctine and thiol) were purchased either from Biomers, IBA Lifetechnologies or Eurofins Genomics GmbH. The DNA samples were used as received. The buffer recipes are presented in Table 3.1. A detailed list of all chemicals which were applied in the scope of this thesis are concluded in Table 3.2.

Table 3.1: Buffer recipes used in the scope of this thesis.

buffer	recipe
1xTE buffer including Mg^{2+} (folding buffer DNA origami)	40 mM Trizma base 2 mM Na_2EDTA pH 8.1 12.5 mM $MgCl_2$
1xTE buffer including Mg^{2+}, Na^+ (buffer for hybrid formation)	40 mM Trizma base 2 mM Na_2EDTA pH 8.1 12.5 mM $MgCl_2$ 300 mM NaCl
0.5xTBE buffer (PAGE running buffer)	44.5 mM Trizma base 44.5 mM Boric acid 1 mM Na_2EDTA pH 8.2
1xTAE buffer including Mg^{2+} (agarose gel running buffer)	40 mM Trizma base 2 mM Na_2EDTA 1.74 mM glacial acetic acid pH 8.1 2.5 mM $MgCl_2$
1xT buffer with Mg^{2+} (electro elution)	40 mM Trizma base 2.5 mM $MgCl_2$

Table 3.2: List of chemicals used in this thesis.

compound	**supplier**	**purity**
3-Thiophene methanol	ABCR	98%
4-Bromo-3-methylaniline	Sigma Aldrich	>97%
Acrylamide/bis-acrylamide, 40% solution	Sigma Aldrich	N/A
Ammonium persulfate	Sigma Aldrich	≥98%
Azidoacetic acid NHS ester	Thermo Sientific	N/A
Biozym LE Agarose	Biozym	N/A
N,N-Diisopropylethylamine	Sigma Aldrich	≥99%
Ethylenediaminetetraacetic acid disodium salt dihydrate	Sigma Aldrich	>99%
Hydrochloric acid	ACS	37%
Hydrochloric acid in methanol	Sigma Aldrich	N/A
Iodine	Sigma Aldrich	>99%
Magnesium chloride	Sigma Aldrich	>97%
Magnesium sulfate (anhydrous)	Alfa Aesar	99.50%
N-Bromosuccinimid	Sigma Aldrich	99%
n-Butyllithium solution (2.5 M in hexanes)	Sigma Aldrich	N/A
Ni(dppe)Cl2	Sigma Aldrich	N/A
Phenyliodoacetat	ABCR	98%
Potassium hydroxide	Riedel-de-Haën	85%
iso-Propyl magnesiumchloride (2 M in THF)	Aldrich	N/A
Pyridin (anhydrous)	Sigma Aldrich	99.80%
Sephadex® G-10	GE Healthcare	N/A
Sodium hydroxide	Riedel-de-Haën	99%
Sodium sulfite	Sigma-Aldrich	98%
Tetrabutylammonium bromide	Sigma Aldrich	>99%
N,N,N',N'-Tetramethylethylenediamine	VWR Chemicals	≥99%
p-Toluenesulfonic acid	Sigma Aldrich	>99%
Triethylenglycolmonomethylether	Sigma Aldrich	≥94.5%
Trimethylsilyl chloride	Sigma Aldrich	≥99%
Trizma® base	Sigma Aldrich	>99%
Zinc chloride (anhydrous)	Sigma Aldrich	99.00%

3.2 Synthesis

3.2.1 NH_2-P3(EO)$_3$T

Synthesis of *N*-(4-bromo-3-methylphenyl)-1,1,1-trimethyl-N-(trimethylsilyl) silanamine (N(TMS)2-Ph-Br)

1 eq. 4-bromo-3-methyl aniline dissolved in THF and cooled down to -78 °C. Subsequently, 1.1 eq. *n*-buthyllithium (*n*-BuLi) (2.5 M in hexane) was added dropwise to this solution, and the reaction mixture was stirred for 1 h. To the warmed up (r.t.) reaction mixture, 1.1 eq. trimethylsilyl chloride was added. Stirring was continued for 6 h. The solution was again cooled down to -78 °C, and the two compounds *n*-BuLi and trimethylsilyl chloride were added in the same procedure. The reaction was stopped with water. The organic phase was separated, and the aqueous phase was extracted for three times with diethyl ether. All collected organic layers were dried over $MgSO_4$, filtrated and dried under reduced pressure. The crude product was filtrated over silica gel (diethyl ether : hexane = 2:1) and purified by distillation (72 °C and 10^{-6} bar). The pure product was obtained as a clear oil. ^{1}H-NMR (500 MHz, chloroform-d): δ ppm = 7.27 (d, J = 8.20 Hz, 1 H, 1); 6.70 (d, J = 2.52 Hz, 1 H, 2); 6.52 (dd, J = 8.20, 2.50 Hz, 1 H, 3); 2.28 (s, 3 H, 4) and 0.00 (s, 18 H, 5).

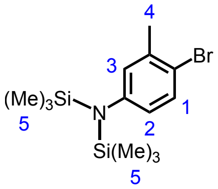

Synthesis of (4-amino-2-methylphenyl)nickel(dppe)chloride (N(TMS)2-Ph-Ni(dppe)Cl)

1 eq. *N*-(4-bromo-3-methyl phenyl)-1,1,1-trimethyl-*N*-(trimethylsilyl)silanamine was dissolved in THF and cooled down to -78 °C. 0.9 eq. *n*-BuLi (2.5 M in hexane) were added and the reaction mixture was stirred for 1 h. In the following, 1.1 eq. anhydrous $ZnCl_2$ (0.5 M in THF) were added and the solution was warmed up to room temperature. The reaction vessel was transferred to the glove-box and added to a suspension of 0.6 eq. Ni(dppe)Cl_2 (0.08 M dispersed in THF). The mixture was stirred until a color-shift was observed from dark-orange to bright-orange. The solution was stirred for another 5 min. The product was stored in the glove-box at -20 °C and used without any further purification.

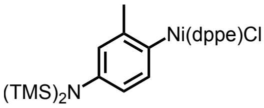

Synthesis of 1-(2-bromo-5-iodothiophen-3-yl)-2,5,8,11-tetraoxadodecane (I-3(EO)3T-Br)

The monomer precursor 1-(2-bromo-5-iodothiophen-3-yl)-2,5,8,11-tetraoxadodecane was synthesized, as described in previous works.[213] The precursor was freshly purified by column chromatography before polymerization (silica gel, ethyl acetate : hexane = 2:1).
^{1}H-NMR (500 MHz, chloroform-d1): δ(ppm) = 7.17 (s, 1 H, 4); 4.43 (s, 2 H, 3); 3.62-3.68 (m, 12 H, 2) and 3.37 (s, 3 H, 1).

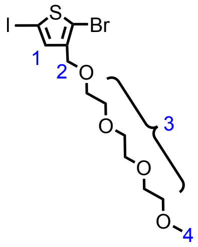

Polymerization of Amine-Functionalized Poly(3-2,5,8,11-tetraoxadodecane thiophene) (NH2-P3(EO)$_3$T)

1 eq. of 3-((2-(2-(2-methoxyethoxy)ethoxy)ethoxy)methyl)-2-bromo-5-iodothiophene was dissolved in THF and cooled to 0 °C. 0.9 eq. of *iso*-propyl magnesium chloride (2 M in THF) was gently added to the solution and stirred for 1 h. The mixture was warmed up to room temperature. 0.01 eq. N(TMS)$_2$-Ph-Ni(dppe)Cl (ca. 0.5 M in THF, the feed ratio was varied for different polymer batches) was rapidly added to the reaction mixture. The proceeding polymerization was apparent by a strong color-shift (yellow → deep red). The reaction was stirred for 30 min and then quenched by the addition of 5 N HCl (in methanol). The crude polymer solution was washed with water. The aqueous layer was extracted three times by chloroform. The collected organic layers were dried over MgSO$_4$ and filtrated. The solvents were removed under reduced pressure. The solid polymer was dissolved in methanol and washed three times with hexane. The methanol layer was collected and dried under reduced pressure. The polymer was dissolved in water containing NH$_4$OH (pH > 9) and washed three times with diethyl ether. The collected aqueous layers were dried under reduced pressure. The polymer was further dried in the vacuum oven overnight at 50 °C. The polymer was obtained as a deep-red solid.
^{1}H-NMR (500 MHz, dichlormethan-d2): δ(ppm) = 7.23 (br.s, n · 1 H, 1); 6.99-7.06 (m, 1 H, 2); 6.58-6.61 (m, 1 H, 3); 6.54 (d, 1 H, J = 10.1 Hz, 4); 4.62-4.72 (m, n · 2 H, 5); 3.40-3.80 (m, n · 12 H, 6); 3.31 (s, n · 3 H, 7) and 2.39 (s, 3 H, 8).

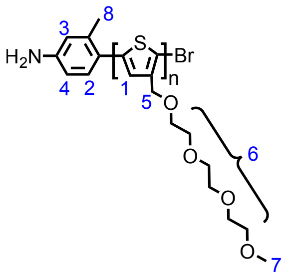

Polymerization of Poly(3-2,5,8,11-tetraoxadodecane thiophene) (P3(EO)$_3$T)

1 eq. of 3-((2-(2-(2-methoxyethoxy)ethoxy)ethoxy)methyl)-2-bromo-5-iodothiophene was dissolved in THF and cooled to 0 °C. 0.9 eq. of *iso*-propyl magnesium chloride (2 M in THF) was gently added to the solution and stirred for 1 h. The solution was warmed up to room temperature. 0.0125 eq. Ni(dppe)Cl_2 (different feed ratios were applied) was dispersed in THF and rapidly added to the reaction mixture. The same purification procedure, as described above, was applied.
^{1}H-NMR (500 MHz, chloroform-d1): δ(ppm) = 7.23 (s, 1 H); 4.66 (s, 2 H); 3.40-3.80 (m, 12 H) and 3.31 (s, 3 H).

3.2.2 N$_3$-P3(EO)$_3$T

In the glove box, 10 eq. of the linker azidoacetic NHS ester were dissolved in acetonitrile in a glass vessel, which was equipped with a stirrer. The vessel was sealed and transferred outside of the glovebox. The solution was cooled to 0 °C. Subsequently, 0.1 eq. N,N-diisopropylethylamine and 1 eq. NH2-P3(EO)$_3$T (dissolved in acetonitrile) were added in an argon-flushed syringe. The reaction mixture was allowed to slowly warm up to room temperature and stirred for 18 h. The solvent was removed under reduced pressure. The polymer was dissolved in a small amount of cold water. The excess of cross-linker was removed by filtration over a size-exclusion column packed with Sephadex® G-10. Water was removed under reduced pressure. The product was dried overnight at 50 °C in a vacuum oven.

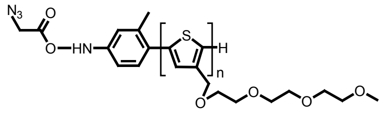

3.2.3 P3(EO)$_3$T-b-ON

1 eq. of N3-P3(EO)$_3$T (c ≈ 800 µM) was dissolved in cold water and filtrated through a 0.45 µm syringe filter. 0.1 eq. of the DBCO-ON (c = 100 µM) were added to the dissolved polymer. The chemical structure of the DBCO-ON is shown Figure 3.1.
The reaction mixture was kept on a thermo-shaker shaking with 350 rpm at 20 °C for at least 24 h. The crude reaction mixture was purified by gel electrophoresis either by a 1 wt.-% agarose gel or 8 to 12 wt.-% polyacrylamide gel (PAGE). The intrinsic

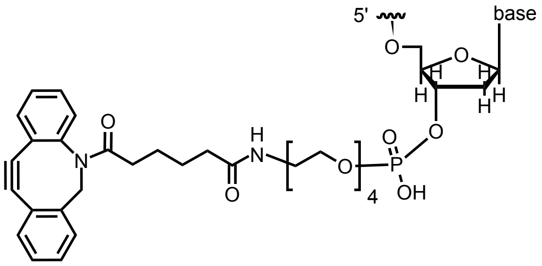

Figure 3.1: Chemical structure of dibenzoyl-octine oligonucleotide.

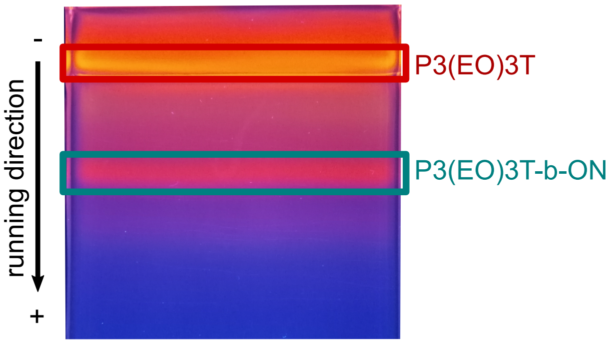

Figure 3.2: 1 wt.-% agarose gel under UV illumination. The gels are not stained, which is why the band of the ON cannot be seen.

fluorescence of P3(EO)$_3$T was used to identify the band of interest. Figure 3.2 shows one exemplary preparative agarose gel under UV illumination. Free P3(EO)$_3$T did not move in the gel. The ON band moved almost twice as fast as P3(EO)$_3$T-b-ON. P3(EO)$_3$T-b-ON was extracted from the gel band by electroelution (3h, 70V in 3.5 kDa Pur-A-Lyzer$^{\text{TM}}$ dialysis tubes). The solution was separated from the remaining gel and filtrated through 0.45 µm syringe filters to remove colloidal gel particles. The solution was desalted by dialysis against millipore water for 36 h and then lyophilized or dried under reduced vacuum.

The purified P3(EO)$_3$T-b-ON was dissolved in millipore water. The concentration was determined by UV/VIS spectroscopy using the absorption of DNA at 260 nm. Since P3(EO)$_3$T also absorbs at 260 nm, the spectra were first normalized to the P3(EO)$_3$T signal at 420 nm and then subtracted by the spectrum of bare P3(EO)$_3$T (normalized to 420 nm). The corrected absorption A$_{260}$ at 260 nm was then used to calculate the concentration of the oligonucleotide, which is equal to the concentration of P3(EO)$_3$T-b-ON, following Lambert Beer's Law (Equation 3.2.3).

$$c = \frac{A_{260,corrected}(BCP)}{\epsilon_{260}(ON) \cdot d} \tag{3.1}$$

The extinction coefficient ε_{260} was used as given from the supplier (biomers.net or IBA lifetechnologies). Measurements were done in standard micro-volume cuvettes with d = 1 cm.

3.2.4 P3(EO)$_3$T@Origami

DNA Origami Assembly

The origami structure was assembled by mixing 1 eq. M13mp18 scaffold strand (20 to 30 nM) and 5 eq. of each staple strand (100 to 150 nM) in the folding buffer. The mixture was heated to 80 °C, then kept for one hour at 53.2 °C and then cooled to 4 °C for at least 10 min. The residual staple strands were removed by filtration through 100 kDa Amicon filter (4000 rpm, 8 min). The solution was washed three times by the addition of 400 µL folding buffer. The DNA origami formation was controlled by AFM measurements. The final concentration was determined by UV/VIS spectroscopy.

P3(EO)$_3$T@pad Assembly

To a solution of 1 eq. DNA origami structure (4 to 5 nM), 10 eq. of P3(EO)$_3$T-b-ON (in 1xTE buffer with 12.5 mM MgCl$_2$) were added. To the folding buffer, additional sodium chloride was added (c = 300 mM). The mixture was hold on a thermomixer at 400 rpm and 15 °C for at least 24 h. The mixture was purified by filtration with Amicon 100 kDa filters. The solution was washed three times with 400 µL folding buffer per washing step. The formation of the hybrid structure was controlled by AFM and gel electrophoresis (Figure 3.3). The concentration was estimated by UV/VIS spectroscopy.

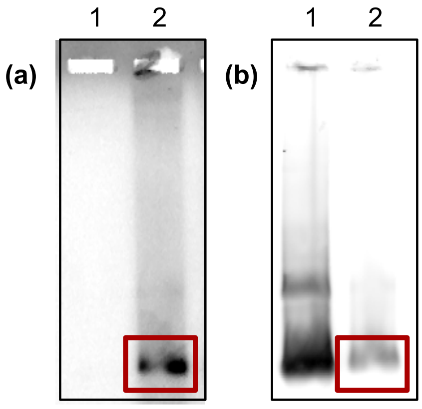

Figure 3.3: (a) Unstained and (b) DNA-stained (Sybr®Gold) 1 wt.-% agarose gel of the bare origami structure pad (1) and the hybrid structure P3(EO)$_3$T@pad (2). Due to the intrinsic fluorescence of P3(EO)$_3$T, the band of P3(EO)$_3$T@pad (marked with a red box) is visible for the unstained gel.

AuNR-P3(EO)$_3$T@pad Assembly

To a solution containing 1 eq. the hybrid structure P3(EO)$_3$T@pad (2 nM) in 300 mM NaCl and folding buffer, 18T-functionalized gold nanorods (2 eq., in water) were added. To the reaction mixture, pluronic® was added to stabilize the target structures in solution. The mixture was annealed for 15 min at 40 °C and cooled to 25 °C for 5 min. The cycle was repeated for at least 120 times. The samples were used without further purification. The successful formation was controlled by TEM.

3.3 Methods and Instrumentation

Asymmetric Flow Field-Flow Fractionation

AF4 experiments were acquired on a Wyatt Eclipse DUALTEC system equipped with an Agilent pump system to control the flow. As channel membrane, a short channel with a channel height of 320 µm and a 5 kDa polyethersulfone channel membrane was used. As carrier medium, a PBS buffer with 0.2 wt.-% sodium azide solution (pH 7.4) was applied. Two detector systems were applied: a DAWN EOS multi-angle scattering detector (Wyatt Technology) and an Agilent Technologies UV-detector (operated at 260 nm and 430 nm). The sample concentration was determined by the UV-detector and the respective extinction coefficients (ε (430 nm) = 13.35 mL/mg*cm and ε (260 nm) = 9.64 mL/mg*cm). Per sample a volume of 50 µL was injected with an average sample concentration of 0.8 mg/mL. The samples were neither purified nor filtrated before measuring. The MW of the dissolved $P3(EO)_3T$ fraction was calculated by applying a Zimm fit (fourth order), the MW of the aggregated $P3(EO)_3T$ fraction by applying a Berry fit (fourth order) and the MW of the $P3(EO)_3T$-b-20N by applying a Zimm fit (fourth order). The results are the average of three measurements.

Atomic Force Microscopy

AFM imaging in the air was performed either on an Asylum Cypher Device (standard scanner) or a Bruker Dimension Icon microscope. Both devices were operated in tapping mode and equipped with silicon tips TESPW-V2 ($f_{resonant}$ ca. 330 kHz, spring constant ca. 40 N/m) with a tip radius around 8 nm. AFM imaging in solution was performed on an Asylum Cypher Device ESTM Environmental AFM operated in tapping mode and blueDrive photothermal excitation. Gold-coated silicon-nitride BL-AC40TS-C2 cantilevers (Olympus) were used with $f_{resonant}$ ca. 25 kHz in water, a spring constant ca. 0.09 N/m and a spring radius around 8 nm. Measurements in solution were performed at 25 °C in 100 µL 1xTE buffer solution with 12.5 mM Mg^{2+} on freshly cleaved mica.

Sample preparation for measurements in air. Polymer thin films were prepared by spin-coating on clean silicon substrates (as described in the thin film fabrication section). DNA origami samples were prepared on freshly cleaved mica. The DNA origami structures were immobilized in their folding buffer (1xTE buffer with 12.5 mM Mg^{2+}) by applying a DNA origami concentration of roughly 1 nM and an adsorption time of 5 to 10 min. The samples were washed three times by millipore water to remove residual buffer and salt and were then dried under an air stream.

Sample preparation for measurements in solution. The freshly cleaved mica substrate was incubated for 45 sec with a polyornithine solution (0.1 mg/mL) to charge the surface positively. The mica substrate was rinsed and air-dried. The DNA origami solution (ca. 1.2 nM in 1xTE buffer with 12.5 mM Mg^{2+}) was left for 10 min on the surface and then partly withdrawn by a tissue or filter paper. Then, the fresh folding buffer was added and used for the measurements.

Attenuated Total Reflection Fourier-Transform Infrared Spectroscopy

ATR-FTIR measurements were acquired on an FTIR-spectrometer Vertex 80v (Bruker) and operated under vacuum conditions. The respective sample was spin-casted on a silicon float zone substrates. The device was equipped with a mercury-cadmium-telluride detector and a 40 mm ATR-Si-wafer unit. A spectroscopic range was covered from 7500 to 1000 cm^{-1} by a spectral resolution of 2 cm^{-1}. In total 500 scans were measured and co-added to a final spectrum. The spectra were baseline corrected. For the analyses of the frequency shift δ from the nitrile stretching mode of F4TCNQ and $F4TCNQ^{-}$ the absorption of the polaron was subtracted by weighted end-points between the region of interest.

Conductivity AFM measurements

AFM scanning under normal conditions was acquired on a Smart-AIST AFM in tapping mode using silicon nitride cantilevers (L = 100 µm, Olympus, OMCL-RC800PSA-W) with resonance frequency of around 70 kHz. cAFM measurements were performed with a Smart-AIST conductive AFM system. The silicon tips were Cr/Pt-coated (Budget Sensors, Multi75E-G). The measurement area containing the desired structure was approached in tapping mode. Conductance of tip and the stationary gold electrode was tested by contacting the stationary electrode in close proximity to the target structure. When a current flow was detected, the structure was considered to be contacted. The tip was then moved within a chosen straight line or polyhedral area of contact points from one measurement to the next. The density of points was varied between 5 to 20 nm resolution. The tip contacted the sample surface only at the specific points within this grid. At each contact point, an $I - V$ curve was recorded with sweeping the voltage from -2.5 to 2.5 V with 200 points per sweep and a sweep time of 200 ms. Thus, the conductivity within the line or area, respectively, was mapped.

Conductivity Measurements

Conductivity measurements were performed in a two-probe set-up with a probe station. For the microchannel electrodes with a distance of 100 µm between the electrodes the polymer thin films were first, spin-coated on the glass substrate and then the gold-contacts were evaporated on the polymer thin film. For the interdigitated electrodes with an electrode distance of 5 µm, the gold electrodes were first, lithographically fabricated on the glass substrate and secondly, the polymer was drop-casted on the electrodes. Current-voltage curves were recorded on a Keysight B1500A Semiconductor Device Analyzer. The current-voltage curves were at least at four different electrode pairs acquired giving the specified error. The film thickness (20-80 nm) was determined for each polymer film (microchannel electrodes) or electrode pair (interdigitated electrodes) by AFM. For the micro-channel electrode, the distance L between the electrodes of the electrodes was determined by light microscopy.

Cyclic Voltammetry

A three-electrode set-up was used for cyclic voltammetry (CV) measurements. As electrolyte solution a 0.1 M tetra-n-butylammonium hexafluorophosphate in anhydrous acetonitrile was used. The electrolyte solution was freshly prepared, flushed for 20 min with nitrogen before each measurement. The electrode set-up comprised a platinum disc working electrode, a platinum wire counter electrode and pseudo-reference electrode (Ag/Ag$^+$; silver wire in an electrolyte solution with 0.01 mol L^{-1} $AgNO_3$). A small amount of P3(EO)$_3$T (ca. 2 mg) was added to the solution and the solution was flushed for other 10 min by nitrogen. It was not possible to fabricate stable polymer films on the working electrode due to the high solubility of P3(EO)$_3$T in acetonitrile. Voltammograms were recorded at a scan rate of 50 m/V and referenced to the signal of the redox couple ferrocene/ferrocenium. The energy of the HOMO level E_{HOMO} was calculated from the onset potential of the oxidation and by applying the following equation:

$$E_{HOMO} = -(5.09 + E_{onset,ox} - E_{1/2,Fc}) \tag{3.2}$$

With $E_{1/2,Fc}$ being the half-wave potential of the reference material ferrocene. Ferrocene was measured before and after each measurement. The mean value was used for the calculation. The energy LUMO level E_{LUMO} was estimated by the sum of E_{HOMO} and $E_{g,opt}$.

$$E_{LUMO} = E_{HOMO} + E_{g,opt} \tag{3.3}$$

Doping of P3(EO)3T@pad Structures

For both procedures, the viability of the hybrid structures was verified by AFM before evaporating the stationary gold electrode.

Doping from solution. The dopant F4TCNQ was used as diluted solution in acetonitrile (c = 1.2 mM). The dopant potassium hexacyano-substituted [3]-radialene radical anion (CN6CPK) (provided by Dr. Yevhen Karpov, Leibniz-Institut für Polymerforschung Dresden e.V.) was used as a diluted solution in the folding buffer (c = 1.2 mM). To the unpurified P3(EO)3T@pad solution (containing 5 µM P3(EO)3T-b-ON, 98 µL), 2 µL of the respective dopant solution were added. The sample was immediately immobilized on the mica substrate following the AFM sample protocol. Kept in solution, the origami structures degraded, most likely due to the strong oxidative stress.

Doping from the gas phase. The P3(EO)3T@pad structures were immobilized on mica, following the AFM sample protocol. The mica was placed in a sealed flask, facing the solid F4TCNQ, which was placed at the bottom of the flask. The dopant was sublimated by applying reduced pressure and increased temperature (by a heat gun, 100 °C). The doping process was monitored by a P3(EO)3T reference film (on glass) in the same flask. After the reference film changed its color (red→purple), the evaporation was stopped.

Dynamic Light Scattering

The measurements were recorded on a Wyatt DynaPro NanoStar. The sample solution (c = 1 mg/mL) was filtrated with 0.45 µm syringe filters. The sample was equilibrated in the device chamber for 5 min at 25 °C. Ten acquisitions per measurement were recorded with an acquisition time of 5 sec. Each series was five-times repeated. The results are the average values of these measurements.

Fluorescence Spectroscopy

Fluorescence measurements were recorded in the steady-state mode on a Horiba Scientific Fluoromax device. As excitation wavelength, the maximum of the absorption was taken of the individual polymer batch (ca. 430 nm).

Gel Documentation

For gels containing DNA without attached P3(EO)$_3$T, the DNA was stained by SYBR®Gold. Otherwise, the intrinsic fluorescence of P3(EO)$_3$T was used to identify the band of interest.

Agarose or PAGE gels were imaged either on a GE Healthcare Typhoon FLA 7000 device ($\lambda_{exc} = 473$ nm and $\lambda_{em} = 580$ nm) or on a LAS 500 device (broadband excitation, emission recorded by CCD camera). Preparative gels were imaged on a transilluminator by UV excitation.

Gel Preparation and Running Conditions

PAGE-gel. The PAGE gels were prepared in an acrylamide range of 8 to 12 wt.-%. The acrylamide is a 40 wt.-% stock solution containing 2 wt.-% bis-acrylamide. This stock solution was mixed with 5xTBE buffer (pH 8) and water to give a final concentration of 0.5xTBE. The precursor solution was thoroughly mixed and then degassed. The polymerization was initiated by the addition of TEMED and 10 wt.-% ammonium persulfate. The solution was quickly filled into the gel cast chamber under gentle shaking to remove any gas bubbles. The casted gel was dried for at least 45 min before running. The gel was run in a 0.5xTBE buffer for at least 90 min at a constant voltage of 120 V.

Agarose gel. Agarose gels were prepared in a range of 0.5 to 1 wt.-%. Agarose was dissolved in 1xTAE buffer containing 5 mM $MgCl_2$ under gentle heating in the microwave. The hot solution was quickly filled into the gel cast chamber and dried for at least 60 min before running. The gel was run in a 1xTAE buffer containing 5 mM $MgCl_2$ for at least 120 min at 90 V.

Gel permeation chromatography

GPC measurements were performed at 40 °C on an Infinity 1260 (Agilent) device equipped with a UV/VIS and refractive index detector. Chloroform was applied as a mobile phase with a flow rate of 1 mL/min. Sample solutions (2 mg/mL) were filtrated (0.2 µm PTFE) prior to usage. Number average molecular weight (M_n) and the dispersity ($= M_w / M_n$) were calculated based on a polystyrene calibration curve.

Image Analysis

AFM images. The raw AFM images were processed by the software Gwyddion[214] to remove scanning errors and artifacts. Typically images were plane-level corrected, rows were aligned by their median of differences, and horizontal scars were removed. In case of larger height differences, the mask tool was used, and the misaligned rows were leveled by the polynomial tool. The size and height of objects, such as the different $P3(EO)_3T$ paths, were measured by the profile tool of Gwyddion. At least two profiles were used for one direction (e.g., length and width). The area of objects was determined by the Particle Analyzer of Fiji (ImageJ) based on a 16bit grey-scale image.[215]

TEM images. The images were processed by the software Fiji. The brightness and contrast of images were modified. The structural dimensions of objects were elucidated by the profile plotting tool of Fiji.[215]

Nuclear magnetic resonance spectroscopy

500 MHz ^{1}H-NMR-spectra were acquired on a Bruker DRX 500 NMR spectrometer. Samples were analyzed as solution dissolved in chloroform-*d*1 or dichloromethane-*d*2 and internally calibrated to the solvent signal.

Substrate Cleaning Procedure

Glass and silicon substrates A. Glass and silicon substrates for most measurements were cleaned by the following procedure; 10 min per solvent in the ultrasonic bath. The solvents were (in this order): Millipore water, ethanol, acetone, chloroform, and isopropanol. After the last step, the substrates were swiveled in a fresh isopropanol bath and dried under a nitrogen stream.

Glass substrates B. Glass substrates, on which the interdigitated electrodes were fabricated, were cleaned for 5 min in a Piranha solution and then rinsed by Millipore water. They were first dried under a nitrogen stream and then further dried on a hotplate at 130 °C for 10 min.

Silicon substrates B. Silicon substrates which were applied for either AFM or ATR-FTIR measurements were cleaned by air (oxygen) plasma for 90 s with 70 W.

Surface Plasmon Resonance Spectroscopy

For the surface plasmon resonance spectroscopy (SPR) spectroscopic measurements were acquired on an SR7500DC system equipped with a two-channel flow cell (Figure 3.4) and an autosampler SR8100 (Reichert Technologies Life Sciences, XanTec bioanalytics GmbH). The channel height of the microfluidic cell was 100 µm. The respective sample solution was sequentially pumped by a syringe pump over the left and afterward over the right channel site. Glass substrates (12 x 12 x 0.3 mm) coated with a 28 nm silver and a 13 nm gold layer were used as SPR chips (XanTec bioanalytics GmbH). The aqueous solutions of the DNA probes (c = 1 µM) were immobilized on the SPR chip with a flow rate of 5 µL/min. The chemical structure of the probes is shown in Figure 3.5. The sequences are listed in Table 3.3.

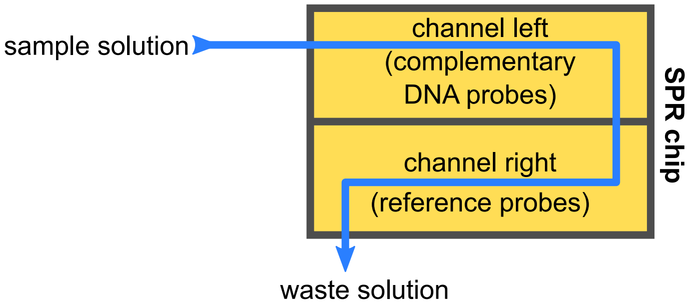

Figure 3.4: Set-up and flow of microfluidic system over the SPR chip.

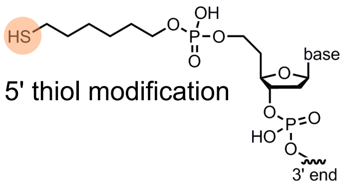

Figure 3.5: Chemical structure of 5'-C6-thiol-functionalized ON probes.

The chips were washed with the blocking reagent (11-mercapto undecyl)tetra(ethylene glycol) (MUTEG) (0.1 mM) to remove non-covalently bound DNA probes, to vertically straighten the bound DNA probes and prevent non-covalently sticking of the DNA samples. Hybridization experiments were performed in a 20 mM $MgCl_2$ solution by applying a flow rate of 2 µL/min. The respective samples (c = 500 nM) contained also 20 mM $MgCl_2$. After each hybridization experiment, the DNA probes were recovered (i.e., de-hybridized) by the following procedure: a Na_2EDTA (10 mM) solution followed by a NaOH (10 mM) solution were run over the chips. All processes were monitored by the shift of the SPR signal.

Table 3.3: Sequences of applied ON probes for SPR experiments.

probe	**5' functionality**	**spacer**	**sequence**
20N'	SH-(CH2)6	TTTTTT	GACAAAGCCGACCACCAAAG
18A	SH-(CH2)6	TTTTTT	AAAAAAAAAAAAAAAAAA
5(AAT)	SH-(CH2)6	CCCCCC	AATAATAATAATAAT
20N	SH-(CH2)6	TTTTTT	CTTTGGTGGTCGGCTTTGTC
18T	SH-(CH2)6	CCCCCC	TTTTTTTTTTTTTTTTTT
5(ATT)	SH-(CH2)6	TTTTTT	TTATTATTATTATTA

Thin Film Fabrication of Doped Polymer Films

The thin film fabrication was conducted under atmospheric conditions. The filtrated (syringe filter 0.45 µm) solutions of P3(EO)$_3$T (in chloroform with c = 10 mg/L) and F4TCNQ (in acetonitrile with c = 5 mg/L) were mixed into the respective molecular ratio. The polymer concentration in the final solution was held constant at 3 mg/mL corresponding to a molar concentration of the monomer unit (EO)3T of 11.6 mM. The dopant was added to in different volumes giving the final concentrations: 0.0 mM (MDR = 0%), via 0.6 mM (5%), 1.2 mM (10%), 1.5 mM (13%), 2.3 mM (20%), 3.9 mM (33%) 5.8 mM (50%) to 11.6 mM (100%). The polymer thin films were spin-casted from these pre-mixed solutions (V = 100 to 200 µL) applying following spinning conditions: 1500 rpm/min for 30 s with an acceleration of 500 rpm/min. The thin films were dried in the vacuum oven under reduced pressure by room temperature for at least one hour.

Transmission Electron Microscopy

Imaging was acquired on a transmission electron microscope LIBRA120 (Carl Zeiss) operating with an acceleration voltage of 120 kV. S162-4 formvar/carbon film on 400 copper mesh (Plano) was used as TEM grids. The sample (V = 5 to 10 µL) was incubated on a plasma-cleaned TEM grid for at least 7 min. The residual solution was removed by a filter paper followed by three washing steps with milipore water. The sample was dried again by a filter paper. The samples was stained by the addition of 5 µL 2 wt.-% uranyl acetate solution, which was incubated for 4 min. The staining solution was washed away and the specimen was dried by a filter paper. The sample was further air-dried for at least 30 min before measuring.

UV/VIS and UV/VIS-NIR Spectroscopy

UV/VIS spectroscopic measurements were recorded on a SPECORD®PLUS device (AnalytikJena). The concentration of DNA origami samples was acquired on a Nanophotometer P360. UV/VIS-NIR spectroscopy was performed on an Agilent Cary5000 device. On all devices, measurements were conducted in the transmission mode.

Samples in solution were measured in UVettes® (Eppendorf) with d = 1cm. For thin film measurements, optically plane-polished coverslips (Thermo scientific) were applied. All samples were referenced against the substrate, solvent or buffer system, respectively. Recorded spectra were further processed by smoothing and in some cases for better comparability by normalization to the maximum and baseline correction.

Variable Angle Spectroscopic Ellipsometry

Measurements were carried out on an M2000 VI ellipsometer (J.A. Woollam Co., Inc.). A wavelength range from 245 to 1680 nm at incidence angles, AOI: 55°, 60°, 65°, 70°, and 75°. The experimental Ψ and Δ spectra were modeled by using three oscillators (one Tauc-Lorentz, two Gaussian) for the 0%-doped polymer film and five oscillators (one Tauc-Lorentz, four Gaussian) for the doped polymer films giving the optical constants n and k.

X-ray Diffraction

Wide-angle x-ray scattering was recorded on a 2-circle diffractometer XRD 3003 T/T (GE Sensing & Inspection Technologies). The measurements were carried out in a symmetric step-scan mode with $2\Theta = 0.05°$ and t = 40 s. Cu$K\alpha$ radiation ($\lambda = 0.1542$ nm) was used which was monochromatized by primary multilayer system and slit geometry 0.2 mm/0.3 mm. The scattering results were plotted as intensity versus the scattering vector q. **1D-Grazing-incident wide-angle scattering** was executed on the same device but in an asymmetric step-scan mode with $2\Theta = 0.05°$ and $t = 20\,s$ and grazing angle 0.7°.

2D-Grazing-incident wide-angle scattering was carried out on a multi-range device Ganesha 300 XL+ (SAXSLAB ApS) operated with Cu$K\alpha$ radiation with $\lambda = 0.1542\,nm$ (monochromatization with bifocal Göbel mirror and µ-focus tube 50 kV/600 mA). The measurements were conducted entirely under vacuum. A two-pinhole configuration was used (cross-section: 400x400 µm^2 and 500x500 µm^2) with an accumulation time of 60 min and an incidence angle of 0.2°. A 2D detector (Pilatus 300K) with a pixel size of 172x172 µm^2 (beam stop diameter 4 mm) was used to accumulate the scattering intensities. The results were presented as 2D scattering patterns lgI (q_{xy}, q_z).

The layer distances d_{hkl} were calculated by the Bragg's equation based on $2\theta_{max}$ of the layer reflections.

$$d_{hkl} = \frac{\lambda}{2 \cdot sin(\theta_{max})} \tag{3.4}$$

4 Results and Discussion

4.1 Synthesis and Characterization of the Polythiophene Derivative

4.1.1 Introduction

Polythiophene derivatives are promising candidates for biomolecular-assembled circuits due to their structural kinship with most biomolecules. They are mechanically flexible and light-weight. Through the variety of organic chemistry, their properties can be custom-tailored within a wide range. In contrast to most polymers, they provide excellent optical and electronic functionality due to their extended π-system along their polymer backbone.

The focus of this project was the controlled incorporation of CPs into DNA-based nanostructures to obtain functional CP-DNA hybrid structures. Such CPs should be structurally defined and provide reliable optoelectronic properties at the nanoscale. Accordingly, a P3RT-type polythiophene derivative was the polymer of choice. These polythiophene derivatives are known for their well-defined molecular structure, their high stability and their self-assembly behavior into ordered structures.[28,216] In contrast to most polymerization approaches, the synthesis of P3RTs, the so-called KCTP, is "quasi"-living and follows, accordingly, a chain-growth mechanism.[116] The corresponding controllable and narrow size-distribution (adjustable MW and a dispersity approaching 1) is advantageous for the applications at the nanoscale. Furthermore, the quasi-living nature of the KCTP enables the introduction of functional hetero-objects and leads to a well-defined regioregular HT-conformation of the MU in the polymer chain.[33] Hence, P3RT-type polythiophenes remain still one of the bestseller polymers and are suitable for DNA-based nanoelectronics.

This chapter presents the design and synthesis of the polythiophene-derivative poly-3(tri-ethylene glycol thiophene) (NH_2-P3(EO)3T) which was applied as functional hetero-object in the DNA origami-based nanostructures. Furthermore, the polymer's structure and optical properties were thoroughly investigated with respect to the subsequent DNA-assembly. The obtained results are part of the publication in the journal *Nano Letters*: Zessin, Johanna; Fischer, Franziska; Heerwig, Andreas; Kick, Alfred; Boye, Susanne; Stamm, Manfred; Kiriy, Anton; Mertig, Michael, "Tunable fluorescence of a semiconducting polythiophene positioned on DNA Origami" *Nano Letters* **2017**, 17, 5163-5170.

4.1.2 Molecular Design of the Customized Polythiophene Derivative

P3RT-type polythiophenes, applicable in nanoscaled DNA-based devices, should provide the following features:

- electronic functionality;
- defined and narrow size distribution;
- soluble in polar solvents;
- compatible to DNA and
- functional end-group for accessibility to DNA attachment.

The extended π-system in the polythiophene backbone provides the first aspect, electronic functionality. Structural modifications address the further features. Bare polythiophenes are hardly soluble in any solvent. Their solubility has been increased tremendously by the introduction of solubilizing side-chains, in case of P3RT-type polythiophenes at the 3'-carbon position. Typically, alkyl-based side-chains are introduced providing solubility in a broad range of non-polar, mostly chlorinated organic solvents. Unfortunately, chlorinated solvents tend to precipitate DNA and are therefore not applicable for the later handling with DNA. Through the introduction of charged ionic groups, e.g., ammonium-, sulfonate- or carboxyl-groups, at the side-chains, water-soluble polythiophenes have been synthesized.[58,86,217] However, DNA itself is negatively charged due to the phosphate backbone. The introduction of charged side-chains, particularly positively charged ones, could lead to unintended interactions, such as aggregation, which would disturb the DNA assembly. Therefore, the non-ionic tri(ethylene glycol) side-chain ((EO)3) was introduced to provide biocompatibility and a reasonable solubility in water.

The assembly of functional hetero-objects on DNA-based nanostructures is commonly directed by the hybridization of short ONs which are linked to the hetero-object, whereas their complementary ONs protrude from the DNA-template. A functional group is required to conjugate an ON to the polythiophene. Such a group could be at the 4'-carbon of the thiophene, at the side- or at the polymer chain-start/end. The focus of this thesis was a well-controlled one-to-one attachment of many polymer molecules to the DNA origami-template in a dense array. Consequently, the functionalization of the chain-end was pursued. This enables the synthesis of a diblock copolymer, which is composed of the polythiophene block and the ON block. The KCTP supports the introduction of functional groups either by transfer from an initiator (i.e., a functionalized catalyst) or from a quencher. To warrant the highest possible DF, the KCTP was *ex-situ* initiated by a functionalized catalyst. Furthermore, polymers synthesized by the *ex-situ* initiated KCTP should yield fully regioregular HT-oriented polythiophenes (Figure 2.11). For this purpose,

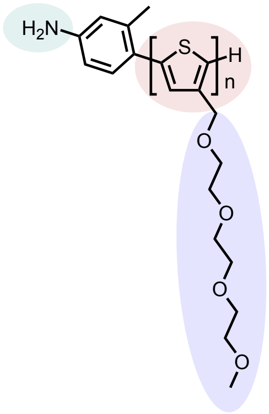

Figure 4.1: Design of the polythiophene derivative NH_2-P3(EO)3T with the polythiophene backbone (red), the solubilizing side-chain (EO)3 (blue), and the functional end-group NH_2 (green).

the synthesis approach of Senkovskyy *et al.*[132] was followed starting from the commercially available precursors 4-bromo-3-methylaniline and Ni(dppe)Cl_2. The target structure of the polymer NH_2-P3(EO)3T is displayed in Figure 4.1.

4.1.3 *Ex-Situ* Initiated Kumada Catalyst-Transfer Polycondensation

The polythiophene derivative NH_2-P3(EO)3T was synthesized by the *ex-situ* initiated Kumada catalyst-transfer polycondensation using the asymmetric monomer 3-((2-(2-(2-methoxyethoxy)ethoxy)ethoxy)methyl)-2-bromo-5-magnesium-halide thiophene (MgCl-3$(EO)_3$T-Br)[213,218] and the *ex-situ* initiator $N(TMS)_2$-Ph-Ni(dppe)Cl (Figure 4.2). The monomer was obtained by an iodine-magnesium exchange of the monomer precursor I-3$(EO)_3$T-Br through ^{i}PrMgCl yielding the Grignard compound MgCl-3$(EO)_3$T-Br. ^{i}PrMgCl was added in a slight shortfall to avoid free ^{i}PrMgCl during the polymerization. The synthesis of the monomer and monomer precursor were presented in a previous study and are not further examined here.[213]

The *ex-situ* initiator was synthesized beforehand starting from the aniline derivative 4-bromo-3-methylaniline (Figure 4.3). The primary amine was protected in two subsequent steps by the rather labile protection group trimethylsilyl (TMS)[219] using *n*-BuLi followed by the addition of trimethylsilyl chloride. Before each polymerization, the product was freshly purified by distillation to remove any primary amines, which would be too reactive for the following metalation reactions and KCTP. The external initiator was synthesized by a modified synthesis route, as reported by Senkovskyy *et al.* previously.[132] For this purpose, the 4' bromo-atom at the Ar-unit of the protected 4-bromo-3-methyl-aniline was exchanged with the active catalytic Ni(dppe)Cl-group over a series of metalation reactions using *n*-BuLi, $ZnCl_2$ and finally Ni(dppe)Cl_2. Ni(dppe)Cl_2 was added in a shortfall (0.6 eq.) to

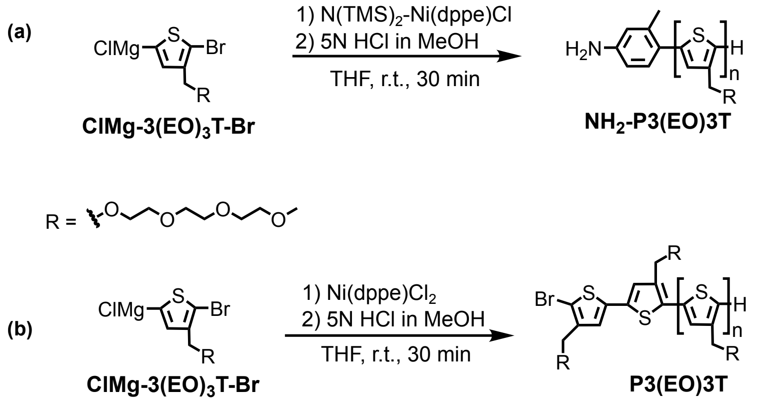

Figure 4.2: Reaction scheme of the (a) *ex-situ* and (b) *in-situ* initiated KCTP yielding (a) NH_2-P3(EO)3T and (b) P3(EO)3T.

ensure that each catalyst is functionalized. The 3' methyl group in ortho position stabilizes the active Ni-center electronically and sterically to prevent homocupling towards Ar-Ar.[125,220] The functional Ni-catalyst $N(TMS)_2$-Ni(dppe)Cl_2 was used as obtained without any further purification.

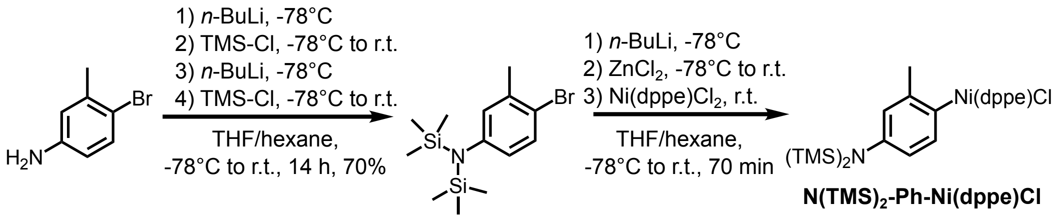

Figure 4.3: Reaction scheme towards $N(TMS)_2$-Ph-Ni(dppe)Cl started from the aniline derivative 4-bromo-3-methylaniline.

Finally, the *ex-situ* initiated KCTP was performed by applying different feed ratios of the *ex-situ* initiator $N(TMS)_2$-Ph-Ni(dppe)Cl to the monomer. Catalyst feed ratios in the range of 1 to 20 mol-% were used. The polymerization reaction was stopped after 30 min by the addition of 5 N HCl (in MeOH). Longer polymerization times and lower catalyst feed ratios were not applied to lower the influence of side reactions, such as re-insertion or random ring-walking of the Ni-catalyst.[120] The 5 N HCl (in MeOH) simultaneously deprotected the amine-group by removing the weakly bound TMS groups. The crude polymer was purified by a sequence of liquid-liquid extraction steps using chloroform/water, methanol/hexane and water/diethyl ether where the first-mentioned phase contained the polymer. The pure polymer was dissolved in chloroform, dried by magnesium sulfate and finally isolated through drying under reduced pressure.

Additionally, two polymer batches (Table 4.1, JZ95 and JZ131) were synthesized by the *in-situ* initiated KCTP (Figure 4.2b) yielding P3(EO)3T without a functional starting group but with a TT-defect at the chain-start. Experiments, which required a high sample amount but not necessarily the functional starting group, were performed with these polymer batches (e.g., molecular doping).

The *in-situ* KCTP polymerization was previously studied concerning its monomer conversion versus MW, optimization of reaction conditions (time, temperature), MW evolution and end-group composition of non-functionalized P3(EO)3T),[213] and is not further discussed here.

4.1.4 Structural Characterization

In order to verify the successful introduction of the amine end-group and to confirm the expected structural definition, the structural features of different polymer batches were analyzed by NMR, GPC and dynamic light scattering (DLS) measurements. The polymer batches applied in further experiments are summarized in Table 4.1.

Table 4.1: Overview of all polymer batches used in further experiments.

Batch	M_n / $\mathrm{g\,mol^{-1}}$	dispersity	DP	end-group
JZ16	3 970	1.27	15	Ar-NH_2
JZ19	2 350	1.27	9	Ar-NH_2
JZ95	3 669	1.19	14	H/Br
JZ36	4 922	1.16	19	Ar-NH_2
JZ32	9 092	1.09	35	Ar-NH_2
JZ107	9 463	1.16	37	Ar-SH
JZ131	21 200	1.06	82	H/Br
JZ197	12 850	1.69	49	Ar-NH_2
JZ200	14 655	1.09	57	Ar-NH_2

^{1}H-NMR Spectroscopy

The DF for the amino-group was determined by ^1H-NMR spectroscopy. The proton signal **a** of the methyl-group at the ortho position of the aniline derivative was used to determine the DF. The proton-signals **a** were identified by 2D-NMR measurements on an oligomeric NH_2-P3(EO)3T batch (DP = 9), as shown in the Appendix in Figure A.2.1. The proton signal **b** of the CH2-group at the side-chain of a terminal thiophene unit was used as reference signal, as depicted in Figure 4.4. The DF was calculated from the ratio of the integral intensities I_A of these two signals ($I_A(a)/I_A(b)$) for selected polymer batches.

An averaged DF of 50% was obtained, which is rather moderate compared to literature, where values over 90% have been reported.[124,127] One reason of incomplete functionalization might be the electron-donating character of the tertiary amine-group -$N(TMS)_2$ and its *para*-position to the Ni-center. According to Doubina

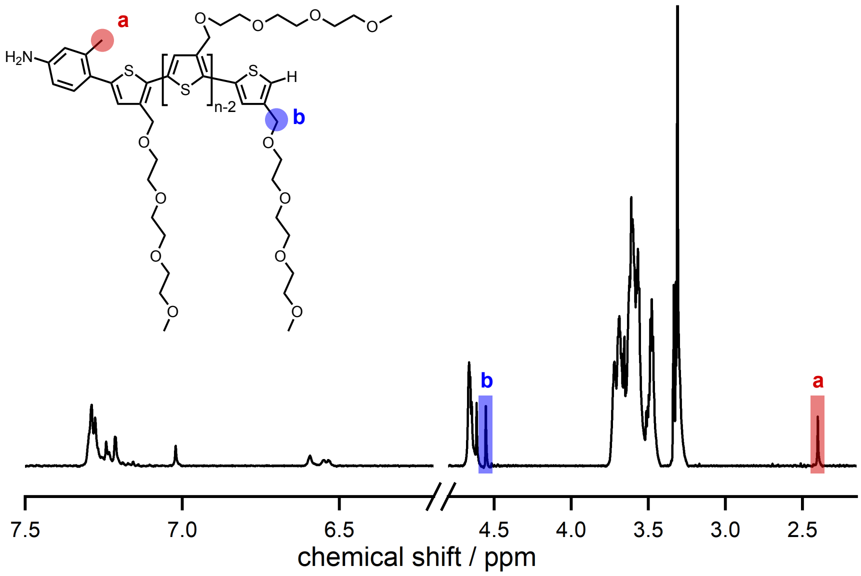

Figure 4.4: ^{1}H-NMR spectrum of NH_2-P3(EO)3T. The integral intensities of the protons **a** and **b** were used to calculate the DF.

et al., electron-donating or -withdrawing groups in *para*-position to the Ni-center lower the stabilizing effects of the aromatic ring. Consequently, such initiators are more susceptible to disproportionation reactions, which can decrease the DF to 20%.[220] However, Smeets *et al.* demonstrated in a later work that the introduction of a methyl group in the *ortho*-position to the Ni-center compensates such side-reactions, which increased the DF to 80%.[124] The best-obtained DF of this work is 71% (Table 4.2), which is close to 80% confirming the results of Smeets *et al.*[124] Moreover, the dispersity of all polymer batches was narrow, which further contradicts the occurrence of disproportionation reactions.

Therefore, it is more probable that the low DF is caused by another reason. The *ex-situ* initiator was used without any purification step. Ni(dppe)Cl_2 was added in a shortfall, which is why intermediate compounds, e.g., N$(TMS)_2$-Ph-ZnCl, are contained as impurities. These compounds lead to side-reactions, such as chain termination followed by reinitiation.[125] Furthermore, it might be possible that Ni(dppe)Cl_2 is not fully converted into N$(TMS)_2$-Ph-Ni(dppe)Cl due to its low solubility in THF. Non-functionalized Ni(dppe)Cl_2 would act as *in-situ* initiator leading to non-functionalized P3(EO)3T molecules. The observed variation of the DF from 71 to 38% in different polymer batches (Table 4.2) endorses that impurities are responsible for the modest DF of 50%. By adding a further purification step, it should be possible to increase the DF distinctly. However, the average DF was reasonable enough, and the dispersity narrow. Since non-functionalized polymers were easy to remove after conjugated to the ON, no purification step of the *ex-situ* initiator was developed in the scope of this thesis.

Table 4.2: DF for selected P3(EO)3T batches.

P3(EO)3T batch	**Integral intensity a**	**Integral intensity b**	**DF / %**
JZ16	0.213	0.455	47
JZ19	0.344	0.485	71
JZ36	0.18	0.47	38
JZ32	0.196	0.45	44

Gel Permeation Chromatography

The polymer batches were further investigated by GPC. The measurements were performed at 40 °C in chloroform. Figure 4.5a displays the GPC profiles of two polymer batches plotted, where the signal of the RI detector is plotted against the retention time. The GPC profiles for almost all polymer batches showed a unimodal peak at a retention time of 15 to 18 min, as the polymer batch with a DP of 19 (Figure 4.5a, black line). For some polymer batches (Figure 4.5a, blue line), peak satellites on the edge to lower retention times were observed.
From these plots, the MW and the dispersity (Table 4.1) were relatively determined against a polystyrene calibration curve. The M_n was further used to calculate the DP by the following equation with M_{MU} being the molecular weight of the MU ($258.14\,\mathrm{g\,mol^{-1}}$).

$$DP = \frac{M_n}{M_{MU}} \tag{4.1}$$

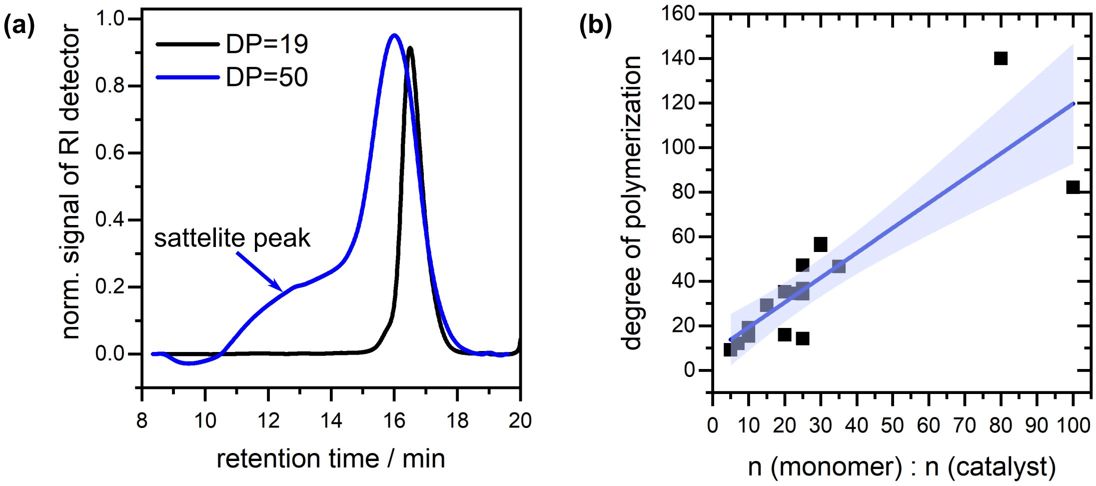

Figure 4.5: Degree of polymerization plotted as a function of the ratio of n(monomer) to n(catalyst). DP was calculated from the M_n obtained from GPC measurements. The blue line is the linear fit ($R^2 = 0.72$) with the 95% confidence interval.

Most polymer batches (10 out of 18) possessed a narrow dispersity below 1.2 which is sufficient for synthetic polymers following a chain-growth mechanism,[221] and excellent compared to polymers following a step-growth mechanism. Polymer batches with "satellite" peaks displayed, as would be expected, an increased dispersity (> 1.4). These satellite peaks occurred for polymer batches with higher MWs and are formed, presumably, due to disproportionation reactions.[222]

Each Ni-catalyst is expected to start one polymer chain, which grows linearly with proceeding monomer conversion. That is why the ratio of monomer to catalyst should define the DP. However, the MW evolution and, correspondingly the DP obtained by GPC, are only relative values. Hence, the catalyst feed ratio might be not directly related to the calculated DP. Nevertheless, the DP and the feed ratio should be linearly proportional. In Figure 4.5b, the ratio of monomer to catalyst is plotted versus the calculated DP. At lower DPs and medium catalyst feed ratios, almost all polymer batches are located in the 95% confidence interval, and only a few exceptions appear. At higher MWs, the values scatter distinctly around the 95% confidence interval. Such behavior is reasonable because with decreasing catalyst feed ratio, the error rate increases. Side reactions due to impurities in the monomer and the catalyst are gaining more influence. Especially, residual MgCl-3$(EO)_3$T-Br can have a pernicious impact on the catalyst and, thus, the chain-growth performance.[116,223] A linear M_n evolution up to a DP of 120 has been reported which could not be verified here.[33]

For the high DPs, the polymer batches were randomly distributed around the confidence interval. Consequently, a systematic error was excluded. More likely, this behavior is a result of the increasing influence of preparative inaccuracies at these extremely low catalyst feed ratios. One issue might be the addition of the Ni(dppe)Cl_2 as suspension leading to a deviations of the concentration. Second, as was evidenced by ^{13}C-NMR, the monomer is impured by its binary iodinated form of I-$(EO)_3$T-Br leading to uncontrolled side reactions. As already mentioned above, the *ex-situ* initiator was added without purification which further introduces impurities. For the future perspective, optimization of the monomer synthesis and the polymerization itself would be useful to obtain structurally well-defined polymers also for higher MWs. Nevertheless, despite the presence of few impurities, the KCTP proceeds reliably and the resulting polymers are well-defined. For higher catalyst feed-ratios, polymers with almost monomodal size-distributions were obtained.

Dynamic Light Scattering

Further experiments concerning the DNA assembly, require the solubility of P3(EO)3T in biocompatible solvents, at best water, down to the molecular level. To assemble structurally defined polymers, uncontrolled aggregation should be excluded. The occurrence of aggregation could affect the bio-conjugation to the ON as well as the attachment to the DNA origami structure. The size-distribution of two polymer batches with a DP of 14 and 35 was investigated in water and acetonitrile (ACN). The aqueous solution was buffered with a 1xTris buffer which is the most common buffer for DNA origami assembly.*11* The dissolved polymer solutions were filtrated by syringe filters (0.45 µm) to remove dispersed aggregates from the solution.

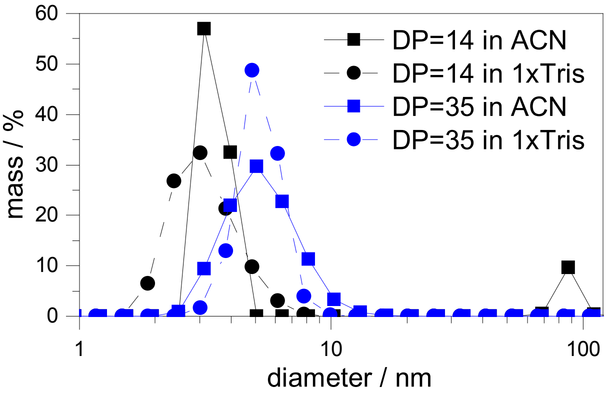

Figure 4.6: Size distribution of two polymer batches with DP = 14 (black lines) and DP = 35 (blue lines) in two different solvents (ACN, solid lines and buffered water, dashed lines).

The resulting size-distributions are displayed in Figure 4.6. In ACN (solid lines), both polymer batches show a monomodal and narrow size distribution with a hydrodynamic diameter of 3 nm (DP = 14) and 6 nm (DP = 35), respectively. For the aqueous solutions, similar hydrodynamic diameters were obtained. The aggregates in the ACN solution of the polymer with DP = 14, are likely a result of pollution, since in no other solution such aggregates were observed. The aqueous solution, possesses also a monomodal size-distribution but not as narrow as for ACN. Water is a strongly polar solvent and non-favorable for the hydrophobic polythiophene backbones. UV/VIS absorption showed that the P3(EO)3T formed collapsed coils in water (following Section 4.1.5, Figure 4.7a). This could explain the presence of smaller particles. Larger particles might be a result of slight aggregation. In combination, the size-distribution is broader, as it is observed (Figure 4.6, dashed lines). However, the formation of larger aggregates can be excluded.

In both solvents, the obtained hydrodynamic diameters correspond to the expected size of the molecularly dissolved polymer chains. For water, the presence of smaller aggregates cannot be ruled out from these measurements. Nevertheless for the following experiments, P3(EO)3T was used as aqueous solution because it provides the highest compatibility to DNA nanostructures.

4.1.5 Optical Characterization

The optical properties of P3RTs depend on their molecular structure and the conformation the polymer chain. Additionally, intermolecular interactions, mainly π-π-aggregation, strongly affect the optical properties of these polymers since they enable, e.g., excitation delocalization, and, thus, create additional, distinct electronic

states. The absorption and emission characteristics and the bandgap energy of P3(EO)3T (DP = 37) as a thin film and as a solution were analyzed by UV/VIS spectroscopy and steady-state fluorescence spectroscopy.
In the scope of this thesis, it was found that the P3(EO)3T is chromic to the following external stimuli. First, due to lower critical solution temperature of the (EO)3 sidechains the polymer's absorption is red-shifted with increasing temperature and precipitates in aqueous solutions above 50 °C. This effect was studied in detail by Ma *et al.* in previous studies on comparable polythiophene derivatives and is not further examined.[224] Second, the optical properties change upon the addition of surfactants, what is surveyed in Section 4.3.5. Third, the P3(EO)3T embedded in a poly(vinyl alcohol) matrix exhibited a red-shift and strong polarizing effects of its absorption when mechanical stress by means of tensile drawing was applied. This effect is assigned to a low conformational order of the polymer chains in the solid state. The mechanochromic behavior of P3(EO)3T was investigated in collaboration with Max Schnepf (Leibniz-Institut für Polymerforschung Dresden e.V.). The results of this work are currently in preparation for a publication: Zessin, Johanna*; Schnepf, Max*; Oertel, Ulrich; Mertig, Michael; König, Tobias; Fery, Andreas; Kiriy, Anton, "Conformational mechanochromic behavior of polythiophene-blended polyvinyl alcohol" *in preparation* **2019** (*shared co-authorship).

Figure 4.7a presents the normalized absorption spectra of P3(EO)3T as solution in solvents with different polarity (c(P3(EO)3T) = 0.1 mg/mL) and as a spin-casted thin film. The spectrum of P3(EO)3T in chloroform is characterized by a narrow absorption band with its maximum at λ_{Max} 436 nm and a λ_{onset} of 533 nm. This peak is attributed to the π-π* transition. With increasing polarity of the solvent (chloroform < THF < ACN < water), the absorption edge λ_{onset} of the π-π*-transition is red-shifted. As thin film, λ_{onset} is maximal red-shifted to 599 nm (Table 4.3a). The red-shift of λ_{onset} is accompanied by a red-shift of the λ_{Max} (Table 4.3) from 436 nm (chloroform) to 457 nm (thin film). Only the aqueous solution is blue-shifted to 406 nm. The absorption peaks of the thin film and the aqueous solution appear broader and possess a shoulder on the peak edge to higher wavelengths. The full width at half maximum (FWHM) is significantly increased for both peaks ($\mathrm{FWHM}_{water} = 194$ nm and $\mathrm{FWHM}_{thinfilm} = 169$ nm) in comparison to the chloroform solution (FWHM = 125 nm).
In chloroform, the P3(EO)3T molecules are supposed to be well-dissolved due to the narrow appearance of the absorption band and the absence of any other absorption feature, such as a shoulder. Thus, the polymer chains are considered as isolated random coils. The solvatochromic-induced red-shift with increasing solvent polarity indicates that the polymer chains turn more rigid and planar. This conformational transformation has been described for polythiophenes in poor solvents to reduce the interaction with the less favorable environment.[225] λ_{Max} in water deviates from this trend. The observed blue-shift might be caused by collapsed coils to minimize interaction with the highly polar solvent water, as it was also implied by the reduced

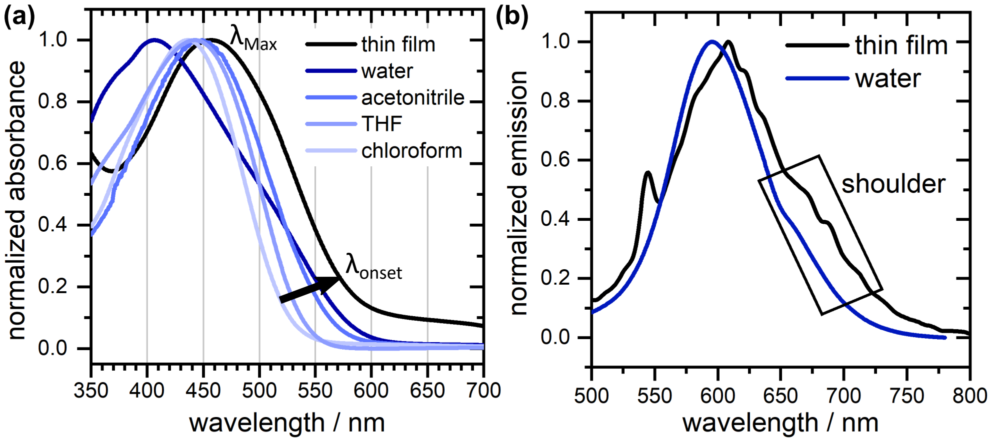

Figure 4.7: (a) Normalized absorption spectra of P3(EO)3T as thin film; and as a solution in different solvents (water, ACN, THF, chloroform). (b) Emission spectra of P3(EO)3T as thin film and as aqueous solution.

hydrodynamic diameter found in DLS measurements (Figure 4.6). In the thin film, the polymer chains are in their most planar form, as a result of their deposition by spin-casting.[226] Strikingly, for P3(EO)3T, the shift from solution to thin film is not as pronounced as for the standard polythiophene P3HT (Appendix, Figure A.3.1). The solution spectra appear almost alike for P3HT and P3(EO)3T indicating a similar electronic energy level distribution. However, the thin film spectra look differently. The bathochromic shift of the absorption maxima as a result of the planarization of the polymer backbones is smaller for P3(EO)3T ($\Delta\lambda = 62\,\text{nm}$) than for P3HT ($\Delta\lambda = 90\,\text{nm}$). Consequently, it is assumed that the P3(EO)3T chains are not fully planar in the thin film.

The shoulder at the lower energy edge (Figure 4.7a), which was observed for the thin film and the water solution, is a result of an additional intermolecular species. According to Spano *et al.* and Clark *et al.*, the absorption bands at 540 to 600 nm originate from vibronic transitions of π-π aggregates.[227,228] The shoulder is only weakly expressed for the aqueous solution of P3(EO)3T (dark blue line in Figure 4.7a). Therefore, it is assumed that the polymer chains are only slightly aggregated in aqueous solution. The P3(EO)3T film also possess only a weak π-π-aggregation band at 606 nm (2.03 eV). However, the presence of π-π-aggregated domains would be favorable in the solid state to promote intermolecular charge transport.

Figure 4.7b displays the normalized steady-state spectra of a P3(EO)3T thin film (black line) and a aqueous solution (blue line). The polymer in solution possess a broad emission band with $\lambda_{Max} = 595\,\text{nm}$ ($\lambda_{excitation} = 430\,\text{nm}$) which corresponds to neutral intrachain excitation of the π-electrons and weakly coupled H-aggregates.[228,229] The thin film spectrum is slightly red-shifted to 609 nm but the shift is not as strong as in the absorption spectra (Figure 4.7a). Both peaks have a shoulder on the edge to higher wavelength which is more expressed in the thin film spectrum. These species might emerge from weakly emissive aggregates.[229] The

Table 4.3: Optical properties of P3(EO)3T in different solvents and as thin film.

	$E_{g,opt}$* / eV	λ_{onset} / nm	λ_{Max} / nm
thin film	2.03	599.2	457
water	2.1	589.3	406.5
ACN	2.18	567.5	449
THF	2.28	542.8	442.5
chloroform	2.33	533.1	436

*calculated from the absorption band edge by the onset-method.

presence of slightly aggregated species in aqueous solution are in good agreement with the observations made in the UV/VIS spectroscopic measurements. The fluorescence properties are further surveyed in Section 4.3.5.

4.1.6 Summary

The polythiophene derivative NH_2-P3(EO)3T functionalized with an amine end-group was successfully synthesized by the *ex-situ* initiated KCTP. The chain-growth mechanism was proven by the correlation of the MW with the applied ratio of monomer to catalyst. This correlation was used to synthesize structurally well-defined polymers with a specific size. Almost all polymer batches were characterized by a narrow size distribution expressed by a dispersity below 1.1. A reasonable DF of the amine end-group up to 71% was found. However, for further experiments an additional purification step of the functionalized ex-situ initiator is desirable. The resulting polymer batches showed reasonable solubility in water down to the molecular level. Only a slight aggregation was observed. Consequentially, aqueous solutions are applicable for the following experiments with DNA. The UV/VIS absorption spectra revealed an optical bandgap 2.03 eV (thin film). The energy of the bandgap is in agreement with the bandgap of semiconductors.[230] In comparison to P3HT, a weaker planarization of the polymer chains upon spin-casting was found, which might suppress intermolecular charge transport. Nevertheless, the polythiophene is expected to be suitable for electronic applications.

Studies on P3(EO)3T revealed exciting optical functionality, such as chromic behavior to external stimuli and strong emission in the visible regime. Correspondingly, P3(EO)3T is an interesting material beyond its electronic functionality. It should be tested, as e.g., mechano-sensing device or optically active element in photonic devices. Akin fundamental optical devices were demonstrated in recent investigations for other DNA origami-templated CPs.[35,37–39]

4.2 Electronic Functionality of P3(EO)3T as 2D Bulk

4.2.1 Introduction

To obtain DNA origami-templated P3(EO)3T-based conductive pathways, it requires at some point the extrinsic incorporation of mobile charge carriers. Recent studies on thin films and 1D nanowires of P3RT-type polythiophenes have demonstrated that by so-called molecular doping stable mobile charge carriers can be introduced into the polymer matrix inducing a conductivity enhancement by several orders of magnitude.[67,69–73]

Nowadays, it is a state-of-the-art procedure to obtain stable and highly conducting materials for transport or injection layers.[41,231] The CT between dopant and CP and the corresponding formation of charge carriers in the polymer matrix is described by two fundamental mechanisms: the IPA or the CTX formation.[41] These two mechanisms differ in whether an integer or a partial number of charges are transferred from the CP's HOMO to the dopant's LUMO level and has to be evaluated for each dopant-CP-system.

One of the standard dopants for p-type organic semiconductors is F4TCNQ, whereas P3HT/F4TCNQ is undoubtedly the best-studied CP/dopant system. Due to the high structural kinship of P3(EO)3T to P3HT the dopant of choice is F4TCNQ, which enables the assessment of occurring processes. Doping of CPs suffers from very low doping efficiencies and requires high dopant feed ratios. The incorporation of high-amounts of hetero-molecules and charged species in the polymer matrix is expected to impact its microstructure and morphology. Disruption, phase separation or dopant aggregation are common effects caused by doping.[232,233] Such introduced disorder can potentially reduce the charge carrier mobility.

Establishing optimal doping conditions demands an evaluation of the structural and optical properties as a function of the dopant concentration. Additionally, understanding the impact of the doping process of P3(EO)3T at the microscale should be helpful for the later application of the polymer at the nanoscale. For this purpose, the chapter presents an in-depth investigation of the molecular p-type doping of P3(EO)3T thin films by the commercial dopant F4TCNQ. The influence on the optical, electronic and morphological properties is analyzed in a wide doping concentration range. The acquired findings were published in the journal *Physica Status Solidi A*: Zessin, Johanna; Bittrich, Eva; Zessin, Jakob, Malanin, Mikhail; Posseckardt, Juliane; Voit, Brigitte; Eichhorn, Klaus-Jochen; Kiriy, Anton; Mertig, Michael, "Molecular Doping of a Water-Soluble Polythiophene Derivative" *Pssa* **2019**, DOI: 10.1002/pssa.201800772.

4.2.2 Solution-Based Doping

There are different approaches on how to incorporate the dopant molecules into the polymer matrix, either by evaporation or from solution. Moreover, the thin film and doping procedure can be done by pre-mixing or by sequential deposition of the compounds. Sequential doping, either from solution or the gas phase, has been proven to be more efficient because it does not disrupt the CP's microstructure as much as by pre-mixed solutions.[234,235] However, concerning the future application in nanoscaled DNA-based devices, a pre-mixing solution-based process seems more appropriate here, particularly, with regard to the control of the dopant incorporation (amount, positioning). Typical p-type dopants, such as F4TCNQ, are soluble in polar solvents, e.g., ACN, or DMSO. Contrary to chlorinated or alcoholic solvents, which precipitate DNA, these solvents are compatible with DNA. Due to the broad solubility of P3(EO)3T, no orthogonal solvent system was found. Hence, it was not possible to establish a sequential-based doping procedure. Accordingly, a solution-based, pre-mixing doping procedure was applied here.

A P3(EO)3T batch with a DP of 82 and a dispersity of 1.05 was used. All polymer films were prepared by the following procedure. Fresh stock solutions of P3(EO)3T (in chloroform) and F4TCNQ (in ACN) were mixed into the desired ratio of dopant to MU. The final concentration of P3(EO)3T was constant at a concentration of $3\,\mathrm{mg\,mL^{-1}}$, which corresponds to $c_{MU} = 11.6\,\mathrm{mM}$ (despite solution-based UV/VIS investigations, which were diluted to $1.2\,\mathrm{mM}$). A wide range of the MDR could be studied because P3(EO)3T is also soluble in ACN. The following MDRs were investigated (concerning the MU): 0%, 5%, 10%, 13%, 20%, 33%, 50% and 100%. Thereby, 0% corresponds to the undoped polymer, and 100% to a doped polymer containing one dopant molecule per MU.

For the diluted, mixed solutions ($0.3\,\mathrm{mg\,mL^{-1}}$), no change in color was observed upon the addition of the dopant. For concentrated solutions ($3.0\,\mathrm{mg\,mL^{-1}}$), an immediately occurring color change of the original bright-orange polymer solution to orange-brownish (for slightly doped solutions) or to dark brown (for the fully doped polymer solution) occurred. For both concentrations, no precipitation was observed, as it has been reported for P3HT. Both solutions, diluted and concentrated, were filtrated by nano-porous syringe filters, without visible decoloring of the solution.

The blend solutions of P3(EO)3T and F4TCNQ were spin-casted on the respective substrate, either glass (optical and electronic studies) or silicon (dielectric function and morphology studies). For the conductivity measurements between interdigitated electrodes (electrode distance of $5\,\mu\mathrm{m}$), the polymer films were prepared by the drop-casting atop the gold electrode due to preparative issues. The thin films showed a clear color-change upon doping, ranging from deep-red for the undoped polymer to purple (5 to 20%), then to brownish (33 to 50%) and finally, to dark-yellow for the 100% doped sample (Appendix, Figure A.4.1).

4.2.3 Charge Transfer Reaction Upon Doping

Whether the CT reaction between P3(EO)3T and F4TCNQ follows an IPA or CTX mechanism, depends on the energy level alignment of the HOMO level of the polymer to the LUMO level of the dopant (Figure 2.5).[41,69]

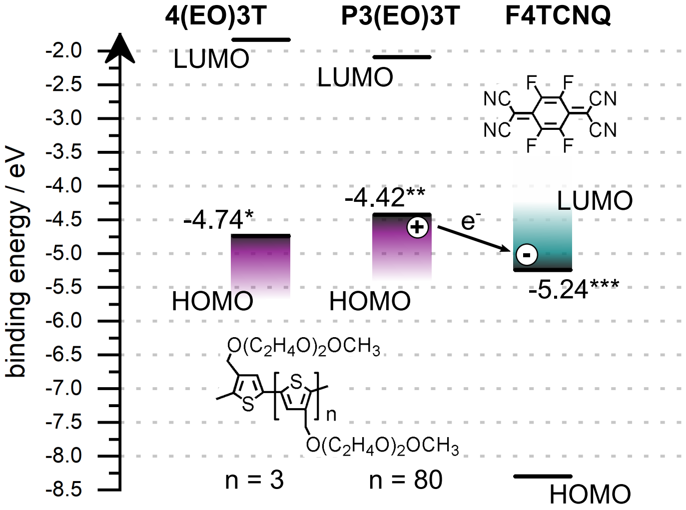

Figure 4.8: Molecular structure and energy level alignment of the investigated polymer P3(EO)3T, the polymer segment 4(EO)3T and F4TCNQ. The doping process is depicted by an integer electron transfer from highest occupied molecular orbital (HOMO) level of the polymer P3(EO)3T to the lowest unoccupied molecular orbital (LUMO) of F4TCNQ. Determined by *DFT, **CV (in solution) and by ***ultraviolet photo-electron spectroscopy (taken from (*63*)).

To this end, Figure 4.8 illustrates the energy level positions of the P3(EO)3T's HOMO to F4TCNQ's LUMO. The HOMO level of P3(EO)3T was -4.42 eV, and was computed from the data obtained by CV measurements. It has to be noted, that the CV measurements on P3(EO)3T were done in solution and not as thin film because P3(EO)3T films were dissolved by the electrolyte solution. The LUMO level of P3(EO)3T was approximated by the addition of the $E_{g,opt}$ to E_{HOMO} (Equation 3.3) giving a value of -2.09 eV. The obtained values agree with simulated values derived from DFT calculations (Appendix, A.5.1). There an E_{HOMO} of -4.89 eV and an E_{LUMO} -2.2 eV were simulated. The LUMO of F4TCNQ is -5.24 eV (taken from Gao *et al.*[63]), and thus, below the HOMO of P3(EO)3T. The corresponding energy difference is 0.82 eV.

According to Pingel *et al.*, not the bulk properties of the polymer are determinant for the CT reaction taking place but the local IE.[71] They found that one F4TCNQ interacts with a chain segment of around four thiophene units in P3HT. Figure 4.8 displays also the energy level alignment of 4(EO)3T, which was simulated by DFT calculations (Appendix, A.5.1). The HOMO level for 4(EO)3T is -4.74 eV, and thus, still 0.5 eV above F4TCNQ's LUMO. In both cases (P3(EO)3T and the 4(EO)3T), a favorable energy difference would be provided for an integer CT from P3(EO)3T to F4TCNQ *via* the IPA mechanism.

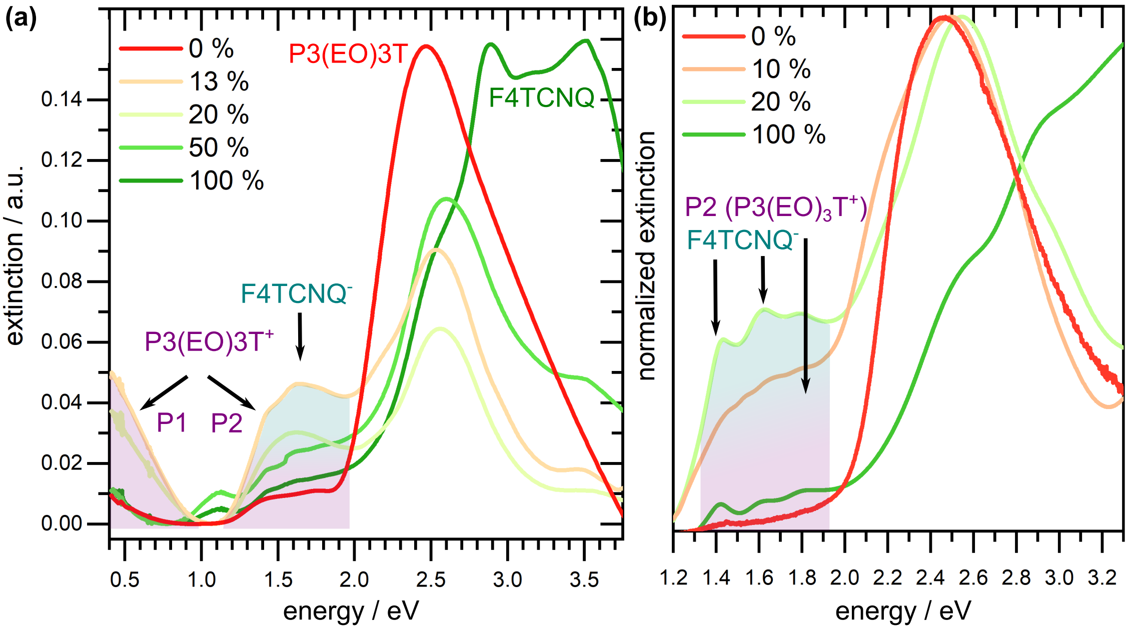

Figure 4.9: (a) UV/VIS-NIR and (b) normalized UV/VIS spectra of doped P3(EO)3T thin films at selected dopant concentrations.

4.2.4 Optical and Vibrational Spectroscopy

The CT reaction between P3(EO)3T and F4TCNQ is accompanied by the formation of newly formed sub-bandgap species, which can be detected by their absorption peaks (Figure 2.3 and 2.4). For the assumed IPA mechanism, this would be the ion pair composed of the cation P3(EO)3T$^+$ and the radical anion F4TCNQ$^-$.[68,71] Therefore, P3(EO)3T thin films (on glass) were spectroscopically investigated upon increasing doping level. The doped films were measured by UV/VIS, and UV/VIS-NIR spectroscopy in the transmission mode. A neat and a 20%-doped polymer film immobilized on silicon wafers were further analyzed by ATR-FTIR-spectroscopy. Finally, doped P3(EO)3T films at MDRs of 0%, 5%, 10% and 20% (on silicon, $t = 35\,\text{nm}$) were measured by Variable angle spectroscopic ellipsometry (VASE).

UV/VIS and UV/VIS-NIR Spectroscopy

The absorption properties of P3(EO)3T thin films upon an increasing F4TCNQ concentration were studied by a combination of UV/VIS and UV/VIS-NIR spectroscopy for the pre-mixed solutions and the corresponding thin films and compared to the system P3HT:F4TCNQ. First, the diluted solutions ($c_{MU} = 1.2\,\text{mM}$) were investigated by UV/VIS spectroscopy. The resulting spectra show only the absorption peaks of the neutral compounds P3(EO)3T and F4TCNQ, indicating that no CT reaction occurred under these conditions (Appendix, Figure A.6.1).

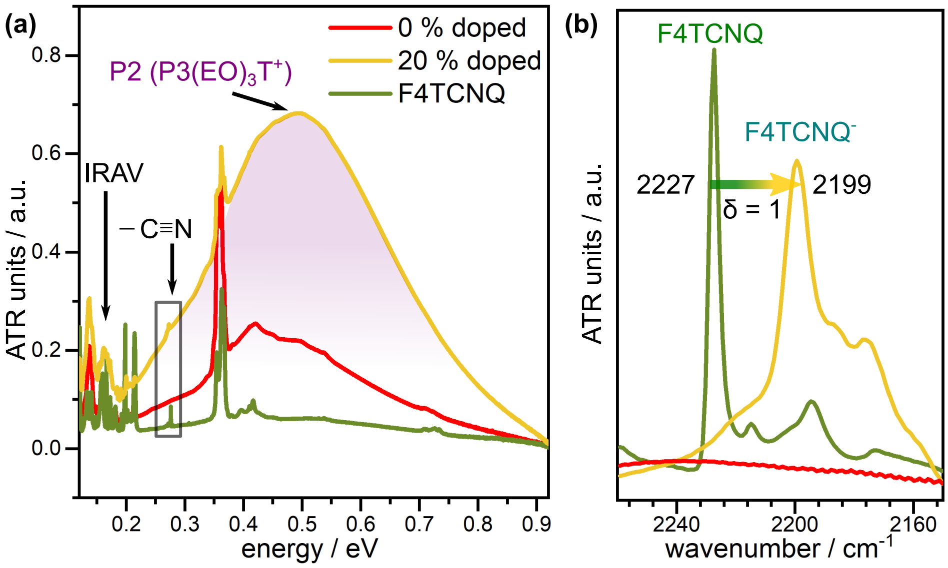

Figure 4.10: (a) ATR-FTIR spectra of F4TCNQ, 0%-doped P3(EO)3T and 20%-doped P3(EO)3T. (b) Section of CN-stretching modes.

Figure 4.9 displays a selection of the recorded spectra of the UV/VIS-NIR and UV/VIS spectra of the thin films. As apparent from the UV/VIS-NIR spectra (Figure 4.9a), with increasing F4TCNQ concentration the absorption changes significantly. The π-π^*-transition band of P3(EO)3T at 2.51 eV decreases. In addition, two new absorption bands evolve, at 1.65 eV and at 0.41 eV. The latter peak also appears weakly in the undoped polymer film. The corresponding high-resolution UV/VIS spectra resolves the band at 1.65 eV to three distinct peaks at 1.43 eV, 1.62 eV and 1.80 eV (Figure 4.9b). These peaks are observed at the lowest investigated doping level of 5%. They further increase upon a doping level of 13 to 20%, while parallely the peak at 2.51 eV decreases. The pure dopant possess two peaks at 2.89 and 3.51 eV.

The absorption peaks at 1.43 and 1.62 eV are assigned to the radical anion of F4TCNQ.[66,76] The broad absorption at 0.41 eV corresponds to the first optical transitions P1 ($\pi \rightarrow$ P*) of the polaron of P3(EO)3T (Figure 2.3b).[76] Even the undoped polymer is already slightly doped, which might be due to oxygen doping, as it has been described for polythiophenes.[236] The second optical transition P2 (P $\rightarrow$ P*), which was has been described as an undefined peak around 1.5 eV, most likely overlaps with the peaks of the radical anion F4TCNQ.[76] The absorption band between 2.5 to 3.5 eV is ascribed to the neutral F4TCNQ. The presence of neutral F4TCNQ implies that the polymer reaches is saturation level at around 20%.

To conclude, the expected ionic species P3(EO)3T$^+$ and F4TCNQ$^-$ were identified by their absorption peaks. Furthermore, it was found that the polymer has its saturation level for the incorporation of the dopant at around 20%. This saturation level corresponds well to the findings of Pingel *et al.* that one F4TCNQ molecule interacts with an 4(EO)3T chain segment.[71]

ATR-FTIR Spectroscopy

To gain more insights into the lower energy region, ATR-FTIR measurements were performed on the 20%-doped polymer film and compared to the neutral compounds F4TCNQ and P3(EO)3T. The measurements were conducted by Dr. Mikhail Malanin (Leibniz-Institut für Polymerforschung Dresden e.V.). Figure 4.10a shows the corresponding spectra. As it has been observed in the UV/VIS-NIR spectrum before, the pure polymer film is already slightly doped as indicated by the peak of the polaron transition P1. Upon incorporation of F4TCNQ this peak increases distinctly with its maximum at 0.49 eV. At lower energies (0.16 eV), additional bands appear. These modes have been explained by amplitude modes[237] and are ascribed as infrared active vibrational (IRAV) modes. In the neutral polymer chains, IRAV are Raman active (resonant Raman scattering modes) but through the charge-introduction by doping they are IR activated.

Intermolecular CT is complemented by a shift of the respective bands in the IR spectrum.[238,239] Thereby, the transition from neutral F4TCNQ to the radical anion F4TCNQ⁻ should be accompanied by a frequency shift. This can be used to assess whether the CT follows an IPA or the CTX mechanism. For F4TCNQ, the frequency shifts of the stretching modes of the nitrile-groups have been used to determine the character of the CT.[69,239] To analyze the shift of the nitrile stretching mode, the broad absorption of the polaron band was subtracted by a base-line correction in the region of interest. The corrected section of the spectra is displayed in Figure 4.10b. The CT δ was calculated from this shift of frequency $\Delta\nu$ by the following equation:

$$\delta = \frac{2\Delta\nu}{\nu_0}\left[1 - \frac{\nu_1^2}{\nu_0^2}\right]^{-1} \tag{4.2}$$

Where ν_0 and ν_1 correspond to the frequency positions of the neutral form or the radical anion, respectively. Investigations on the alkali salt of F4TCNQ revealed that an integer CT, as would be expected for the IPA mechanism, leads to a $\Delta\nu$ of 33 cm^{-1} and a $\delta = 1.0$.[240,241] Values of 7 to 12 cm^{-1} for $\Delta\nu$ and a corresponding $\delta = 0.25$[69] have been reported in the case of partially transferred charges, as it would be the case for the CTX mechanism. As shown in Figure 4.10b, the nitrile stretching band is here shifted from 2 227 (pure F4TCNQ) to 2 199 cm^{-1} in the doped P3(EO)3T matrix, giving a $\Delta\nu$ of 28 cm^{-1}. δ is correspondingly 1.0, which verifies an integer CT. Accordingly, the doping reaction between P3(EO)3T and F4TCNQ follows the IPA mechanism.

Variable Angle Spectroscopic Ellipsometry

The influence of the doping process on the optical properties of P3(EO)3T was further investigated by VASE. During ellipsometric measurements two independent parameters, the modulus Ψ and the phase Δ of the polarized beam, are recorded at

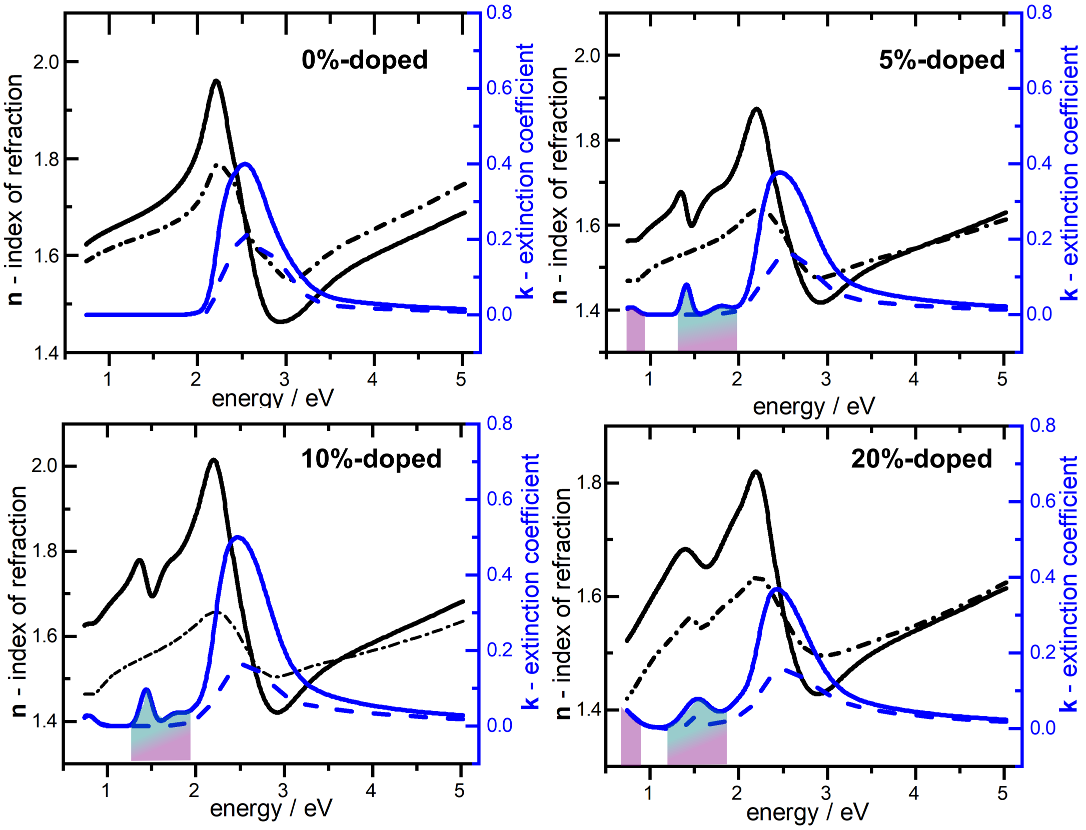

Figure 4.11: Refractive index n and extinction coefficient k of 0%- and 20%-doped P3(EO)3T plotted as function of photon energy. The signals were acquired in plane, which means parallel to the substrate (solid lines) and out-of-plane, which corresponds to the perpendicular to the substrate (dashed lines).

the same time supplying more information than conventional spectroscopic methods. The dielectric function $\epsilon = n^2 + k^2$, with n being the refractive index and k the extinction coefficient can be modeled from these two parameters. ϵ is the direct optical response of the material containing all optical properties of the material, and is not affected by the substrate.[242] Optical properties of the thin film are probed at a much smaller scale as with conventional reflection or transmission modes.[242] As a result, complementary information to the beforehand discussed optical measurements were expected from these investigations. Recording and data modeling were performed by Dr. Eva Bittrich (Leibniz-Institut für Polymerforschung Dresden e.V.). Figure 4.11 displays n and k, which are obtained through modeling of the ellipsometric parameters Ψ and Δ, plotted as function of the photon energy. The neat P3(EO)3T film ($t = 35\,\mathrm{nm}$) is characterized by the absorption of the $\pi-\pi^*$-transition with its maximum n at 2.20 eV and a slightly blue-shifted maximum for k at 2.52 eV. Both n and k exhibit a uniaxial optical anisotropic behavior, which is expressed in a stronger absorption of the in-plane compounds ($n_{in-plane}$, $k_{in-plane}$) than the out-of-plane ($n_{out-of-plane}$, $k_{out-of-plane}$) compounds. The ratio of $k_{in-plane}/k_{out-of-plane}$ at its maximum is 1.9 (Table 4.4). Such behavior is typical for CPs, which were spin-coated from solution.[243,244] A molecular ordering is obtained because the polymer chains arrange themselves with their axis parallel to the substrate plane causing a stronger in-plane absorption. In the plane of the substrate though, the backbones remain randomly distributed.

The birefringence Δn is calculated in the transparent region of P3(EO)3T at 1.03 eV from the difference of $n_{in-plane}$ and $n_{out-of-plane}$ (Figure 4.11, black lines).[245] A rather weak birefringence of 0.04 is obtained (Table 4.4) in comparison to common values for CP ranging from 0.1 to 0.4.[243] The birefringence correlates for polythiophenes with the amount of $\pi - \pi$-stacking and, thus, the crystalline regions in the film.[246] Consequentially, the birefringence of 0.04 indicates a rather low degree of crystallinity in the P3(EO)3T films. The mean orientation angle α was calculated from the order parameter S ($k_{in-plane}$, $k_{out-of-plane}$)[247] giving a value of 63±1°. α corresponds to the transition dipole moment concerning the surface normal. For planar organic molecules, where the transition dipole moment is nearly parallel to the axis of the molecule, the molecule's orientation to the substrate is extracted from this angle. For polymers though, the alignment of the dipole moment is not as clear. Hence, α allows only a rough prediction of the polymer chain alignment. Xiao *et al.* could show by sum frequency generation vibration spectroscopy that the side-chains tend to penetrate between thiophene and substrate. As a result, the polythiophene backbones are not parallelly aligned to the substrate.[248] Side-chains with polar groups interacted more strongly with the substrate leading to an increased α. For the long and polar (EO)3 side-chain, the large α of 63° is reasonable. Further insights into the microstructure of P3(EO)3T were obtained by X-ray scattering investigations (Section 4.2.5).

The introduction of F4TCNQ leads to the appearance of new peaks, located at 1.42 eV and 0.76 eV. For n, these signals are less defined why in the following only k is discussed. The position of these peaks is comparable to the peaks observed in the UV/VIS-NIR and ATR-FTIR spectra (Figures 4.9a and 4.10a), which were assigned to the radical F4TCNQ^{-}. These peaks are only visible for the in-plane compounds (Figure 4.11, solid lines). For F4TCNQ the transition dipole moment is parallel to the molecule's axis. Therefore, this might be an indication that the dopant molecules prefer to align themselves parallel to the substrate. However, the intensity of the out-of-plane compounds is distinctly lower and the signals of F4TCNQ might be not visible due to the noise level. At higher doping levels (MDR = 20%), the two peaks concur and appear as one broad peak (1.6 eV) in the in-plane and out-of-plane compounds. The transition P2 of P3(EO)3T^{+} (expected at 1.4 eV), overlaps with the dopant features and might be the reason that at higher MDRs the peaks also emerges for the out-of-plane compounds. For the doped polymer films, the values of $k_{in-plane}$ and $k_{out-of-plane}$ of the π-π^{*} transition band (2.64 eV) are slightly decreased but not as strong as in the UV/VIS-NIR spectra. Almost no change was observed for α (66° at MDR = 20%) indicating that the microstructure of P3(EO)3T does not dramatically change upon a doping level of 20% and the F4TCNQ molecules are well-distributed in the polymer matrix.

Table 4.4: Results of VASE measurements at different MDRs.

MDR	t / nm	r / nm	Δn	$k_{in-plane}$/ $k_{out-of-plane}$	α
0	33	3.1	0.04	1.90	63.1±1°
5	35.6	1.6	0.1	2.34	66.0±1°
10	27.2	7.8	0.18	3.12	68.0±1°
20	39.5	2.6	0.11	2.40	66.0±1°

4.2.5 Microstructure and Morphology

The molecular packing order and microstructure of solidified CPs plays an important role for their charge carrier transport properties. The incorporation of charges and hetero molecules is known to compromise the structural order of organic semiconductors.[78,249] To that end, the neat and 20%-doped P3(EO)3T were analyzed as thin films ($t = 30$ to 35 nm) on silicon substrates by 1D and 2D-grazing-incident wide-angle X-ray scattering (GIWAXS). The bulk material was additionally investigated by wide-angle X-ray scattering (WAXS). Dr. Dieter Jehnichen conducted the measurements and processed the data. The polymer matrix has a certain level of saturation upon the dopant molecules can be incorporated. Beyond this saturation level, the F4TCNQ molecules form clusters, which are not available as electron acceptors.[232] The change of the surface morphology and the formation of clusters dependening on the doping level was studied by AFM.

Study of the Thin Film Microstructure by X-ray Diffraction

A schematic model of the semicrystalline organization of the P3(EO)3T molecules is illustrated in Figure 4.12a. High charge-transport can be expected along the direction of conjugation, which is the intermolecular charge-transport, and along the π-π-stacking direction, corresponding to the fast intermolecular charge transport. Unfavorable transport occurs along the lamellar stacking direction.[250] It should be considered that x-rays mainly display the structure of the crystalline regions but CPs are semicrystalline. The amorphous fraction in the thin P3(EO)3T films is expected to be higher than in P3HT and most likely affects the charge transport.

First, the bulk samples of P3(EO)3T were analyzed by WAXS in its bulk state (Figure 4.12b, black line). The neat polymer shows peaks at q (hkl): 0.26 Å^{-1} (*100*), 0.52 Å^{-1} (*200*) and 0.79 Å^{-1} (*300*) corresponding to the layer formation of the (EO)3 side-chains through interlamellar-stacking. The (*100*) orientation corresponds to an interlayer spacing d_{100} of 2.32 nm. This value is larger than the interlayer spacing reported for P3HT, which is 1.6 nm.[69,251] It was found that the interlayer spacing depends on the length of the side-chain.[252,253] Therefore, the large spacing distance is reasonable, since the (EO)3 side-chain is around twice as long as the hexyl-side-chain of P3HT. The diffraction signal allocated to π-π-aggregates appears at a 1.67 Å^{-1} (*010*) giving a spacing distance of 0.39 nm, which is close to the value of

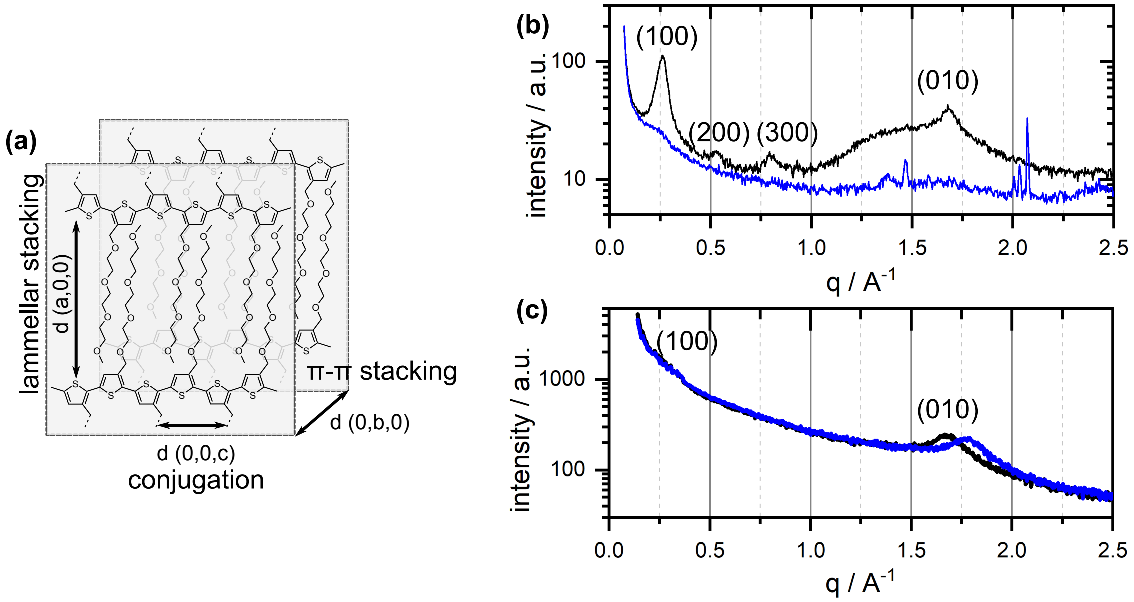

Figure 4.12: (a) Scheme of the crystalline structure of P3(EO)3T. (b) WAXS pattern of bulk material and (c) 1D-GIWAXS pattern of thin films measurements for 0% (black line) and 20% (blue line) doped P3(EO)3T.

P3HT (0.38 nm).[250] The broad underground below this reflection is associated to amorphous domains in P3(EO)3T. For the 20%-doped P3(EO)3T, significantly less sample mass was measured resulting in a low resolution, as can be seen in Figure 4.12b, blue line. Hence, only the main reflection (*100*) is visible as a slight shoulder at $0.22\,\text{Å}^{-1}$ corresponding to an increasing interlayer distance of 2.62 nm. The small increase of the side-chain stacking distance is a result of incorporated F4TCNQ molecules into the interlamellar-stacked region.[68,254] The diffraction signal of the π-π-aggregates was not resolvable anymore from the background due to the low sample amount.

Next, thin films of neat and 20%-doped P3(EO)3T were investigated by 1D-GIWAXS. The diffraction patterns are displayed in Figure 4.12c. The lamellar stacking peaks were not visible, but the π-π-crystallites gave a diffraction peak at $1.67\,\text{Å}^{-1}$ corresponding to a stacking distance of 0.38 nm. This value is in agreement with the WAXS investigations. Upon doping a new peak emerge at higher q values ($1.78\,\text{Å}^{-1}$) corresponding to a d_{010} of 0.35 nm (Figure 4.12c, blue line). Such a decrease of the π-π-stacking distance was also observed for F4TCNQ-doped P3HT.[68–70] In early studies, it was assumed that the F4TCNQ stack to the polymer backbone forming F4TCNQ:P3HT co-crystallites.[68,69] However, in recent studies, it was verified that F4TCNQ does not intercalate into the π-π-stacked crystallites.[70,234] Moreover, the shift to higher q values was ascribed to the compression of the polymer backbones due to the delocalization of the polarons over adjoining chains.

The thin films of the neat and 20%-doped P3(EO)3T were further investigated by 2D-GIWAXS (Figure 4.13). For the undoped sample, the interlayer ($d_{100} = 2.13\,\text{nm}$)

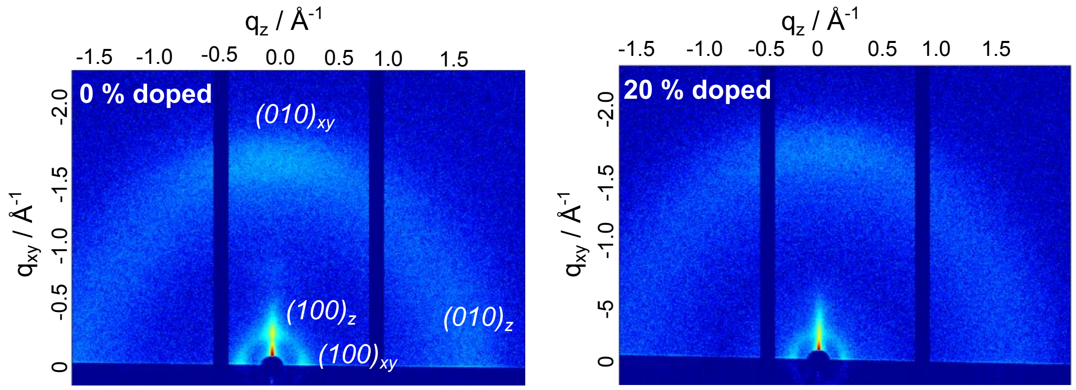

Figure 4.13: 2D GIWAXS measurements of 0% and 20% doped P3(EO)3T thin films with xy being parallel and z being perpendicular to the surface.

and π-π-stacking ($d_{010} = 0.39\,\text{nm}$) distance were in agreement with the previous measurements. The doped sample showed similarly shifted peaks for the interlayer distance to lower q values and for the π-π-stacking to higher q values (Appendix, Figure A.7.1). In both thin films, the signals are weakly pronounced indicating a low degree of ordered regions, as was already assumed from the UV/VIS measurements (Section 2.3.2).

Additionally, the predominant orientation of the polythiophene backbones to the surface was derived from the 2D-GIWAXS measurements. As can be seen from the 2D-GIWAXS pattern, the signals of the π-π-stacked crystallites (*010*) are more pronounced in the xy-plane (in-plane) and the signals of the interlamellar stacking (*100*) are more pronounced in the z-plane (out-of-plane) (Figure 4.13). This corresponds to face-on orientation where the π-π-stacked crystallites are parallel and the interlamellar stacking perpendicular to the surface. The same orientation was observed for spin-casted P3HT processed from low-boiling point solvents, such as chloroform.[255] However, weak signals are also found for the edge-on orientation indicating that the polythiophenes are not uniformly face-on oriented. These results correspond to the α of 63° found by VASE measurements (Table, 4.4) based on the supposition that the transition dipole moment is most likely aligned within the plane of the polymer chain. For the 20%-doped film, a clear assertion is hardly possible due to the overall lower intensity. Further in-depth studies are desirable to gain more insights into the microstructure of doped P3(EO)3T.

Study of the Thin Film Morphology by AFM

Figure 4.14 presents AFM images of the thin films at selected dopant concentrations. An overview of all AFM images can be found in the Appendix, Figure A.8.1.

The film morphology of P3(EO)3T in its undoped state is uniform and smooth with an average roughness of 1.88 nm. Perceptible is the presence of nanosized pinholes in the polymer thin film. Such pinholes are an indicator of dewetting processes during the film-wetting. For polymer thin films, two film rupture processes have

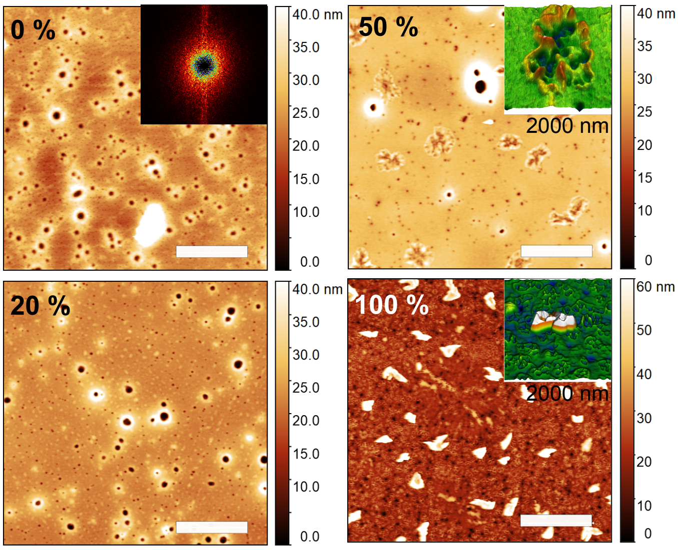

Figure 4.14: (a) AFM an MDR of 0%, 20%, 50% and 100% dopant content. Inset at 0% displays the 2D FFT of the image, scale bars: 4 µm. Inset in 50%-doped and 100%-doped samples are 3D AFM images of an island and a crystals.

been described in the literature, which is nucleation-based or spinodal dewetting.[256] The latter is accompanied by a correlating hole formation pattern, which can be detected from a specific wavelength λ_s in the fast Fourier transform (FFT).[256] The inset in Figure 4.14 shows the respective 2D-FFT of the 0%-doped P3(EO)3T film where no specific λ_s is observed. Hence, the occurrence of spinodal dewetting is excluded. No hetero particles, such as dust, are recognized in the holes. Therefore, it is assumed that thermal nucleation-based dewetting takes place. Such type of dewetting is reasonable because the glass transition temperature T_g of P3(EO)3T is with -9.7 °C below room temperature (estimated by differential scanning calorimetry, Appendix, Section A.1).

The thin films were further analyzed regarding their roughness, given as root mean square (rms), and the density of pinholes by the semi-automatic particle analyzer of ImageJ.[215] Figure 4.15 presents these results as function of the MDR. Further results of the semi-automatic particle analysis are summarized in the Appendix, Table A.8.1.

Depending on the MDR, three states of the P3(EO)3T film morphology was found. First, up to a dopant content of 33% the surface morphology is smooth and regular, as it is confirmed by a stable roughness of rms 1.2±0.3 nm. This is in agreement with the VASE measurements, where α was also relatively constant up to an MDR of 20% (Figure 4.11). Only the number of pinholes reduced from 1.2 holes (0%) to 0.09 holes per µm^2 (33%). This effect is attributed to the increasing amount of ACN in the precursor solution and an improved film-making process. Solutions with the same ACN amount but without dopant lead to films with reduced pinholes as well. At an MDR of 50%, the appearance of the thin film changes. Micro-sized islands are observed in the polymer film, as can be seen in the AFM image at an MDR of

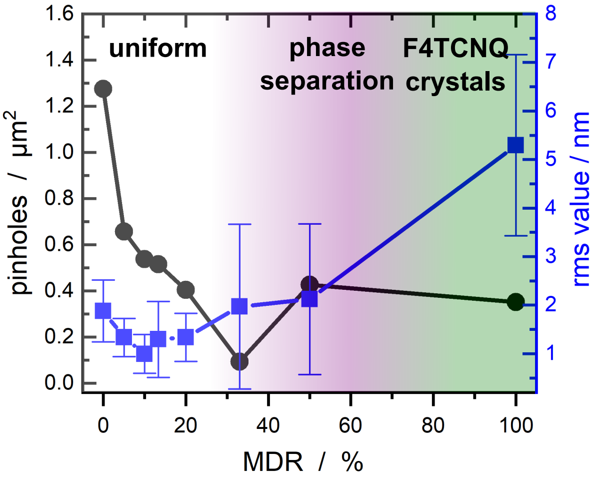

Figure 4.15: Semi-automatic particle analysis of AFM images (black line with dots) on the pinholes and the roughness (given as rms, blue line with squares) plotted against the MDR. The lines are just for guidance of the eyes.

50% in Figure 4.14 and also the slightly increased surface roughness up to 2.1 nm. The formation of such islands (inset in Figure 4.14, 50%-doped film) is a product of phase separation of the neutral dopant from the fully doped polymer phase. Phase separation at high dopant concentrations has been described for other CPs as an indication point that the doped polymer matrix reached its saturation level.[68,73,232] The saturation level of P3(EO)3T is between 33 to 50%. As mentioned above, one F4TCNQ molecule interacts with a chain polymer segment of roughly four thiophene units, which would point to a saturation level at around 25%.[71] For P3HT, the formation of neutral F4TCNQ in the doped polymer matrix has been observed even at dopant concentrations below 20%.[68,232] The polar side-chains (EO)3 most likely support the formation of stable complexes between P3(EO)3T and F4TCNQ in solution and the film, increasing thus, the saturation level.[72] The last state, at an MDR of 100%, the phase segregation is further progressed. More but smaller clusters are embedded in the doped polymer film (inset in Figure 4.14, 100%-doped film). Additionally, neutral F4TCNQ crystals (inset in Figure 4.14) are observed on the film surface leading to a rise of the surface roughness (rms 5.3 nm). The appearance of phase separation of the neutral F4TCNQ from the doped polymer and the occurrence of F4TCNQ crystals on the polymer films is in good agreement with the UV/VIS-NIR results where the neutral F4TCNQ is the dominant compound at higher MDRs (Figure 4.9a).

4.2.6 Electrical Characterization

The conductivity was investigated as a function of the MDR. $I-V$ curves of the P3(EO)3T films at different MDRs were recorded by a two-point set-up within two different electrode designs. The electrodes were provided by Dr. Juliane Posseckardt

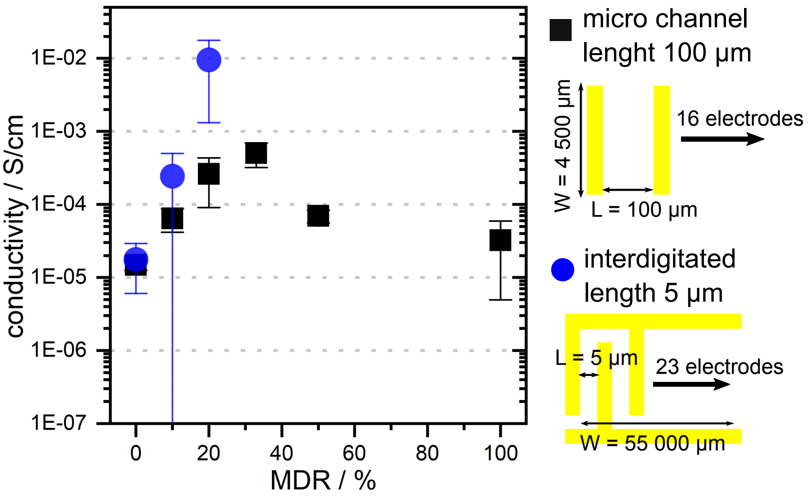

Figure 4.16: Conductivity of P3(EO)3T plotted as a function of the MDR. Black squares refer to results obtained for micro-channel electrodes (L = 100 µm), and the blue dots refer to results obtained for interdigitated electrodes (L = 5 µm).

(Kurt-Schwabe Institut für Mess- und Sensortechnik Meinsberg e.V.) and Jakob Zessin (Technische Universität Dresden). In the first set-up, so-called micro channel gold electrodes with an inter-electrode distance of ca. 100 µm were evaporated on the respective polymer film ($t = 35$ to $50\,\mathrm{nm}$), which was deposited on a glass substrate. In the second set-up, photolithographically fabricated, interdigitated gold electrodes (on glass) were used. The doped P3(EO)3T films were deposited atop the electrodes by drop-casting.

The respective volume resistance R of the polymer films was calculated by fitting the $I-V$ curves in the Ohmic regime between -0.1 to 0.1 V. L and t were determined for each sample by light microscopy and AFM, respectively. The cross-section area A ($t \cdot W$) was then calculated for each channel. Per sample, the volume resistance was measured between at least four different electrode pairs. The conductivity σ was calculated by the Equation 2.2 as inverse of the resistivity ρ. The averaged values of σ are displayed in Figure 4.16 as function of the MDR.

Micro Channel Gold Electrodes (L = 100 µm)

σ of the undoped P3(EO)3T is, as expected, low with a value of $1.5{\cdot}10^{-5}\,\mathrm{S\,cm^{-1}}$. With increasing F4TCNQ concentration in the polymer matrix, σ firstly increases by one order of magnitude reaching its highest value of $5{\cdot}10^{-4}\,\mathrm{S\,cm^{-1}}$ (MDR = 33%). With further increasing dopant concentration, σ drops again to $6.9{\cdot}10^{-5}\,\mathrm{S\,cm^{-1}}$ for the 100%-doped polymer film. The drop of σ at higher MDRs originates most likely from the phase separation of the neutral dopant and the doped polymer film, as was observed in the UV/VIS-NIR (Figure 4.9) and morphology studies (Figure 4.14). The higher degree of disorder in the polymer matrix leads to an increased number

of scattering centers for the free charge carriers. Consequentially, their mobility is reduced and, thus, σ.
It should be annotated that the increase of σ up to $5{\cdot}10^{-4}\,\mathrm{S\,cm^{-1}}$ is rather low compared to results obtained for F4TCNQ-doped P3HT. An enhancement of σ up to 5 orders of magnitude was reported for comparable doping procedures for P3HT resulting in maximum values of 0.1 to $8.0\,\mathrm{S\,cm^{-1}}$.[67,249,257] Absorption spectroscopy confirmed that a significant CT occurred between P3(EO)3T and F4TCNQ (Figure 4.10), similarly to the P3HT:F4TCNQ system. Therefore, it is assumed that the charge carrier concentration is alike. However, for organic semiconductors, the charge carrier concentration is not only determining σ. The mobility of these charge carriers is equally important.[34] Due to high binding energies, the polarons are not necessarily available for charge carrier transport. They may stay coulombically bound to the counterions, and thus, immobile.[73,233] Another possible reason of the low charge carrier mobility and conductivity is an absence of efficient conductive pathways caused by a morphological disorder.

The observed low conductivity is not necessarily caused by a disorder at all scales. Moreover, it might be a result of the absence of sufficiently long conductive pathways spanning over the whole channel. As it was revealed by AFM imaging, the thin films contained pinholes (Figure 4.14). Even though, the pinhole area is relatively small (<1% compared to the total area), they might prevent the long-range alignment of the polymer chains to connect micro-structured crystalline domains. Additionally, the interfaces at the pinholes introduce regions with a high density of traps into the polymer film that can act as scattering centers for the charge carriers.

Interdigitated Gold Electrodes (L = 5 µm)

To minimize the influence of the long-range order and simultaneously increase the probability of contacting crystalline domains, another electrode design was developed. The inter-electrode distance L was decreased from 100 to 5 µm and the channel width was increased from 4 500 µm to 55 000 µm. As can be seen in Figure 4.16 (blue dots), σ measured on such devices at the MDR of 20% is equal to $1{\cdot}10^{-2}\,\mathrm{S\,cm^{-1}}$, which is two order of magnitude higher than the value of the device with an interelectrode distance of 100 µm. These results emphasize the assumption that defects and a low order in the P3(EO)3T thin films is the main limiting factor of efficient charge carrier transport over a long range. Within such ordered regions, the charge carrier transport is much higher. Nevertheless, compared to P3HT, the conductivity is lower by two to three orders of magnitude. This difference might be a result of the less-ordered short-range structure. A lower degree of crystalline domains than e.g., in P3HT, was found by absorption spectroscopy (Section 4.2.4) and WAXS/GIWAXS (Section 4.2.5). The comparison of the thin film absorption spectra of P3(EO)3T and P3HT further confirmed the less pronounced planarized state of the solidified P3(EO)3T's backbones (Appendix, Figure A.3.1).

4.2.7 Summary

In the scope of this chapter, it was found that neat P3(EO)3T films possess a low σ of $1.5 \cdot 10^{-5}\,\mathrm{S\,cm^{-1}}$ at the micrometer scale. An enhanced conductivity up to $5 \cdot 10^{-4}\,\mathrm{S\,cm^{-1}}$ was obtained when doped with the strong electron acceptor F4TCNQ. The observed increase was modest compared to similar polythiophene derivatives.[67,69,233] A sufficient charge-transfer from P3(EO)3T's HOMO to F4TCNQ's LUMO was verified. The charge species F4TCNQ^{-} and P3(EO)3T^{+} were identified by their optical and vibrational features. Hence, a low charge-carrier concentration was ruled out as a possible origin of the less pronounced conductivity enhancement upon the doping.

Studies on the microstructure of the P3(EO)3T films revealed, that the polymer chains self-assemble into crystalline domains upon solidification. However, the order of these crystalline domains was less pronounced than in other polythiophene derivatives. Upon the spin-casting processing, the chains were planarized but weaker than in P3HT. The higher degree of amorphous domains was supposed as a result of mobile polymer chains in the thin films. It was further hypothesized that the higher intra- and intermolecular disorder is the origin of the less efficient charge-transport. This hypothesis was verified by an enhanced σ up to two orders of magnitude to a maximum value of $1 \cdot 10^{-2}\,\mathrm{S\,cm^{-1}}$ through the reduction of the influence of long-range disorder. These results are promising concerning the planned implementation of P3(EO)3T at the nanoscale. Consequentially, P3(EO)3T might be not the optimal material for large-scale circuits but is expected to be functional at small scales.

4.3 DNA Origami-Templated Formation of Polythiophene Filaments

4.3.1 Introduction

DNA-based nanostructures have been discussed as molecular breadboards for sophisticated optical or electronic circuits. Their advantage is first, the parallel assembly of many structures within one batch and second, the precise arrangement of hetero-objects. In this work, the DNA origami technique was applied to construct a supramolecular polythiophene filament, which are potentially applicable as nanowires in electronic devices. In contrast to previous works, this polymer wire is composed of a defined number of polythiophene molecules. As already mentioned in Section 4.2, charge-transport between adjacent chains requires π-π-stacking and must be considered by arranging the polymer molecules on the DNA origami template.

The integration of hetero-objects into DNA origami nanostructures is mostly executed by short ONs. The staple strands of the DNA origami template are extended by approximately 8 to 30 nucleotides, which protrude from the template. The parallel attachment of different objects is realized by the deployment of differing, non-complementary sequences of these staple extensions. The most natural sequence would be a mononucleotide sequence, e.g., poly-A. The most variety is provided by an entirely specific sequence poly-(random nucleotide (N)). A compromise would be a repetitive sequence, e.g., poly-(AAT). Here, each P3(EO)3T molecule is equipped with exactly one ON block which then site-specifically binds to one extended staple strand on the DNA template - and is termed as one-to-one attachment in the following. Since only one ON per functional object is available, the attachment of P3(EO)3T to the DNA template is expected to be more sensitive. Therefore, it is crucial to rule out any side reactions, such as agglomeration. Furthermore, it is also required to provide a reliable and specific hybridization ability of the ON conjugated to P3(EO)3T.

This chapter reports, firstly, about the diblock copolymer composed of the functional block P3(EO)3T and a modified ON with a specially designed sequence. Unless not otherwise noted, a polymer batch with an $DP = 19$ (JZ36) was used for all experiments. The composure and the MW evolution of the diblock copolymer in aqueous solution about agglomeration were analyzed by AF4. Furthermore, the hybridization kinetics of different ON sequences in the diblock copolymer on surface-immobilized ON probes were investigated by SPR.

Secondly, this chapter presents the DNA-templated formation of confined P3(EO)3T filaments. Furthermore, the characterization of these supra-polymer structures as entities and as a bulk, is reported concerning structural, optical and electronic properties. Parts of this chapter can be found in the publication in the journal *Nano Letters*: Zessin, Johanna; Fischer, Franziska; Heerwig, Andreas; Kick, Alfred; Boye, Susanne; Stamm, Manfred; Kiriy, Anton; Mertig, Michael, "Tunable fluorescence of a semiconducting polythiophene positioned on DNA Origami" *Nano Letters* **2017**, 17, 5163-5170.

4.3.2 Block Copolymer Formation

The amine-group of NH_2-P3(EO)3T was converted into an azide group to make the polymer accessible to click chemistry. The NHS-activated linker molecule azidoacetic acid was added to NH_2-P3(EO)3T yielding the azide hetero-object-functionalized polymer N_3-P3(EO)3T (Figure 4.17).

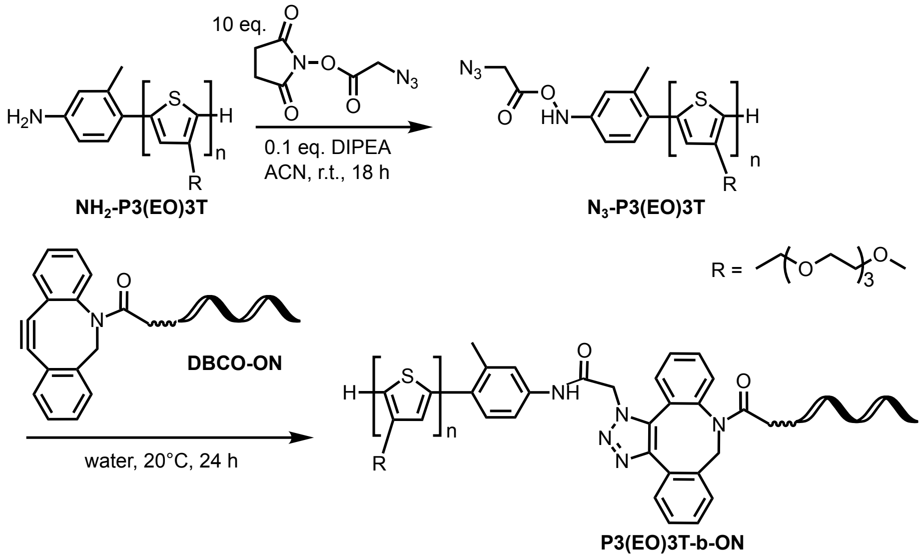

Figure 4.17: Reaction scheme of P3(EO)3T-b-ON formation starting from NH_2-P3(EO)3T, followed by the conversion to N_3-P3(EO)3T and conjugation to DBCO-ON.

N_3-P3(EO)3T was added in a minimum tenfold excess to the dibenzoyl-octine (DBCO)-functionalized, synthetic ON (the precise chemical structure can be found in Figure 3.1). As depicted in Figure 4.17, the diblock copolymer P3(EO)3T-b-ON formed *via* the strain-promoted alkyne-azide cycloaddition. The block copolymer formation, its reaction kinetics and yield were examined in detail beforehand[258] and are not further discussed.

Depending on the MW of the diblock copolymer either agarose or PAGE gel electrophoresis was applied to confirm the successful diblock copolymer formation (Figure 3.2). The diblock copolymer band was then cut-off the gel and re-extracted by electro elution or Freeze'N'Scqueeze.

Size-Distribution of P3(EO)3T-b-ON by AF4 Measurements

The size distribution of an untreated P3(EO)3T-b-ON solution (in buffered water) was analyzed by AF4. For a similar diblock copolymer composed of a polythiophene and ON block, Kamps *et al.* reported the assembly into micro-sized vesicles.[259] For P3(EO)3T-b-ON, a similar formation of such vesicles appears probable due to the

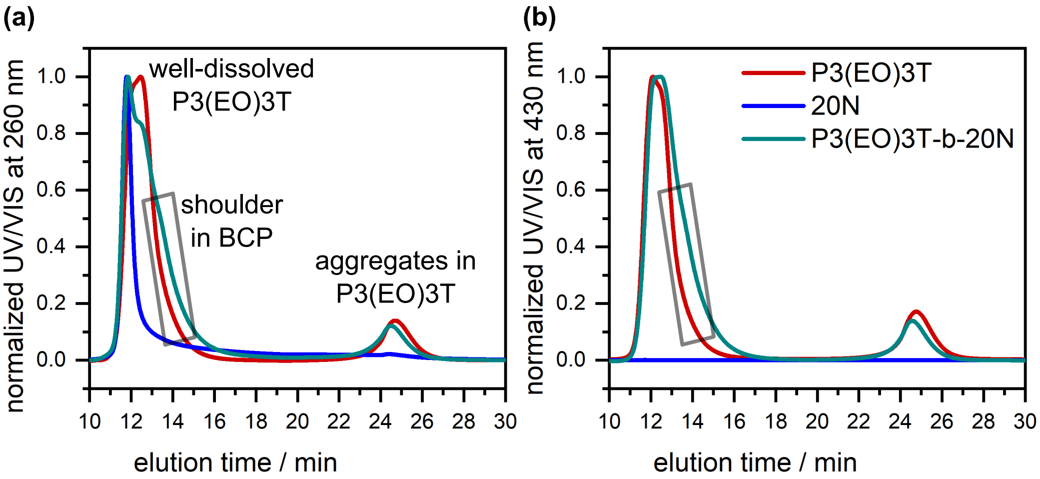

Figure 4.18: Fractogram from UV/VIS detector of the bare P3(EO)3T (red line), bare 20N ON (blue line) and the P3(EO)3T-b-20N (cyan line) at (a) 260 nm and (b) 430 nm (wavelength UV/VIS detector).

amphiphilic character of the diblock copolymer but would tremendously change the following DNA origami assembly procedure. First, the effective diblock copolymer concentration would be distinctly lower and, thus, changing the hybridization kinetics. Second, the large size of the DNA (around 100 nm) templates and the even larger size of the vesicles (0.4 to 1 µm), might turn the direct hybridization too slow due to high diffusion barriers. Therefore, the presence of such vesicles during the assembly process was undesired for this work.

To analyze whether the diblock copolymer P3(EO)3T-b-ON also tends to a vesicle assembly, the aqueous solution of P3(EO)3T-b-20N (1xPBS buffer) was separated by AF4 and analyzed by its size. The eluent was detected by a multi-angle light scattering (MALS) detector and a UV/VIS detector. The diblock copolymer was compared to its bare compounds P3(EO)3T (DP = 35) and ON 20N. All samples were analyzed without further treatment, such as filtration. The UV/VIS detector was operated at the maximum absorption of the bare compounds, which was 260 nm for DNA and 430 nm for P3(EO)3T. The obtained data from both detectors was further used to extract the MW evolution of the individual fractions. Measurements and MW calculations were conducted by Dr. Susanne Boye (Leibniz-Institut für Polymerforschung Dresden e.V.).

Figure 4.18 presents the fractograms from the UV/VIS detector at 260 nm (Figure 4.18a) and 430 nm (Figure 4.18b). The solution of the bare P3(EO)3T (red line) contains two fractions, which are visible at both wavelengths. The main fraction elutes at 12.1 min ($I_A = 1.8$) and the second, minor one, at 24.6 min ($I_A = 0.4$). The first fraction of the bare polymer sample is assigned to well-dissolved polymer molecules and the second fraction to aggregated P3(EO)3T molecules stably dispersed in the aqueous solution. Such aggregates are typically observed in CP solutions and are removable through filtration (Section 4.1.4, Figure 4.6). For the

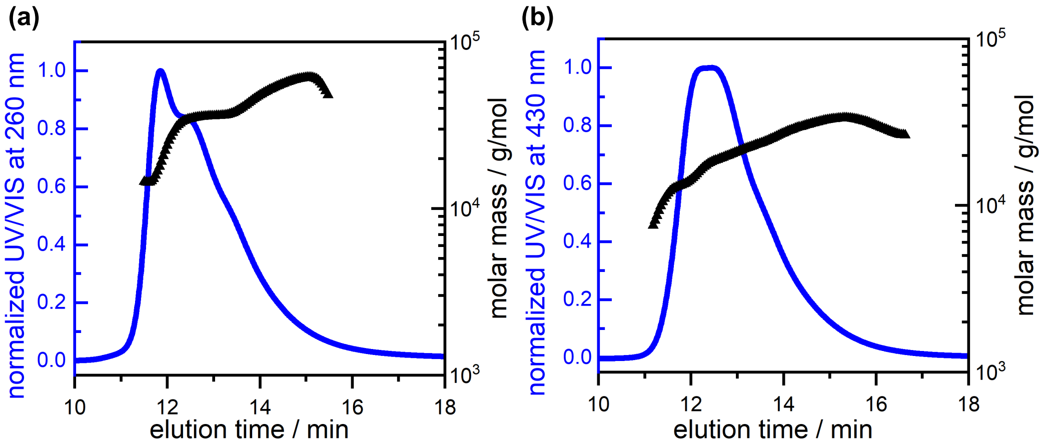

Figure 4.19: MW evolution and superimposed UV/VIS response at (a) 260 nm and (b) 430 nm of P3(EO)3T-b-20N plotted against elution time.

bare ON, one narrow fraction eluted around 11.8 min was observed, which is only detectable at 260 nm (Figure 4.18a, blue line). The P3(EO)3T-b-20N solution, shows two fractions (Figure 4.18a, green line) for both wavelengths similarly to the bare P3(EO)3T sample. The first fraction is slightly shifted to a higher elution time of 12.5 min and possesses a shoulder on peak edge to higher elution times. These effects are allocated to the successful formation of the diblock copolymer. The second fraction remains unchanged. Accordingly, this fraction is allocated to the aggregated P3(EO)3T molecules, which apparently do not participate in the click reaction. A new fraction was not observed in the solution of P3(EO)3T-b-ON. Accordingly, the assembly of P3(EO)3T-b-20N into vesicles, as reported by Kamps *et al.*[259], was ruled out under the here applied conditions. However, it might be possible to induce such a self-assembly into larger particles by changing the physical or chemical properties of the solvent system.

The fractions of the well-dissolved P3(EO)3T and P3(EO)3T-b-20N were further analyzed concerning their molecular weight distribution. The MW was calculated from the MALS and UV/VIS data by Zimm analysis.[260,261] The given values are the average of three measurements. The M_n of P3(EO)3T, estimated by GPC measurements, is 9 092 g mol^{-1} (DP = 35) with a dispersity of 1.09. The M_n extracted from the AF4 analysis is 16 200 g mol^{-1} with a dispersity of 1.13. Linear polymers in the lower mass regime are commonly overestimated by AF4 measurements because smaller polymers tend to leak through the semipermeable membrane. Furthermore, the GPC measurements were performed in chloroform providing a better solubility and less aggregated species than in aqueous solution.

The resulting MW evolution of P3(EO)3T-b-20N is displayed in Figure 4.19 (black lines) based on the 260 nm (Figure 4.19a) and 430 nm (Figure 4.19b) fractograms. The corresponding M_n and dispersity are summarized in Table 4.5. Averaging both results, an M_n of 24 950 g mol^{-1} was obtained. This value corresponds with the theoretical value of 22 000 g mol^{-1}, as it would be expected fro m the MWs of the bare compounds. As mentioned above, the MW calculations were based on the molar extinction coefficients ε_{260} and ε_{430} of the bare compounds. The extinction coefficient at 260 nm was estimated as an average of 20N and P3(EO)3T. Hence, ε_{260} is considered more error-prone than ε_{430}, which is only determined by P3(EO)3T. The obtained MW of 21 200 g mol^{-1} shows a high coincidence with the expected value of 22 000 g mol^{-1}. The obtained dispersity of 1.1 is in agreement with the dispersity of the P3(EO)3T block, which is also 1.1. This analysis revealed that the well-defined molecular structure of the P3(EO)3T block is maintained in the diblock copolymer.

Table 4.5: Results of molecular weight calculations obtained by AF4 measurements.

	at 260 nm	**at 430 nm**	**average**
M_n / g mol^{-1}	28 700 ± 3 320	21 200 ± 1 530	24 950
M_w / g mol^{-1}	32 400 ±3 090	22 700 ± 1 580	27 550
dispersity	1.13 ± 0.03	1.08 ± 0.01	1.11

Hybridization Kinetics by SPR measurements

The thermodynamics of the DNA hybridization process are well-understood and allow to accurately predict melting temperature and the minimum free energy structure in dependency on salt concentration and sequence.[262,263] On the contrary, only rough approximations for the hybridization kinetics have been attained from developed models. Consequently, there is still a need to individually determine the reaction rate constants for ONs under specific conditions.[264] Presumptions are further complicated for the P3(EO)3T-b-ON molecule. The challenge emerged how the P3(EO)3T block influences the hybridization performance of the ON under certain conditions. SPR is a highly sensitive tool to study the kinetics of biomolecular binding events at the sensor surface.[265,266] Furthermore, it allows to study the binding conditions, such as temperature and salt concentration.

The hybridization kinetics of the diblock copolymer P3(EO)3T-b-ON at surface-tethered complementary DNA probes were analyzed by SPR. The SPR

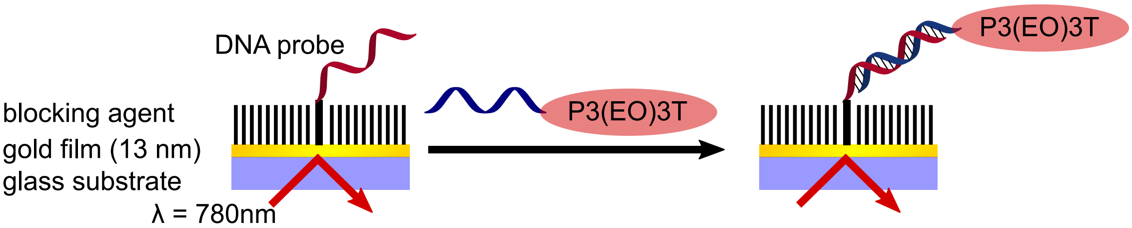

Figure 4.20: Scheme of a P3(EO)3T-b-ON hybridizing to a surface-tethered DNA probe while monitored by SPR. The surface plasmon of the thin gold film on the glass substrate is excited by a LED with a wavelength of λ = 780 nm.

measurements were conducted in collaboration with Dr. Alfred Kick (Kurt-Schwabe Institut für Mess- und Sensortechnik Meinsberg e.V.). diblock copolymer with three different sequences were investigated: the non-repetitive sequence 20N, the repetitive sequence 5(ATT) and the mononucleotide sequence 18T. The SPR experiments were conducted in a microfluidic system at a constant flow velocity. The SPR chip was divided into two separated channels with one channel bearing the complementary DNA probe (20N', 5(AAT) and 18A) and one channel the non-complementary DNA probe (20N, 5(ATT), 18T) taken as the reference system (Figure 3.4). The sequence and the chemical structure of the probes are presented in Table 3.3 and Figure 3.5. The specificity of the P3(EO)3T-b-5(ATT) was further tested on 18A probes.

The thiol-functionalized DNA probes were immobilized on the gold surface of an SPR chip. Non-covalently attached probes were removed by several washing steps. The bound probes were straightened by the blocking agent MUTEG. The attachment of the DNA probes and the blocking agent on the gold surface resulted in a shift of the SPR minimum, which stayed stable after several washing steps. The new position of this SPR minimum was used as a baseline for the subsequent hybridization experiments. As illustrated in Figure 4.20, the diblock copolymer was flushed over the DNA-probes while the shift of the SPR signal was recorded. The rate constants of the hybridization were calculated by fitting the kinetics of the increasing SPR signal. After each hybridization experiment, the probes were recovered by de-hybridization.

The hybridization of the 20N sequence on the 20N' probes and its kinetics were analyzed. First, the accessibility and specificity of the 20N' probes were tested by running the bare ON 20N over complementary DNA probes 20N' and non-complementary DNA probes 20N. On the chip site with the complementary probes 20N', a shift of the SPR minimum was detected (Figure 4.21a, blue line). The hybridization reaction of the ON proceeded with a rate constant of $2.32 \cdot 10^4\ \mathrm{M^{-1}\,s^{-1}}$.

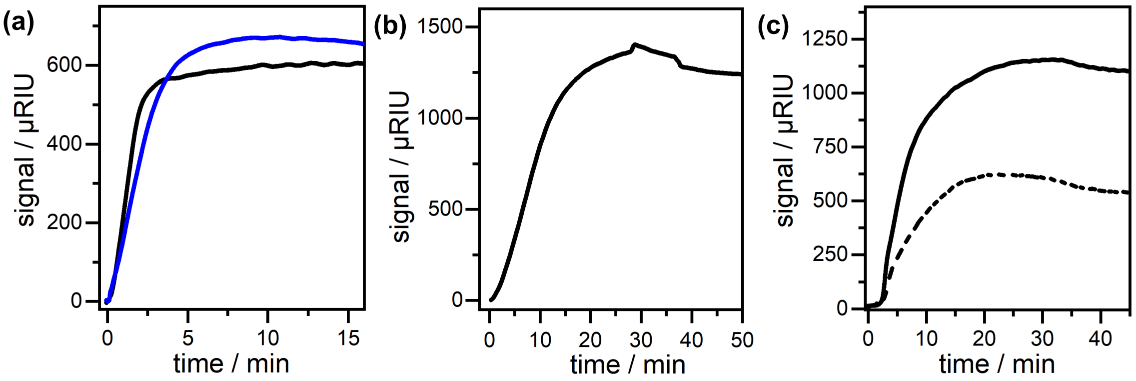

Figure 4.21: (a) SPR signals plotted as a function of time during the hybridization of (a) P3(EO)3T-b-20N (black line) and the bare 20N (blue line) on 20N' probes; (b) P3(EO)3T-b-18T on 18A probes and (c) P3(EO)3T-b-5(ATT) on 5(AAT) probes (solid line) and 18A probes (dashed line).

On the non-complementary probes, no shift was detected, verifying the reliability of the set-up. Next, the hybridization of P3(EO)3T-b-20N was analyzed. The diblock copolymer also bound to the complementary 20N'-probes as it was accompanied by an increase of the SPR signal (Figure 4.21a, black line). A hybridization rate constant of $1.26{\cdot}10^{4}\,\mathrm{M^{-1}\,s^{-1}}$ was computed. Second, the mononucleotide diblock copolymer P3(EO)3T-b-18T was studied on its complementary probes 18A. Additionally, this diblock copolymer was also tested on 5(AAT) probes. On the 18A probes, the SPR signal shifted (Figure 4.21b) and a reaction rate constant of $1.44{\cdot}10^{4}\,\mathrm{M^{-1}\,s^{-1}}$ was determined. No binding event was detected on the 5(AAT) probes (not depicted). In a final step, the diblock copolymer P3(EO)3T-b-5(ATT) with the repetitive sequence was analyzed on its complementary probes 5(AAT) (Figure 4.21c, solid line) and on 18A probes (Figure 4.21c, dashed line) as well. On both probes, a shift of the SPR signal was observed confirming the hybridization. Reaction rate constants of $3.91{\cdot}10^{4}\,\mathrm{M^{-1}\,s^{-1}}$ on the 5(AAT) probes and $1.43{\cdot}10^{4}\,\mathrm{M^{-1}\,s^{-1}}$ on 18A probes were calculated, respectively. The reaction rate constants are collected in Table 4.6.

The hybridization rate constant of P3(EO)3T-b-20N is 0.54 times slower in comparison to the bare ON 20N. This is reasonable because its MW is 1.6 times higher than the bare ON 20N. The MW should correlate with the hydrodynamic radius, which is why the diffusion of the diblock copolymer is expected to be lower. The hybridization rate constants of the diblock copolymers bearing the repetitive sequences 5(ATT) and 18T are distinctly faster than the non-repetitive 20N. Ouldridge *et al.* demonstrated by simulations that non-repetitive sequences hybridize with lower rate constants than repetitive ones.[267] This result was explained by differences in the duplex formation mechanism. For a non-repetitive sequence, only a few interactions are possible between misaligned DNA strands. A positive binding event of complementary bases initiates the formation of a DNA duplex. The associated bp can either dissociate or initiate more base-pairing. The latter is called zippering and leads to a fully paired DNA duplex.[267,268] For repetitive sequences, another mechanism was found being responsible for the duplex formation. Many metastable structures are present in misaligned duplexes. These misaligned strands

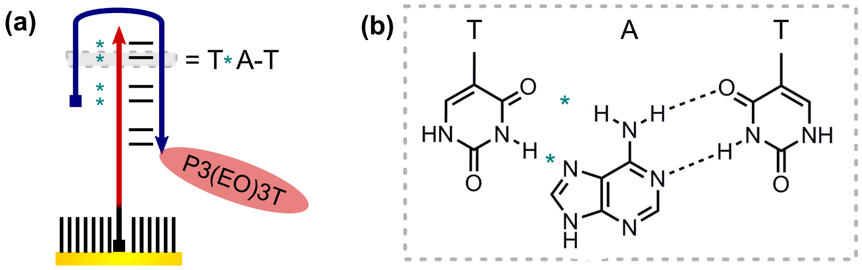

Figure 4.22: (a) Triplex DNA (square = 5'-end, arrow = 3'-end) formed by the 18A probe and one P3(EO)3T-b-5(ATT) molecule, which binds from two sites to the probe over Watson-Crick base pairing (marked by line) and Hoogsteen base pairing (marked by asterisk). (b) Chemical structure of the base triplex T*A-T.

arrange themselves either *via* a pseudoknot or inchworm displacement into the aligned duplex. The rate constants are increased because many intermediate states lead to the duplex formation instead of only one positive binding event, as in case of the non-repetitive sequence. Accordingly, for an efficiently proceeding attachment of hetero-objects *via* sticky ends, it is advantageous to use such repetitive sequences. Why the rate constant of the mononucleotide sequence 18T is only slightly increased, but the constant of the 5(ATT) is more than doubled, is not clear. A higher rate would be expected due to more possible metastable states. A potential reason might be lower thermodynamic stability of the formed duplex.

Intriguingly, P3(EO)3T-b-18T did not bind to 5(AAT) probes, but P3(EO)3T-b-5(ATT) bound to the 18A probes (Figure 4.21c, dashed line), even so, significantly slower than to 5(AAT). This could potentially disturb the utilization of both sequences on one DNA origami structure. A possible reason might be cross-hybridization of these ONs due to their partially coinciding nucleotides (AT-rich sequence). However, it would be expected that both, P3(EO)3T-b-5(ATT) and P3(EO)3T-b-18T, would cross-hybridize on the respective not completely complementary probe. Another reason might be the formation of a triple helix *via* Hoogsteen bp.[269] Figure 4.22a proposes a possible triplex formation between one P3(EO)3T-b-5(ATT) and the 18A probe. The diblock copolymer can bind on two sites forming the base triplex T*A-T (Figure 4.22b), where the asterisk corresponds to the Hoogsteen bond and the line the normal Watson-Crick bond. This DNA form was found particularly stable for the base triple TAT.[270] Due to loosely bond Watson-Crick bps, the increased local concentration around the probes might kinetically promote the triplex formation. A similar triplex formation might also be feasible for the 5(AAT) probes and P3(EO)3T-b-18T, but this was not observed. Due to the shorter length of the probe, steric effects of the P3(EO)3T block might hinder the formation of such a triplex. The triplex was found to be thermodynamically less stable.[271] Hence, it should be possible to suppress its occurrence by tuning the environmental conditions. The experiment was repeated by slowly increasing the temperature. No hybridization occurred anymore above 31 °C. In addition to the higher reaction rate constant, the duplex formation between P3(EO)3T-b-5(ATT) and 5(AAT) is kinetically and thermodynamically preferred over P3(EO)3T-b-5(ATT) and 18A. Therefore, both sequences should be applicable for one DNA origami template.

4.3.3 Planar DNA Origami Template

The formation of confined polythiophene nanostructures was templated by a DNA origami structure. A rectangular-shaped 2D DNA origami template, referred to as the pad, was used for all experiments. The design of the DNA origami structure is based on the scaffold strand M13mp18 and was developed by Dr. Andreas Heerwig (Kurt-Schwabe-Institut für Mess- und Sensortechnik e.V. Meinsberg). 16 double

Table 4.6: Reaction rate constants obtained by the SPR measurements.

sample/probe	**20N' probe**	**5(AAT) probe**	**18A probe**
20N	$2.32{\cdot}10^4\,\mathrm{M^{-1}\,s^{-1}}$	not measured	not measured
P3(EO)3T-b-20N	$1.26{\cdot}10^4\,\mathrm{M^{-1}\,s^{-1}}$	not measured	not measured
P3(EO)3T-b-5(ATT)	not measured	$3.91{\cdot}10^4\,\mathrm{M^{-1}\,s^{-1}}$	$1.43{\cdot}10^4\,\mathrm{M^{-1}\,s^{-1}}$
P3(EO)3T-b-18T	not measured	no hybridization	$1.69{\cdot}10^4\,\mathrm{M^{-1}\,s^{-1}}$

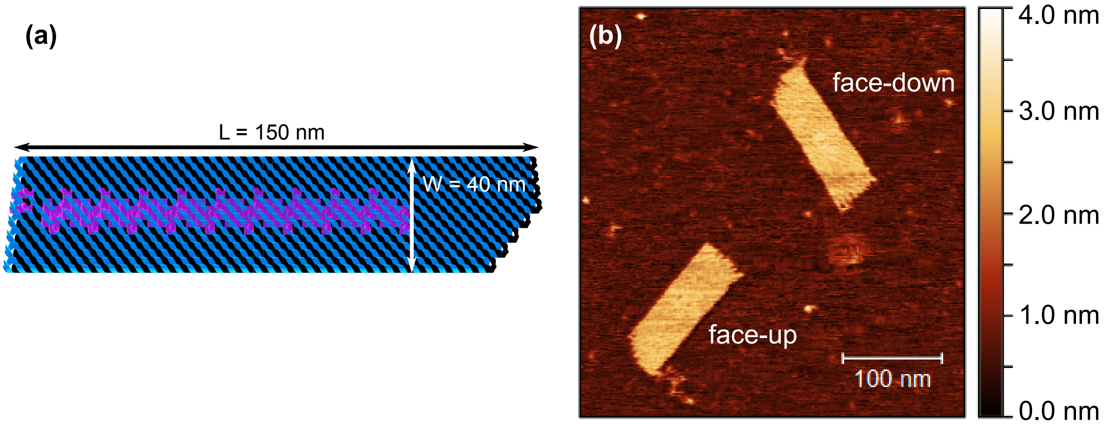

Figure 4.23: (a) Three-dimensional folding scheme of the pad (pad40), which is composed of 16 double helices where the scaffold strand is blue, the staple strands are black and the extended staple strands are purple. (b) AFM image of bare pads with face-on (right) and face-up (left) with regard to the attachment sites. Face-on means then, the attachment sites are facing to the mica surface and face-up, they are facing to the tip.

helices form the pad, which are cross-linked by a staple strand every 1.5 helical turn. The theoretical dimensions of the pad derived from the design are 150 x 40 x 2 nm (L x W x H). Experimental values obtained by, e.g., AFM measurements can vary due to the influence of cations, interactions with the surface or tip pressure. The lower right corner of the pad is cut-off. The upper right corner comprises a single-stranded loop, which is an unpaired residual of the scaffold strand (457 bases). These two features introduce chirality into the appearance of the pad and allows to identify whether a structure is face-down or face-up when immobilized on a surface (concerning the direction of the attachment sites). Figure 4.23a illustrates the three-dimensional structure of the pad. Figure 4.23b shows an AFM image of a face-down and face-up pad structure immobilized on mica. The design of the pad was twist-corrected by skipping a base after six helical turns to eliminate the simplification of the CaDNAno program, which calculates with a helical turn after 10.67 bp instead of 10.5 bp (canonical B-DNA).[11,177]

The pad design was further adjusted concerning the location of the extended staple strands for the hetero-object attachment. In the following, these extended staple strands are termed as attachment sites. The attachment site patterns are later presented in detail. The given distances between the attachment sites are theoretical values assuming an interhelical distance of 0.5 nm,[11] a diameter of 2 nm for the DNA double helix[141] and a distance of 0.34 nm between adjacent bases along one DNA double helix. The position *a* refers to the site where the extension of the staple strand protrudes from the DNA origami surface. The letters *b*, *c*, *d*, *x*, *y* and *z* label distances between these protruding extensions (i.e., attachment site). The term *lane* (L1, L2, etc.) relates to a double helix and the corresponding attachment sites, which are positioned on this helix (exemplarily labeled for pad40, Figure 4.24a).

(a) pad40

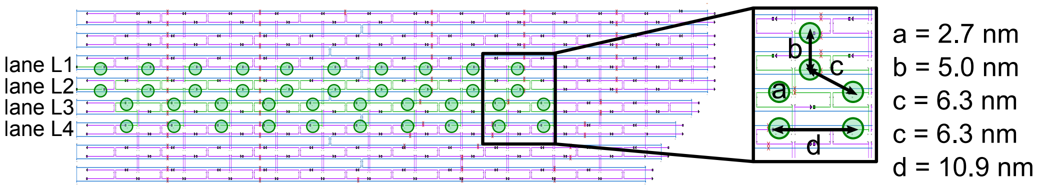

(b) pad82

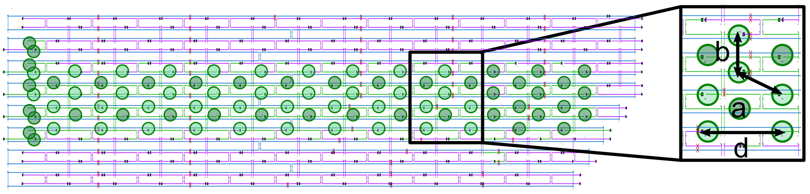

(c) pad105

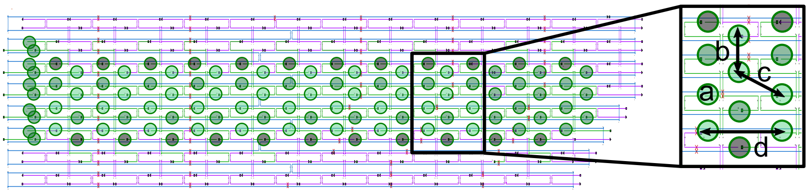

(d) pad15-48

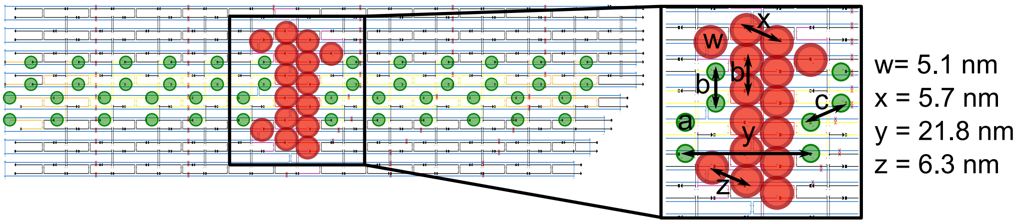

Figure 4.24: Schemes of scaffold strand and staple strands alignment of the origami structure pad. The dots mark where the extended staple strands protrude from the pad. The attachment site patterns are displayed for (a) pad40, (b) pad82, (c) pad105 and (d) pad15-48. The radius of the dots correlates with the length of the staple strand's extension protruding from the pad.

Pad40 has 40 attachment sites which protrude from the middle of the pad in four parallel lanes with ten sites per lane (Figure 4.24a). The intra-lane distance between two adjacent attachment sites is 10.9 nm. An outer and inner lane is separated by one double helix corresponding to an inter-lane distance of the attachment sites of 5 nm. The two inner lanes are on adjacent double helices but displaced by 17 bases corresponding to an inter-lane distance of 6.3 nm. The sequence of the attachment sites is 8A which relates to a length of 2.7 nm. The overall attachment array is 103 nm long and 15 nm wide.

Pad82 is an extension of pad40 with 82 attachment sites in total (Figure 4.24b). The 10 attachment sites along one double helix is extended by three additional sites. Furthermore, on the free double helix between L1 and L2 (and in the same way between L3 and L4), are additionally filled with 13 attachments sites. The sequence of the attachment sites is 8A. The attachment array spreads over an area of 132 nmx15 nm (LxW).

Pad105 is a further extension of pad82 with 105 attachment sites in total (Figure 4.24c). In addition to the extension in length, the attachment array is widened. To this end, the adjacent double helices of L1 and L4 were equipped with 13 attachment sites. Further attachment sites were added at the left side of the pad. The whole attachment array has a length of 132 nm and a width of 20 nm. The sequence of the additional attachment sites is 10A (length = 3.4 nm).

Pad15-48 was designed to arrange two different hetero-objects (Figure 4.24d), and is based on pad40. On the right and left side of the pad are 24 attachment sites each with the sequence 8A. These sites are arranged in the same way as in pad40. However, they are not connected but have a gap of 16.7 nm. In this gap, 15 additional attachment sites are located with another repetitive sequence 5(AAT) covering an area of 5 nm x30 nm.

4.3.4 Synthesis of P3(EO)3T@pad Hybrid Structure

The diblock copolymer was added in a minimum fivefold excess to the number of attachment sites present on the DNA origami template (e.g., for pad40, a 200-fold excess to the DNA origami concentration). In the resulting hybrid structure P3(EO)3T@pad, a filament composed of many P3(EO)3T molecules was formed (Figure 4.25a). In general, the maximum DNA origami concentration was 4 nM. At higher DNA origami concentrations, aggregation of the P3(EO)3T@origami hybrid structures occurred, most likely due to cross-hybridization of aggregated diblock copolymers. The diblock copolymer was attached while gently shaking at a moderate temperature of 15 °C to increase the solubility of the P3(EO)3T block due to its lower critical solution temperature (Section 4.1.5) and prevent further aggregation. Sodium chloride was added to the folding buffer to promote the hybridization and reduce electrostatic repulsion of the DNA phosphate backbones of the densely packed attachment sites. The excess of the diblock copolymer was removed by filtration through 100 kDa Amicon® filter.

The formation of the hybrid structures was investigated by high-resolution liquid AFM imaging. The attached diblock copolymers were identified by an increased height H ($H = 3.3$ nm to substrate) in comparison to the bare DNA origami template ($H = 1.5$ nm) appearing at the expected attachment sites (Figure 4.25b).

Generally, all results, unless otherwise specified, were obtained from measurements

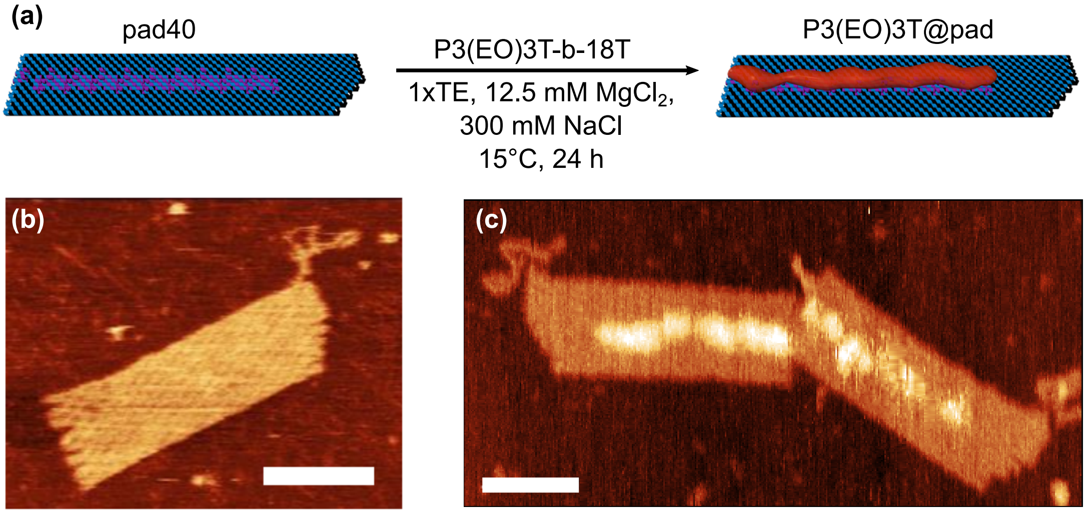

Figure 4.25: (a) Exemplary attachment scheme of P3(EO)3T-b-18T to the DNA origami structure pad40 yielding the hybrid structure P3(EO)3T@pad. High-resolution AFM images of the (b) bare pad and (c) hybrid structure P3(EO)3T@pad, scale bars: 50 nm.

performed in solution. The application of the P3(EO)3T@pad hybrid structure as polymer wire in electronic devices, however, is envisaged in the dry state. Therefore, it should be taken into account that the observed results might be not fully adequate for the dry state.

Yield of the P3(EO)3T@pad Formation

The yield of the hybrid formation is discussed based on pad40 structure. The high-resolution AFM images of the P3(EO)3T@pad hybrid structures were quantitatively studied concerning the attachment yield and its dependence on the attachment sequence. For this purpose, an image routine was performed based one FindFoci.[272] This image routine was developed and conducted by Franziska Fischer (Technische Universität Dresden).[258,273] The polythiophene chains do not possess a defined shape as, e.g., metallic nanoparticles. Therefore, it was not possible to clarify by AFM whether an imaged object is composed of a single molecule or aggregated molecules. Consequentially, in the following discussion, the term polymer object is used instead of polymer molecule and is not considered as an absolute evaluation of the attachment yield but an estimation.

Almost all DNA origami structures were equipped with at least one polymer object (yield per pad $>90\%$). The mean of the yield per individual attachment site, on the contrary, is modest. For the mononucleotide sequence 18T, a yield up to 33% was obtained.[273] The yield for the non-repetitive sequence 20N was even lower with 29%. The lower yield of the 20N sequence correlates well with the different reaction rate constants obtained by the SPR measurements (Section 4.3.2). Altogether, the yield per attachment site appears to be modest compared to literature. For other hetero-objects, e.g., metallic nanoparticles, yields of over 90% were reported.[9,187] For a bottle-brush-type CP with ON-sidechains (Figure 2.18g), the group of Gothelf reported a yield of approximately 50%.[38] However, all of these works used hetero-objects with many ON functionalities. As opposed to this, a one-to-one attachment was applied here. Each P3(EO)3T molecule bears only one ON functionality (Figure 4.17). The origami structure also possesses only one attachment site to capture one P3(EO)3T-b-ON molecule. The reports mentioned earlier for metallic nanoparticles[187] and CPs[35] used many ONs per functional object and at least three attachment sites (depending on the shape of the hetero-object) on the origami structure to capture the functional object. For the one-to-one attachment, any impurities due to production errors in the ONs or incompletely folded origami structures inhibit a successful binding event and cannot be compensated by other ONs. The similar approach of Wang *et al.* (Figure 2.18h), which used two ONs per hetero-object, resulted in an equivalently low yield of 20%.[37] Therefore, it is assumed that the low yield is indeed an inherent of the one-to-one attachment approach. In addition to the shortcomings of the one-to-one attachment, the following aspect might effect the achievable yield negatively: the attachment site patterns were relatively dense compared to patterns applied for metallic nanoparticles. Thereby, attachment sites might be sterically blocked by already attached polymer objects and not accessible to hybridization.

Modulation of the P3(EO)3T@pad Filaments

In further experiments, the ability to modulate the P3(EO)3T filament's dimensions with the DNA origami template was investigated. The length and width of the supra-polymer structures based on different attachment site patterns (pad40, pad82, pad105, and pad15-48) were extracted from the AFM images and compared to their theoretical values. For pad15-48, only the 15 5(AAT) attachment sites were used for attachment (Appendix, Figure A.9.1d). For each pad type, five structures with a high attachment yield were measured by the profile tool of Gwyddion.[214] The overall area of the P3(EO)3T filament was derived by the Particle Analyzer of ImageJ.[215] The given values are averaged values of the five structures, and their errors the corresponding standard deviation. All investigated hybrid structures are displayed in the Appendix, in Figure A.9.1.

The results of the pads pad40 and pad105 are displayed in Figure 4.26. The attachment site pattern of pad40 predetermined a length of 103 nm, a width of 15 nm and an overall area of 1 545 nm^2 (Figure 4.26a). The experimental data resulted in a length of 94±8 nm, a width of 14±1 nm and an overall are of 1 212±126 nm. Hence, theoretical and experimental dimensions correlated well. For pad105, the attachment site pattern was horizontally and vertically extended by 68 additional attachment sites and was expected to be 132 nm long and 20 nm wide. As apparent from the high-resolution AFM image, the resulting P3(EO)3T filament structure appeared distinctly broader and longer (Figure 4.26b). This observation was

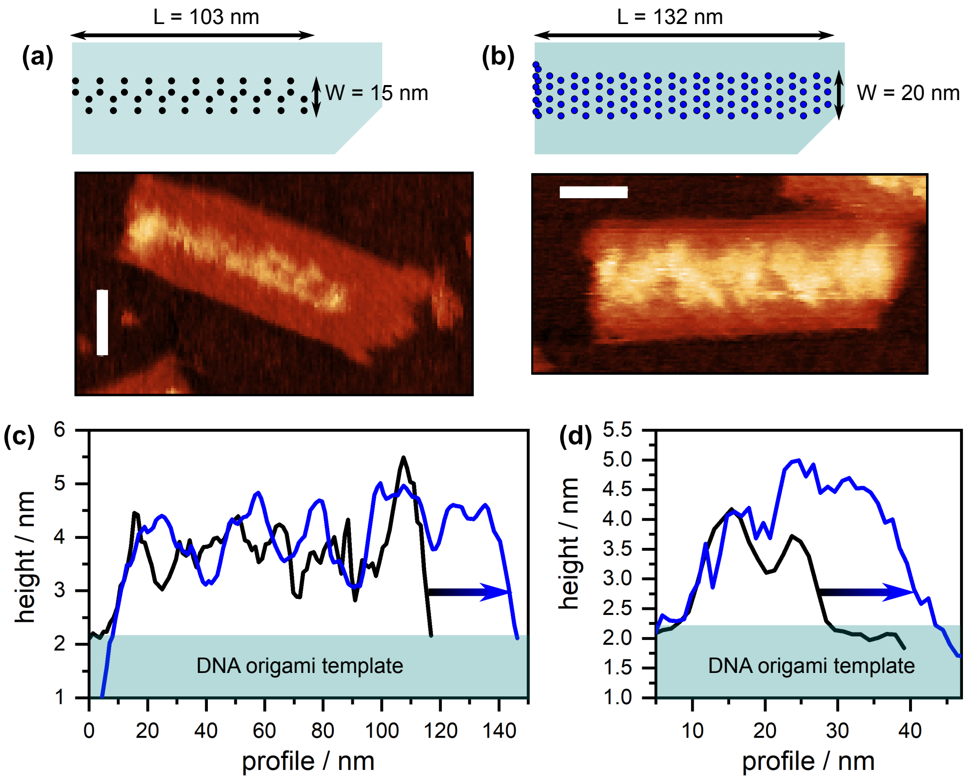

Figure 4.26: (a) Scheme of pad40 and AFM image of the resulting P3(EO)3T filament. (b) Scheme of pad105 and AFM image of the resulting P3(EO)3T filament. Scale bars: 30 nm. Height profiles along (c) length *L* and (d) width *W*.

confirmed by extracting the profile lines along the length (Figure 4.26c) and the width (Figure 4.26d). The length was extended by 15 nm to 129±3 nm and the width was increased by 7 nm to 23±4 nm. The overall area of 2 505±421 nm^2 is in good agreement with the theoretical expected value of 2 640 nm^2.

For the other pad types, the resulting P3(EO)3T structures also correlated well with the design of the attachment site patterns (Table 4.7). Generally, the experimental area of the supramolecular polymer is smaller than the theoretical one. It would be expected that the area is larger due to the additional volume of the P3(EO)3T molecules. However, the rather low attachment yield might reduce the total area. An exception was found for pad15-48, where the experimental area (511±60 nm^2) was three time bigger than the theoretical area (150 nm^2). The following reasons might explain this deviation. First, the steric hindrance may be distinctly reduced since the attachment site pattern is composed of only two parallel lines (in one direction). Second, due to the small dimensions (30 x 5 nm), the geometrical shape of the AFM-tip has a countable influence on the lateral values. Objects scanned along the x-scanning direction most likely appear too broad.[274]

Overall, it was demonstrated that the shape of the DNA origami-templated P3(EO)3T filaments is programmable in two dimensions by the attachment sites

Table 4.7: Theoretical and experimental dimensions of the DNA origami-templated P3(EO)3T filaments based on the different pads.

	Theory		**AFM analysis**	
	L x W / nm	area / nm^2	L x W / nm	area / nm^2
pad40	103 x 15	1 545	94±8 x 14±1	1 212±126
pad82	132 x 15	1 980	129±14 x 14±1	1 786±194
pad105	132 x 20	2 640	129±3 x 23±4	2 505±421
pad15-48	5 x 30	150	15±3 x 35±4	511±60

patterns. The obtained results confirm the versatility and modularity of the DNA origami technique as a molecular breadboard for confined nanostructures.

4.3.5 Tunable Fluorescence of P3(EO)3T@pad Hybrid Structures

The high-resolution AFM images were further quantitatively analyzed with respect to the positioning of the polymer objects compared to the position of the attachment sites.[258,273] As apparent from the 3D AFM image (Figure 4.27a), the polymer objects appeared to be concentrated in the middle of the pad forming a filament instead of being statistically distributed over the four lanes. This observation was evidenced by image analyses of the AFM images (conducted by Franziska Fischer, Technische Universität Dresden).[273] The yield per attachment site was not equal over the whole pad but was dependent on the attachment site's position. As depicted in Figure 4.27b, the probability for occupation was distinctly higher on the inner lanes than on the outer lanes. Around 70% of the polymer objects were located on the inner lanes L2 and L3 (Figure 4.24a). Only 30% were found on the outer lanes L1 and L4.

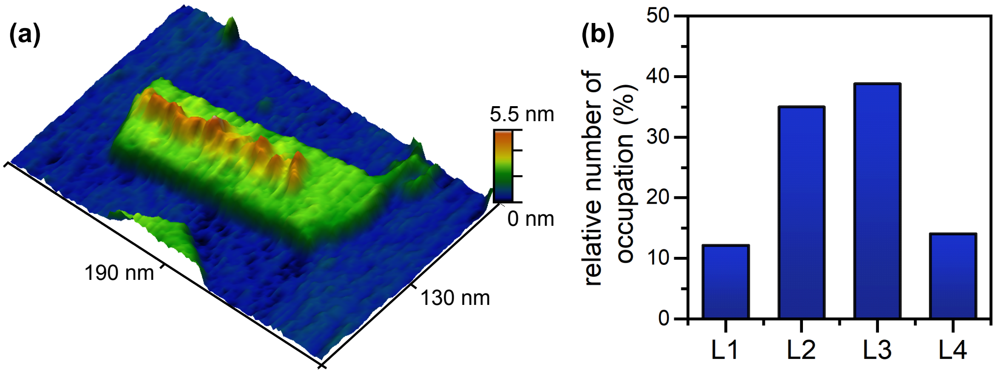

Figure 4.27: (a) 3D AFM image of P3(EO)3T@pad based on pad40 with a polymer filament in the middle of the pad. (b) Distribution of the polymer objects on the four lanes L1, L2, L3 and L4 on pad40 found by quantitative analyses on high-resolution AFM images.

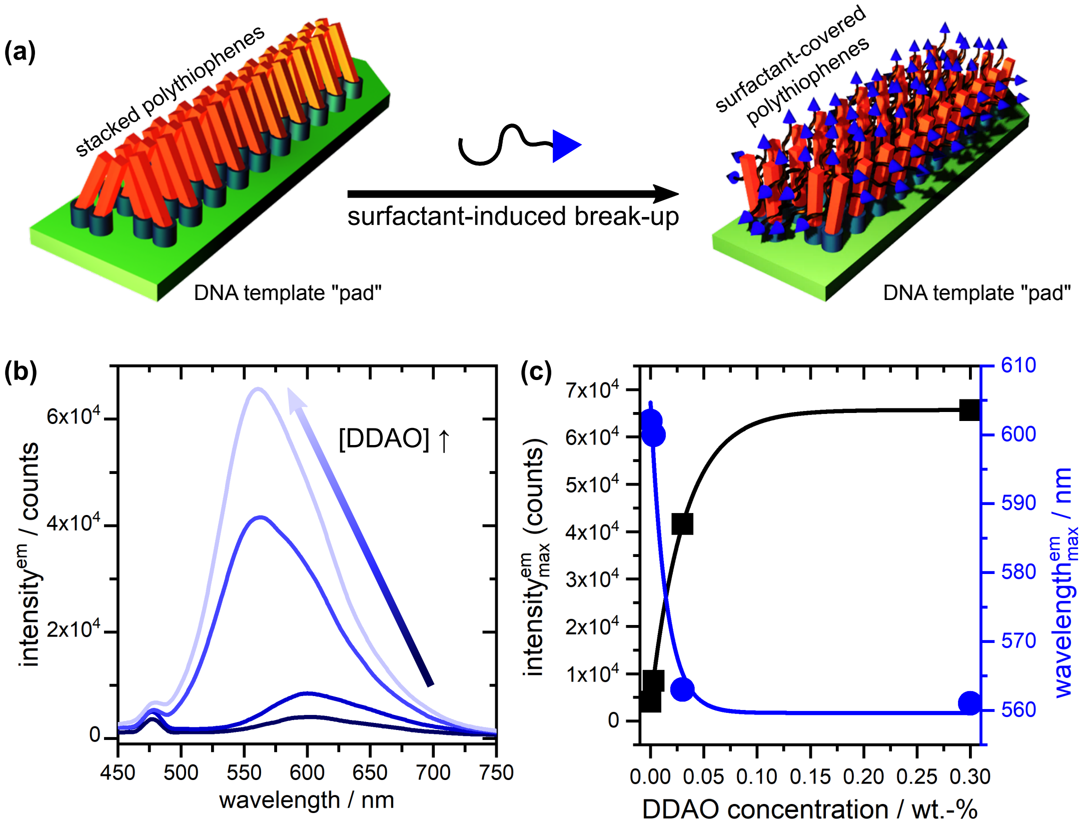

Figure 4.28: (a) Scheme of surfactant-induced (surfactant: *N*,*N*-dimethyldodecylamine *N*-oxide (DDAO)) break-up of the DNA-templated stacked polythiophene backbones. (b) Fluorescence spectra of P3(EO)3T@pad at different DDAO concentrations (0 wt.-%, 0.003 wt.-%, 0.03 wt.-%, and 0.3 wt.-%). (c) Intensity (black square) and wavelength (blue dots) of the emission's maximum plotted against DDAO concentration of the P3(EO)3T@pad sample. The lines are just for guidance of the eyes.

For hetero-objects with a charged surface (e.g., metallic nanoparticles), the opposite distribution would be expected due to electrostatic repulsion. Accordingly, the preferential allocation of the polymer objects in the middle of the pad was attributed to attractive interactions. A possible reason for these interactions might be π-π-stacking between the densely packed polythiophene backbones. The presence of π-π-stacked zones, as it was already observed for the thin films (Figure 4.13a), would be favorable. Such zones serve as conducting pathways and, thus, make these polythiophene filaments applicable as conducting wires.

The question arose how to proof the presence of π-π-stacked zones on the DNA origami template. In previous studies, it was demonstrated that such aggregated CPs can be effectually broken by surfactants.[275–277] A similar behavior was expected for the P3(EO)3T@pad hybrid structures. The potential surfactant-induced break-up of a π-π-stacked polythiophene filament on an ideal, fully occupied origami structure is schemed in Figure 4.28a. In general, CPs, and more particularly P3(EO)3T (Section 4.1.5), show strong optical responses to changes of their conformation and intermolecular packing structure. Therefore, such a surfactant-induced break-up can be monitored by the CP's optical response (absorption and/or emission).[275–277] To that end, the emission of P3(EO)3T was analyzed upon an increasing surfactant concentration. The non-ionic and rather small surfactant DDAO was used for these experiments to prevent any degradation of the DNA origami structure. The viability of the hybrid structures was verified by AFM up to a DDAO concentration of 0.03 wt.-% (for higher DDAO concentrations, AFM-imaging was not possible anymore). The following DDAO concentrations were investigated: 0 wt.-%, 0.003 wt.-%, 0.03 wt.-%, and 0.3 wt.-% by a constant hybrid structure concentration. The resulting fluorescence spectra for the different DDAO concentrations are displayed in Figure 4.28b.

With increasing surfactant concentration, the maximum of the emission band was blue-shifted from 602 to 561 nm, and the emission intensity increased from 4 062 to 65 659 counts (Figure 4.28c). The blue-shift and the correspondingly decreased Stokes shift λ_S down to 144 nm was attributed to the changing chemical surrounding of the polythiophene backbone. Due to the accretion of the DDAO's alkyl tail at and between the polythiophene backbones (Figure 4.28a), the polarity is lower than the pure aqueous solution. As a result, the excited states are less stabilized and the Stokes shift decreases.[278] Furthermore, the attachment of the bulky surfactant tails can, first, partially twist the polymer backbones and, second, break-up the π-π-aggregated polymer chains. For both cases, the conjugation length would be decreased leading to a blue-shifted emission band. The assumption of the break of the stacked polymer chains is also supported by the intensification of the emission to a 16time higher value. Interchain self-quenching of CPs due to π-π-aggregation is a known effect which, for example, emerges upon the transition from the dissolved to solid state.[279] Hence, the substantial increase of the emission intensity with increasing DDAO concentration is considered a reliable indicator for the presence of π-π-stacked polythiophenes on the DNA origami structure.

The overall motivation of this project was to apply the DNA origami-templated P3(EO)3T filaments as conductive units for nanoelectronic circuits. As discussed in Section 2.1.1, reasonable conductivity requires the presence of π-π-aggregated zones. Accordingly, these findings imply that these supramolecular polythiophene filaments could indeed conduct current.

4.3.6 Potential as Conducting Wire

Finally, the DNA origami-templated P3(EO)3T filaments were electrically characterized to assess their potential as polymer wire. To this end, the structures were analyzed by a two-probe set up. The electrical contacts were provided by a stationary gold electrode and a mobile electrode which was a conducting AFM tip. In the scope of this thesis though, it was not possible to verify the filament's ability to conduct. Nevertheless, the fundamental insights, which were gained for

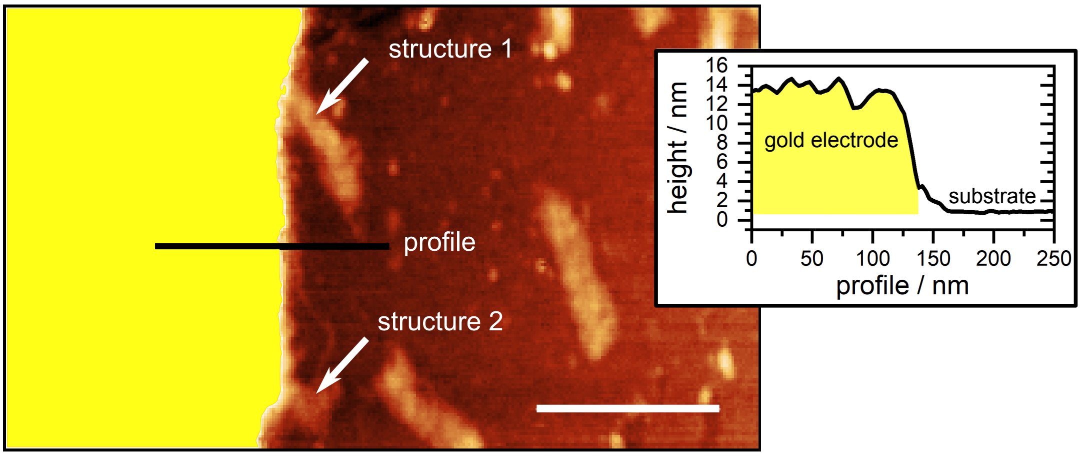

Figure 4.29: AFM image of gold electrode (dyed yellow) evaporated on an immobilized P3(EO)3T@pad sample, scale bar: 200 nm. Inset: height profile along the electrode's edge (black line in AFM image).

the electrical characterization of such delicate nanostructures, are presented in the following. The measurements were performed at the Hebrew University Jerusalem, Israel in collaboration with the group of Prof. Danny Porath. Nitzan Yanay and Avigail Stern, who are students of Porath's group, assisted in the sample preparation and measurements.

To obtain P3(EO)3T@origami structures, which are accessible to such cAFM measurements, the initial hybrid structure was modified (pad40 and polymer batch DP = 19). The dimensions of the DNA origami-templated filaments are at the lower limit to be reliably contacted by the stationary gold electrode and the AFM tip. A structure should distinctly protrude from the stationary electrode (approximately 20 to 30 nm). Otherwise, it is not ensured whether the cAFM tip contacts each target structure due to the conical shape of the tip (radius < 25 nm). For this purpose, pad82 and pad105 were designed (Figure 4.24b,c). There, the length of the attachment pattern was extended from 103 to 132 nm. For pad40, most of the filaments were defective and are expected to be non-functional as a wire. To reduce defects, the empty double helices were filled with additional attachment sites (Section 4.3.3). For (DNA-templated) nanowires, a low width was found to be a critical parameter.[165,212] Therefore, pad105 was developed with an increased width of 20 nm (Figure 4.24c). For a wider polymer filament, additional conducting pathways could be available in case of minor defects.
A further adjustment was done concerning the polymer's MW. For low MW polythiophenes, a reduced charge transport mobility was found. Even though, low MW showed a better packing order.[48,94] However, the increased influence of chain ends leads to more intermolecular hopping transport, which is slower than intramolecular transport. Furthermore, the side-chains act as non-conducting layer between the conjugated backbones. In low MW polymers, less pathways are

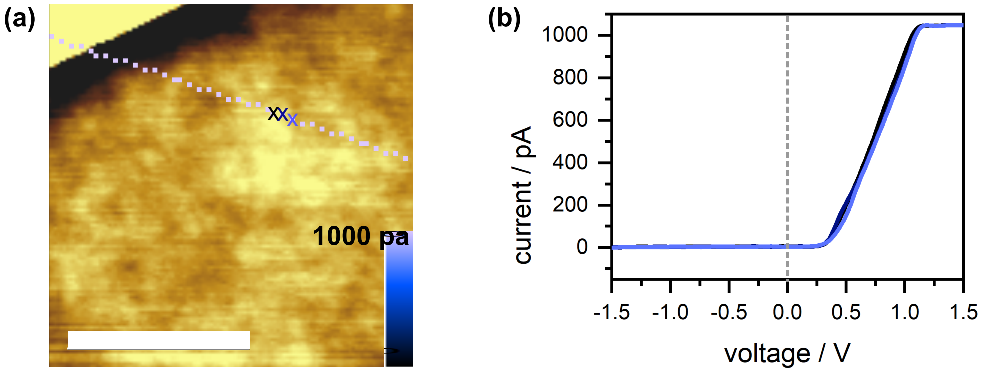

Figure 4.30: (a) Current line along doped P3(EO)3T film measured by cAFM as overlap of topography image, scale bar: 200 nm. (b) Individual $I-V$ curves taken from three spots of the measured line.

available to overcome such non-conducting zones.[94] Therefore, a polymer batch with an increased MW (DP = 56) was used to synthesize the P3(EO)3T@pad hybrid structure.

As discussed in Section 4.2.6, σ of neat P3(EO)3T is low ($10^{-5}\,\mathrm{S\,cm^{-1}}$) due to the low charge carrier concentration. Accordingly, P3(EO)3T@pad structures were also investigated in their doped state. The dopants F4TCNQ and CN6CPK were incorporated from the gas phase (sequential doping) and from solution (premixing).

Conductive AFM Measurements on P3(EO)3T@pad

Atop the randomly distributed P3(EO)3T@pad structures, a stationary gold electrode was deposited by stencil lithography following the procedure of Livshits *et al.*[206] An AFM image of the electrode's edge is shown in Figure 4.29. As can be seen from the height profile along this edge, the average H is around 10 to 12 nm (inset in Figure 4.29). At this height, the gold electrode's surface was smooth and regular. The edges were sharp and low enough to enable contacting of the short P3(EO)3T@pad structures by the AFM tip. As second electrode, the cAFM tip was used to site-specifically contact DNA origami-templated P3(EO)3T paths protruding from the stationary gold electrode. For example, in the displayed AFM image in Figure 4.29, two structures protrude from the stationary gold electrode, and could be contacted by the tip. $I-V$ curves were recorded while contacting the samples with the AFM tip at different positions. To eliminate the influence of drifts of the microscope or the sample, the environment of the structure was measured, too, either as a straight line or as a polyhedral area.

First, a drop-casted thin film of doped P3(EO)3T (DP = 82) was measured by cAFM to test the set-up. The $I-V$ measurements were recorded in a straight line randomly positioned on the polymer film (Figure 4.30a). The resulting $I-V$ characteristics at three different cAFM-tip positions along this line are displayed in Figure 4.30b. In the case of positive voltages, a conducting behavior was found,

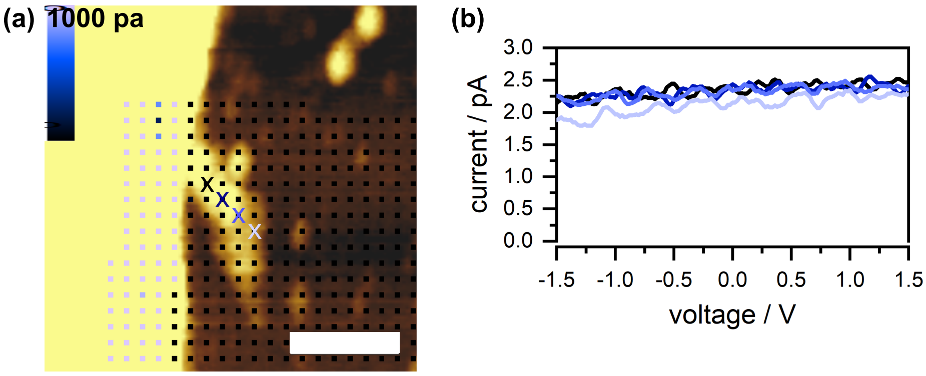

Figure 4.31: (a) Polyhedral current map of doped P3(EO)3T@pad structures as overlay of topography image measured by cAFM, scale bar: 100 nm. (b) Individual $I-V$ curves taken from four spots positioned on the P3(EO)3T@pad hybrid structure.

similar to the measurements obtained for the thin films (Section 4.2.6). The $I-V$ curves show an asymmetric, non-linear conducting behavior, similar to a forward-biased Schottky diode. For negative voltages, the film appears to be non-conducting. More likely, it is rectifying and the breakthrough voltage was just not reached. Such nonlinear, rectifying $I-V$ curves have been observed for cAFM measurements on semiconductors. They are attributed to metal-induced in-gap states, which are a result of a Schottky barrier between the semiconducting P3(EO)3T and the metallic tip.[280,281]

Next, the DNA origami-templated P3(EO)3T filaments were investigated. In the following discussion, the results based on the hybrid structure composed of pad105 and the polymer batch with DP = 56 are presented. Figure 4.31a displays the locally recorded $I-V$ curves from the cAFM measurements. Due to the low size of the investigated structure and drifting of the AFM, $I-V$ curves were acquired in a polyhedron covering the target structure and its surroundings. In Figure 4.31b, four $I-V$ curves are plotted exemplarily. No current above noise was recorded. In total over 120 individual structures were measured for different samples (Appendix, Table A.10.1). However, it was not possible to record any current above the noise. The question appears whether the current is too low to be measured or is there no current because the P3(EO)3T filaments are non-conducting.
To answer the question, whether the current can be measured by the applied method, the theoretical current was estimated from Equation 2.2. Presuming the following parameters, a σ of around $10^{-4}\,\mathrm{S\,cm^{-1}}$ as for doped P3(EO)3T (Figure 4.16) and a polythiophene filament with the dimensions 129 x 23 x 1 nm (L x W x H, experimental data), a current of approximately 10 pA could be expected. This value would be above the noise-level. However, for the hybrid structures the doping level is not as defined as for the bulk samples. Therefore, the DNA origami-templated polythiophenes might be undoped or over-doped, which would strongly influence σ (Figure 4.16). Presuming a σ of $10^{-5}\,\mathrm{S\,cm^{-1}}$, as for the undoped or over-doped

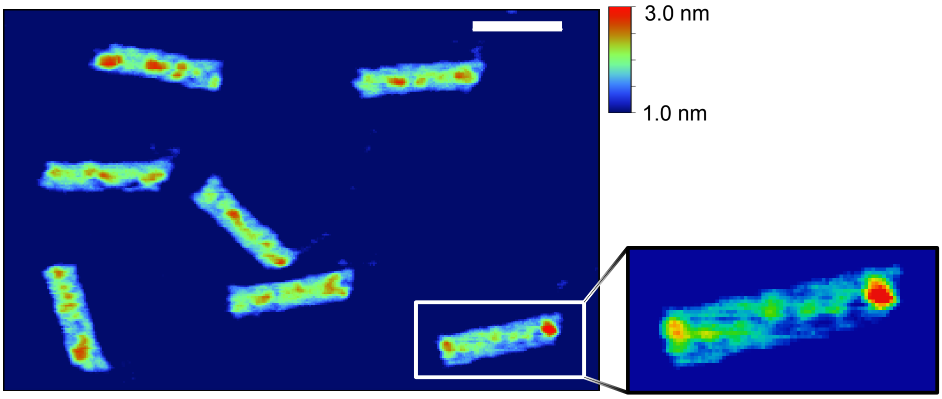

Figure 4.32: AFM image of P3(EO)3T@pad105 recorded at air on a SMART-AIST AFM. Instead of continuous lines, grains (average area 340 nm^2) were observed, scale bar: 100 nm.

P3(EO)3T (Figure 4.16), a current of around 1 pA could be anticipated. This value would disappear in the noise current of 2 pA (Figure 4.31b). Accordingly, under certain circumstances it might be that the current cannot be finally detected from the noise. Further investigation, such as UV/VIS-NIR spectroscopy of the doped hybrid structures, are required to estimate the conductivity for these filaments better. This should allow to calculate reliably the expected current flow. Due to the high number of measured samples and the large variation of the studied parameters, it should be likely that at least for some structures a current above noise level flowed, which was not observed at all.

Despite the low current flow, the filaments themselves are considered in the following. In general, defects are found to be the most critical issue limiting charge transport through nanowires. So far, all AFM images of the P3(EO)3T@pad structures were obtained in solution (Section 4.3.4). It was not possible to image the attached polythiophenes at air. However, the cAFM measurements were acquired at air. In contrast to previous measurements, it was possible to image the attached polymer objects also at air, as shown in Figure 4.32. The polymer objects ($H = 1.7$ nm to substrate) are roughly 1 nm higher than the DNA origami template ($H = 0.8$ nm). The attached polythiophenes did not appear anymore as a filament but as individual grains (inset in Figure 4.32). The transformation from a filament to a grain structure might be a result of drying-induced shrinking of the P3(EO)3T molecules. For such defective structures, charge transport cannot be expected anymore, as it was confirmed by the cAFM measurements. For future studies, these polythiophenes filaments should be stabilized towards drying.

Gold Nanorods as Nano-Electrodes for the Hybrid Structure P3(EO)3T@pad

Several approaches are conceivable how to circumvent the formation of drying-induced grains. First, the drying of the filaments could be prevented by applying extremly humid conditions. However, with increasing humidity, the probability for ionic conductivity (e.g., by Mg^{2+} or other ions bound at the DNA) would be higher.

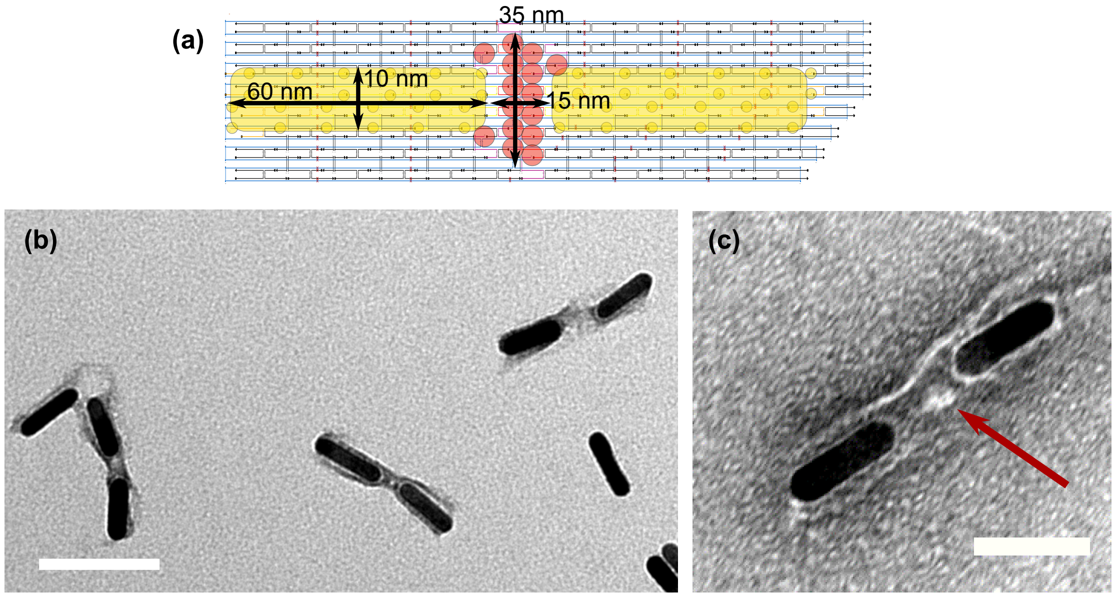

Figure 4.33: (a) Scheme of AuNR-P3(EO)3T@pad immobilized on pad15-48; given dimensions were obtained by TEM (AuNR) and AFM (P3(EO)3T) measurements. (b) TEM image of AuNR-P3(EO)3T@pad hybrid structure, scale bar: 100 nm. (c) TEM image of AuNR-P3(EO)3T@pad hybrid structure with increased gap between the two AuNRs. The bright dot is assigned to P3(EO)3T, scale bar: 50 nm.

For further conductivity measurements, it would be desirable to verify whether electronic or ionic conductivity occurs. Another approach would be to stabilize the polymer filaments against drying by, e.g., cross-linking. For self-assembled polythiophene nanowires, which were used in OFETs, an improved stability upon cross-linking was reported.[282,283] However, the introduction of cross-linking groups requires a modification of the molecular structure and, thus, an elaborate synthesis procedure.

A further option would be to decrease the probability of defects to a minimum. The average size of the grains formed by drying was 340 nm^2. Based on pad15-48, an attachment site pattern was designed providing a size below this value (150 nm^2, Table 4.7). As was discussed before, structures below 100 nm are not reliably contactable by the stationary electrode and the cAFM's tip. For this purpose, two gold nanorods (AuNRs) were introduced as nano-electrodes to contact the P3(EO)3T particle, as illustrated in Figure 4.33a. Using AuNRs as contacts is additionally advantageous for a later application in devices. It is not practical to carry a probe microscope, such as a cAFM, to read out the electrical current flowing through the polymer wire.

The two hetero-objects were organized on the DNA origami template pad15-48 (Figure 4.24d). First, the diblock copolymers P3(EO)3T-b-5(ATT) were attached to the 5(AAT) sites in the middle of pad15-48. Second, AuNRs were added in a 2:1 ratio ([AuNR]:[P3(EO)3T@origami]) to the purified hybrid structures P3(EO)3T@pad yielding the structure AuNR-P3(EO)3T@pad. The AuNRs were functionalized by 18T-ONs. These ONs provided stabilization in the saline buffer solution and enabled the site-specific attachment to the 8A-sites on the pad. The AuNRs were synthesized, functionalized and DNA origami-templated by Dr. Mathias Lakatos (Technische Universität Dresden).

The nanorod-attachment was conducted by a special annealing program, where the solution was heated in multi-cycles from 25 to 40 °C. This enforces the AuNRs to position themselves onto their thermodynamic optimum, which corresponds to hybridize to all accessible attachment sites.[284] The melting temperature of the 5(AAT)-ON (37.2 °C in 300 mM NaCl)[263] is below 40 °C though, which is why the P3(EO)3T-b-5(ATT) could partially melt during the annealing program. After the nanorod attachment, AFM imaging could not identify the P3(EO)3T objects anymore (Appendix, Figure A.11.1a,b) due to the geometry of the tip and the large diameter of the AuNRs (around 10 nm). Therefore, an experiment was conducted to indirectly ensure the stability of the P3(EO)3T@pad structures to the heating. A P3(EO)3T@pad sample without AuNRs was annealed with the same program, and then investigated by AFM imaging (Appendix, Figure A.11.1c,d). The appearance of the P3(EO)3T@pad hybrid structures did not change after the annealing program proving their stability under these conditions up to temperatures of 40 °C.

The target sample AuNR-P3(EO)3T@pad was used without purification due to the low concentration of the sample (< 1 nM). The structure formation was analyzed by TEM imaging, as shown in Figure 4.33b. Further TEM images are given in the Appendix, Figure A.11.2. The formation of the target structure was reasonably high with 74%. However, larger aggregates of AuNRs were neglected for this analysis. Furthermore, 44% of the AuNR-P3(EO)3T@pad structures were twisted on the substrate. It is likely that the twisting is an effect of the immobilization process due to the rather large mass of the AuNRs and the rather soft DNA template. For non-twisted structures, an gap between the two AuNRs of 22.3 ± 7.0 nm ($N = 7$) was measured, which is slightly larger than the design input, and more importantly, the size of the P3(EO)3T particle (15 ± 3 nm). In previous studies it was found, that the gap between such DNA origami-templated AuNRs depends on the length of the AuNRs.[284] For AuNRs smaller than 60 nm, more thermodynamic minima are available, and, thus, an increase of the gap. Measurements of the AuNRs' lengths proved that almost all rods were shorter than 60 nm. For gaps larger than 15 nm, the P3(EO)3T particle would be insufficiently contacted. For further experiments, it is desired to either optimize the AuNRs's length or to adjust the design of the attachment sites.

It was not possible to identify the attached P3(EO)3T in the gap of the AuNRs, neither by TEM nor by AFM imaging. However, for AuNR-P3(EO)3T@pad structures with a larger gap, the polymer was visualized as a bright spot, as displayed in Figure 4.33c. For AuNR@pad structures without P3(EO)3T, these spots were not observed. In the scope of this thesis, these structures were not electrically characterized.

4.3.7 Summary

In the final part of this thesis, the organization of the polythiophene derivative P3(EO)3T into a confined, functional nanostructure was demonstrated. The polythiophene was conjugated to pre-designed oligonucleotides with different sequences yielding the diblock copolymer P3(EO)3T-b-ON. Analyses of the MW evolution confirmed their well-defined, structural composition. It was further found that P3(EO)3T-b-ONs bearing repetitive sequences hybridize faster than non-repetitive sequences.

The site-specific binding of P3(EO)3T-b-ON to densely packed attachment sites on a DNA origami template was confirmed by high-resolution AFM imaging. It was demonstrated that the shape of the resulting P3(EO)3T@origami hybrid structures is programmable by the DNA origami template. The statistical analysis indicated that such organized polythiophenes attract each other and assemble into a supramolecular filament. The attractive interactions were hypothesized as π-π-stacking interactions of the polythiophene backbones. Upon surfactant-induced, gradual reduction of these stacking interactions, the polythiophene's emission was blue-shifted and its maximum intensity was enhanced by a factor of 16. This behavior could be utilized to fine-tune the polymer's optical properties for photonic devices, which would circumvent tedious changes of the chemical structure. Furthermore, these π-π-stacked zones may serve as conducting pathways for an efficient charge carrier transport. This would be required to apply these filaments as electronic functional building block.

The potential of these DNA origami-templated polythiophene filaments as nanowires was assessed by measuring their conductance. However, in the scope of this work, these filaments were found to be non-conducting. Most likely, these supramolecular polymer wires are too defective in their current state.

5 Conclusions and Future Perspectives

5.1 Conclusions

In the scope of this thesis, a new approach was established to organize a functional material - a semiconducting polymer - into a confined, functional nanostructure templated by the DNA origami technique.

To this end in a first step, the synthesis of an end-functionalized, water-soluble polythiophene derivative NH2-P3(EO)3T with custom-tailored chemical and physical properties was established by the *ex-situ* initiated KCTP. Polymers with an adjustable molecular weight and a narrow size distribution were obtained due to the KCTP's quasi-living character. In a second step, this polythiophene was conjugated to end-functionalized oligonucleotides, which differed from each other by their pre-designed sequences, yielding the respective diblock copolymer P3(EO)3T-b-ON. In a third step, a protocol was developed how to template these block copolymers site-specifically on a planar DNA origami structure resulting in the P3(EO)3T@origami hybrid structure. It was demonstrated that such templated polymers form a supramolecular filament atop the DNA origami template guided by attractive interactions. It was evidenced that these attractive interactions are a result of π-π-stacking between the densely packed polythiophene backbones. Furthermore, the versatility and modularity of the DNA origami technique was verified by precisely programming the width and length of the polythiophene filaments by the design of the attachment sites' pattern. These DNA-polythiophene hybrid structures expand the range of functional building blocks towards self-assembled circuits.

Studies on P3(EO)3T as bulk material revealed its optical and electronic functionality. In solution and as a thin film, the polythiophene possessed a strong absorption and emission in the visible region of the electromagnetic spectrum. Both absorption and emission showed a chromic behavior to different external stimuli. Despite its optical functionality, the polythiophene derivative displayed electronic functionality as 2D bulk material. The neat polymer film showed a low conductivity of $1.5 \cdot 10^{-5}\,\mathrm{S\,cm^{-1}}$. However, molecularly doped polymer films revealed an enhanced conductivity up to $5.0 \cdot 10^{-4}\,\mathrm{S\,cm^{-1}}$. Low conformational order as a result of mobile polymer chains was found as a limiting factor for the charge transport mobility and, thus, the conductivity. The hypothesis was verified by an enhanced conductivity $1.0 \cdot 10^{-2}\,\mathrm{S\,cm^{-1}}$ for measurements with minimized influence of long-range disorder.

Further studies addressed the optical and electronic functionality of the P3(EO)3T as a confined, functional nanstructure integrated in the P3(EO)3T@origami. First, the optical functionality of the polythiophene filaments was ascertained by tuning the polymer's fluorescence. By oppressing the interchain interactions of the π-π-stacked polythiophene backbones, it was possible to shift the emission band and at the same time increase its intensity. This surfactochromic behavior can be useful in optical switches or sensing devices. Also for the potential application of the polythiophene filaments as photonic wire, the observed effects might be beneficial. The optical properties could be fine-tuned concerning emitter and/or receiver without elaborate synthesis.

Encouraged by the preceding results, the electronic functionality of the polythiophene filaments was exploited. It was hypothesized, that the π-π-stacked zones provide conducting pathways along the polythiophene backbones. However, in the scope of this thesis, these filaments turned out to be non-conductive. To advance the utilization of these polymer-DNA hybrid structures in electronic circuits, the challenge is to obtain stable, electronically functional P3(EO)3T@origami filaments.

The key findings of this thesis expand the scope of functional structures accessible by DNA-based self-assembly approaches. Additionally, the establishment of a new approach lays the foundation for the assembly of conjugated polymers by the DNA origami technique and can be utilized for future research towards functional polymer-DNA hybrid structures. The customizability of the functional material polythiophene and the modularity of the DNA origami technique will undoubtedly contribute to the bottom-up fabrication of sophisticated devices for electronic or photonic circuits.

5.2 Future Perspectives

This thesis focused on the fundamental establishment of a multi-step protocol towards a functional polymer-DNA based hybrid structure. To obtain reliably assembled devices, each step should be further optimized. It is desired to study polythiophenes with MWs above 20000 $\mathrm{g\,mol^{-1}}$, which hold promise to better charge transport.[48,94] Such high-MW polymers would require further optimization of the *ex-situ* KCTP, such as an additional purification step of the *ex-situ* initiator. Several options exist to advance the design of the polythiophenes further. The side-chain can be used to introduce further functional groups, such as cross-linking groups. Thus, the stability of the polythiophene filaments towards drying could be enhanced.[282] Another possibility would be the incorporation of strong electron accepting groups to obtain polymers with a defined degree of doping.[88] With respect to the attachment of the polythiophenes to the DNA origami template, it might be useful to apply different DNA origami templates, which offer more versatility for the arrangement of the polythiophenes. For example, planar DNA origami structures, which can roll up into tubes,[285] might be useful to enhance the density and stability of the final polymer filaments.

Such improved polythiophene-DNA hybrid structures are desired to be broadly studied concerning their applicability. Polythiophenes are not limited to electronic devices, but have been also used as optical material.[28,86] One potential optical device, as was demonstrated for other DNA origami-templated CPs, would be a photonic wire.[38,39] It might be interesting how efficient such a supramolecular polymer can wire light, since the existing work focuses mainly on single polymer molecules. An advantage towards existing work, would be the ability to fine-tune the polythiophene's emission by changing the intermolecular interactions. Thus, a broader range of possible transmitters/transceivers is accessible without lavishly synthesizing new polymers. Another potential application would be to use the chromic behavior in a optochemical modulator, as was recently demonstrated by Wang *et al.* for conjugated oligomers,[37] or as sensing device.

The electronic functionality of the polythiophene was only demonstrated as bulk material. As mentioned above, there is still plenty of room for improvement to obtain a electronic functional polymer-DNA nanostructure. The polymer could be then utilized as semiconducting material for nanoscaled electronic devices, such as a field-effect transistor. For this purpose, the site-specific deposition of these nanostructures into larger, ordered circuits, in best case on the wafer-level, is desired. As was demonstrated with this work and other reports from literature, DNA nanostructures are ideal breadboards to parallelly arrange multiple hetero-objects with nanometer-precision in a highly parallel manner with basic lab-equipment. However, all investigations done in this thesis, were either conducted in solution or on individual, randomly deposited nanostructures. This missing link towards a broad applicability, is one of the main challenges DNA-based nanotechnology faces at the moment. Only few reports exists, which demonstrate the large-scale immobilization of DNA origami structures into ordered arrays by lithographically patterned substrates.[286,287] Future work requires the combination of DNA nanotechnology and lithography to approach the large-scale. Thus, DNA origami-breadboards could serve as great complement to conventional top-down approaches. They would facilitate the demands on the lithography and, thus, pave the way towards cheaper and faster fabrication of sophisticated circuits.

A Supplementary Information

A.1 Calorimetric Investigation of P3(EO)3T

The polymer batch JZ107 was thermally analyzed by differential scanning calorimetry to determine the glass transition temperature T_g. A T_g of -49°C±7K was obtained. The glass transition of the polymer batch JZ131 was estimated from T_g of the polymer batch JZ107 and by the ratio of the melting temperatures T_m of both polymer batches:

$$T_g(JZ131) = \frac{T_m(JZ131)}{T_m(JZ107)} \cdot T_g(JZ107) \tag{A.1}$$

The measurements were recorded on a DSC Q 2000 device (TA Instruments). Starting from an equilibration temperature of 25°C (for 5 min), the following scanning program was proceeded: ramp with $10°\mathrm{C}\cdot \mathrm{min}^{-1}$ to 80°C kept for 5 min, ramp with $10°\mathrm{C}\cdot \mathrm{min}^{-1}$ to 150°C kept for 5 min, again ramp with $10°\mathrm{C}\cdot \mathrm{min}^{-1}$ to 80°C and isothermal for 5 min and finally ramp with $10°\mathrm{C}\cdot \mathrm{min}^{-1}$ to 150°C and kept for 5 min. T_g was determined by a narrower temperature range from 40 to 80°C.

A.2 H,H-COSY-NMR Spectrum of NH2-P3(EO)3T

The 2D-NMR measurements were conducted and analyzed by Dr. Hartmut Komber (Leibniz-Institut für Polymerforschung Dresden e.V.). The H,H-cosy-NMR spectrum (Figure A.2.1) of NH_2-P3(EO)3T revealed a coupling between the proton of the thiophene backbone **c** and the protons of the sidechain **b** with the protons of the aniline end-group (**d, e, f**). A coupling was found between **b-d**, and **a-c**. Thus, the successful incorporation of the aniline as end-group was demonstrated. The protons of the methyl-group were used for following experiments for the determination of a successful end-group functionalization.

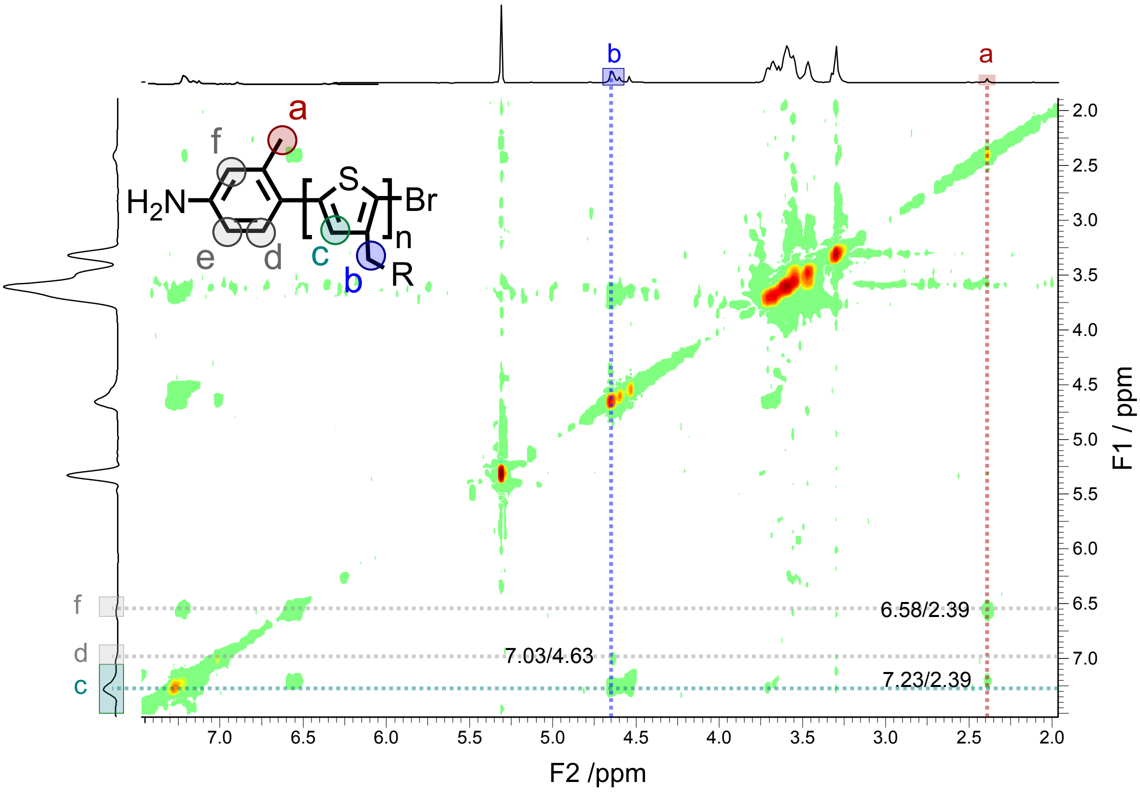

Figure A.2.1: H,H-Cosy-NMR spectrum of NH2-P3(EO)3T (polymer batch JZ19, DP=9).

A.3 UV/VIS Spectra of P3(EO)3T and P3HT

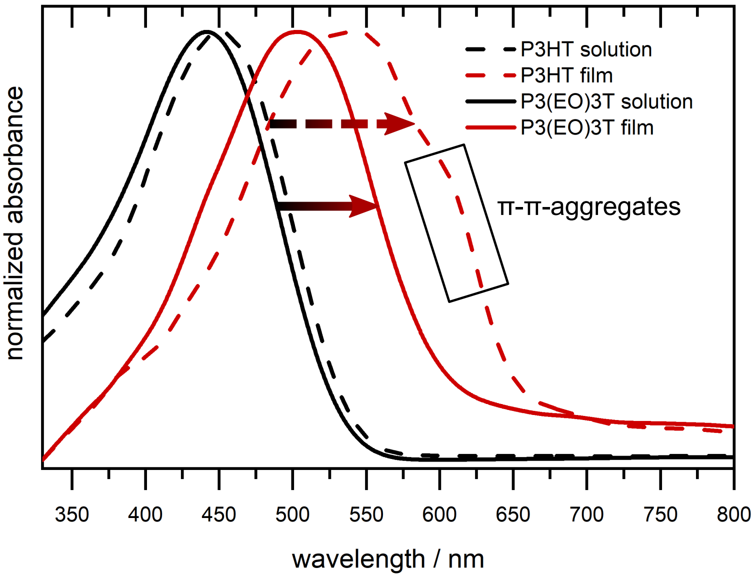

Figure A.3.1: UV/VIS spectra of P3HT (dashed lines) and P3(EO)3T (solid lines) as chloroform solution (black lines) and as thin film (red lines).

A.4 Optical Appearance of Doped P3(EO)3T Films

Figure A.4.1: Photographs of the spin-coated P3(EO)3T thin films at different doping levels.

A.5 Density Function Theory of P3(EO)3T

The calculations were done by Deyan Raychev (Leibniz Institut für Polymerforschung Dresden e.V.) based on DFT/B3LYP/6-31G* (ε=0) and extrapolation.

Table A.5.1: Summary of all energies as a result of DFT calculations of NH2-P3(EO)3T

N (MU)	LUMO / eV / nm	HOMO / eV
1	-0.40	-5.09
2	-1.03	-4.86
4	-1.61	-4.61
∞	-2.04	-4.43

A.6 UV/VIS Spectra of Doped P3(EO)3T in Solution

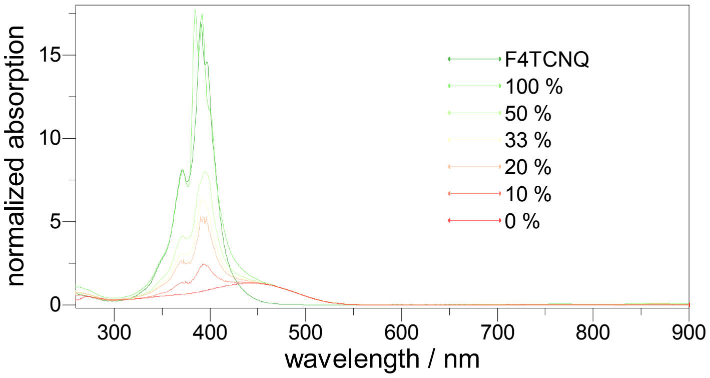

Figure A.6.1: UV/VIS spectra of F4TCNQ and P3(EO)3T in chloroform solution (and addtional acetonitrile) at different dopant concentrations.

A.7 2D GIWAXS Spectra of Doped P3(EO)3T Films

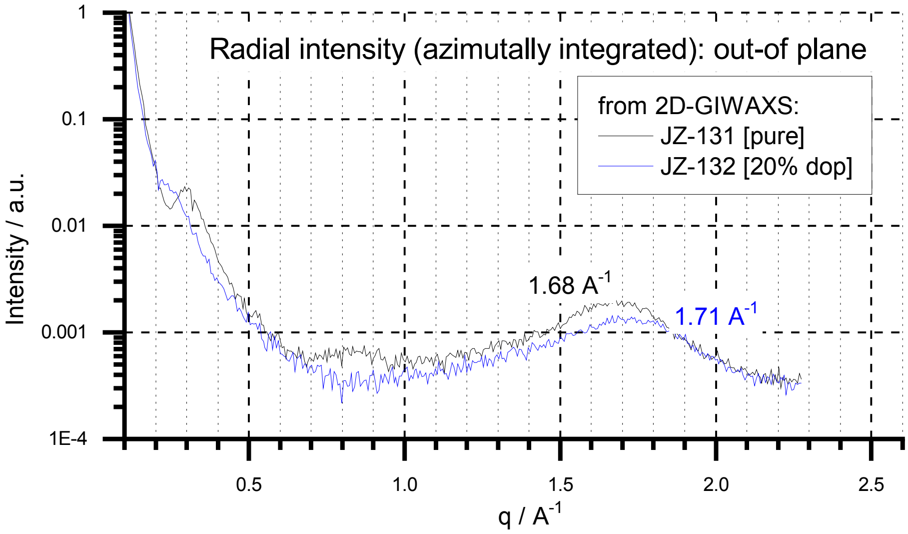

Figure A.7.1: Azimuthally integrated out-of-plane (q$_z$=0) 2D GIWAXS pattern at incident angle of 0.2° of 0% and 20%-doped P3(EO)3T film.

A.8 AFM Images of Doped P3(EO)3T Films

Table A.8.1: Results of the semi-automatic particle (pinholes) analyses of the AFM and SEM images

MDR	**rms / nm** / nm	**N** / µm^2	**ratio area**
0%	1.9±0.6	1.28	0.027
5%	1.3±0.4	0.66	0.010
10%	1.0±0.4	0.54	0.012
13%	1.3±0.8	0.52	0.010
20%	1.3±0.5	0.40	0.011
33%	2.0±1.7	0.09	0.007
50%	2.12±1.6	0.43	0.007
100%	5.30±1.9	0.35	0.024

The roughness parameter root-mean-square (rms) was determined by using the software Gwyddion. Six profile lines were measured per image and the given error is the standard deviation of these values. Z-scan AFM images were analyzed by the particle analyzer of ImageJ to estimate the amount of pinholes. For the doping levels 50 and 33%the results are too high. It results from the particle counting method, which cannot distinguish between F4TCNQ crystals and pinholes.

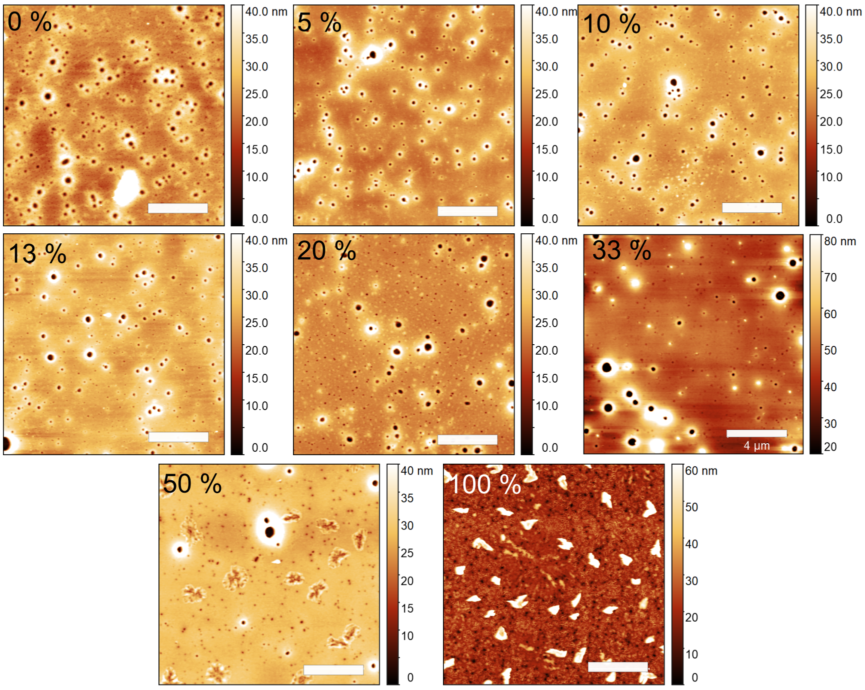

Figure A.8.1: AFM images of doped P3(EO)3T thin films at different doping levels. Scale bars: 4 µm.

A.9 AFM Imaging P3(EO)3T@pad Structures

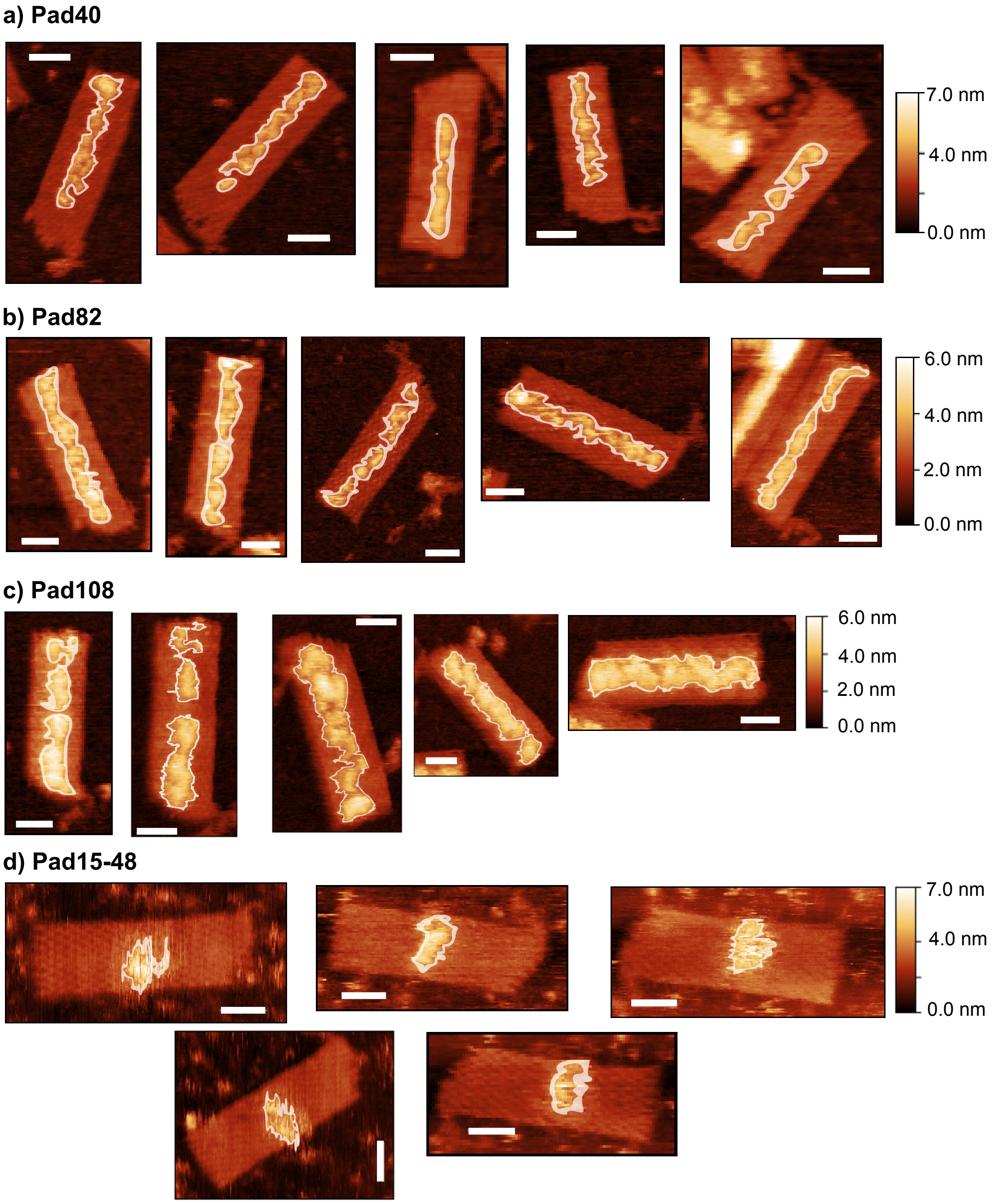

Figure A.9.1: P3(EO)3T paths at (a) pad40, (b) pad82, (c) pad105 and (d) pad15-48, where only P3(EO)3T-b-(ATT)5 was added, scale bars: 30 nm. For each pad-type five hybrid structures with a high attachment yield were analyzed (Table 4.7).

A.10 cAFM Measurements on P3(EO)3T@pad

Table A.10.1: Results of electrical characterization by cAFM of various P3(EO)3T@pad structures.

origami template	polymer batch	doping	additional comments
pad82	14000 g/mol	CN6CPK, solution	10 structures no conductivity
pad82	4900 g/mol	F4TCNQ, gas phase	31 structures no conductivity
pad132	14000 g/mol	CN6CPK, solution	>40 structures no conductivity
pad132	14000 g/mol	F4TCNQ, solution	>40 structures no conductivity

A.11 AuNR-P3(EO)3T@pad

After the AuNR attachment it is not clear whether the P3(EO)3T is still attached to the DNA origami template is not unambigous, as can be seen from the Figure A.11.1a. The slight increase in height could be a result of the geometrical shape of the tip, attached P3(EO)3T or DNA origami substrate. Therefore, the P3(EO)3T@pad structures were treated the same way, as would be applied for the AuNR-attachment. Instead of AuNR water was added. The annealing program was performed for 120 cycles. The stability was tested in the following by high-resolution AFM. The resulting structures were still equipped with P3(EO)3T objects, as apparent from Figure A.11.1c.

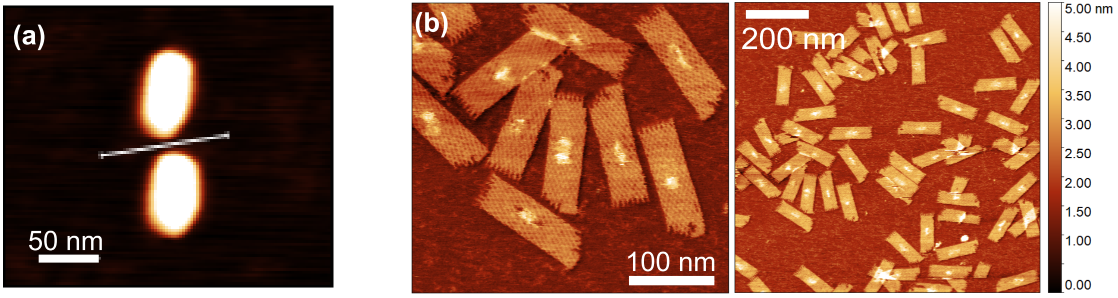

Figure A.11.1: (a) AFM image measured on air AuNR-P3(EO)3T@pad, scale bar: 50 nm. (b) High-resolution AFM image after annealing program, scale bar: 100 nm and 200 nm.

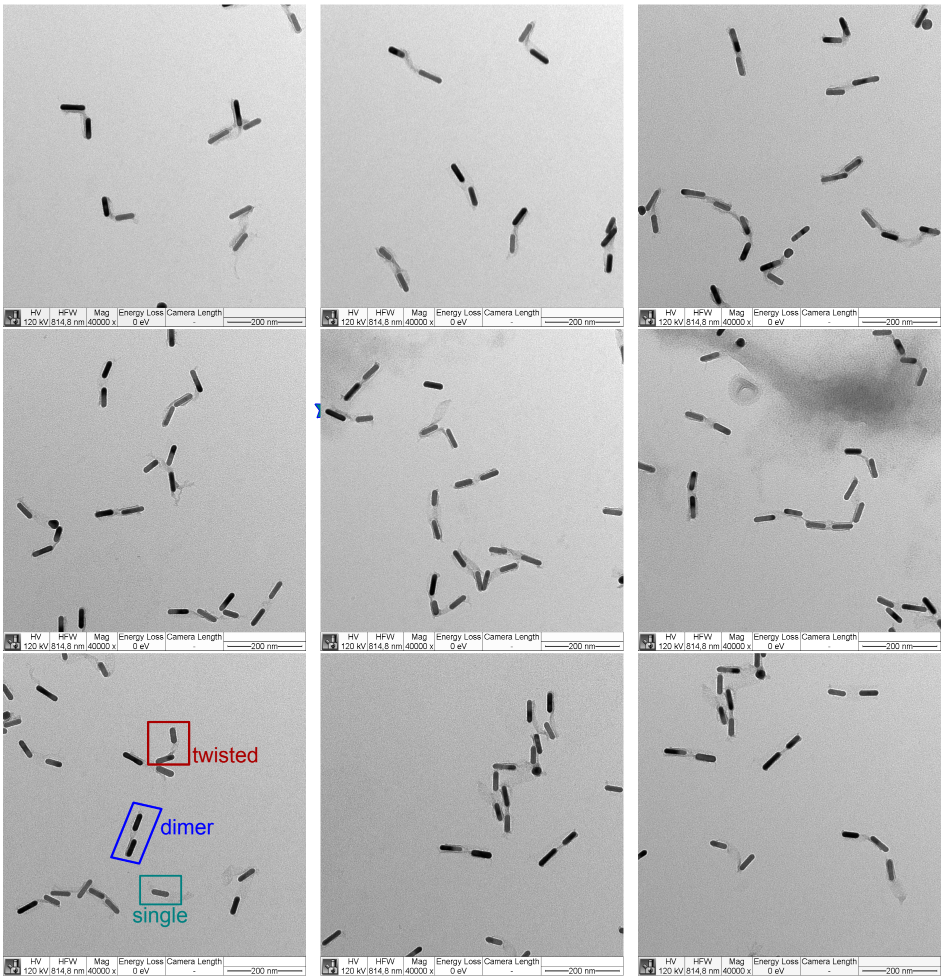

Figure A.11.2: Selection of TEM images of AuNR-P3(EO)3T@pad.

B DNA Origami Sequences

The pad40 design is defined as basic design and contains all staple strands. For the pads pad82, pad105 and pad15-48 only the additional extended staple strands are given. Staple strands are defined by their position where the first number gives the double helices (up → down = 0 → 15) and the number in brackets gives the nucleotide's position (left → right = 29 → 466). Staple extensions are bold.

B.1 DNA Origami Template - pad40

Table B.1.1: Staple strands of pad40.

5'-end	**3'-end**	**sequence**
5[29]	18[40]	GCGCTGGCAAGTGTAGCGG-**8A**
6[127]	19[135]	TGCCTGAGCAACAGAGATAGAACCGAGGTGAG-**8A**
6[159]	19[167]	CAATACTGTAAGAATACGTGGCACCGAACG-**8A**
6[191]	19[199]	AGTCTGTCAATGGCTATTAGTCTTACTGATAG-**8A**
6[223]	19[231]	TTTTTATACTCATAGTTAGCGTAAGTACAAAC-**8A**
6[255]	19[263]	AAAATACGCGTCTTTCCAGACGTTCCCATGTA-**8A**
6[287]	19[295]	TTTTTCATTGTATGGGATTTTGCTTCATTTTC-**8A**
6[319]	19[327]	CAACGGCTTTTCAGCGGAGTGAGACCTCAGAA-**8A**
6[351]	19[359]	GCAGCGAATAAAGGAATTGCGAATGGTTTAGT-**8A**
6[63]	19[71]	AGCCATTGATGGATTATTTACATTGAAAAATC-**8A**
6[95]	19[103]	TGCTGGTACACGACCAGTAATAAACAGTGC-**8A**
7[112]	18[104]	ATTCTGGCTAGAAGAACTCAAACTGTACTATG-**8A**
7[144]	18[136]	CTGAAAGCTCTTTGATTAGTAATAGTGCTTTC-**8A**
7[176]	18[168]	TATTTTTGCATCACGCAAATTAACTAAACAGG-**8A**
7[208]	18[200]	AGACAGCCATCAGTGAGGCCACCGAGGAACGG-**8A**
7[240]	18[232]	AGTTTTGTTAATGCCACTACGAAGAAAACGAA-**8A**
7[272]	18[264]	AATTTTCGAGGAAGTTTCCATTACTCATCT-**8A**
7[29]	20[40]	CTACATTTTGACGCTCAAT-**8A**
7[304]	18[296]	TTCAACAGACAGAGGCTTTGAGGAGCGCGAAA-**8A**
7[336]	18[328]	GAACAACAGACAGCATCGGAACATCGCCTG-**8A**
7[80]	18[72]	CACCAGTCAATATCCAGAACAATACCGCCGCG-**8A**
8[127]	21[135]	GCGGTCAGATAGATTAGAGCCGTCTGGCAATT-**8A**
8[159]	21[167]	AACCACCGAGGATTTAGAAGTAAATTATCA-**8A**
8[191]	21[199]	CCCTAAAAATTCGACAACTCGTATTTGCGGAA-**8A**
8[223]	21[231]	TACAACGCACGTTATTAATCCTCATAAATTTT-**8A**
8[255]	21[263]	CCGTAACAAAGCGCAGTCTCTGAATCAGACGA-**8A**
8[287]	21[295]	AGGGATAGGCGTCATACATGGCTTGCCGCCAG-**8A**
8[319]	21[327]	CCGCCACCGTACTGGTAATAAGTTCAGAGCCG-**8A**
8[351]	21[359]	ACCGCCACCTTGAGTAACAGTGCCCTCAGAAC-**8A**

start	**end**	**sequence**
8[63]	21[71]	TAAAGCATAATCAACAGTTGAAAGACCTACCA-**8A**
8[95]	21[103]	CACGCTGTCTAAAATATCTTTAGATTATAC-**8A**
9[112]	20[104]	AACAACTATATTAACACCGCCTGCAAAGGGAC-**8A**
9[144]	20[136]	ATACATTTAGCAGAAGATAAAACACTTCTGAC-**8A**
9[176]	20[168]	TACAAACACATCGCCATTAAAAATACAGACAA-**8A**
9[208]	20[200]	TTGCCCGACTGTAGCATTCCGCGATAATGCAC-**8A**
9[240]	20[232]	AGAATGGACTGAGTTTCGTCACCACGATCTAA-**8A**
9[272]	20[264]	TCCAGTAACAAGCCCAATAGGAAAGTAAATG-**8A**
9[304]	20[296]	ACAGGAGTCTCAGAGCCACCACCCAAACAACT-**8A**
9[336]	20[328]	GTCAGTGCCCTCAGAACCGCCACATAGAAAG-**8A**
9[80]	20[72]	GAAGGTTAAGAGCCAGCAGCAAATGGCAGATT-**8A**
0[103]	2[96]	CTGGCGAAAGGGGGACCGAGCTCGAATTCGTTCACCAG
0[135]	2[128]	GATCGGTGCGGGCCTCTGTTTCCTGTGTGAAATTTGCGTA
0[167]	2[160]	CCATTCAGGCTGCGCATTCCACACAACATAAATGAATC
0[199]	2[192]	CTGGTGCCGGAAACCAAGTGTAAAGCCTGGGGCCAGTCGG
0[231]	2[224]	TCGCACTCCAGCCAGCTAACTCACATTAGGTCATAAGAAT
0[263]	2[256]	AGGGGACGACGACAGTTAGAGCTTAATTGCTGGGATTAGA
0[295]	2[288]	GGCGCATCGTAACCGTCTCAACATGTTTTAAAAACCAGAC
0[327]	2[320]	CCGTAATGGGATAGGTGGTGTCTGGAAGTTTCAAATATCG
0[359]	2[352]	GGATTCTCCGTGGGAATGATTCCCAATTCTGCAAAAAGAT
0[423]	2[416]	CGCGTCTGGCCTTCCTAATAACCTGTTTAGCTCCATAAAT
0[471]	2[448]	TACACTTACTAATAGTAGTAGCATTATAGG AACCGCGAGCTGAAAAGGTAATGCTTT
0[71]	2[64]	TAAGTTGGGTAACGCCCCTGCAGGTCGACTCTCCTTCACC
00[391]	2[384]	CAACATTAAATGTGAGTTTGACCATTAGATACCTATTATA
01[112]	0[104]	GTCATAGCTTCGCTATTACGCCAG
01[144]	0[136]	CGCTCACAAACTGTTGGGAAGGGC
01[176]	0[168]	AAGCATAAGGCAAAGCGCCATTCG
01[208]	0[200]	GAGTGAGCTTTCCGGCACCGCTT
01[240]	0[232]	GGATGGCTATCGGCCTCAGGAAGA
01[272]	0[264]	GCTGTAGGCATCTGCCAGTTTG
01[304]	0[296]	TAAAGTACCACGTTGGTGTAGATG
01[336]	0[328]	TAACAGTCAAACGGCGGATTGA
01[36]	0[36]	GCCAGTGCCAAGCTTGCATGAGGGTTTTCCCAGTCACGAC
01[368]	0[360]	AGATTTAGCGAGTAACAACCCGTC
01[400]	0[392]	AATGGTCGTAGCCAGCTTTCAT
01[432]	0[424]	ATTTGGGGGCCATCAAAAATAATT
01[80]	0[72]	CCCGGGTATGTGCTGCAAGGCGAT
02[127]	4[128]	TTGGGCGCGGGTTGAGTGTTGTTCACTAAATC
02[159]	4[160]	GGCCAACTCCACTATTAAAGAACAAGTTTT
02[191]	4[192]	GAAACCTGAAAGGGCGAAAAACCGCGATGGCC
02[223]	4[224]	TGCGTTGCATTACAGGTAGAAAGAAAATCTAC
02[255]	4[256]	GAGTACCTTAGGAATACCACATTCGCTCATTA
02[287]	4[288]	CGGAAGCAATAACGCCAAAAGGAATGTGAATT
02[319]	4[320]	CGTTTTAAGAGCAACACTATCATAGCTTGAGA
02[351]	4[352]	TAAGAGGAACGACGATAAAAACCAACGAGAAA
02[383]	4[384]	GTCAGAAGTTGCAAAAGAAGTTTTAGCTGCTC
02[415]	4[416]	CAAAAATCAGTAAAATGTTTAGACCGGATATT
02[447]	4[448]	AAACAGTTCTGCGGAATCGTCATATGACCTTC
02[471]	1[471]	TACACTAATCCCCCTCAGGCATCAATTCTACACT

start	**end**	**sequence**
02[63]	4[64]	GCCTGGCCCTGTTTGATGGTGGTTGGCGAGAA
02[95]	4[96]	TGAGACGCCCTTATAAATCAAATTAGAGCT
03[112]	1[111]	CCGAGATACAGGGTGGTTTTTCTTTAATCATG
03[144]	1[143]	AACAAGAGGCGCGGGGAGAGGCGGTTGTTATC
03[176]	1[175]	CCAACGTCTCGTGCCAGCTGCATTCGAGCCGG
03[208]	1[207]	ACAACATTGCTCACTGCCCGCTTTTGCCTAAT
03[240]	1[239]	TTGAGATTTTAATTGCTCCTTTTGATTTTTGC
03[272]	1[271]	CAGATACAACTCCAACAGGTCAAATATAAT
03[304]	1[303]	CATAGTAATTCGAGCTTCAAAGCGTATGCAAC
03[336]	1[335]	TTACCAGAGCCCGAAAGACTTCATTCCATA
03[36]	2[36]	TGCCCCAGCAGGCGAAAATCCTGAGAGAGTTGCAGCAAGC
03[368]	1[367]	AGAGGCTTCAAAGCGGATTGCATCGAACGAGT
03[400]	1[399]	GGGTAATAGGTCTTTACCCTGAATTTCGCA
03[432]	1[431]	GTCCAATACAGAAAACGAGAATGAATATTTTC
03[80]	1[79]	GGCAAAATGGCAACAGCTGATTGCAGAGGATC
04[127]	6[128]	GGAACCCTGACGAGCACGTATAACACATCACT
04[159]	6[160]	TTGGGGTAATCAGAGCGGGAGCCGTTGTAG
04[191]	6[192]	CACTACGTTAAAGGGATTTTAGACAGTAAAAG
04[223]	6[224]	GTTAATAAAATCCTGAGAAAACCTGCACCGTG
04[255]	6[256]	TACCAGTCAAGAATACACTAAAACAAACGGGT
04[287]	6[288]	ACCTTATGCCAGCGATTATACCAACTAAAGAC
04[319]	6[320]	TGGTTTAAAACGGAGATTTGTATCGAGGGTAG
04[351]	6[352]	CACCAGAAGTGTCGAAATCCGCGACACCCTCA
04[383]	6[384]	ATTCAGTGTAGCCGGAACGAGGCGCAGGGAGT
04[415]	6[416]	CATTACCCAAGGGAACCGAACTGACATAACCG
04[447]	6[448]	ATCAAGAGACAGATGAACGGTGTATGCGCCGA
04[471]	3[471]	TACACTCATAGGCTGGCAATATTCATTGTACACT
04[63]	6[64]	AGGAAGGGCGCGTAACCACCACACTTACCGCC
04[95]	6[96]	TGACGGGGCCGCTACAGGGCGCATCGGCCT
05[112]	3[111]	GTTGCTTTAAAGGGAGCCCCCGATAGAATAGC
05[144]	3[143]	CTCGTTAGCGAGGTGCCGTAAAGCCAGTTTGG
05[176]	3[175]	AGGCCGATGAACCATCACCCAAATCGTGGACT
05[208]	3[207]	TACGCCAGAACGAACTAACCAGGGTCTATGGA
05[240]	3[239]	AGAGGCAAAGGACGTTGGGAAGAATTCATCAG
05[272]	3[271]	TTGACCCCGATTTTAAGAACTGAACTAATG
05[304]	3[303]	CAAAGTACTTTCAACTTTAATCATTTACGAGG
05[336]	3[335]	ATAAATTCGAGTAGTAAATTGGACCCTCGT
05[368]	3[367]	ATGTTACTAATAAGGCTTGCCCTGAAATAGCG
05[400]	3[399]	CAATCATAAATCAACGTAACAAGCCAGAGG
05[432]	3[431]	GAAAGAGGTAATCTTGACAAGAACTGGATAGC
05[48]	4[36]	TCACGCTGAAGAAAGCGAAAGGAGCGGG
05[80]	3[79]	CTTAATGCGAAAGCCGGCGAACGTCCGAAATC
06[383]	8[384]	TAAAGGCCTGAAAATCTCCAAAAAAGCCCGGA
06[415]	8[416]	ATATATTCAGCCTTTAATTGTATCTAAGTGCC
06[447]	7[471]	CAATGACATTCGAGGTGAATTTCTTAAACAGCTTGTACACT
06[471]	5[471]	TACACTATACCGATAGTCAGACCAGGCGTACACT
07[368]	5[367]	TTTCACGTGCTTTTGCGGGATCGTCCTGCTCC
07[400]	5[399]	CAAAAGGGGTCGCTGAGGCTTGCAGACGGT
07[432]	5[431]	AGCTTGCTACAACCATCGCCCACGCCAACTTT
07[48]	6[36]	CGTCTGAACAACAGGAAAAACGCTCATG
08[383]	10[384]	ATAGGTGTGCCCCCTGCCTATTTCCACCGGAA

5’-end	**3’-end**	**sequence**
08[415]	10[416]	GTCGAGAGGAAACATGAAAGTATTTTCATAAT
08[460]	9[460]	TACACTGATTAGCGGGGTTTTGTCAAGAGAAGGATTAGTACACT
09[36]	8[36]	CAATATCTGGTCAGTTGGCACACCTTGCTGAACCTCAAAT
09[368]	7[367]	CAGTTAATATCACCGTACTCAGGAAATAATTT
09[400]	7[399]	ATTATTCTGGTTGATATAAGTATAAAGGCTC
09[432]	7[431]	GAGACTCCCTCAGTACCAGGCGGAGGTTTATC
10[127]	12[128]	CATCAATATGCTTTGAATACCAAGATAAATCA
10[159]	12[160]	TCATATTAGGCGAATTATTCATTTTGAATT
10[191]	12[192]	CAAAGAAAAAAGAAGATGATGAAAGAAAACAA
10[223]	12[224]	AAAAGTTTATTGACGGAAATTATTAGGGCGAC
10[255]	12[256]	TTGGCCTTTCACCGTCACCGACTATTCATA
10[287]	12[288]	CATTGACATAGAGCCAGCAAAATCGAATAAGT
10[319]	12[320]	CCACCAGCCATTAGCAAGGCCGCAACATAT
10[351]	12[352]	CGCCACCCAACCATCGATAGCAGCAGCAAACG
10[383]	12[384]	CCGCCTCACAGAATCAAGTTTGATGATTAA
10[415]	12[416]	CAAAATCAGTAGCGCGTTTTCATCGCAATAAT
10[449]	9[431]	TACACTCTTATTAGCGTTTGCCATCTTAAGAGGCT
10[63]	12[64]	TATCAAAATCAGATGAATATACAGCCTTAGAA
10[95]	12[96]	TTCTGAAATCGGGAGAAACAATTTCTGTAA
11[112]	9[111]	CGCCTGATTAATCCTGATTGTTTGGGAGCACT
11[144]	9[143]	TCGCGCAGCCTGATTATCAGATGAAATAGATA
11[176]	9[175]	CCTGAGCACCACCAGAAGGAGCGGTTAGACTT
11[208]	9[207]	AGGTAAATGAGTAACATTATCATTTAAATCCT
11[240]	9[239]	GTGAATTAGATATTCACAAACAAATTAAAGCC
11[272]	9[271]	TTGGGAATGGAGGTTGAGGCAGGTTTACCGT
11[304]	9[303]	CACCATTAAACCACCACCAGAGCCTTGATGAT
11[336]	9[335]	ACCAATGATCAGAGCCACCACCCTTTAACGGG
11[36]	10[36]	GTAGATTTTCAGGTTTAACGTTATTTGCACGTAAAACAGA
11[368]	9[367]	CAGTAGCGCCTCAGAGCCGCCACCCGTATAAA
11[400]	9[399]	GTCAGACTCCGGAACCAGAGCCACGGAACCT
11[424]	11[449]	GGCATTTTCGGTCATAGCCCCTACACT
11[80]	9[79]	CCTTTTACTAATGGAAGGGTTAGAGAATTGAG
12[127]	14[128]	ATATATGTTGTAAATGCTGATGCATACAAATT
12[159]	14[160]	ACCTTTTAAAGAACGCGAGAAAAGAAAAAG
12[191]	14[192]	AATTAATTTTTAGTTAATTTCATCAAATAAGA
12[223]	14[224]	ATTCAACCATGGTTTGAAACAGGGAAAAATAC
12[255]	14[256]	TGGTTTACAGAATTAACTGAACACGAAAATAG
12[287]	14[288]	TTATTTTGGGGTAATTGAGCGCTATAAGAAAC
12[319]	14[320]	AAAAGAAACCCACAAGAATTGAGTTAAACAGC
12[351]	14[352]	TAGAAAATAGCAAGAAACAATGAATCTTTCCA
12[383]	14[384]	GACTCCTTTTACCGAAGCCCTTTTTTATCCTG
12[415]	13[423]	AACGGAATATAGCCGAACAAAGTT
12[439]	13[439]	TACACTACCGAGGAAACACCAGAAGGAATACACT
12[63]	14[64]	TCCTTGAAAAAATCATAGGTCTGATTAACAAC
12[95]	14[96]	ATCGTCGCCTCCGGCTTAGGTTAACAGTAG
13[112]	11[111]	TAACTATAGAGTGAATAACCTTGCAACGGATT
13[144]	11[143]	CGCAAGACTTAATGGAAACAGTACTTACAAAA
13[176]	11[175]	AAATATATACATTTAACAATTTCATTCAATTA
13[208]	11[207]	TAAATTTAGATTGAGGGAGATCAACAAACGGA
13[240]	11[239]	TAGACGGGCAGCGCCAAAGACAAACATTAAAG
13[272]	11[271]	AAGTCAGATCACAATCAATAGAAATGAGCCAT

5'-end	**3'-end**	**sequence**
13[304]	11[303]	AGAGATAACGCAAAGACACCACGACCAGTAG
13[336]	11[335]	ATAATAAGACATACATAAAGGTGGGAAACGTC
13[36]	12[36]	GAGTCAATAGTGAATTTATCAACATAGCGATAGCTTAGAT
13[368]	11[367]	AGCTATCATTACGCAGTATGTTACCGTAAT
13[400]	11[399]	GTAAGCAGACCCAAAAGAACTGGCCCTTTAGC
13[80]	11[79]	CTTTTTAACTATTAATTAATTTTCTAACAGTA
14[127]	15[135]	CTTACCAGGCGCCTGTTTATCAAC
14[159]	15[167]	CCTGTTTACAAGAAAAATAATA
14[191]	15[199]	ATAAACACGAGCATGTAGAAACCA
14[223]	15[231]	CGACCGTGCTTTCCTTATCATTC
14[255]	15[263]	CAGCCTTTACCAAGTACCGCACTC
14[287]	15[295]	GATTTTTTCCGTTTTTATTTTCAT
14[319]	15[327]	CATATTATCGCGCCCAATAGCAAG
14[351]	15[359]	GAGCCTAAGGCTTATCCGGTATTC
14[383]	15[391]	AATCTTACTTTTAGCGAACCTCCC
14[428]	15[428]	TACACTGATTAGTTGCTATTTTTGAAGCCTTAAATCAATACACT
14[63]	15[71]	GCCAACATCAAAAGGTAAAGTAAT
14[95]	15[103]	GGCTTAACAATAAACAACATGT
15[104]	13[111]	TCAGCTAATGCAGAACTATAAAGCCAACGCTCGGGTTATA
15[136]	13[143]	AATAGATAAGTCCTGAAGTATCATATGCGTTAAATCCAAT
15[168]	13[175]	TCCCATCCTAATTTACCGGAATCATAATTACTACTTTTTC
15[200]	13[207]	ATCAATAATCGGCTGTTGATAAATAAGGCGTTTTCTGACC
15[232]	13[239]	CAAGAACGGGTATTAAACAGAGAGAATAACATAAGCGCAT
15[264]	13[271]	ATCGAGAACAAGCAAGGTTTAACGTCAAAAATCCTGAACA
15[296]	13[303]	CGTAGGAATCATTACTTATCCCAATCCAAAATATCAG
15[328]	13[335]	CAAATCAGATATAGAATTTGCCAGTTACAAAATAAGCCCA
15[36]	14[36]	AAGAGAATATAAAGTACCGAGTAATTTAGGCAGAGGCATT
15[360]	13[367]	TAAGAACGCGAGGCGCAACGCTAACGAGCGATAGCAAT
15[392]	13[399]	GACTTGCGGGAGGTTTGCACCCAGCTACAATTTAAGAAAA
15[72]	13[79]	TCTGTCCAGACGACGATTGAGAATCGCCATATGAGACTAC

B.2 DNA Origami Template - pad82

Table B.2.1: Staple strands of pad82.

5'-end	**3'-end**	**sequence**
03[48]	25[48]	CGAAAATCCTGAGAGAGTTGCA-**8A**
03[26]	16[40]	TACACGCTGGTTTGCCCCAGCAGG-**8A**
03[48]	25[48]	CGAAAATCCTGAGAGAGTTGCA-**8A**
04[127]	23[135]	GGAACCCTGACGAGCACGTATAACACATCACT-**8A**
04[159]	23[167]	TTGGGGTAATCAGAGCGGGAGCCGTTGTAG-**8A**
04[191]	23[199]	CACTACGTTAAAGGGATTTTAGACAGTAAAAG-**8A**
04[223]	23[231]	GTTAATAAAATCCTGAGAAAACCTGCACCGTG-**8A**
04[255]	23[263]	TACCAGTCAAGAATACACTAAAACAAACGGGT-**8A**
04[287]	23[295]	ACCTTATGCCAGCGATTATACCAACTAAAGAC-**8A**
04[319]	23[327]	TGGTTTAAAACGGAGATTTGTATCGAGGGTAG-**8A**
04[351]	23[359]	CACCAGAAGTGTCGAAATCCGCGACACCCTCA-**8A**

5'-end	**3'-end**	**sequence**
04[383]	23[391]	ATTCAGTGTAGCCGGAACGAGGCGCAGGGAGT-**8A**
04[415]	23[423]	CATTACCCAAGGGAACCGAACTGACATAACCG-**8A**
04[63]	23[71]	AGGAAGGGCGCGTAACCACCACACTTACCGCC-**8A**
04[95]	23[103]	TGACGGGGCCGCTACAGGGCGCATCGGCCT-**8A**
06[383]	19[391]	TAAAGGCCTGAAAATCTCCAAAAAAGCCCGGA-**8A**
06[415]	19[423]	ATATATTCAGCCTTTAATTGTATCTAAGTGCC-**8A**
07[400]	18[392]	CAAAAGGGGTCGCTGAGGCTTGCAGACGGT-**8A**
07[432]	18[424]	AGCTTGCTACAACCATCGCCCACGCCAACTTT-**8A**
07[48]	23[48]	CGTCTGAACAACAGGAAAAACG-**8A**
08[383]	21[391]	ATAGGTGTGCCCCCTGCCTATTTCCACCGGAA-**8A**
08[415]	21[423]	GTCGAGAGGAAACATGAAAGTATTTTCATAAT-**8A**
09[26]	22[40]	TACACTCCCTCAATCAATATCTGGTC-**8A**
09[368]	20[360]	CAGTTAATATCACCGTACTCAGGAAATAATTT-**8A**
09[400]	20[392]	ATTATTCTGGTTGATATAAGTATAAAGGCTC-**8A**
09[432]	20[424]	GAGACTCCCTCAGTACCAGGCGGAGGTTTATC-**8A**
09[48]	19[48]	AGTTGGCACACCTTGCTGAACC-**8A**
10[449]	22[424]	TACACTCCTTATTAGCGTTTGCCATCTTAAGAGGCT-**8A**
11[112]	22[104]	CGCCTGATTAATCCTGATTGTTTGGGAGCACT-**8A**
11[144]	22[136]	TCGCGCAGCCTGATTATCAGATGAAATAGATA-**8A**
11[176]	22[168]	CCTGAGCACCACCAGAAGGAGCGGTTAGACTT-**8A**
11[208]	22[200]	AGGTAAATGAGTAACATTATCATTTAAATCCT-**8A**
11[240]	22[232]	GTGAATTAGATATTCACAAACAAATTAAAGCC-**8A**
11[26]	24[40]	TACACAAATTGCGTAGATTTTCAG-**8A**
11[272]	22[264]	TTGGGAATGGAGGTTGAGGCAGGTTTACCGT-**8A**
11[304]	22[296]	CACCATTAAACCACCACCAGAGCCTTGATGAT-**8A**
11[336]	22[328]	ACCAATGATCAGAGCCACCACCCTTTAACGGG-**8A**
11[368]	22[360]	CAGTAGCGCCTCAGAGCCGCCACCCGTATAAA-**8A**
11[400]	22[392]	GTCAGACTCCGGAACCAGAGCCACGGAACCT-**8A**
11[48]	21[48]	GTTTAACGTTATTTGCACGTAA-**8A**
11[80]	22[72]	CCTTTTACTAATGGAAGGGTTAGAGAATTGAG-**8A**
13[368]	24[360]	AGCTATCATTACGCAGTATGTTACCGTAAT-**8A**

B.3 DNA Origami Template - pad105

Table B.3.1: Staple strands of pad105.

5'-end	**3'-end**	**sequence**
05[208]	3[207]	TACGCCAGAACGAACTAACCAGGGTCTATGGA-**8A**
05[112]	3[111]	GTTGCTTTAAAGGGAGCCCCCGATAGAATAGC-**8A**
05[144]	3[143]	CTCGTTAGCGAGGTGCCGTAAAGCCAGTTTGG-**8A**
05[176]	3[175]	AGGCCGATGAACCATCACCCAAATCGTGGACT-**8A**
05[240]	3[239]	AGAGGCAAAGGACGTTGGGAAGAATTCATCAG-**8A**
05[272]	3[271]	TTGACCCCGATTTTAAGAACTGAACTAATG-**8A**
05[304]	3[303]	CAAAGTACTTTCAACTTTAATCATTTACGAGG-**8A**
05[336]	3[335]	ATAAATTCGAGTAGTAAATTGGACCCTCGT-**8A**
05[368]	3[367]	ATGTTACTAATAAGGCTTGCCCTGAAATAGCG-**8A**
05[400]	3[399]	CAATCATAAATCAACGTAACAAGCCAGAGG-**8A**

5'-end	**3'-end**	**sequence**
05[432]	3[431]	GAAAGAGGTAATCTTGACAAGAACTGGATAGC-**10A**
05[48]	27[48]	TCACGCTGAAGAAAGCGAAAGG-**10A**
05[80]	3[79]	CTTAATGCGAAAGCCGGCGAACGTCCGAAATC-**10A**
10[127]	12[128]	CATCAATATGCTTTGAATACCAAGATAAATCA-**10A**
10[159]	12[160]	TCATATTAGGCGAATTATTCATTTTGAATT-**10A**
10[191]	12[192]	CAAAGAAAAAAGAAGATGATGAAAGAAAACAA-**10A**
10[223]	12[224]	AAAAGTTTATTGACGGAAATTATTAGGGCGAC-**10A**
10[255]	12[256]	TTGGCCTTTCACCGTCACCGACTATTCATA-**10A**
10[287]	12[288]	CATTGACATAGAGCCAGCAAAATCGAATAAGT-**10A**
10[319]	12[320]	CCACCAGCCATTAGCAAGGCCGCAACATAT-**10A**
10[351]	12[352]	CGCCACCCAACCATCGATAGCAGCAGCAAACG-**10A**
10[383]	12[384]	CCGCCTCACAGAATCAAGTTTGATGATTAA-**10A**
10[415]	12[416]	CAAAATCAGTAGCGCGTTTTCATCGCAATAAT-**10A**
10[63]	12[64]	TATCAAAATCAGATGAATATACAGCCTTAGAA-**10A**
10[95]	12[96]	TTCTGAAATCGGGAGAAACAATTTCTGTAA-**10A**

B.4 DNA Origami Template - pad15-48

Table B.4.1: Staple strands of pad15-48.

5'-end	**3'-end**	**sequence**
05[29]	18[40]	GCGCTGGCAAGTGTAGCGG-**8A**
06[383]	19[391]	TAAAGGCCTGAAAATCTCCAAAAAAGCCCGGA-**8A**
06[415]	19[423]	ATATATTCAGCCTTTAATTGTATCTAAGTGCC-**8A**
06[63]	19[71]	AGCCATTGATGGATTATTTACATTGAAAAATC-**8A**
07[29]	20[40]	CTACATTTTGACGCTCAAT-**8A**
07[400]	18[392]	CAAAAGGGGTCGCTGAGGCTTGCAGACGGT-**8A**
07[432]	18[424]	AGCTTGCTACAACCATCGCCCACGCCAACTTT-**8A**
07[80]	18[72]	CACCAGTCAATATCCAGAACAATACCGCCGCG-**8A**
08[383]	21[391]	ATAGGTGTGCCCCCTGCCTATTTCCACCGGAA-**8A**
08[415]	21[423]	GTCGAGAGGAAACATGAAAGTATTTTCATAAT-**8A**
08[63]	21[71]	TAAAGCATAATCAACAGTTGAAAGACCTACCA-**8A**
09[40]	19[39]	ATCTGGTCAGTTGGCACACCTTGCTGAACCTCAAATATCA-**8A**
09[400]	20[392]	ATTATTCTGGTTGATATAAGTATAAAGGCTC-**8A**
09(432)	20[424]	GAGACTCCCTCAGTACCAGGCGGAGGTTTATC-**8A**
09(80)	20(72)	GAAGGTTAAGAGCCAGCAGCAAATGGCAGATT-**8A**
11(40)	21(39)	ATTTTCAGGTTTAACGTTATTTGCACGTAAAACAGAAATA-**8A**

5'-end	**3'-end**	**sequence**
0[231]	23[231]	TCGCACTCCAGCCAGCTAACTCACATTAGGTCATAAGAATAAAG-**5(AAT)**
02[223]	25[231]	TGCGTTGCATTACAGGTAGAAAGAAAATCTACAAAG-**5(AAT)**
02[255]	25[263]	GAGTACCTTAGGAATACCACATTCGCTCATTAAAAG-**5(AAT)**
04[223]	27[231]	GTTAATAAAATCCTGAGAAAACCTGCACCGTGAAAG-**5(AAT)**
05[208]	16[200]	TACGCCAGAACGAACTAACCAGGGTCTATGGAAAAG-**5(AAT)**
05[240]	16[232]	AGAGGCAAAGGACGTTGGGAAGAATTCATCAGAAAG-**5(AAT)**
06[223]	19[231]	TTTTTATACTCATAGTTAGCGTAAGTACAAACAAAG-**5(AAT)**
07[240]	18[232]	AGTTTTGTTAATGCCACTACGAAGAAAACGAAAAAG-**5(AAT)**
08[223]	21[231]	TACAACGCACGTTATTAATCCTCATAAATTTTAAAG-**5(AAT)**
09[240]	20[232]	AGAATGGACTGAGTTTCGTCACCACGATCTAAAAAG-**5(AAT)**
10[223]	17[231]	AAAAGTTTATTGACGGAAATTATTAGGGCGACAAAG-**5(AAT)**
11[240]	24[232]	GTGAATTAGATATTCACAAACAAATTAAAGCCAAAG-**5(AAT)**
13[208]	26[200]	TAAATTTAGATTGAGGGAGATCAACAAACGGAAAAG-**5(AAT)**
13[240]	26[232]	TAGACGGGCAGCGCCAAAGACAAACATTAAAGAAAG-**5(AAT)**
15[232]	28[232]	CAAGAACGGGTATTAAACAGAGAGAATAACATAAGCGCATAAAG-**5(AAT)**

Abbreviations

1D	one dimensional
2D	two dimensional
3D	three dimensional
A	adenine
ACN	acetonitrile
AFM	atomic force microscopy
AF4	asymmetric flow field-flow fractionation
Ar	Aryl
ATR-FTIR	attenuated total reflection Fourier-transform infrared spectroscopy
AuNRs	gold nanorods
bp	base pair
bpy	2,2'-bipyridine
n-**BuLi**	*n*-buthyllithium
C	cytosine
cAFM	conductive atomic force microscopy
CP	π-conjugated polymer
CN6CPK	potassium hexacyano-substituted [3]-radialene radical anion
CT	charge transfer
CTX	ground-state charge transfer
CV	cyclic voltammetry
DDAO	*N*,*N*-dimethyldodecylamine *N*-oxide
DF	degree of functionalization
DFT	density functional theory
DP	degree of polymerization
DLS	dynamic light scattering
DMSO	dimethyl sulfoxide
DNA	deoxyribonucleic acid
DP	degree of polymerization
EA	electron affinity
F4TCNQ	2,3,5,6-tetrafluoro-7,7,8,8-tetracyanoquinodimethane
FFT	fast Fourier transform
FWHM	full width at half maximum
G	guanine
GIWAXS	grazing-incident wide-angle X-ray scattering
GPC	gel permeation chromatography
HH	head-to-head

HOMO	highest occupied molecular orbital
HT	head-to-tail
IE	ionization energy
IPA	ion pair
IRAV	infrared active vibrational
$I - V$	current-voltage
KCTP	Kumada catalyst-transfer polycondensation
LUMO	lowest unoccupied molecular orbital
MALS	multi-angle light scattering
MDR	molecular doping ratio
MU	monomer unit
MUTEG	(11-mercapto undecyl)tetra(ethylene glycol)
MW	molecular weight
N	random nucleotide
NMR	nuclear magnetic resonant spectroscopy
OFET	organic field effect transistor
OLED	organic light emitting diode
ON	oligodeoxynucleotide
P3HT	poly(3-hexylthiophene)
P3RT	poly(3'-substituted thiophene)
PEDOT	poly(3,4-ethylenedioxythiophene)
PAGE	polyacrylamide gel
RI	refractive index
rms	root mean square
SPR	surface plasmon resonance spectroscopy
T	thymine
TCNQ	tetracyanoquinodimethane
TEM	transmission electron microscopy
TMS	trimethylsilyl
TT	tail-to-tail
VASE	Variable angle spectroscopic ellipsometry
WAXS	wide-angle X-ray scattering

List of Symbols

A	cross-section area
α	mean orientation angle (ellipsometry)
c	velocity of light
d	interlayer distance
δ	degree of charge transfer
Δ	phase (ellipsometry)
E	energy
$E_{g,opt}$	energy of optical bandgap
ϵ	dielectric function
H	height
I	current
I_A	integral intensity
k	extinction coefficient
k_B	Boltzmann constant
L	length
λ	wavelength
M_n	number average molecular weight
M_w	weight average molecular weight
M_{MU}	molecular weight of monomer unit
n	refractive index
ν	wavenumber
Ψ	modulus (ellipsometry)
q	scattering vector
r	roughness
R	resistance
ρ	resistivity
σ	conductivity
t	film thickness
T	temperature
θ	scattering angle
T_g	glass transition temperature
T_m	melting temperature
V	voltage

Bibliography

(*1*) Feynman, R. (1959). There's Plenty of Room at the Bottom. *Engineering and Science 23*, 22–36.

(*2*) EPA; U.S. Environmental Protection Agency Nanotechnology white paper., tech. rep., Washington, DC: U.S. Environmental Protection Agency, 2007.

(*3*) Seeman, N. C., *Structural DNA Nanotechnology*; Seeman, N. C., Ed.; Cambridge University Press: Cambridge, 2016.

(*4*) Sun, H., Luo, Q., Hou, C., and Liu, J. (2017). Nanostructures based on protein self-assembly: From hierarchical construction to bioinspired materials. *Nano Today 14*, 16–41.

(*5*) Ramos-Cabrer, P., and Campos, F. (2013). Liposomes and nanotechnology in drug development : Focus on ocular targets. *International Journal of Nanomedicine 8*, 951–960.

(*6*) Douglas, T., and Young, M. (1998). Host-guest encapsulation of materials by assembled virus protein cages. *Nature 393*, 152–155.

(*7*) Seeman, N. C. (1982). Nucleic acid junctions and lattices. *Journal of Theoretical Biology 99*, 237–247.

(*8*) Winfree, E., Liu, F., Wenzler, L. A., and Seeman, N. C. (1998). Design and self-assembly of two-dimensional DNA crystals. *Nature 394*, 539–44.

(*9*) Klein, W. P., Schmidt, C. N., Rapp, B., Takabayashi, S., Knowlton, W. B., Lee, J., Yurke, B., Hughes, W. L., Graugnard, E., and Kuang, W. (2013). Multiscaffold DNA origami nanoparticle waveguides. *Nano Letters 13*, 3850–3856.

(*10*) Benson, E., Mohammed, A., Gardell, J., Masich, S., Czeizler, E., Orponen, P., and Högberg, B. (2015). DNA rendering of polyhedral meshes at the nanoscale. *Nature 523*, 441–444.

(*11*) Rothemund, P. W. K. (2006). Folding DNA to create nanoscale shapes and patterns. *Nature 440*, 297–302.

(*12*) Douglas, S. M., Dietz, H., Liedl, T., Högberg, B., Graf, F., and Shih, W. M. (2009). Self-assembly of DNA into nanoscale three-dimensional shapes. *Nature 459*, 414–418.

(*13*) Stein, I. H., Schüller, V., Böhm, P., Tinnefeld, P., and Liedl, T. (2011). Single-molecule FRET ruler based on rigid DNA origami blocks. *ChemPhysChem 12*, 689–695.

(*14*) Kuzyk, A., Jungmann, R., Acuna, G. P., and Liu, N. (2018). DNA Origami Route for Nanophotonics. *ACS Photonics 5*, 1151–1163.

(*15*) Fu, J., Liu, M., Liu, Y., Woodbury, N. W., and Yan, H. (2012). Interenzyme substrate diffusion for an enzyme cascade organized on spatially addressable DNA nanostructures. *Journal of the American Chemical Society 134*, 5516–5519.

(*16*) Pei, H., Zuo, X., Pan, D., Shi, J., Huang, Q., and Fan, C. Scaffolded biosensors with designed DNA nanostructures., 2013.

(*17*) Schreiber, R., Kempter, S., Holler, S., Schüller, V., Schiffels, D., Simmel, S. S., Nickels, P. C., and Liedl, T. (2011). DNA Origami-Templated Growth of Arbitrarily Shaped Metal Nanoparticles. *Small 7*, 1795–1799.

(*18*) Shirakawa, H., Louis, E. J., MacDiarmid, A. G., Chiang, C. K., and Heeger, A. J. (1977). Synthesis of electrically conducting organic polymers: halogen derivatives of polyacetylene, (CH)x. *Journal of the Chemical Society, Chemical Communications*, 578.

(*19*) Chiang, C. K., Park, Y. W., Heeger, A. J., Shirakawa, H., Louis, E. J., and MacDiarmid, A. G. (1978). Conducting polymers: Halogen doped polyacetylene. *The Journal of Chemical Physics 69*, 5098.

(*20*) Karg, S., Riess, W., Dyakonov, V., and Schwoerer, M. (1993). Electrical and optical characterization of poly(phenylene-vinylene) light emitting diodes. *Synthetic Metals 54*, 427–433.

(*21*) Rivnay, J., Owens, R. M., and Malliaras, G. G. (2014). The rise of organic bioelectronics. *Chemistry of Materials 26*, 679–685.

(*22*) Burroughes, J. H., Jones, C. A., and Friend, R. H. (1988). New semiconductor device physics in polymer diodes and transistors. *Nature 335*, 137–141.

(*23*) Yu, G., Gao, J., Hummelen, J. C., Wudl, F., and Heeger, A. J. (1995). Polymer Photovoltaic Cells: Enhanced Efficiencies via a Network of Internal Donor-Acceptor Heterojunctions. *Science 270*, 1789–1791.

(*24*) Thomas, S. W., Joly, G. D., and Swager, T. M. (2007). Chemical sensors based on amplifying fluorescent conjugated polymers. *Chemical Reviews 107*, 1339–86.

(*25*) Prins, P., Grozema, F. C., Galbrecht, F., Scherf, U., and Siebbeles, L. D. (2007). Charge transport along coiled conjugated polymer chains. *Journal of Physical Chemistry C 111*, 11104–11112.

(*26*) Swager, T. M. (1998). The Molecular Wire Approach to Sensory Signal Amplification. *Accounts of Chemical Research 31*, 201–207.

(*27*) Wan, M. (2008). A Template-Free Method Towards Conducting Polymer Nanostructures. *Advanced Materials 20*, 2926–2932.

(*28*) Kaloni, T. P., Giesbrecht, P. K., Schreckenbach, G., and Freund, M. S. (2017). Polythiophene: From Fundamental Perspectives to Applications. *Chemistry of Materials 29*, 10248–10283.

(*29*) Shao, M., He, Y., Hong, K., Rouleau, C. M., Geohegan, D. B., and Xiao, K. (2013). A water-soluble polythiophene for organic field-effect transistors. *Polymer Chemistry 4*, 5270.

(*30*) Zhao, D., Li, L., Niu, W., and Chen, S. (2016). Chemical Highly conductive polythiophene films doped with chloroauric acid for dual-mode sensing of volatile organic amines and thiols. *Sensors & Actuators: B. Chemical 243*, 380–387.

(*31*) Le Floch, F., Ho, H. A., and Leclerc, M. (2006). Label-free electrochemical detection of protein based on a ferrocene-bearing cationic polythiophene and aptamer. *Analytical Chemistry 78*, 4727–4731.

(*32*) Bérn Abérem, M., Najari, A., Ho, A. A., Gravel, J. F., Nobert, P., Boudreau, D., and Leclerc, M. (2006). Protein detecting arrays based on cationic polythiophene-DNA-aptamer complexes. *Advanced Materials 18*, 2703–2707.

(*33*) Kiriy, A., Senkovskyy, V., and Sommer, M. (2011). Kumada Catalyst-Transfer Polycondensation: Mechanism, Opportunities, and Challenges. *Macromolecular rapid communications 32*, 1503–1517.

(*34*) Bässler, H. In *Unimolecular and Supramolecular Electronics I*, Metzger, R. M., Ed., 312th ed.; Springer, Berlin, Heidelberg: Heidelberg, 2012; Vol. 313; Chapter 1, pp 1–66.

(*35*) Knudsen, J. B. et al. (2015). Routing of individual polymers in designed patterns. *Nature nanotechnology 10*, 892–898.

(*36*) Wang, Z.-G., and Ding, B. (2014). Engineering DNA Self-Assemblies as Templates for Functional Nanostructures. *Accounts of chemical research 47*, 1654–62.

(*37*) Wang, X., Li, C., Niu, D., Sha, R., Seeman, N. C., and Canary, J. W. (2018). Construction of a DNA Origami Based Molecular Electro-optical Modulator. *Nano Letters 18*, 2112–2115.

(*38*) Krissanaprasit, A., Madsen, M., Knudsen, J. B., Gudnason, D., Surareungchai, W., Birkedal, V., and Gothelf, K. V. (2016). Programmed Switching of Single Polymer Conformation on DNA Origami. *ACS nano 10*, 2243–50.

(*39*) Madsen, M., Christensen, R. S., Krissanaprasit, A., Bakke, M. R., Riber, C. F., Nielsen, K. S., Zelikin, A. N., and Gothelf, K. V. (2017). Preparation, Single-Molecule Manipulation, and Energy Transfer Investigation of a Polyfluorene-graft-DNA polymer. *Chemistry - A European Journal 23*, 10511–10515.

(*40*) Shirakawa, H., and Macdiarmid, A. G. (1977). Electrical Conductivity in doped Polyacetylene. *Physical Review Letters 39*, 1098–1101.

(*41*) Salzmann, I., Heimel, G., Oehzelt, M., Winkler, S., and Koch, N. (2016). Molecular Electrical Doping of Organic Semiconductors: Fundamental Mechanisms and Emerging Dopant Design Rules. *Accounts of Chemical Research 49*, 370–378.

(*42*) Yamamoto, T., Sanechika, K., and Yamamoto, A. (1980). Preparation of thermostable and electric-conducting poly(2,5-thienylene). *Journal of Polymer Science: Polymer Letters Edition 18*, 9–12.

(*43*) McCarley, T. D., Noble, C. O., DuBois, C. J., and McCarley, R. L. (2001). MALDI-MS evaluation of poly(3-hexylthiophene) synthesized by chemical oxidation with FeCl3. *Macromolecules 34*, 7999–8004.

(*44*) Yokoyama, A., Miyakoshi, R., and Yokozawa, T. (2004). Chain-Growth Polymerization for Poly(3-hexylthiophene) with a Defined Molecular Weight and a Low Polydispersity. *Macromolecules 37*, 1169–1171.

(*45*) Loewe, R. S., Ewbank, P., Liu, J., Zhai, L., and McCullough, R. (2001). Regioregular, head-to-tail coupled poly(3-alkylthiophenes) made easy by the GRIM method: Investigation of the reaction and the origin of regioselectivity. *Macromolecules 34*, 4324–4333.

(*46*) Peierls, R. E., *Quantum Theory of Solids*, 23rd ed.; Oxford University Press: Oxford, 1955.

(*47*) Brütting, W., and Rieß, W. (2008). Grundlagen der organischen Halbleiter. *Physik Journal 7*, 33–38.

(*48*) Kline, R. J., McGehee, M. D., Kadnikova, E. N., Liu, J., Fréchet, J. M., and Toney, M. F. (2005). Dependence of regioregular poly(3-hexylthiophene) film morphology and field-effect mobility on molecular weight. *Macromolecules 38*, 3312–3319.

(*49*) Sirringhaus, H. (2005). Device physics of solution-processed organic field-effect transistors. *Advanced Materials 17*, 2411–2425.

(*50*) Blom, P., de Jong, M., and van Munster, M. (1997). Electric-field and temperature dependence of the hole mobility in poly(p-phenylene vinylene). *Physical Review B - Condensed Matter and Materials Physics 55*, R656–R659.

(*51*) Collini, E., and Scholes, G. D. (2009). Coherent Intrachain Energy Migration in a Conjugated Polymer at Room Temperature. *Science 323*, 369–373.

(*52*) Coropceanu, V., Cornil, J., da Silva Filho, D. A., Olivier, Y., Silbey, R., and Bredas, J.-L. (2007). Charge transport in organic semiconductors. *Chemical Reviews 107*, 926–952.

(*53*) Prins, P., Grozema, F. C., Schins, J. M., Patil, S., Scherf, U., and Siebbeles, L. D. A. (2006). High intrachain hole mobility on molecular wires of ladder-type poly(p-phenylenes). *Physical Review Letters 96*, 1–4.

(*54*) Hertel, D., Scherf, U., and Bässler, H. (1998). Charge Carrier Mobility in a Ladder-Type Conjugated Polymer. *Advanced Materials 10*, 1119–1122.

(*55*) van Hutten, P., and Hadziioannou, G. In *Handbook of organic conductive molecules and polymers, Volume 3*, Nalwa, H. S., Ed.; John Wiley and Sons: New York, 1997.

(*56*) Lei, T. Design, Synthesis, and Structure-Property Relationship Study of Polymer Field-Effect Transistors., Dissertation, Beijing University, 2015.

(*57*) Bredas, J.-L., and Street, G. B. (1985). Polarons , Bipolarons , and Solitons in Conducting Polymers. *Accounts of chemical research 18*, 309–315.

(*58*) Patil, A. O., Ikenoue, Y., Basescu, N., Colaneri, N., Chen, J., Wudl, F., and Heeger, A. J. (1987). Self-doped conducting polymers. *Synthetic Metals 20*, 151–159.

(*59*) Kaloni, T. P., Schreckenbach, G., and Freund, M. S. (2015). Structural and electronic properties of pristine and doped polythiophene: Periodic versus molecular calculations. *Journal of Physical Chemistry C 119*, 3979–3989.

(*60*) Ramírez-Solís, A., Kirtman, B., Bernal-Jáquez, R., and Zicovich-Wilson, C. M. (2009). Periodic density functional theory studies of Li-doped polythiophene: Dependence of electronic and structural properties on dopant concentration. *Journal of Chemical Physics 130*, 164904.

(*61*) Koller, G. (2007). Intra- and intermolecular band dispersion in an organic crystal. *Science 318*, 44.

(*62*) Parthasarathy, G., Shen, C., Kahn, A., and Forrest, S. R. (2001). Lithium doping of semiconducting organic charge transport materials. *Journal of Applied Physics 89*, 4986–4992.

(*63*) Gao, W., and Kahn, A. (2001). Controlled p-doping of zinc phthalocyanine by coevaporation with tetrafluorotetracyanoquinodimethane: A direct and inverse photoemission study. *Applied Physics Letters 79*, 4040–4042.

(*64*) Kanai, K., Akaike, K., Koyasu, K., Sakai, K., Nishi, T., Kamizuru, Y., Nishi, T., Ouchi, Y., and Seki, K. (2009). Determination of electron affinity of electron accepting molecules. *Applied Physics A: Materials Science and Processing 95*, 309–313.

(*65*) Méndez, H., Heimel, G., Opitz, A., Sauer, K., Barkowski, P., Oehzelt, M., Soeda, J., Okamoto, T., Takeya, J., Arlin, J. B., Balandier, J. Y., Geerts, Y., Koch, N., and Salzmann, I. (2013). Doping of organic semiconductors: Impact of dopant strength and electronic coupling. *Angewandte Chemie - International Edition 52*, 7751–7755.

(*66*) Dixon, D. A., Calabrese, J. C., and Miller, J. S. (1989). Crystal and molecular structure of the 2:1 charge-transfer salt of decamethylferrocene and perfluoro-7,7,8,8-tetracyano-p-quinodimethane. *The Journal of Physical Chemistry 93*, 2284–2291.

(*67*) Aziz, B. E. F., Vollmer, A., Eisebitt, S., Eberhardt, W., Pingel, P., Neher, D., and Koch, N. (2007). Localized Charge Transfer in a Molecularly Doped Conducting Polymer. *Advanced Materials 19*, 3257–3260.

(*68*) Duong, D. T., Wang, C., Antono, E., Toney, M. F., and Salleo, A. (2013). The chemical and structural origin of efficient p-type doping in P3HT. *Organic Electronics: physics, materials, applications 14*, 1330–1336.

(*69*) Méndez, H., Heimel, G., Winkler, S., Frisch, J., Opitz, A., Sauer, K., Wegner, B., Oehzelt, M., Röthel, C., Duhm, S., Többens, D., Koch, N., and Salzmann, I. (2015). Charge-transfer crystallites as molecular electrical dopants. *Nature Communications 6*, 8560.

(*70*) Scholes, D. T., Yee, P. Y., Lindemuth, J. R., Kang, H., Onorato, J., Ghosh, R., Luscombe, C. K., Spano, F. C., Tolbert, S. H., and Schwartz, B. J. (2017). The Effects of Crystallinity on Charge Transport and the Structure of Sequentially Processed F4TCNQ-Doped Conjugated Polymer Films. *Advanced Functional Materials 27*, 1–13.

(*71*) Pingel, P., Zhu, L., Park, K. S., Vogel, J. O., Janietz, S., Kim, E. G., Rabe, J. P., Brédas, J. L., and Koch, N. (2010). Charge-transfer localization in molecularly doped thiophene-based donor polymers. *Journal of Physical Chemistry Letters 1*, 2037–2041.

(*72*) Kroon, R., Kiefer, D., Stegerer, D., Yu, L., Sommer, M., and Müller, C. (2017). Polar Side Chains Enhance Processability, Electrical Conductivity, and Thermal Stability of a Molecularly p-Doped Polythiophene. *Advanced Materials 29*, 35–37.

(*73*) Cochran, J. E., Junk, M. J., Glaudell, A. M., Miller, P. L., Cowart, J. S., Toney, M. F., Hawker, C. J., Chmelka, B. F., and Chabinyc, M. L. (2014). Molecular interactions and ordering in electrically doped polymers: Blends of PBTTT and F4TCNQ. *Macromolecules 47*, 6836–6846.

(*74*) Karpov, Y., Kiriy, N., Al-Hussein, M., Hambsch, M., Beryozkina, T., Bakulev, V., Mannsfeld, S. C., Voit, B., and Kiriy, A. (2018). Hexacyano-[3]-radialene anion-radical salts: A promising family of highly soluble p-dopants. *Chemical Communications 54*, 307–310.

(*75*) Gao, Z. Q., Mi, B. X., Xu, G. Z., Wan, Y. Q., Gong, M. L., Cheah, K. W., and Chen, C. H. (2008). An organic p-type dopant with high thermal stability for an organic semiconductor. *Chemical Communications*, 117–119.

(*76*) Pingel, P., and Neher, D. (2013). Comprehensive picture of p-type doping of P3HT with the molecular acceptor F4TCNQ. *Physical Review B - Condensed Matter and Materials Physics 87*, 1–9.

(*77*) Ghani, F., Opitz, A., Pingel, P., Heimel, G., Salzmann, I., Frisch, J., Neher, D., Tsami, A., Scherf, U., and Koch, N. (2015). Charge transfer in and conductivity of molecularly doped thiophene-based copolymers. *Journal of Polymer Science, Part B: Polymer Physics 53*, 58–63.

(*78*) Salzmann, I., Heimel, G., Duhm, S., Oehzelt, M., Pingel, P., George, B. M., Schnegg, A., Lips, K., Blum, R. P., Vollmer, A., and Koch, N. (2012). Intermolecular hybridization governs molecular electrical doping. *Physical Review Letters 108*, 1–5.

(*79*) Lin, J. W.-P., and Dudek, L. P. (1980). Synthesis and properties of poly(2,5-thienylene). *Journal of Polymer Science: Polymer Chemistry Edition 18*, 2869–2873.

(*80*) Berlin, A., Pagani, G. A., and Sannicolò, F. (1986). New synthetic routes to electroconductive polymers containing thiophene units. *Journal of the Chemical Society, Chemical Communications*, 1663–1664.

(*81*) Yamamoto, T., Morita, A., Miyazaki, Y., Maruyama, T., Wakayama, H., hua Zhou, Z., Nakamura, Y., Kanbara, T., Sasaki, S., and Kubota, K. (1992). Preparation of π-Conjugated Poly(thiophene-2,5-diyl), Poly(p-phenylene), and Related Polymers Using Zerovalent Nickel Complexes. Linear Structure and Properties of the π-Conjugated Polymers. *Macromolecules 25*, 1214–1223.

(*82*) Ballauff, M. (1989). Stiff-Chain Polymers—Structure, Phase Behavior, and Properties. *Angewandte Chemie International Edition in English 28*, 253–267.

(*83*) Jen, K. Y., Oboodi, R., and Elsenbaumer, R. L. In *Polymeric Materials Science and Engineering, Proceedings of the ACS Division of Polymeric Material*, ACS: 1985; Vol. 53, pp 79–83.

(*84*) Elsenbaumer, R. L., Jen, K. Y., and Oboodi, R. (1986). Processible and environmentally stable conducting polymers. *Synthetic Metals 15*, 169–174.

(*85*) McCullough, R. D., and Lowe, R. D. (1992). Enhanced electrical conductivity in regioselectively synthesized poly(3-alkylthiophenes). *Journal of the Chemical Society, Chemical Communications*, 70.

(*86*) Ho, H. A., Najari, A., and Leclerc, M. (2008). Optical detection of DNA and proteins with cationic polythiophenes. *Accounts of Chemical Research 41*, 168–178.

(*87*) Kokil, A., Ponrathnam, T., Kumar, A., Nagarajan, R., and Kumar, J. (2010). Soluble Pegylated Polythiophenes : Synthesis and Nitroaromatic Sensing. *PMSE*, 4–5.

(*88*) Öktem, G., Sahre, K., Voit, B., Jordan, R., and Kiriy, A. (2017). Facile synthesis of oligo(3-hexylthiophene)s conductive wires with charge-transfer functions. *Polymer Chemistry 8*, 2675–2685.

(*89*) Sheina, E. E., Khersonsky, S. M., Jones, E. G., and McCullough, R. D. (2005). Highly Conductive, Regioregular Alkoxy-Functionalized Polythiophenes: A New Class of Stable, Low Band Gap Materials. *Chemistry of Materials 17*, 3317–3319.

(*90*) McCullough, R. D., and Williams, S. P. (1993). Toward tuning electrical and optical properties in conjugated polymers using side-chains: highly conductive head-to-tail, heteroatom functionalized polythiophenes. *Journal of the American Chemical Society 115*, 11608–11609.

(*91*) McCullough, R. D., Tristram-Nagle, S., Williams, S. P., Lowe, R. D., and Jayaraman, M. (1993). Self-orienting head-to-tail poly(3-alkylthiophenes): new insights on structure-property relationships in conducting polymers. *Journal of the American Chemical Society 115*, 4910–4911.

(*92*) Mccullough, R. D., Williams, S. P., Tristram-nagle, S., Jayaraman, M., Ewbank, P. C., and Miller, L. (1995). The first synthesis and new properties of regioregular, head-to-tail coupled polythiophenes. *Synthetic Metals 69*, 279–282.

(*93*) Mccullough, R. D. (1998). The Chemistry of Conducting Polythiophenes*. *Advanced Materials 10*, 93–116.

(*94*) Kline, R. J., and McGehee, M. D. (2006). Morphology and charge transport in conjugated polymers. *Polymer Reviews 46*, 27–45.

(*95*) Panzer, F., Bässler, H., Lohwasser, R., Thelakkat, M., and Köhler, A. (2014). The impact of polydispersity and molecular weight on the order-disorder transition in poly(3-hexylthiophene). *Journal of Physical Chemistry Letters 5*, 2742–2747.

(*96*) Kiriy, N., Jähne, E., Kiriy, A., and Adler, H.-J. (2004). Conformational transitions and aggregations of regioregular polyalkylthiophenes. *Macromolecular Symposia 210*, 359–367.

(*97*) Na, J. Y. et al. (2015). Understanding Solidification of Polythiophene Thin Films during Spin-Coating: Effects of Spin-Coating Time and Processing Additives. *Scientific Reports 5*, 13288.

(*98*) Lee, M. J., Gupta, D., Zhao, N., Heeney, M., Mcculloch, I., and Sirringhaus, H. (2011). Anisotropy of charge transport in a uniaxially aligned and chain-extended, high-mobility, conjugated polymer semiconductor. *Advanced Functional Materials 21*, 932–940.

(*99*) Roncali, J. (1992). Conjugated poly(thiophenes): synthesis, functionalization, and applications. *Chemical Reviews 92*, 711–738.

(*100*) Sarhan, A. A., and Bolm, C. (2009). Iron(iii) chloride in oxidative C-C coupling reactions. *Chemical Society Reviews 38*, 2730–2744.

(*101*) Hohnholz, D., MacDiarmid, A. G., Sarno, D. M., and Jones, W. E. (2001). Uniform thin films of poly-3,4-ethylenedioxythiophene (PEDOT) prepared by in-situ deposition. *Chemical Communications 23*, 2444–2445.

(*102*) Iarossi, D., Mucci, A., Schenetti, L., Seeber, R., Goldoni, F., Affronte, M., and Nava, F. (1999). Polymerization and Characterization of 4,4-Bis(alkylsulfanyl)-2,2-bithiophenes. *Macromolecules 32*, 1390–1397.

(*103*) Osakada, K., *Organometallic Reactions and Polymerization*; Springer: Heidelberg, 2014; Vol. 85.

(*104*) Yamamoto, T., Sanechika, K., and Yamamoto, A. (1983). Preparation and Characterization of Poly(thienylene)s. *Bulleting Chemical Society Japan 56*, 1497–1502.

(*105*) Guillerez, S., and Bidan, G. (1998). New convenient synthesis of highly regioregular poly(3-octylthiophene) based on the Suzuki coupling reaction. *Synthetic Metals 93*, 123–126.

(*106*) Giovannitti, A., Sbircea, D.-T., Inal, S., Nielsen, C. B., Bandiello, E., Hanifi, D. A., Sessolo, M., Malliaras, G. G., McCulloch, I., and Rivnay, J. (2016). Controlling the mode of operation of organic transistors through side-chain engineering. *Proceedings of the National Academy of Sciences 113*, 12017–12022.

(*107*) Chen, T. A., and Rieke, R. D. (1992). The First Regioregular Head-to-Tail Poly(3-hexylthiophene-2,5-diyl) and a Regiorandom Isopolymer: Ni vs Pd Catalysis of 2(5)-Bromo-5(2)-(bromozincio)-3-hexylthiophene Polymerization. *Journal of the American Chemical Society 114*, 10087–10088.

(*108*) Chen, T. A., Wu, X., and Rieke, R. D. (1995). Regiocontrolled Synthesis of Poly(3-alkylthiophenes) Mediated by Rieke Zinc: Their Characterization and Solid-State Properties. *Journal of the American Chemical Society 117*, 233–244.

(*109*) Loewe, R. S., Khersonsky, S. M., and McCullough, R. D. (1999). A Simple Method to Prepare Head-to-Tail Coupled, Regioregular Poly(3-alkylthiophenes) Using Grignard Metathesis. *Advanced Materials 11*, 250–253.

(*110*) Guo, X., Quinn, J., Chen, Z., Usta, H., Zheng, Y., Xia, Y., Hennek, J. W., Ortiz, R. P., Marks, T. J., and Facchetti, A. (2013). Dialkoxybithiazole: A new building block for head-to-head polymer semiconductors. *Journal of the American Chemical Society 135*, 1986–1996.

(*111*) Flory, P. J. (1936). Molecular Size Distribution in Linear Condensation Polymers. *Journal of the American Chemical Society 58*, 1877–1885.

(*112*) Flory, P. J. (1946). Fundamental principles of condensation polymerization. *Chemical Reviews 39*, 137–197.

(*113*) Kornberg, A. (1960). Biologic synthesis of deoxyribonucleic acid. *Science 131*, 1503–1508.

(*114*) Sheina, E. E., Liu, J., Iovu, M. C., Laird, D. W., and McCullough, R. D. (2004). Chain Growth Mechanism for Regioregular Nickel-Initiated Cross-Coupling Polymerizations. *Macromolecules 37*, 3526–3528.

(*115*) Iovu, M. C., Sheina, E. E., Gil, R. R., and McCullough, R. D. (2005). Experimental Evidence for the Quasi-“Living” Nature of the Grignard Metathesis Method for the Synthesis of Regioregular Poly(3-alkylthiophenes). *Macromolecules 38*, 8649–8656.

(*116*) Miyakoshi, R., Yokoyama, A., and Yokozawa, T. (2005). Catalyst-transfer polycondensation. mechanism of Ni-catalyzed chain-growth polymerization leading to well-defined poly(3-hexylthiophene). *Journal of the American Chemical Society 127*, 17542–7.

(*117*) Beryozkina, T., Senkovskyy, V., Kaul, E., and Kiriy, A. (2008). Kumada Catalyst-Transfer Polycondensation of Thiophene-Based Oligomers: Robustness of a Chain-Growth Mechanism. *Macromolecules 41*, 7817–7823.

(*118*) Lanni, E. L., and McNeil, A. J. (2009). Mechanistic Studies on Ni(dppe)Cl2-Catalyzed Chain-Growth Polymerizations: Evidence for Rate-Determining Reductive Elimination. *Journal of American Chemical Society 131*, 16573–16579.

(*119*) Zenkina, O. V., Karton, A., Freeman, D., Shimon, L. J., Martin, J. M., and Van Der Boom, M. E. (2008). Directing aryl-I versus aryl-Br bond activation by nickel via a ring walking process. *Inorganic Chemistry 47*, 5114–5121.

(*120*) Tkachov, R., Senkovskyy, V., Komber, H., Sommer, J.-U., and Kiriy, A. (2010). Random catalyst walking along polymerized poly(3-hexylthiophene) chains in Kumada catalyst-transfer polycondensation. *Journal of the American Chemical Society 132*, 7803–10.

(*121*) Verswyvel, M., Monnaie, F., and Koeckelberghs, G. (2011). AB Block Copoly(3-alkylthiophenes): Synthesis and Chiroptical Behavior. *Macromolecules 44*, 9489–9498.

(*122*) Senkovskyy, V., Khanduyeva, N., Komber, H., Oertel, U., Stamm, M., Kuckling, D., and Kiriy, A. (2007). Conductive polymer brushes of regioregular head-to-tail poly(3-alkylthiophenes) via catalyst-transfer surface-initiated polycondensation. *Journal of the American Chemical Society 129*, 6626–32.

(*123*) Khanduyeva, N., Senkovskyy, V., Beryozkina, T., Bocharova, V., Simon, F., Nitschke, M., Stamm, M., Grötzschel, R., and Kiriy, A. (2008). Grafting of Poly(3-hexylthiophene) from Poly(4-bromostyrene) Films by Kumada Catalyst-Transfer Polycondensation: Revealing of the Composite Films Structure. *Macromolecules 41*, 7383–7389.

(*124*) Smeets, A., Van den Bergh, K., De Winter, J., Gerbaux, P., Verbiest, T., and Koeckelberghs, G. (2009). Incorporation of Different End Groups in Conjugated Polymers Using Functional Nickel Initiators. *Macromolecules 42*, 7638–7641.

(*125*) Senkovskyy, V., Tkachov, R., Beryozkina, T., Komber, H., Oertel, U., Horecha, M., Bocharova, V., Stamm, M., Gevorgyan, S. A., Krebs, F. C., and Kiriy, A. (2009). "Hairy" poly(3-hexylthiophene) particles prepared via surface-initiated Kumada catalyst-transfer polycondensation. *Journal of the American Chemical Society 131*, 16445–53.

(*126*) Senkovskyy, V., Beryozkina, T., Bocharova, V., Tkachov, R., Komber, H., Lederer, A., Stamm, M., Severin, N., Rabe, J. P., and Kiriy, A. (2010). A core-first preparation of poly(3-alkylthiophene) stars. *Macromolecular Symposia 291-292*, 17–25.

(*127*) Bronstein, H. A., and Luscombe, C. K. (2009). Externally initiated regioregular P3HT with controlled molecular weight and narrow polydispersity. *Journal of the American Chemical Society 131*, 12894–12895.

(*128*) Doubina, N., Stoddard, M., Bronstein, H. A., Jen, A. K., and Luscombe, C. K. (2009). The effects of binding ligand variation on the nickel catalyzed externally initiated polymerization of 2-bromo-3-hexyl-5- iodothiophene. *Macromolecular Chemistry and Physics 210*, 1966–1972.

(*129*) Doubina, N., Paniagua, S. A., Soldatova, A. V., Jen, A. K., Marder, S. R., and Luscombe, C. K. (2011). Steric effects of the initiator substituent position on the externally initiated polymerization of 2-bromo-5-iodo-3-hexylthiophene. *Macromolecules 44*, 512–520.

(*130*) Chatt, B. J., and Shaw, B. L. (1960). Alkyls and Aryls of Transition Metals, Part III Nickel (II) Derivatives. *Journal of the Chemical Society 0*, 1718–1729.

(*131*) Kaul, E., Senkovskyy, V., Tkachov, R., Bocharova, V., Komber, H., Stamm, M., and Kiriy, A. (2010). Synthesis of a Bifunctional Initiator for Controlled Kumada Catalyst-Transfer Polycondensation/Nitroxide-Mediated Polymerization and Preparation of Poly(3-hexylthiophene)Polystyrene Block Copolymer Therefrom. *Macromolecules 43*, 77–81.

(*132*) Senkovskyy, V., Sommer, M., Tkachov, R., Komber, H., Huck, W. T. S., and Kiriy, A. (2010). Convenient Route To Initiate Kumada Catalyst-Transfer Polycondensation Using Ni(dppe)Cl2 or Ni(dppp)Cl2 and Sterically Hindered Grignard Compounds. *Macromolecules 43*, 10157–10161.

(*133*) Jeffries-EL, M., Sauvé, G., and McCullough, R. D. (2004). In-Situ End-Group Functionalization of Regioregular Poly(3-alkylthiophene) Using the Grignard Metathesis Polymerization Method. *Advanced Materials 16*, 1017–1019.

(*134*) Thacker, V. V., Herrmann, L. O., Sigle, D. O., Zhang, T., Liedl, T., Baumberg, J. J., and Keyser, U. F. (2014). DNA origami based assembly of gold nanoparticle dimers for surface-enhanced Raman scattering. *Nature communications 5*, 3448.

(*135*) Lan, X., Chen, Z., Dai, G., Lu, X., Ni, W., and Wang, Q. (2013). Bifacial DNA origami-directed discrete, three-dimensional, anisotropic plasmonic nanoarchitectures with tailored optical chirality. *Journal of the American Chemical Society 135*, 11441–4.

(*136*) Liu, J., Geng, Y., Pound, E., Gyawali, S., Ashton, J. R., Hickey, J., Woolley, A. T., and Harb, J. N. (2011). Metallization of Branched DNA Origami for Nanoelectronic Circuit Fabrication. *ACS nano 5*, 2240–7.

(*137*) Watson, J., and Crick, F. (1953). Molecular structure of nucleic acids. *Nature. 171*, 737–8.

(*138*) Crick, F. H. C., and Watson, J. D. (1954). The Complementary Structure of Deoxyribonucleic Acid. *Proceedings of the Royal Society A: Mathematical, Physical and Engineering Sciences 223*, 80–96.

(*139*) Wing, R., Drew, H., Takano, T., Broka, C., Tanaka, S., Itakura, K., and Dickerson, R. E. (1980). Crystal structure analysis of a complete turn of B-DNA. *Nature 287*, 755–758.

(*140*) Wang, A. H., Quigley, G. J., Kolpak, F. J., Crawford, J. L., Van Boom, J. H., Van Der Marel, G., and Rich, A. (1979). Molecular structure of a left-Handed double helical DNA fragment at atomic resolution. *Nature 282*, 680–686.

(*141*) Dickerson, R. E., and Ng, H.-L. (2001). DNA structure from A to B. *Proceedings of the National Academy of Sciences 98*, 6986–6988.

(*142*) Pray, L. A. (2008). Discovery of DNA Structure and Function: Watson and Crick. *Nature Education 1*, 100.

(*143*) Yakovchuk, P., Protozanova, E., and Frank-Kamenetskii, M. D. (2006). Base-stacking and base-pairing contributions into thermal stability of the DNA double helix. *Nucleic Acids Research 34*, 564–574.

(*144*) Schildkraut, C., and Lifson, S. (1965). Dependence of the Melting Temperature of DNA on Salt Concentration. *Biopolymers 3*, 195–208.

(*145*) Bloom, K. S. (2008). Beyond the code: the mechanical properties of DNA as they relate to mitosis. *Chromosoma 117*, 103–110.

(*146*) Hagerman, P. J., and Zimm, B. H. (1981). Monte Carlo approach to the analysis of the rotational diffusion of wormlike chains. *Biopolymers 20*, 1481–1502.

(*147*) Hagerman, P. J. (1981). Investigation of the flexibility of DNA using transient electric birefringence. *Biopolymers 20*, 1503–1535.

(*148*) Geggier, S., and Vologodskii, A. (2010). Sequence dependence of DNA bending rigidity. *Proceedings of the National Academy of Sciences 107*, 15421–15426.

(*149*) Braun, E., Eichen, Y., Sivan, U., and Ben-Yoseph, G. (1998). DNA-templated assembly and electrode attachment of a conducting silver wir. *Nature 391*, 775.

(*150*) Richter, J., Mertig, M., Pompe, W., Mönch, I., and Schackert, H. K. (2001). Construction of highly conductive nanowires on a DNA template. *Applied Physics Letters 78*, 536–538.

(*151*) Hassanien, R., Al-Hinai, M., Farha Al-Said, S. A., Little, R., Siller, L., Wright, N. G., Houlton, A., and Horrocks, B. R. (2010). Preparation and characterization of conductive and photoluminescent DNA-templated polyindole nanowires. *ACS Nano 4*, 2149–2159.

(*152*) Ongaro, A., Griffin, F., Beecher, P., Nagle, L., Iacopino, D., Quinn, A., Redmond, G., and Fitzmaurice, D. (2005). DNA-templated assembly of conducting gold nanowires between gold electrodes on a silicon oxide substrate. *Chemistry of Materials 17*, 1959–1964.

(*153*) Becerril, H. A., Ludtke, P., Willardson, B. M., and Woolley, A. T. (2006). DNA-templated nickel nanostructures and protein assemblies. *Langmuir 22*, 10140–10144.

(*154*) Richter, J. (2003). Metallization of DNA. *Physica E: Low-dimensional Systems and Nanostructures 16*, 157–173.

(*155*) Chen, Z., Liu, C., Cao, F., Ren, J., and Qu, X. (2018). DNA metallization: Principles, methods, structures, and applications. *Chemical Society Reviews 47*, 4017–4072.

(*156*) Puchkova, A. O., Sokolov, P., Petrov, Y. V., and Kasyanenko, N. A. (2011). Metallization of DNA on the Surface. *Journal of Structural Chemistry 52*, 1195–1201.

(*157*) Mertig, M., Colombi Ciacchi, L., Seidel, R., Pompe, W., and De Vita, A. (2002). DNA as a Selective Metallization Template. *Nano Letters 2*, 841–844.

(*158*) Watson, S. M., Pike, A. R., Pate, J., Houlton, A., and Horrocks, B. R. (2014). DNA-templated nanowires: Morphology and electrical conductivity. *Nanoscale 6*, 4027–4037.

(*159*) Richter, J., Seidel, R., Kirsch, R., Mertig, M., Pompe, W., Plaschke, J., and Schackert, H. K. (2000). Nanoscale Palladium Metallization of DNA. *Advance 12*, 507–510.

(*160*) Monson, C. F., and Woolley, A. T. (2003). DNA-templated construction of copper nanowires. *Nano Letters 3*, 359–363.

(*161*) Ford, W. E., Harnack, O., Yasuda, A., and Wessels, J. M. (2001). Platinated DNA as precursors to templated chains of metal nanoparticles. *Advanced Materials 13*, 1793–1797.

(*162*) Seidel, R., Ciacchi, L. C., Weigel, M., Pompe, W., and Mertig, M. (2004). Synthesis of platinum cluster chains on DNA templates: Conditions for a template-controlled cluster growth. *Journal of Physical Chemistry B 108*, 10801–10811.

(*163*) Houlton, A., and Watson, S. M. D. (2011). DNA-based nanowires. Towards bottom-up nanoscale electronics. *Annual Reports Section "A" (Inorganic Chemistry) 107*, 21.

(*164*) Watson, S. M. D., Galindo, M. A., Horrocks, B. R., and Houlton, A. (2014). Mechanism of Formation of Supramolecular DNA-Templated Polymer Nanowires. *Journal of the American Chemical Society 136*, 6649–6655.

(*165*) Watson, S. M. D., Hedley, J. H., Galindo, M. A., Al-Said, S. A. F., Wright, N. G., Connolly, B. A., Horrocks, B. R., and Houlton, A. (2012). Synthesis, characterisation and electrical properties of supramolecular DNA-templated polymer nanowires of 2,5-(bis-2-thienyl)-pyrrole. *Chemistry - A European Journal 18*, 12008–19.

(*166*) Ma, Y., Zhang, J., Zhang, G., and He, H. (2004). Polyaniline nanowires on Si surfaces fabricated with DNA templates. *Journal of the American Chemical Society 126*, 7097–7101.

(*167*) Dong, L., Hollis, T., Fishwick, S., Connolly, B. A., Wright, N. G., Horrocks, B. R., and Houlton, A. (2007). Synthesis, manipulation and conductivity of supramolecular polymer nanowires. *Chemistry - A European Journal 13*, 822–828.

(*168*) Farha Al-Said, S. A., Hassanien, R., Hannant, J., Galindo, M. A., Pruneanu, S., Pike, A. R., Houlton, A., and Horrocks, B. R. (2009). Templating Ag on DNA/polymer hybrid nanowires: Control of the metal growth morphology using functional monomers. *Electrochemistry Communications 11*, 550–553.

(*169*) Han, D., Pal, S., Nangreave, J., Deng, Z., Liu, Y., and Yan, H. (2011). DNA Origami with Complex Curvatures in Three-Dimensional Space. *Science 332*, 342–346.

(*170*) Andersen, E. S., Dong, M., Nielsen, M. M., Jahn, K., Lind-Thomsen, A., Mamdouh, W., Gothelf, K. V., Besenbacher, F., and Kjems, J. (2008). DNA origami design of dolphin-shaped structures with flexible tails. *ACS nano 2*, 1213–8.

(*171*) Andersen, E. S., Dong, M., Nielsen, M. M., Jahn, K., Subramani, R., Mamdouh, W., Golas, M. M., Sander, B., Stark, H., Oliveira, C. L. P., Pedersen, J. S., Birkedal, V., Besenbacher, F., Gothelf, K. V., and Kjems, J. (2009). Self-assembly of a nanoscale DNA box with a controllable lid. *Nature 459*, 73–6.

(*172*) Liedl, T., Högberg, B., Tytell, J., Ingber, D. E., and William, M. (2011). Self-assembly of 3D prestressed tensegrity structures from DNA. *Nature Nanotechnologies 5*, 520–524.

(*173*) Nickels, P. C., Wünsch, B., Holzmeister, P., Bae, W., Kneer, L. M., Grohmann, D., Tinnefeld, P., and Liedl, T. (2016). Molecular force spectroscopy with a DNA origami-based nanoscopic force clamp. *Science 354*, 305–308.

(*174*) Gu, H., Chao, J., Xiao, S.-J., and Seeman, N. C. (2010). A proximity-based programmable DNA nanoscale assembly line. *Nature 465*, 202–206.

(*175*) Kuzyk, A., Laitinen, K. T., and Törmä, P. (2009). DNA origami as a nanoscale template for protein assembly. *Nanotechnology 20*, 235305.

(*176*) Ding, B., Deng, Z., Yan, H., Cabrini, S., Zuckermann, R. N., and Bokor, J. (2010). Gold Nanoparticle Self-Similar Chain Structure Organized by DNA Origami. *Journal of American Chemical Society 132*, 3248–3249.

(*177*) Conway, N., and Douglas, S. Cadnano., 2012.

(*178*) Beater, S., Raab, M., and Tinnefeld, P. In *Methods in Cell Biology*, 1st ed.; Elsevier Inc.: 2014; Vol. 123, pp 449–466.

(*179*) Lin, C., Jungmann, R., Leifer, A. M., Li, C., Levner, D., Church, G. M., Shih, W. M., and Yin, P. (2012). Submicrometre geometrically encoded fluorescent barcodes self-assembled from DNA. *Nature Chemistry 4*, 832–839.

(*180*) Maune, H. T., Han, S.-P., Barish, R. D., Bockrath, M., Iii, W. A. G., Rothemund, P. W. K., and Winfree, E. (2010). Self-assembly of carbon nanotubes into two-dimensional geometries using DNA origami templates. *Nature nanotechnology 5*, 61–6.

(*181*) Saccà, B., Meyer, R., Erkelenz, M., Kiko, K., Arndt, A., Schroeder, H., Rabe, K. S., and Niemeyer, C. M. (2010). Orthogonal protein decoration of DNA origami. *Angewandte Chemie - International Edition 49*, 9378–9383.

(*182*) Deng, Z., Samanta, A., Nangreave, J., Yan, H., and Liu, Y. (2012). Robust DNA-functionalized core/shell quantum dots with fluorescent emission spanning from UV-vis to near-IR and compatible with DNA-directed self-assembly. *Journal of the American Chemical Society 134*, 17424–7.

(*183*) Pal, S., Deng, Z., Wang, H., Zou, S., Liu, Y., and Yan, H. (2011). DNA directed self-assembly of anisotropic plasmonic nanostructures. *Journal of the American Chemical Society 133*, 17606–9.

(*184*) Samanta, A., Zhou, Y., Zou, S., Yan, H., and Liu, Y. (2014). Fluorescence quenching of quantum dots by gold nanoparticles: a potential long range spectroscopic ruler. *Nano letters 14*, 5052–7.

(*185*) Steinhauer, C., Jungmann, R., Sobey, T. L., Simmel, F. C., and Tinnefeld, P. (2009). DNA origami as a nanoscopic ruler for super-resolution microscopy. *Angewandte Chemie (International ed. in English) 48*, 8870–3.

(*186*) Wang, Z.-G., Liu, Q., and Ding, B. (2014). Shape-Controlled Nanofabrication of Conducting Polymer on Planar DNA Templates. *Chemistry of Materials 26*, 3364–3367.

(*187*) Gür, F. N., Schwarz, F. W., Ye, J., Diez, S., and Schmidt, T. L. (2016). Toward Self-Assembled Plasmonic Devices: High-Yield Arrangement of Gold Nanoparticles on DNA Origami Templates. *ACS Nano 10*, 5374–5382.

(*188*) Kühler, P., Roller, E.-M., Schreiber, R., Liedl, T., Lohmüller, T., and Feldmann, J. (2014). Plasmonic DNA-Origami Nanoantennas for Surface-Enhanced Raman Spectroscopy. *Nano Letters 14*, 2914–9.

(*189*) Dutta, P. K., Varghese, R., Nangreave, J., Lin, S., Yan, H., and Liu, Y. (2011). DNA-directed artificial light-harvesting antenna. *Journal of the American Chemical Society 133*, 11985–11993.

(*190*) Hemmig, E. A., Creatore, C., Wünsch, B., Hecker, L., Mair, P., Parker, M. A., Emmott, S., Tinnefeld, P., Keyser, U. F., and Chin, A. W. (2016). Programming Light-Harvesting Efficiency Using DNA Origami. *Nano Letters 16*, 2369–2374.

(*191*) Helmi, S., Ziegler, C., Kauert, D. J., and Seidel, R. (2014). Shape-Controlled Synthesis of Gold Nanostructures Using DNA Origami Molds. *Nano Letters 14*, 6693–6698.

(*192*) Teschome, B., Facsko, S., Schönherr, T., Kerbusch, J., Keller, A., and Erbe, A. (2016). Temperature-Dependent Charge Transport through Individually Contacted DNA Origami-Based Au Nanowires. *Langmuir 32*, 10159–10165.

(*193*) Schreiber, R., Do, J., Roller, E.-M. M., Zhang, T., Schüller, V. J., Nickels, P. C., Feldmann, J., and Liedl, T. (2014). Hierarchical assembly of metal nanoparticles, quantum dots and organic dyes using DNA origami scaffolds. *Nature Nanotechnology 9*, 74–78.

(*194*) Geng, Y., Pearson, A. C., Gates, E. P., Uprety, B., Davis, R. C., Harb, J. N., and Woolley, A. T. (2013). Electrically conductive gold- and copper-metallized DNA origami nanostructures. *Langmuir 29*, 3482–3490.

(*195*) Bayrak, T., Helmi, S., Ye, J., Kauert, D., Kelling, J., Schönherr, T., Weichelt, R., Erbe, A., and Seidel, R. (2018). DNA-Mold Templated Assembly of Conductive Gold Nanowires. *Nano Letters 18*, 2116–2123.

(*196*) Sun, W., Boulais, E., Hakobyan, Y., Wang, W. L., Guan, A., Bathe, M., and Yin, P. (2014). Casting inorganic structures with DNA molds. *Science 346*, 1258361.

(*197*) Kaliginedi, V., Moreno-García, P., Valkenier, H., Hong, W., García-Suárez, V. M., Buiter, P., Otten, J. L., Hummelen, J. C., Lambert, C. J., and Wandlowski, T. (2012). Correlations between molecular structure and single-junction conductance: A case study with oligo(phenylene-ethynylene)-type wires. *Journal of the American Chemical Society 134*, 5262–5275.

(*198*) Knudsen, J. B. Integration of Conjugated Polymers in DNA Nanostructures., Dissertation, Aarhus University, Denmark, 2014.

(*199*) Messaud, F. A., Sanderson, R. D., Runyon, J. R., Otte, T., Pasch, H., and Williams, S. K. R. (2009). An overview on field-flow fractionation techniques and their applications in the separation and characterization of polymers. *Progress in Polymer Science 34*, 351–368.

(*200*) Williams, S. K. R., Benincasa, M.-A., and Ashames, A. In *Encyclopedia of Analytical Chemistry*, Meyers, R., and Meyers, R., Eds., 2009; Chapter Field Flow.

(*201*) Giddings, J. C. (1993). Field-flow fractionation: analysis of macromolecular, colloidal, and particulate materials. *Science 260*, 1456–65.

(*202*) Erni, R., Rossell, M. D., Kisielowski, C., and Dahmen, U. (2009). Atomic-resolution imaging with a sub-50-pm electron probe. *Physical Review Letters 102*, 1–4.

(*203*) Garcia, R., and Herruzo, E. T. (2012). The emergence of multifrequency force microscopy. *Nature Nanotechnology 7*, 217–226.

(*204*) Department of Defense, U. MIL-STD-883E Test Method Standard Microcircuits., Columbus, 1996.

(*205*) Pearson, A. C., Liu, J., Pound, E., Uprety, B., Woolley, A. T., Davis, R. C., and Harb, J. N. (2012). DNA origami metallized site specifically to form electrically conductive nanowires. *The journal of physical chemistry. B 116*, 10551–60.

(*206*) Livshits, G. I., Stern, A., Rotem, D., Borovok, N., Eidelshtein, G., Migliore, A., Penzo, E., Wind, S. J., Di Felice, R., Skourtis, S. S., Cuevas, J. C., Gurevich, L., Kotlyar, A. B., and Porath, D. (2014). Long-range charge transport in single G-quadruplex DNA molecules. *Nature Nanotechnology 9*, 1040–1046.

(*207*) Chen, W., Ahmed, H., and Nakazoto, K. (1995). Coulomb blockade at 77 K in nanoscale metallic islands in a lateral nanostructure. *Applied Physics Letters 66*, 3383–3384.

(*208*) Reed, M., Zhou, C., Muller, C., Burgin, T., and Tour, J. (1997). Conductance of a molecular junction. *Science 278*, 252–254.

(*209*) Kubatkin, S., Danilov, A., Hjort, M., Cornil, J., Brédas, J. L., Stuhr-Hansen, N., Hedegård, P., and Bjørnholm, T. (2003). Single-electron transistor of a single organic molecule with access to several redox states. *Nature 425*, 698–701.

(*210*) Li, T., Hu, W., and Zhu, D. (2010). Nanogap electrodes. *Advanced Materials 22*, 286–300.

(*211*) He, J., Fu, Q., Lindsay, S., Ciszek, J. W., and Tour, J. M. (2006). Electrochemical origin of voltage-controlled molecular conductance switching. *Journal of the American Chemical Society 128*, 14828–14835.

(*212*) Stern, A., Eidelshtein, G., Zhuravel, R., Livshits, G. I., Rotem, D., Kotlyar, A., and Porath, D. (2018). Highly Conductive Thin Uniform Gold-Coated DNA Nanowires. *Advanced Materials 1800433*, 1–5.

(*213*) Zessin, J. Synthese eines elektrisch leitfähigen Polymers für die Integration in DNA-Origami-Strukturen., Master thesis, Technische Universität Dresden, 2014.

(*214*) Nečas, D., and Klapetek, P. (2012). Gwyddion: an open-source software for SPM data analysis. *Central European Journal of Physics 10*, 181–188.

(*215*) Schindelin, J. et al. (2012). Fiji: an open-source platform for biological-image analysis. *Nature Methods 9*, 676–682.

(*216*) Ludwigs, S., *P3HT Revisited – From Molecular Scale to Solar Cell Devices*; Ludwigs, S., Ed.; Springer, Berlin, Heidelberg: Heidelberg, 2014; Vol. 265.

(*217*) Chayer, M., Faïd, K., and Leclerc, M. (1997). Highly Conducting Water-Soluble Polythiophene Derivatives. *Chemistry of Materials 9*, 2902–2905.

(*218*) Adachi, I., Miyakoshi, R., Yokoyama, A., and Yokozawa, T. (2006). Synthesis of Well-Defined Polythiophene with Oxyethylene Side Chain: Effect of Phosphine Ligands on Catalyst-Transfer Polycondensation. *Macromolecules 39*, 7793–7795.

(*219*) Lu, B., Li, G., Rodriguez, S., Liu, J., Eriksson, M., Tan, Z., Song, J., Yee, N., Farina, V., and Senanayake, C. (2013). Development of a Practical Synthesis of 4-[6-(Morpholinomethyl)-pyridin-3-yl]naphthalen-1-amine, a Key Intermediate for the Synthesis of BIRB 1017, a Potent p38 MAP Kinase Inhibitor. *SynLett 24*, 317–322.

(*220*) Doubina, N., Ho, A., Jen, A. K., and Luscombe, C. K. (2009). Effect of initiators on the Kumada catalysttransfer polycondensation reaction. *Macromolecules 42*, 7670–7677.

(*221*) Webster, O. W. (1991). Living Polymerization Methods. *Science 251*, 887–893.

(*222*) Yokozawa, T., Muroya, D., Sugi, R., and Yokoyama, A. (2005). Convenient method of chain-growth polycondensation for well-defined aromatic polyamides. *Macromolecular Rapid Communications 26*, 979–981.

(*223*) Lohwasser, R. H., and Thelakkat, M. (2011). Toward Perfect Control of End Groups and Polydispersity in Poly(3-hexylthiophene) via Catalyst Transfer Polymerization. *Macromolecules 44*, 3388–3397.

(*224*) Ma, Y.-Z., Shaw, R. W., Yu, X., O'Neill, H. M., and Hong, K. (2012). Excited-state dynamics of water-soluble polythiophene derivatives: temperature and side-chain length effects. *The journal of physical chemistry. B 116*, 14451–60.

(*225*) Bertinelli, F., and Delia Casa, C. (1996). Solvatochromism in poly[3-(10-hydroxydecyl)]thiophene: A spectrokinetic study of the conformational transition. *Polymer 37*, 5469–5475.

(*226*) Tremel, K., and Ludwigs, S. (2014). Morphology of P3HT in thin films in relation to optical and electrical properties. *Advances in Polymer Science 265*, 39–82.

(*227*) Spano, F. C. (2010). The Spectral Signatures of Frenkel Polarons in. *Accounts of Chemical Research 43*, 429–439.

(*228*) Clark, J., Chang, J. F., Spano, F. C., Friend, R. H., and Silva, C. (2009). Determining exciton bandwidth and film microstructure in polythiophene films using linear absorption spectroscopy. *Applied Physics Letters 94*, 2007–2010.

(*229*) Clark, J., Silva, C., Friend, R. H., and Spano, F. C. (2007). Role of intermolecular coupling in the photophysics of disordered organic semiconductors: Aggregate emission in regioregular polythiophene. *Physical Review Letters 98*, 1–4.

(*230*) Wiberg, N., *Lehrbuch der Anorganischen Chemie*, 102nd ed.; Holleman, A., Wiberg, N., and Wiberg, E., Eds.; Walter de Gruyter: Berlin, 2008.

(*231*) Walzer, K., Männig, B., Pfeiffer, M., and Leo, K. (2007). Highly efficient organic devices based on electrically doped transport layers. *Chemical Reviews 107*, 1233–1271.

(*232*) Deschler, F., Riedel, D., Deák, A., Ecker, B., Von Hauff, E., and Da Como, E. (2015). Imaging of morphological changes and phase segregation in doped polymeric semiconductors. *Synthetic Metals 199*, 381–387.

(*233*) Jacobs, I. E., and Moulé, A. J. (2017). Controlling Molecular Doping in Organic Semiconductors. *Advanced Materials 1703063*, 1–39.

(*234*) Hamidi-Sakr, A., Biniek, L., Bantignies, J. L., Maurin, D., Herrmann, L., Leclerc, N., Lévêque, P., Vijayakumar, V., Zimmermann, N., and Brinkmann, M. (2017). A Versatile Method to Fabricate Highly In-Plane Aligned Conducting Polymer Films with Anisotropic Charge Transport and Thermoelectric Properties: The Key Role of Alkyl Side Chain Layers on the Doping Mechanism. *Advanced Functional Materials 27*, 1–13.

(*235*) Scholes, D. T., Hawks, S. A., Yee, P. Y., Wu, H., Lindemuth, J. R., Tolbert, S. H., and Schwartz, B. J. (2015). Overcoming Film Quality Issues for Conjugated Polymers Doped with F4TCNQ by Solution Sequential Processing: Hall Effect, Structural, and Optical Measurements. *Journal of Physical Chemistry Letters 6*, 4786–4793.

(*236*) Meijer, E. J., Detcheverry, C., Baesjou, P. J., Van Veenendaal, E., De Leeuw, D. M., and Klapwijk, T. M. (2003). Dopant density determination in disordered organic field-effect transistors. *Journal of Applied Physics 93*, 4831–4835.

(*237*) Vardeny, Z., Ehrenfreund, E., Brafman, O., and Horovitz, B. (1983). Resonant Raman Scattering from Amplitude Modes in trans-(CH)x and -(CD)x. *Physical Review Letters 51*, 2326–2329.

(*238*) Mulliken, R. S., and Person, W. B. (1969). Molecular Compounds and their Spectra. XXI. Some General Considerations. *Journal of American Chemical Society 91*, 3409–3413.

(*239*) Tietze, M. L., Kampar, E., and Neilands, O. (1986). Related content Degree of Charge Transfer in Donor – Acceptor Systems of the $\pi - \pi$ Type Degree of Charge Transfer in Donor-Acceptor Systems of the p-p Type. *Russian Chemical Reviews 55*, 637–651.

(*240*) Chappell, J. S., Bloch, A. N., Bryden, W. A., Maxfield, M., Poehler, T. O., and Cowan, D. O. (1981). Degree of charge-transfer in organic conductors by infrared-absorption spectroscopy. *Journal of the American Chemical Society 103*, 2442–2443.

(*241*) Meneghetti, M., and Pecile, C. (1986). Charge–transfer organic crystals: Molecular vibrations and spectroscopic effects of electron–molecular vibration coupling of the strong electron acceptor TCNQF4. *The Journal of Chemical Physics 84*, 4149–4162.

(*242*) Collins, R. W., and Kim, Y. T. (1990). Ellipsometry for Thin-Film and Surface Analysis. *Analytical Chemistry 62*, 887–900.

(*243*) Campoy-Quiles, M., Alonso, M. I., Bradley, D. D., and Richter, L. J. (2014). Advanced ellipsometric characterization of conjugated polymer films. *Advanced Functional Materials 24*, 2116–2134.

(*244*) Prest, W. M., and Luca, D. J. (1979). The origin of the optical anisotropy of solvent cast polymeric films. *Journal of Applied Physics 50*, 6067–6071.

(*245*) Campoy-Quiles, M., Etchegoin, P. G., and Bradley, D. D. C. (2005). On the optical anisotropy of conjugated polymer thin films. *Physical Review B 72*, 045209.

(*246*) Chuang, S. Y., Chen, H. L., Lee, W. H., Huang, Y. C., Su, W. F., Jen, W. M., and Chen, C. W. (2009). Regioregularity effects in the chain orientation and optical anisotropy of composite polymer/fullerene films for high-efficiency, large-area organic solar cells. *Journal of Materials Chemistry 19*, 5554–5560.

(*247*) Frischeisen, J., Yokoyama, D., Adachi, C., and Brütting, W. (2010). Determination of molecular dipole orientation in doped fluorescent organic thin films by photoluminescence measurements. *Applied Physics Letters 96*, 2008–2011.

(*248*) Xiao, M., Jasensky, J., Zhang, X., Li, Y., Pichan, C., Lu, X., and Chen, Z. (2016). Influence of the side chain and substrate on polythiophene thin film surface, bulk, and buried interfacial structures. *Physical Chemistry Chemical Physics 18*, 22089–22099.

(*249*) Jacobs, I. E., Aasen, E. W., Oliveira, J. L., Fonseca, T. N., Roehling, J. D., Li, J., Zhang, G., Augustine, M. P., Mascal, M., and Moulé, A. J. (2016). Comparison of solution-mixed and sequentially processed P3HT:F4TCNQ films: Effect of doping-induced aggregation on film morphology. *Journal of Materials Chemistry C 4*, 3454–3466.

(*250*) Brinkmann, M. (2011). Structure and morphology control in thin films of regioregular poly(3-hexylthiophene). *Journal of Polymer Science, Part B: Polymer Physics 49*, 1218–1233.

(*251*) Duong, D. T., Phan, H., Hanifi, D., Jo, P. S., Nguyen, T. Q., and Salleo, A. (2014). Direct observation of doping sites in temperature-controlled, p-doped p3ht thin films by conducting atomic force microscopy. *Advanced Materials 26*, 6069–6073.

(*252*) Kohn, P., Rong, Z., Scherer, K. H., Sepe, A., Sommer, M., Müller-Buschbaum, P., Friend, R. H., Steiner, U., and Hüttner, S. (2013). Crystallization-induced 10-nm structure formation in P3HT/PCBM blends. *Macromolecules 46*, 4002–4013.

(*253*) Müller-Buschbaum, P. (2014). The active layer morphology of organic solar cells probed with grazing incidence scattering techniques. *Advanced Materials 26*, 7692–7709.

(*254*) Patel, S. N., Glaudell, A. M., Peterson, K. A., Thomas, E. M., O'Hara, K. A., Lim, E., and Chabinyc, M. L. (2017). Morphology controls the thermoelectric power factor of a doped semiconducting polymer. *Science Advances 3*, 24–26.

(*255*) Nagamatsu, S., Takashima, W., Kaneto, K., Yoshida, Y., Tanigaki, N., Yase, K., and Omote, K. (2003). Backbone arrangement in "friction-transferred" regioregular poly(3-alkylthiophene)s. *Macromolecules 36*, 5252–5257.

(*256*) Seemann, R., Herminghaus, S., and Jacobs, K. (2001). Dewetting patterns and molecular forces: A reconciliation. *Physical Review Letters 86*, 5534–5537.

(*257*) Glaudell, A. M., Cochran, J. E., Patel, S. N., and Chabinyc, M. L. (2015). Impact of the doping method on conductivity and thermopower in semiconducting polythiophenes. *Advanced Energy Materials 5*, 1401072.

(*258*) Fischer, F. Development of new approaches for characterising DNA origami-based nanostructures with atomic force microscopy and super-resolution microscopy., Dissertation, Technische Universität Dresden, 2018.

(*259*) Kamps, A. C., Cativo, M. H. M., Chen, X.-J., and Park, S.-J. (2014). Self-Assembly of DNA-Coupled Semiconducting Block Copolymers. *Macromolecules 47*, 3720–3726.

(*260*) Zimm, B. H. (1948). The Scattering of Light and the Radial Distribution Function of High Polymer Solutions. *The Journal of Chemical Physics 16*, 1093.

(*261*) Wyatt, P. J. Light scattering and the absolute characterization of macromolecules., 1993.

(*262*) Zuker, M. (2003). Mfold web server for nucleic acid folding and hybridization prediction. *Nucleic Acids Research 31*, 3406–3415.

(*263*) Kibbe, W. A. (2007). OligoCalc: An online oligonucleotide properties calculator. *Nucleic Acids Research 35*, 43–46.

(*264*) Zhang, J. X., Fang, J. Z., Duan, W., Wu, L. R., Zhang, A. W., Dalchau, N., Yordanov, B., Petersen, R., Phillips, A., and Zhang, D. Y. (2017). Predicting DNA hybridization kinetics from sequence. *Nature Chemistry 10*, 91.

(*265*) Thiel, A. J., Frutos, A. G., Jordan, C. E., Corn, R. M., and Smith, L. M. (1997). In Situ Surface Plasmon Resonance Imaging Detection of DNA Hybridization to Oligonucleotide Arrays on Gold Surfaces. *Analytical Chemistry 69*, 4948–4956.

(*266*) Nelson, B. P., Grimsrud, T. E., Liles, M. R., Goodman, R. M., and Corn, R. M. (2001). Surface Plasmon Resonance Imaging Measurements of DNA and RNA Hybridization Adsorption onto DNA Microarrays. *Analytical Chemistry 73*, 1–7.

(*267*) Ouldridge, T. E., Šulc, P., Romano, F., Doye, J. P., and Louis, A. A. (2013). DNA hybridization kinetics: Zippering, internal displacement and sequence dependence. *Nucleic Acids Research 41*, 8886–8895.

(*268*) Craig, M. E., Crothers, D. M., and Doty, P. (1971). Relaxation kinetics of dimer formation by self complementary oligonucleotides. *Journal of Molecular Biology 62*, 383–401.

(*269*) Hoogsteen, K. (1963). The crystal and molecular structure of a hydrogen-bonded complex between 1-methylthymine and 9-methyladenine. *Acta Crystallographica 16*, 907–916.

(*270*) Idili, A., Vallée-Bélisle, A., and Ricci, F. (2014). Programmable pH-triggered DNA nanoswitches. *Journal of the American Chemical Society 136*, 5836–5839.

(*271*) Plum, G. E., Park, Y. W., Singleton, S. F., Dervan, P. B., and Breslauer, K. J. (1990). Thermodynamic characterization of the stability and the melting behavior of a DNA triplex: a spectroscopic and calorimetric study. *Proceedings of the National Academy of Sciences 87*, 9436–9440.

(*272*) Herbert, A. D., Carr, A. M., Hoffmann, E., and Lichten, M. (2014). FindFoci: A focus detection algorithm with automated parameter training that closely matches human assignments, reduces human inconsistencies and increases speed of analysis. *PLoS ONE 9*, e114749.

(*273*) Zessin, J., Fischer, F., Heerwig, A., Kick, A., Boye, S., Stamm, M., Kiriy, A., and Mertig, M. (2017). Tunable fluorescence of a semiconducting polythiophene positioned on DNA Origami. *Nano Letters 17*, 5163–5170.

(*274*) Ricci, D., and Braga, P. C. In *Atomic Force Microscopy*; Humana Press: New York, 2004; Vol. 242, pp 25–38.

(*275*) Knaapila, M., Evans, R. C., Gutacker, A., Garamus, V. M., Torkkeli, M., Adamczyk, S., Forster, M., Scherf, U., and Burrows, H. D. (2010). Solvent dependent assembly of a polyfluorene-polythiophene "rod-Rod" block copolyelectrolyte: Influence on photophysical Properties. *Langmuir 26*, 5056–5066.

(*276*) Al Attar, H. A., and Monkman, A. P. (2007). Effect of surfactant on water-soluble conjugated polymer used in biosensor. *Journal of Physical Chemistry B 111*, 12418–12426.

(*277*) Shen, H., Kou, C., He, M., Yang, H., and Liu, K. (2014). Synthesis and surfactochromicity of 1,4-diketopyrrolo[3,4-c]pyrrole(DPP)- based anionic conjugated polyelectrolytes. *Journal of Polymer Science, Part A: Polymer Chemistry 52*, 739–751.

(*278*) Lakowicz, J. R. In *Principles of Fluorescence Spectroscopy*, 3rd ed.; Springer: Boston, 2006, pp 205–235.

(*279*) Jenekhe, S. A., and Osaheni, J. A. (1994). Excimers and exciplexes of conjugated polymers. *Science 265*, 765–768.

(*280*) Scorzoni, A., and Finetti, M. (1988). Metal / Semiconductor Contact Resistivity and Its Determination From Contact. *Materials Science reports 3*, 79–138.

(*281*) Kwon, S., Lee, S. J., Kim, S. M., Lee, Y., Song, H., and Park, J. Y. (2015). Probing the nanoscale Schottky barrier of metal/semiconductor interfaces of Pt/CdSe/Pt nanodumbbells by conductive-probe atomic force microscopy. *Nanoscale 7*, 12297–12301.

(*282*) Hammer, B. A., Reyes-Martinez, M. A., Bokel, F. A., Liu, F., Russell, T. P., Hayward, R. C., Briseno, A. L., and Emrick, T. (2014). Reversible, self cross-linking nanowires from thiol-functionalized polythiophene diblock copolymers. *ACS Applied Materials and Interfaces 6*, 7705–7711.

(*283*) Kim, H. J., Skinner, M., Yu, H., Oh, J. H., Briseno, A. L., Emrick, T., Kim, B. J., and Hayward, R. C. (2015). Water Processable Polythiophene Nanowires by Photo-Cross-Linking and Click-Functionalization. *Nano Letters 15*, 5689–5695.

(*284*) Brunner, H. Aufbau von DNA-Origami/Nanopartikel-Hybridstrukturen., Master thesis, Technische Universität Dresden, 2017.

(*285*) Wang, D., Zhang, Y., Wang, M., Dong, Y., Zhou, C., Isbell, M. A., Yang, Z., Liu, H., and Liu, D. (2016). A switchable DNA origami nanochannel for regulating molecular transport at the nanometer scale. *Nanoscale 8*, 3944.

(*286*) Gopinath, A., Miyazono, E., Faraon, A., and Rothemund, P. W. K. (2016). Engineering and mapping nanocavity emission via precision placement of DNA origami. *Nature 535*, 401–405.

(*287*) Gopinath, A., and Rothemund, P. W. K. (2014). Optimized assembly and covalent coupling of single-molecule DNA origami nanoarrays. *ACS Nano 8*, 12030–12040.

Publications and Conference Contributions

Publications

"Tunable fluorescence of a semiconducting polythiophene positioned on DNA origami."; J. Zessin, F. Fischer, A. Heerwig, A. Kick, M. Stamm, A. Kiriy, M. Mertig; *Nano Letters* 2017; 17(8): 5163-5170.

"Molecular doping of a water-soluble polythiophene derivative."; J. Zessin, E. Bittrich, J. Zessin, M. Malanin, J. Posseckardt, B. Voit, K.-J. Eichhorn, A. Kiriy, M. Mertig; *Physica Status Solidi A* 2019; published (online): doi.org/10.1002/pssa.201800772.

"Synthesis and characterization of a regioregular side-chain semifluorinated polythiophene", C. Horn, D. Pospiech, J. Zessin, S. Stein, D. Jehnichen, H. Komber, M. Göbel, B. Voit, A. Kiriy; *Physica Status Solidi A* 2019; published (online): doi.org/10.1002/pssa.201800747.

Conference Contributions

Oral Presentations

Future Trends in DNA-based Nanotechnology, International Workshop in Dresden 2017, Germany; J. Zessin, F. Fischer, A. Heerwig, A. Kick, A. Kiriy, M. Mertig; “Semiconducting polythiophenes on a 2D DNA origami template”

14th European Conference on Molecular Electronic in Dresden 2017, Germany; J. Zessin, F. Fischer, A. Heerwig, A. Kick, B. Voit, A. Kiriy, M. Mertig; “DNA origami-templated formation of semiconducting polythiophene wires”

International Workshop on Advanced 3D Patterning in Dresden 2017, Germany; J. Zessin, F. Fischer, A. Heerwig, A. Kick, A. Kiriy, M. Mertig; “Positioning of a semiconducting polythiophene on a DNA origami template”

Biomolecular Electronics, International Conference in Madrid 2018, Spain; J. Zessin, F. Fischer, M. Lakatos, B. Voit, A. Kiriy, M. Mertig; “DNA-Templated Formation of Polythiophene Paths”

Poster Presentations

Engineering of Functional Interfaces, International Workshop in Hannover 2015, Germany; J. Zessin, F. Fischer, A. Heerwig, A. Kick, A. Kiriy, M. Mertig; "Synthesis of a polythiophene-oligonucleotide-conjugate for site-specific integration into DNA origami"

18th International Symposium on Field- and Flow-Based Separations in Dresden 2016, Germany, J. Zessin, F. Fischer, A. Heerwig, S. Boye, A. Kiriy, M. Mertig; "Synthesis of a polythiophene-oligodeoxynucleotide block copolymer for the site-specific attachment to DNA origami"

22nd International Conference on DNA Computing and Molecular Programming in München 2016, Germany, J. Zessin, F. Fischer, A. Heerwig, A. Kick, A. Kiriy, M. Mertig; "Site-specific attachment of a semiconducting polythiophene-derivate to DNA origami structures"

International Conference NanoBioMater in Bad Herrenalb 2017, Germany; J. Zessin, F. Fischer, A. Heerwig, A. Kick, A. Kiriy, M. Mertig; "Synthesis, characterization and DNA-templated arrangement of a semiconducting polymer"; third place for poster award

Engineering of Functional Interfaces, International Workshop in Marburg 2017, Germany; J. Zessin, F. Fischer, A. Heerwig, A. Kick, A. Kiriy, M. Mertig; "Synthesis, characterization and DNA-templated arrangement of a semiconducting polythiophene"

13. Dresdner Sensor-Symposium in Dresden 2017, Germany; J. Zessin, F. Fischer, A. Heerwig, A. Kick, A. Kiriy, M. Mertig; "Tensid-induzierte optische Reaktion einer Polythiophen-DNA-Origami Hybridstruktur"

Hebrew University Jerusalem Israel Nano Center Annual Conference at The Dead Sea 2018, Israel; J. Zessin, F. Fischer, A. Heerwig, A. Kick, A. Kiriy, M. Mertig; Optically responsive functionality of a polythiophene-DNA origami hybrid-structure"

15th Annual Conference on foundations of nanoscience in Snowbird 2018, USA; J. Zessin, F. Fischer, A. Heerwig, A. Kick, B. Voit, A. Kiriy, M. Mertig; "DNA origami-templated formation of semiconducting polythiophene wires"

Engineering of Functional Interfaces, International Workshop in Wittenberg 2018, Germany; J. Zessin, E. Bittrich, M. Malanin, J. Posseckardt, B. Voit, M. Mertig, A. Kiriy, K.J. Eichhorn; "A conducting polythiophene for bioelectronics"

Versicherung

Hiermit versichere ich, dass ich die vorliegende Arbeit ohne unzulässige Hilfe Dritter und ohne Benutzung anderer als der angegebenen Hilfsmittel angefertigt habe; die aus fremden Quellen direkt oder indirekt übernommenen Gedanken sind als solche kenntlich gemacht. Die Arbeit wurde bisher weder im Inland noch im Ausland in gleicher oder ähnlicher Form einer anderen Prüfungsbehörde vorgelegt.

Die vorliegende Dissertation wurde in dem Zeitraum von Juni 2015 bis Februar 2019 unter der wissenschaftlichen Betreuung von Herr Prof. Michael Mertig (TU Dresden) und Dr. Anton Kiriy (IPF Dresden) angefertigt. Die Arbeit wurde am Leibniz-Institut für Polymerforschung Dresden e.V. und der Technischen Universität Dresden durchgeführt. Ausgewählte Experimente wurden am Kurt-Schwabe Institut für Mess- und Sensortechnik durchgeführt. Leitfähigkeitsmessungen an den Nanostrukturen wurden in Zusammenarbeit der Arbeitsgruppe von Prof. Danny Porath (Hebrew University of Jerusalem, Israel).

Frühere Promotionsverfahren fanden nicht statt.

Ich erkenne die Promotionsordnung der Fakultät Mathematik und Naturwissenschaften der Technischen Universität Dresden vom 23.02.2011 in zuletzt geänderter Fassung vom 15.06.2011 und 18.06.2014 in vollem Umfang an.

Dresden den 04.03.2019,

Johanna Zessin